SPECTROSCOPIC CHARACTERIZATION OF MONOMETALLIC AND BIMETALLIC MODEL CATALYSTS

A Dissertation

by

KAI LUO

Submitted to the Office of Graduate Studies of
Texas A&M University
in partial fulfillment of the requirements for the degree of

DOCTOR OF PHILOSOPHY

May 2006

Major Subject: Chemistry

SPECTROSCOPIC CHARACTERIZATION OF MONOMETALLIC AND BIMETALLIC MODEL CATALYSTS

A Dissertation

by

KAI LUO

Submitted to the Office of Graduate Studies of
Texas A&M University
in partial fulfillment of the requirements for the degree of

DOCTOR OF PHILOSOPHY

Approved by:

Chair of Committee,	D. Wayne Goodman
Committee Members,	David H. Russell
	Simon W. North
	Donald G. Naugle
Head of Department	Emile A. Schweikert

May 2006

Major Subject: Chemistry

ABSTRACT

Spectroscopic Characterization of Monometallic and Bimetallic Model Catalysts.

(May 2006)

Kai Luo, B.S., Jilin University;

M.S., Texas A& M University

Chair of Advisory Committee: Dr. D. Wayne Goodman

Monometallic and bimetallic model catalysts on either refractory metal single-crystals as planar surfaces or oxide supports as nano-size clusters have been systematically studied using X-ray photoemission spectroscopy (XPS), low energy ion scattering spectroscopy (LEIS), low energy electron diffraction (LEED), infrared reflection absorption spectroscopy (IRAS), and temperature programmed desorption (TPD) under ultra-high vacuum (UHV) conditions. Of particular interest in this investigation is the characterization of the surface composition, morphology, and electronic/geometric structure of the following catalysts: Au/TiOx, Au-Pd/Mo(110), Au-Pd/SiO_2, Cu-Pd/Mo(110), and Sn/Pd(100). Structure-reactivity correlations during surface-alloy formation and adsorption-desorption processes were explained in terms of ensemble and ligand effects. Prospects of translating the accumulated atomic-level information into more efficient “real world” catalysts were discussed.

DEDICATION

To my parents and my wife

ACKNOWLEDGMENTS

I would like to express my deepest gratitude to my advisor, Dr. D. Wayne Goodman, for his expert guidance and encouragement. My academic journey at Texas A&M University began in Fall 1997 when I joined the Ph.D. program in Chemistry under the tutelage of Dr. Goodman. Challenges on the family front pushed me to switch to a Master's Degree program in August 2000. My four-year hiatus, however, did not deter Dr. Goodman from encouraging me to reactivate my research work and ultimately finish my Ph.D. degree. I remain ever grateful to Dr. Goodman for offering me a rare second opportunity to fulfill a life-long dream.

Special thanks go to my wife, my parents, and my sister for their tremendous support during the trying times of my graduate studies.

I sincerely appreciate the contributions of Dr. Russell, Dr. North, and Dr. Naugle for having been part of my research evaluation committee.

Past and present members of Dr. Goodman's research group, specifically Dr. Mingshu Chen, Dr. W. T. Wallace, Dr. Sunsik Lee, Dr. C.-W. Yi, Dr. Paul Bagus, Dr. D. Y. Kim, Dr. Q. Guo, Dr. Todd St. Clair, Dr. C. C. Chusuei, Dr. K. Davis, T. Wei, definitely deserve special mention. Thanks are due to Ms. Amy Liu for her kind words of encouragement. Special thanks also go to Jack Baricuatro, Susan Dean, Stephanus Axnanda, and Dr. Patrick Han for proof reading my manuscript.

Funding from the Department of Energy, National Science Foundation, and the Welch Foundation is gratefully acknowledged.

Finally, I thank God for his endless love and blessing.

TABLE OF CONTENTS

Page

LIST OF FIGURES

Page

Page

Page

Page

Page

Page

Page

LIST OF TABLES

Page

INTRODUCTION

The ability of certain chemical species to alter reaction pathways, without itself being consumed at the end of a chemical reaction, has long been the subject of scientific investigations. In the early 1800's, Mitscherlic and Berzelius conducted pioneering studies on catalysis involving sugar fermentation and oxidation of ethanol.[1,2] Interest on the field was further invigorated by the works of de Saussure, Faraday, and Liebig who catalogued a wide variety of catalytic reactions.[1,2] Langmuir's introduction of the so-called checkerboard model dramatically steered the direction of heterogeneous catalysis research towards correlating the catalytic phenomena with physicochemical properties of the solid surface.[3] More than two centuries have passed and this fundamental goal continues to be pursued using now an arsenal of modern surface science techniques.

The quest for high-performing catalysts has spawned research that employs multimetallic and supported catalytic systems. Because of the inherently complex nature of these proposed catalysts, it is not surprising to learn that the scientific underpinnings of some promising results remain phenomenological and speculative. Adding to the challenge is the fact that, for multimetallic systems such as alloys, the intended bulk composition of a catalyst does not necessarily represent its surface composition. To address such a multivariate problem requires the use of model systems that not only

---

This dissertation follows the style of the *Journal of Physical Chemistry B.*

mimic efficient "real world" catalysts but also allow a study of the fundamental science behind the observed efficacy.

Surface science investigations of model catalysts allow systematic surface property-reactivity correlations that are otherwise cumbersome, if not impossible, to establish using real industrial-grade catalysts. Strategic use of well-characterized mono- and bimetallic model catalysts has provided atomic-level information on heterogeneous catalysis involving transition metals. The present investigation examines the surface structure, composition, electronic properties, and chemisorptive behavior of five model catalysts, *viz.* Au/TiOx, Au-Pd/Mo(110), Au-Pd/SiO_2, Cu-Pd/Mo(110), and Sn/Pd(100). A detailed rationale for each chosen system is described in the succeeding sections.

Monometallic Model Catalysts

A fascinating case that illustrates the need for model catalysts is the unusual activity of Au at the nanometer regime. The origin of the extraordinary catalytic activity of oxide-supported nano-sized Au for low temperature CO oxidation[4,5] and selective propylene oxidation[6] has stimulated considerable interest in literature. Various mechanisms, including particle size effects and metal-support interactions, have been proposed to account for the unusual Au catalytic activity; however, a definitive explanation is still in question.[7-10] A re-visitation of these experiments using model catalysts that are well-characterized and probed by surface-sensitive techniques is one of the specific goals of the current research.

Recent studies from our group have shown that a Au bilayer grown on an ultra-thin reduced titania exhibits a substantially higher CO oxidation turnover frequency (TOF)

compared to a high surface-area Au/TiO_2 catalyst.[11] Results from Auger electron spectroscopy (AES) and high resolution electron energy loss spectroscopy (HREELS) indicated wetting of Au overlayers on the titania support, therefore eliminating particle-shape and support effects as the cause of the improved catalytic activity; a Au-only reaction pathway has been invoked.[11,12] As an extension of this work, the present study investigates the growth mode, electronic properties, and bonding strength of Au grown on a reduced TiOx film using low energy ion scattering spectroscopy (LEIS), low energy electron diffraction (LEED), X-ray photoelectron spectroscopy (XPS), and temperature programmed desorption (TPD).

Bimetallic Model Catalysts

Bimetallic catalysts are often deemed more superior over their single-metal counterparts because of a possible synergism of properties resulting from the combination; better catalytic reactivity, selectivity, and stability have been reported for various heterogeneous catalytic reactions.[13,14] A major objective of the present investigation is to enrich the fundamental understanding of surface morphology, composition, geometric structure, and electronic properties of bimetallic alloy catalysts. The establishment of surface-structure-reactivity relationships is expected to serve as blueprint for designing high-performing catalysts.

Ligand vs. Ensemble Effects

Catalysis by bimetallic systems is commonly viewed in terms of two effects: ligand effects and ensemble effects.

Adsorbate-surface bond strength plays a crucial role in catalytic reactions. For a bimetallic surface made from metals A and B, electronic properties of a particular constituent are often perturbed by nearby atoms. Resultant modifications in the adsorbate-surface bonding eventually lead to changes in the reaction mechanism. This effect is referred to as ligand effect.

A good example is provided by CO TPD studies of Pd overlayers on Mo(110).[15] Multiple deposition of Pd overlayers onto Mo(110) surface is known to yield a bulk-like Pd(111) surface structure. Thus, at a low CO coverage, the TPD CO desorption feature at 480 K resembles that of a TPD spectrum of a pristine Pd(111) surface. However, for a Mo(110) surface modified by 1.0 monolayer (ML) Pd with a (111) texture, the CO desorption temperature decreases dramatically to 290 K, representing a 12 kcal/mol decrease in binding energy. A similar phenomenon was observed for pseudomorphic Pd monolayer on other transition-metal surfaces, like W and Ta.[16,17] These data indicate that the Mo substrate substantially modifies the electronic structure of the Pd monolayer, resulting to a significant decrease in Pd-CO bonding energy.

The addition of a second metal B into metal A can induce changes in geometric surface structure. Since catalytic reactions often require a prescribed number of surface constituent atoms to be available in a certain geometric configuration, the introduction of a foreign adatom gives rise to the so-called ensemble effects.

The adsorption and subsequent reaction of 1,3-butadiene on Sn-modified Pt(111) surfaces have been ascribed to ensemble effects.[18] Well-defined Sn-Pd ensembles were found to be formed on (2x2) and ($\sqrt{3}$ x $\sqrt{3}$)*R*30^{o} Sn/Pt(111) alloy surfaces. A large

amount of reversibly adsorbed 1,3-butadiene was preserved, suggesting that the observed surface ensembles inhibited the decomposition pathway of the diene. Ensemble effects can, therefore, be utilized to tailor pathways for selective hydrogenation of butadiene to certain products.[19]

Although a stark differentiation of ligand and ensemble effects could be quite difficult, thorough studies of these effects will definitely improve our understanding of reaction mechanisms and our capability of tailoring the reaction pathways/optimizing of catalyst design.

Synthesis of Bimetallic Model Catalysts

Typically, two types of bimetallic model catalyst, planar bimetallic surfaces and oxide supported bimetallic nano-particles (clusters), were utilized in the studies of heterogeneous catalysis.

First, a vapor deposition of one metal A on a second well-defined single crystal metal B surface is widely applied to achieve a bimetal surface. Due to the well defined surface electronic and structural properties of the substrate surface B and an atomic layer deposition control of metal A, the system offers an excellent avenue of research into the catalytic properties of bimetal systems. However, due to the bulk atomic ratio of substrate metal B to the deposited metal A overlayers is always infinite in the case above; certain difficulties exist under the situation of studying surface properties with different bulk and surface compositions. Alternatively, another approach of sequential depositing both metals on a third well-defined single crystal substrate is employed. With this method, we can easily change the surface/bulk composition with varying the deposition

ratio and good temperature control, and thus obtain a desired surface composition and/or structure. In this work, both approaches are utilized to prepare planar bimetallic model catalysts in our investigation.

Moreover, the high level complexity of particle size effect and metal-support interaction in catalysis requires higher level model systems. Recently, an approach of synthesizing a planar and well-characterized oxide thin film support and subsequent sequential bimetal vapor deposition offers a new methodology to simulate the oxide-support interactions in high surface area catalysts. With such a model system and utilization of the complementary modern surface sensitive techniques, the complex issues on "real world" catalysts can be directly studied and addressed. In our work, the Au-Pd bimetal nano clusters are synthesized on an amorphous ultra-thin SiO_2 film, serving as an excellent oxide-support bimetallic model catalyst.

Au-Pd, Cu-Pd, Sn-Pd Model Catalysts

Compared to monometallic Pd catalysts, nano-sized bimetallic catalysts composed of Pd coupled with noble metal modifiers such as Au, Cu, Sn, exhibit dramatic enhancement in activity and selectivity for different heterogeneous reactions.[20-32] The use of surface-sensitive spectroscopic and microscopic techniques to acquire atomic-level information regarding the surface composition, morphology, physical/electronic structure, and chemisorptive/catalytic properties of bimetallic model catalysts is essential in understanding the role of noble metals (Au, Cu, Sn) in enhancing the catalytic properties of Pd.

Au-Pd

Au-Pd bimetallic catalysts have been found to have much higher reaction activity in vinyl acetate synthesis than monometallic Pd catalysts.[20] A significant selectivity increase for the products in acetylene hydrogenation,[21] vinyl acetate synthesis,[22,23] and CCl_2F_2 hydrodechlorination[24,25] has been reported using Au-Pd catalysts on silica supports.

It is essential to understand the interaction between planar Au and Pd metal films. Au and Pd are completely miscible at any ratio to form a solid solution after high temperature annealing.[33,34] Au-Pd alloy surfaces have been synthesized using different methods, such as mixing of compound solutions and physical evaporations, and studied by various surface techniques, such as AES, XPS, LEED.[35-38]

Wise et al.[35] claimed that the surface and bulk Pd-to-Au molar ratios were the same for Au-Pd alloy microspheres; this conclusion was derived from Auger studies pretreated at 725 K in atmospheric O_2 environment. Also, Pd surface segregation in a Pd-enriched alloy resulted after a prolonged heating in O_2 atmosphere. Maire et al.[39] also reported Pd-Au surface molar ratio of 1 : 1 for the bulk 50%-50% Au-Pd alloy cleaned by Ar^+ sputtering. However, Somorjai and coworkers[36] reported that significant Au surface segregation occurred after annealing at 600 ^oC in vacuum; a slightly Pd-enriched surface was seen in their AES studies after an extensive 1.5 keV Ar^+ sputtering. Swartzfager et al.'s Ne^+ scattering data[40] on Au-Pd alloy surfaces were in agreement to Somorjai's results.

Au-segregated surface on a carbon supported Au-Pd alloy annealed at 873 K were reported by Anton et al.[41] using AES and X-ray fluorescence spectroscopy; the segregation was more pronounced in low to medium Au concentrations. Moreover, by utilizing a more surface-sensitive technique- LEIS, Varga et al.[37] observed a Au enriched surface after Ar^+ sputtering, although XPS data indicated no differences between surface and bulk composition.

The electronic properties of Au-Pd alloys have been studied by X-ray absorption near-edge spectra (XANES), XPS and computation modeling.[42] It was proposed that d and sp orbital charge redistribution between Au and Pd occurred, thereby shifting negatively Au 4f and Pd 3d core level bind energies (CLBE) from the bulk values.

In studies of alloy growth on well-ordered single crystal surfaces, Au overlayer growth on Pd(111) was investigated by Spicer et al,[43] and Au diffusion into the Pd matrix was observed. A new electronic state, different from that of pure Au or Pd metallic structures, was observed in the photoemission spectra; such a electronic state was proposed to contribute to the orbital hybridization in Au-Pd alloying. Ultra-thin Pd films grown on Au(111) were studied by Koel et al.[44] using LEIS, XPS and LEED. An epitaxial growth of the first few Pd layers over Au(111) surfaces was seen at 150 K. Upon Pd deposition at 300 K, surface alloying was observed in their studies. Interdiffusion between Pd an Au started early at 240 K. After annealing at 650 K, a surface composed of 80% Au was obtained. Using electrochemical processes,[45] Behm and coworkers synthesized a PdAu(111) alloy on Au(111) surfaces. Combined atomic-resolved scanning tunneling microscopy (STM) images and IR data clearly indicated

ensemble effects for CO and H adsorption on the alloy surfaces. Previous LEIS work[46] in our group also indicated Au surface segregation in Pd(1.0 ML)/Au(1.0 ML)/Mo(110) and Au(1.0 ML)/Pd(1.0 ML)/Mo(110) upon annealing to 800 K.

Several studies have addressed oxide-supported Au-Pd catalysts.[47-50] Structural properties of silica supported Au-Pd catalysts prepared from colloid precursors were studied using X-ray diffraction (XRD), extended X-ray absorption fine structure (EXAFS), and XANES.[48-50] Davis, et al., concluded that Pd atoms decorated a core of Au atoms using EXAFS.[48] Utilizing similar techniques, Lamb, et al., also concluded that a partial monolayer of Pd atoms decorated a Au-rich core.[49] On the other hand, Kaszkur [50] used XRD to show that a Pd-decorated surface can be transformed to a Au-decorated surface with a pulse of H_2. Related infrared studies from our laboratories of CO adsorption on alumina-supported Au-Pd and Cu-Pd clusters[47] suggested that a geometrical rather than a ligand effect was dominant.

Cu-Pd

Cu-Pd catalysts have been widely used in alkenes oxidation, hydrogenation of benzene, NO reduction, and CO oxidation.[26-28] Cu-Pd alloys, in particular, have attracted a host of structural, electronic, and gas adsorption studies.[51-61] These investigations typically employ Cu-Pd surface alloys that are grown on well-defined single crystal surfaces.

X-ray photoelectron diffraction (XPD) and LEED analyses of Pd/Cu(111) revealed the formation of a random surface alloy in the first three layers.[51] Bowker and coworkers presented a systematic study characterizing the Pd/Cu(110) system using

STM, XPS, LEED and TPD.[52] At coverages lower than 1.0 ML, a (2 x 1) surface structure can be discerned, albeit with a high level of disorder. Large, rectangular, flat-on-the-top Pd clusters emerged at higher Pd coverages. Extensive surface-layer intermingling transpired between 500 to 600 K, suggesting Cu-Pd alloy formation as evidenced by XPS core level binding energy shifts. Considerable surface morphological changes were detected by STM after annealing at and above 600 K. Acquisition of relatively large, flat domains at 720 K indicated thermal effects on surface morphology. Consistent with experimental results, theoretical studies on Pd/Cu(110) and Pd/Cu(100) demonstrated Cu-Pd surface alloying processes.[53,54] LEED and medium energy ion scattering (MEIS) studies of 0.5 ML Pd on Cu(100) showed a c(2x2) LEED pattern with 1/4 of Pd occupying second-layer sites.[55]

Earlier XPS work on Cu/Pd(111)[56] concluded that a layer-by-layer growth at 300K without alloying effects. The alloying process started at 450 K and exhibited a large negative Cu core level shift (CLS) of 0.9 eV relative to the Cu surface layer at 900 K. Initial- and final-state effect contributions to the shift were invoked. Asonen et al. claimed that a Stranski-Krastanov (SK) growth mode of Cu overlayers on Pd(100) surface.[57] Cu grew pseudomorphically up to 4 ML as can be gleaned from the (1x1) LEED pattern. The XPS CLBE converged to the bulk Cu(100) value up to 65 ML.

Growth of Cu-Pd overlayers on Mo(110) was probed by LEIS and XPS.[46] The LEIS experiments of Cu/Pd (1.0 ML/10.0 ML) and Pd/Cu (1.0 ML/10.0 ML) sequential deposition on Mo(110) upon annealing served as a good example for the surface composition studies. Depending on the deposition sequence and annealing temperature,

the variation of Cu and Pd surface composition (calculated from the normalized Pd and Cu scattering peak intensity) strongly indicated surface alloy formation. In addition, the Pd and Cu CLBE shifts upon annealing and alloying process were consistent with previously reported theoretical work.[58] Recent photoemission studies of Cu-Pd surface alloy on Ru(0001) also indicated alloy states between Pd 4d and Cu 3d valence bands.[60]

Studies of temperature-induced processes on bulk 1:1 PdCu(110) single-crystal showed that different Cu:Pd atomic ratios in the uppermost surface layer and in the surface region could be achieved with different thermal treatments.[61] Notably, an uppermost layer composed of *ca.* 90 -100% Cu was obtained after sputtering and annealing at 735 K.

In addition, theoretical studies of CO oxidation and NO reduction on Pd(111), Cu(111) and Pd-Cu(111) were reported.[59] Different active sites on the alloy surfaces were unveiled for both reactions. Three-fold hollow sites consisting of three Cu atoms were found active for NO reduction, while three-fold hollow sites consisting of either three Cu atoms or two Cu-one Pd atoms were found requisite for CO oxidation. The bulk Cu-Pd equimolar cluster composed of 586 atoms showed a predominance of Pd on the surface; Cu atoms preferred to grow on the corner and edge sites.

Sn-Pd

Surface alloys synthesized by depositing Sn on low-index Pd single crystal surfaces are excellent models in tailoring surface reactivity and/or selectivity for various catalytic reactions.[29-32,62] For example, Logan et al. reported a dramatic increase in turnover frequency and a lowering of activation energy for CO oxidation on *c*(2x2)Sn/Pd(100)

alloy surface in comparison to Pd(100).[29,62] Becker and coworkers found that a weaker benzene-Pd bonding resulted from Sn alloying; benzene decomposition was greatly suppressed on both *p*(2x2) and ($\sqrt{3}$ x $\sqrt{3}$)*R*30^{o} surfaces.[30] Electronic properties of alloy surfaces with various Sn concentration were also reported.[30-32]

Recently, the activity of Au-Pd bimetallic model catalysts of planar and cluster surfaces has been reported.[63-65] An ensemble consisting of noncontiguous, Pd dimers on Pd/Au(100) was proposed to lead to an unusually high reactivity (turnover frequency or TOF) for vinyl acetate synthesis.[65] The excellent lattice match of *c*(2x2)Sn/Pd(100) to the noncontiguous Pd dimers on Pd/Au(100) offers great potential in further establishing surface structure-reactivity correlations.

EXPERIMENTAL METHODS

UHV Surface Analysis Chamber

Experimental work was mainly performed in a multi-technique ultra-high vacuum chamber with a base pressure of 2.0 x 10^{-10} torr. The schematic of this chamber is shown in Figure 1.[66] The chamber was equipped with XPS, LEIS, AES, LEED, and TPD. The single-crystal samples were supported by high purity (99.95%) tantalum wires. The sample could be heated to 1500 K resistively or to 2400 K by an e-beam and cooled to 90 K by a liquid nitrogen reservoir attached to the copper leads. The sample temperature was measured using a C-type thermo couple (W-5% Re/W-26% Re) spot-welded on the back of the sample. The Pd, Au, Cu or other metal dosers were made by wrapping high purity metal wires around a tungsten wire. Both dosing metals and W wires were thoroughly degassed for hours to remove impurity. The dosing rates were calibrated by TPD, LEIS and XPS.

Infrared studies were carried in a second chamber, equipped with AES, IRAS, and TPD with a base pressure of 1 x 10^{-10} Torr. The IR cell was equipped with CaF_2 windows and could be pressurized to several torr. The sample can be cooled and heated as described above.

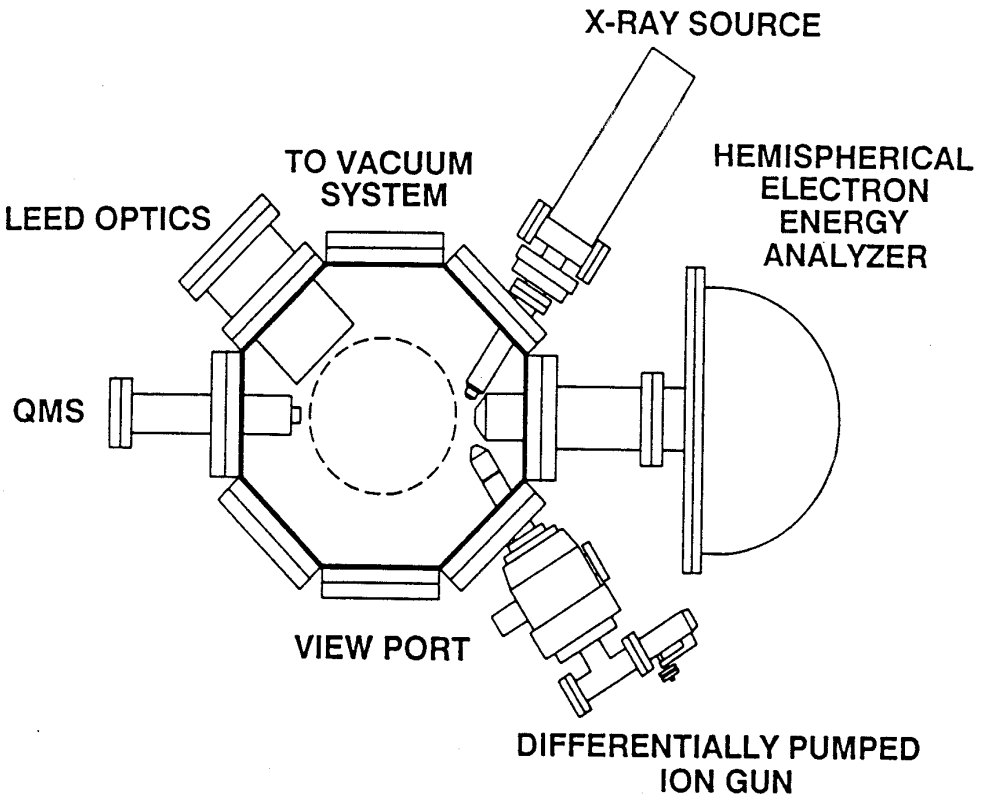

Figure 1. Top view of the multi-technique UHV chamber.

Low Energy Ion Scattering Spectroscopy (LEIS)

In low energy ion scattering spectroscopy (LEIS), a monoenergetic ion beam is directed to a target surface and the primary backscattered ions are detected at a defined direction. He^+, Ne^+, and Ar^+ ions are commonly used as incident ions. Beam energy ranges from a few hundred to a few thousand electron volt (eV). Figure 2 illustrates the ion scattering process: E_0 and M_1 are the energy and mass of the incident gas ion, respectively; M_2 is the mass of the target surface atom. Based on the conservation of energy and momentum, when M_1 is scattered by M_2 through an angle (θ), the energy E_1 of the scattered ion is given by:

$$E_1/E_0 = [1/(1 + A)^2][\cos\theta \pm (A^2 - \sin^2\theta)^{1/2}]^2 \quad (1)$$

A is equal to mass ratio, M_2/M_1; it is '+' is for A>1 and '±' for A<1.

By virtue of shadowing effects, scatters lying within the shadow cone, e.g., the second layer atoms, are severely shadowed and thereby poorly detected by the analyzer. Therefore, LEIS is a very surface-sensitive technique for determining the composition of the topmost surface layer and the growth mode of overlayers.

.

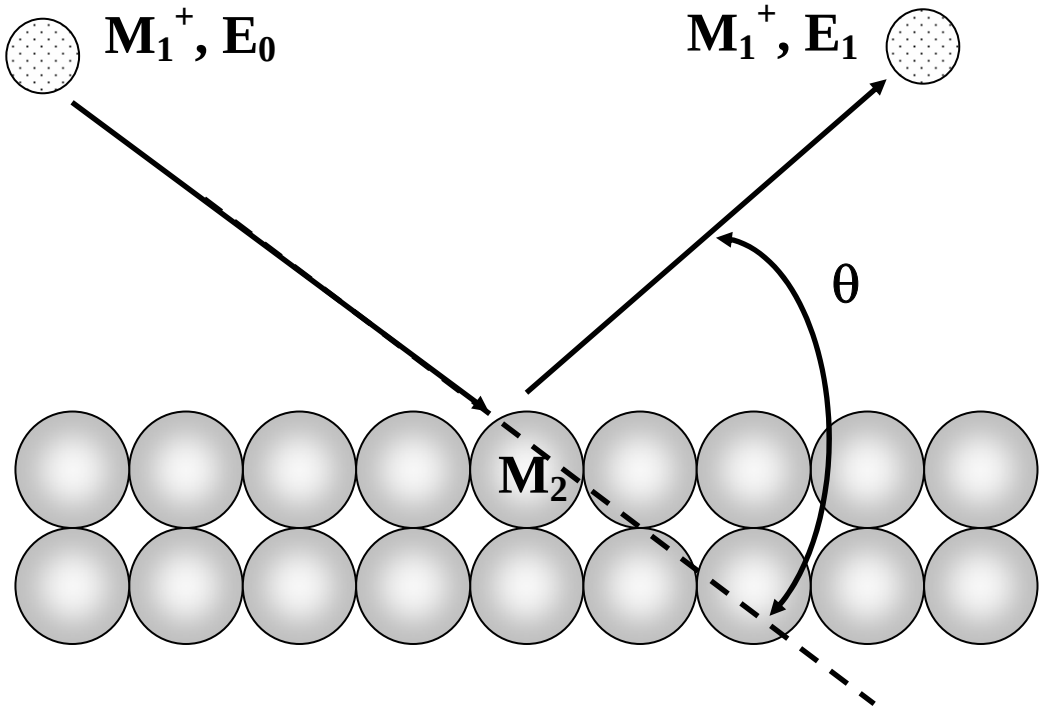

Figure 2. Diagram of LEIS ion scattering process.

X-ray Photoelectron Spectroscopy (XPS)

X-ray photoelectron spectroscopy (XPS) is a widely used technique in surface analysis. The X-ray photoemission process is illustrated in Figure 3. A monoenergetic photon beam is directed at the sample surface. A core-level electron (e.g., in 1*s* level) absorbs the photon energy ($h\nu$), overcomes the binding energy (E_b) and surface work function (Φ), and emerges from the solid with a kinetic energy (E_{kin}). The kinetic energy of a photoemitted electron is given by:

$$E_{kin} = h\nu - E_b - \Phi \qquad (2)$$

The electrons in the vacuum are collected and detected in the analyzer, and E_{kin} is measured.

In this work, XPS was employed as the main technique to explore electronic properties in the model catalyst systems. The binding energy studies of surface atom core level peaks provided insights into the electronic structures of bimetals and the interfacial reaction between metal clusters and oxide substrates. A better understanding of electronic properties, combined with LEIS and STM data, greatly helped to elucidate and differentiate ensemble and/or ligand effects for gas adsorption and catalytic reactions on the studied surfaces.

XPS data were collected using a Mg Kα source (Perkin-Elmer). The incident angle was approximately 45° from the surface normal direction. The photoelectrons were collected and analyzed by a concentric hemispherical analyzer (PHI, SCA 10-360).

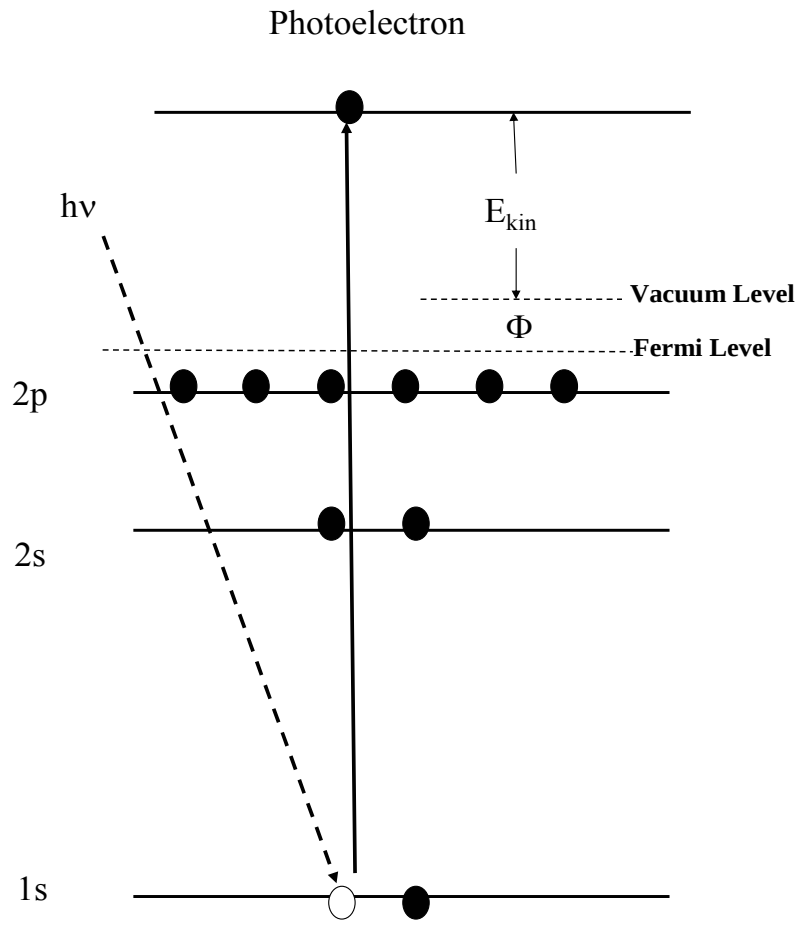

Figure 3. Diagram of photoemission process.

Temperature Programmed Desorption (TPD)

Temperature programmed desorption (TPD) is a simple yet useful technique for studying surface-adsorbate bonding energies and desorption kinetics. TPD is also often used for calibrating surface coverage of adsorbates.

The sample was heated at a linear rate, and the desorbing species at different temperature were detected by a quadrupole mass spectrometer (QMS). From Redhead or leading edge analysis, desorption energies of the surface adsorbates can be calculated from the collected spectra.

TPD was primarily employed in this work to study CO adsorption on different bimetallic surfaces. CO desorption temperature and its shift were used to identify the surface adsorption sites and related ligand effect due to alloying. Bonding energy measurements and dosing coverage calibration for Au, Pd, and Cu were performed using TPD. Surface structure-reactivity correlations for the adsorption of ethylene and acetic acid were established by analyzing TPD spectra.

TPD experiments were carried out using a close-coupled (~ 1 mm), line-of-sight quadruple mass spectrometer with a differential pumping setup. The linear heating rate was 5 K/second.

Low Energy Electron Diffraction (LEED)

Low energy electron diffraction (LEED) is a surface technique that primarily used to characterize the periodicity of surface structures. The instrumentation of LEED is illustrated in Figure 4. A monoenergetic low energy electron beam (10 ~ 300 eV) is directed at the surface perpendicularly. The backscattered electrons pass through a set of grids to reduce the undesirable electrostatic diffracted electrons, which allows only the elastically scattered electrons to go through and hit the fluorescent screen. The elastic scattered electrons form constructive interference patterns on the screen when scattered from an ordered surface. The LEED pattern represents surface periodicity in the reciprocal space. Due to the energy range of the primary incident electrons and small mean free path (a few Å) of these electrons, LEED is a surface sensitive technique.

In this work, LEED was employed to characterize Au growth on TiOx surface for structure identification. It was also used for the Sn/Pd(100) system to correlate structural properties with composition and chemisorptive behavior.

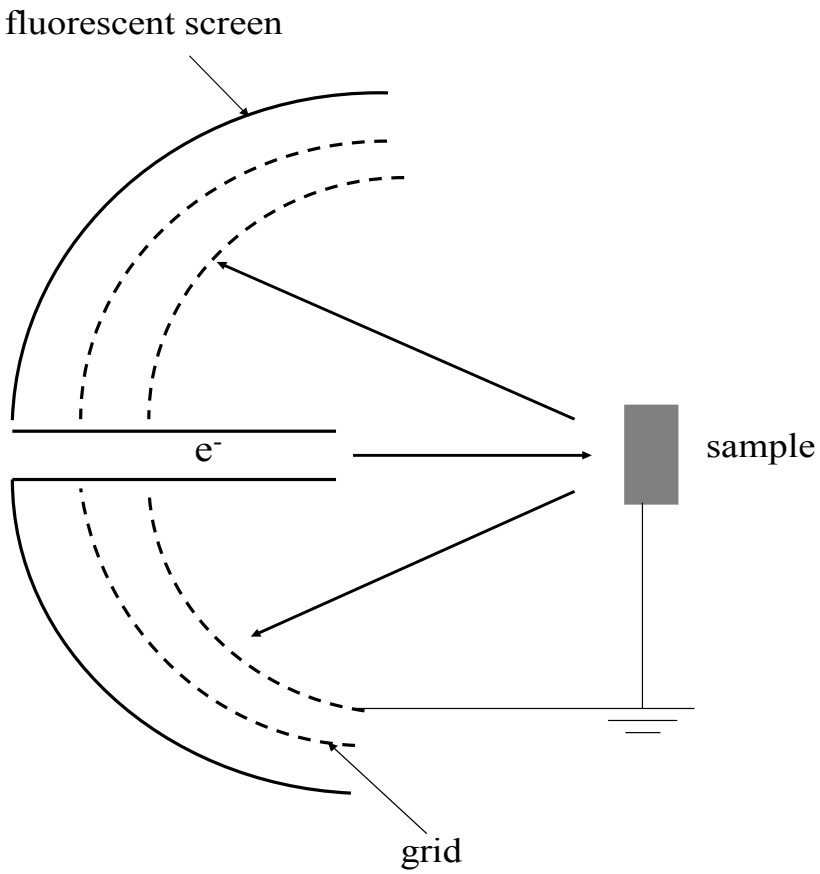

Figure 4. Schematic diagram of LEED optics.

Infrared Reflection Absorption Spectroscopy (IRAS)

Infrared reflection absorption spectroscopy (IRAS) is a vibrational spectroscopic technique extensively used in surface chemistry, physics, and other related studies. Surface dipoles of adsorbates are excited upon the absorption of infrared radiation; the generated spectral fingerprints are then used to identify adsorbates and study their surface orientation and bonding strength. [67]

The IRAS surface dipole selection rule is illustrated in Figure 5. E_s and $E_{s'}$ represent the incident and reflected vectors of s-polarised radiation. E_p and $E_{p'}$ represent the incident and reflected vectors of p-polarised radiation. Reversal of s-polarised components upon reflection leads to cancellation; however, the p-components are enhanced via a phase change resulting in a nearly doubled electric vector perpendicular to the surface. As a result, IRAS is only sensitive to the surface dipole perpendicular to the surface. Thus, IRAS is a very valuable tool to probe the adsorption sites, local chemical environment, and bonding strength of the surface adsorbates.

IRAS was primarily applied in this work to identify adsorption sites for CO onto bimetallic model catalysts. A Mettson Cygus 100 IRAS spectrometer was used. The incident angle of IR beam was ~ 85^o and the resolution of the spectrometer was 4 cm^{-1} with 256 scans.

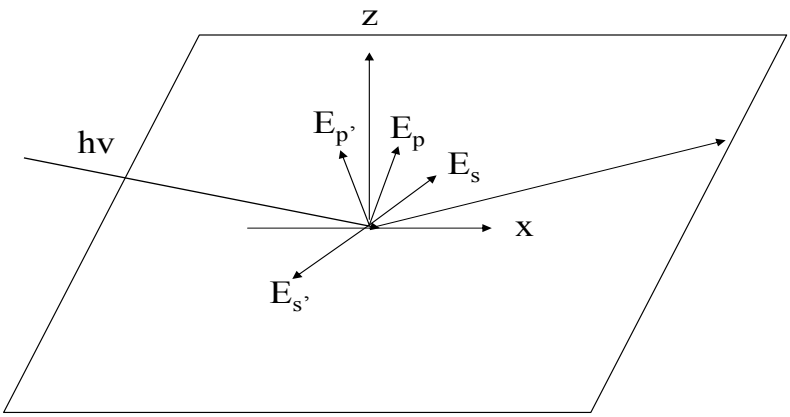

Figure 5. Diagram of IRAS surface dipole selection rule.

Sample and Doser Preparation

Experimental work on Au-TiO_x work involved the evaporation of Au and Ti from dosers made of high-purity Au and Ti wires (99.99%) wrapped around a Ta filament. The Au doser was calibrated with respect to the Mo(112) surface as monitored by TPD, LEIS, and XPS. A dosing rate of ~ 10 minutes per equivalent monolayer was explored. The Ti doser was calibrated by LEIS and XPS with a dosing rate of ~ 5 minutes per equivalent monolayer. Ultra-high purity O_2 gas (99.98%) was introduced using leak values into the vacuum during the oxidation process.

Titania films were synthesized using the following procedures: (i) oxidizing the Mo(112) surface to obtain an O-induced *p*(2x3) surface; (ii) depositing, oxidizing, and annealing a Si monolayer to obtain a *c*(2x2)- SiO_2 ultra-thin film; (iii) depositing, oxidizing, and annealing a Ti monolayer to obtain a well-ordered (8x2)- TiO_x ultra-thin film. Details of the film preparation are described elsewhere.[11,68]

A distinct LEED pattern was observed for each film. The TiO_x films were also characterized by XPS and no Si signal was detectable, consistent with previous AES studies.[11,68] Various coverages of Au were deposited at 300 K and annealed to 900 K in 5 $x10^{-9}$ torr O_2.

Bimetallic model catalysts were prepared by evaporating Pd, Au, and Cu dosers made of high-purity wires (99.99%) wrapped around Ta filaments. Corresponding Pd, Au, and Cu coverages on a Mo substrate were calibrated using TPD, LEIS, XPS, and AES. Ultra-high purity O_2 (99.98%, Matheson Tri-gas), CO (99.99%, Matheson Tri-gas), deuterated ethylene (99%, Aldrich), and acetic acid vapor (at room temperature)

were introduced into the ultra-high vacuum chamber using leak valves. Silicon dosers were wrapped with W wires and resistively heated during deposition. Details of the SiO_2 films preparation have been described previously.[69] Surface characterization by AES and XPS showed that the SiO_2 films were fully oxidized. The thickness of the SiO_2 films was measured using the attenuation of the Mo substrate signals and the known mean free paths of the X-ray and Auger electrons.

Repeated cycles of Ar^+ sputtering and surface annealing at 1100 K were applied [70] to obtain a contaminant-free and ordered Pd(100) surface. A sharp (1x1) LEED feature was evident. The Sn doser was made with high purity 99.99% Sn wires inserted into a W wire-wrapped alumina tube. The tube was resistively heated by a DC power supply and thoroughly outgassed for several hours to remove the impurity. The Sn doser was calibrated using XPS, LEIS and LEED. The Sn: Pd ratio of the XPS 3d core-level peak areas was plotted as a function of deposition time. At a Sn dosing current of 2.95 A, the calibration plot revealed a break-point at 10 minutes; this deposition time was therefore, used to define 1.0 ML coverage of Sn. LEED results further supported that the acquisition of a c(2x2) pattern after 5 minutes of deposition and 500 K annealing indicated a surface coverage of 0.5 ML. A full coverage of Sn was, hence, achieved at 10 minutes.

Due to the small difference in atomic mass between Sn and Pd, the two elements could not be readily discriminated by LEIS using He^+ probe. Hence, Ne^+ was used as the incident ion probe with a kinetic energy of 0.75 keV. The incident angle was ~ 45^o from the surface normal.

RESULTS AND DISCUSSION

Monometallic Model Catalysts

Au/TiOx

The growth of Au on TiO_2(110) has been extensively investigated experimentally and theoretically with respect to the growth mode, metal-support interaction, and electronic structure.[71-80] In short, quasi-two-dimensional (2D) growth at coverages less than 0.1 ML was observed with LEIS and STM. At higher Au coverages, three dimensional (3D) cluster growth was noted.[71,72] The electronic properties of Au deposited onto TiO_2 have been studied extensively by XPS,[71,73] scanning tunneling spectroscopy (STS),[72] and with theoretical calculations.[74-78,80] Although the origin of the positive shift in the XPS Au core level binding energies for Au on titania is still in debate, the electronic perturbation of Au overlayers by the titania support was proposed to play an important role.[71,73-79] Studies using CO as a probe combined with IRAS indicated a substantial increase in the CO heat of adsorption (~ 7 kcal/mol) on a ~ 3.0 nm Au cluster compared to bulk Au.[81] The rate of CO oxidation on Au supported on TiO_2(110) and on a high-surface-area TiO_2 support showed a maximum in the rate (turnover frequency, TOF, or molecules of CO_2 produced per Au atom site per second) at a Au cluster size of ~ 3.0 nm, indicating a correlation between the Au cluster size and reactivity.[72] The nucleation and sintering of Au clusters have been studied at UHV and at ambient pressures.[72,82] In addition, Au growth on TiO_2(001) thin films was studied with STM and TPD.[83] A homogeneous Au cluster growth mode was observed and the Au sublimation energy (E_{sub}) measured to be *ca.* 50 kcal/mol, independent of the

coverage. Christmann and coworkers also reported improved CO oxidation efficiency for Au on a reduced titania surface.[84] Recently, a substantially higher CO oxidation TOF was observed for a Au bi-layer on a reduced (8 x 2) TiOx surface compared with a Au/TiO_2 high surface area catalyst.[11] In this study, a combination of techniques, including XPS, LEIS, TPD, and LEED, was utilized to investigate the surface morphology, growth mode, electronic properties, and bond strength between Au and this reduced titania surface.

LEIS data for Au on (8x2)-TiO_x film were shown in Figure 6 where the LEIS Au peak intensity was plotted as a function of the Au coverage. The filled data and line corresponded to results for Au on (8x2)-TiO_x film at a coverage between 0 - 1.5 ML. The dashed line corresponded to the LEIS behavior predicted for 2D growth of Au on Mo(112), based on the Au LEIS peak intensity for 1.0 ML Au on the clean Mo(112) surface. Up to ~ 0.8 ML, the Au peak intensity increased linearly, consistent with a 2D growth mode.[11,71] At higher Au coverages (1.15 to 1.5 ML) the Au LEIS intensity plateaued, very near to the Au value corresponding to 1.0 ML Au/Mo(112). In comparison to the layer-by-layer growth observed for Au/Mo(112), the LEIS intensities for Au on titania were slightly lower (~ 8 %). These results could be a consequence of the difference in packing density, i. e. the number of the surface Ti atoms in the (8x2)-TiO_x film being only 7/8 of that of the topmost Mo atoms in the Mo(112).[11] The Ti LEIS signals were also monitored. In the inset of Figure 6, the normalized Ti scattering

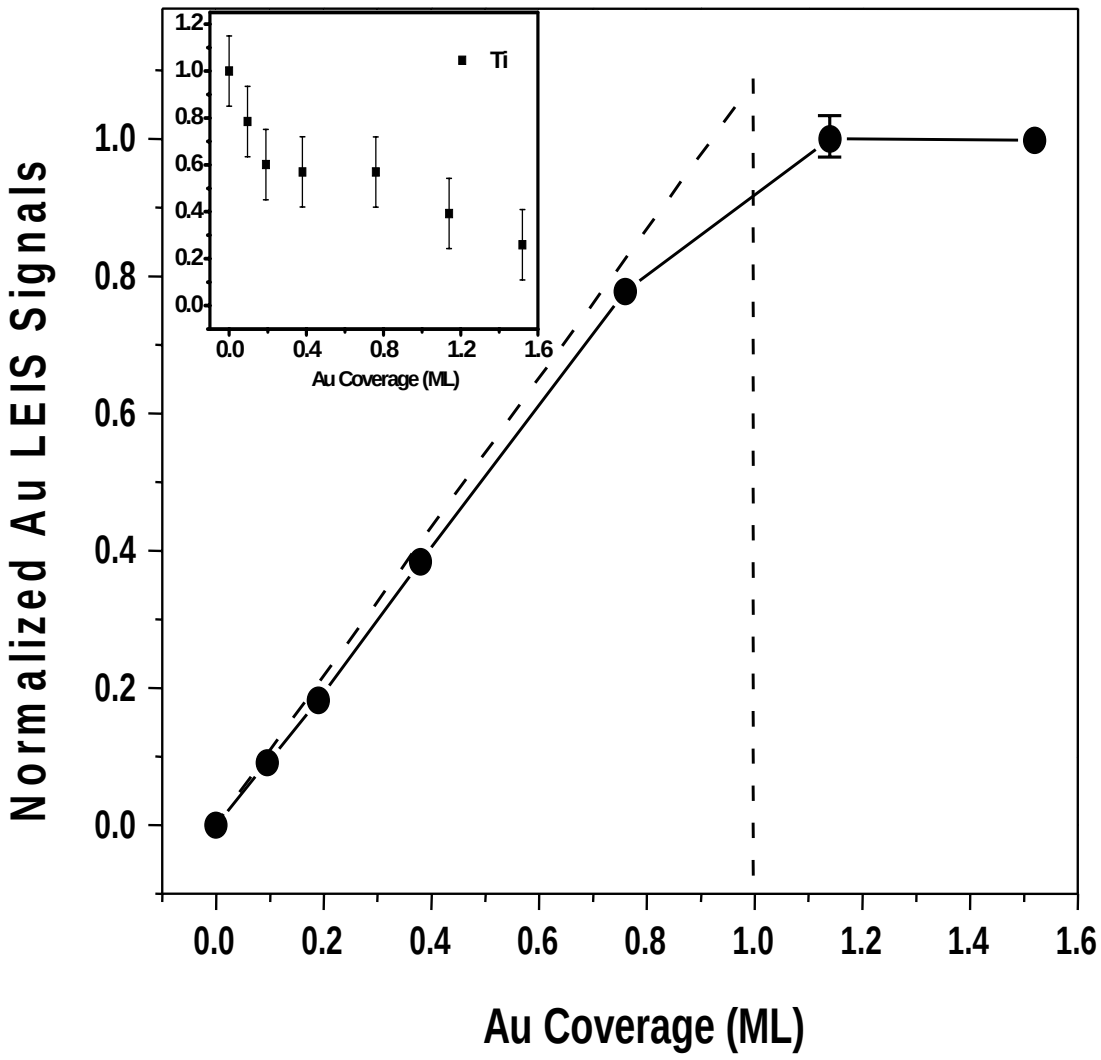

Figure 6. Au LEIS intensity as a function of Au coverage (0 - 1.52 ML) on TiO_x/Mo(112); filled circles are the data and the dashed line indicates the LEIS behavior for ideal growth of Au on Mo(112). The inset shows normalized Ti LEIS intensity as a function of Au coverage.

signals were plotted out as a function of Au coverage. The Ti signal decreased significantly as the Au coverage increased. With 1.5 ML Au deposition, the intensity of Ti was approximately 25% of the initial value. That the Ti scattering intensity did not drop to zero at 1.0 ML Au was likely due to contributions of the second surface layer to the LEIS signal or Au to some extent was on Ti bridging sites.[11]

From the LEIS studies, a 2D Au growth mode on (8x2)-TiO_x/Mo(112) was observed to a Au coverage of ~ 1.0 ML; a 1x1 LEED pattern was seen with an onset at 0.8 ML Au. These results were consistent with the AES and LEED work reported recently,[22] and showed direct evidence for Au wetting the reduced titania film.

XPS Au 4f core level features have been reported to shift 0.4 - 0.8 eV toward a higher binding energy (BE) with decreasing Au coverages on TiO_2(110).[71,73,79] In Figure 7, the Au 4f core level features were shown as a function of Au coverage (0.19 - 4.85 ML) on the (8 x 2)-TiO_x ultra-thin film. The Au 4f peak intensity increased with Au coverage, and the centroid of the Au $4f_{7/2}$ and $4f_{5/2}$ features shifted slightly to higher BE with decreasing coverage. To illustrate this shift, the Au $4f_{7/2}$ peak centroids were plotted as a function of Au coverage on TiO_x in Figure 8. Only a + 0.25 eV Au $4f_{7/2}$ CLBE shift was detected at 0.1 ML Au on TiO_x relative to bulk Au. The shift gradually decreased and reached the bulk Au value at ~ 3 ML Au coverage. The overall CLBE shift of + 0.25 eV for Au on TiO_x was relatively small compared to the + 0.8 eV shift for Au/TiO_2(110)[10] and the + 1.6 eV shift for Au/SiO_2.[69]

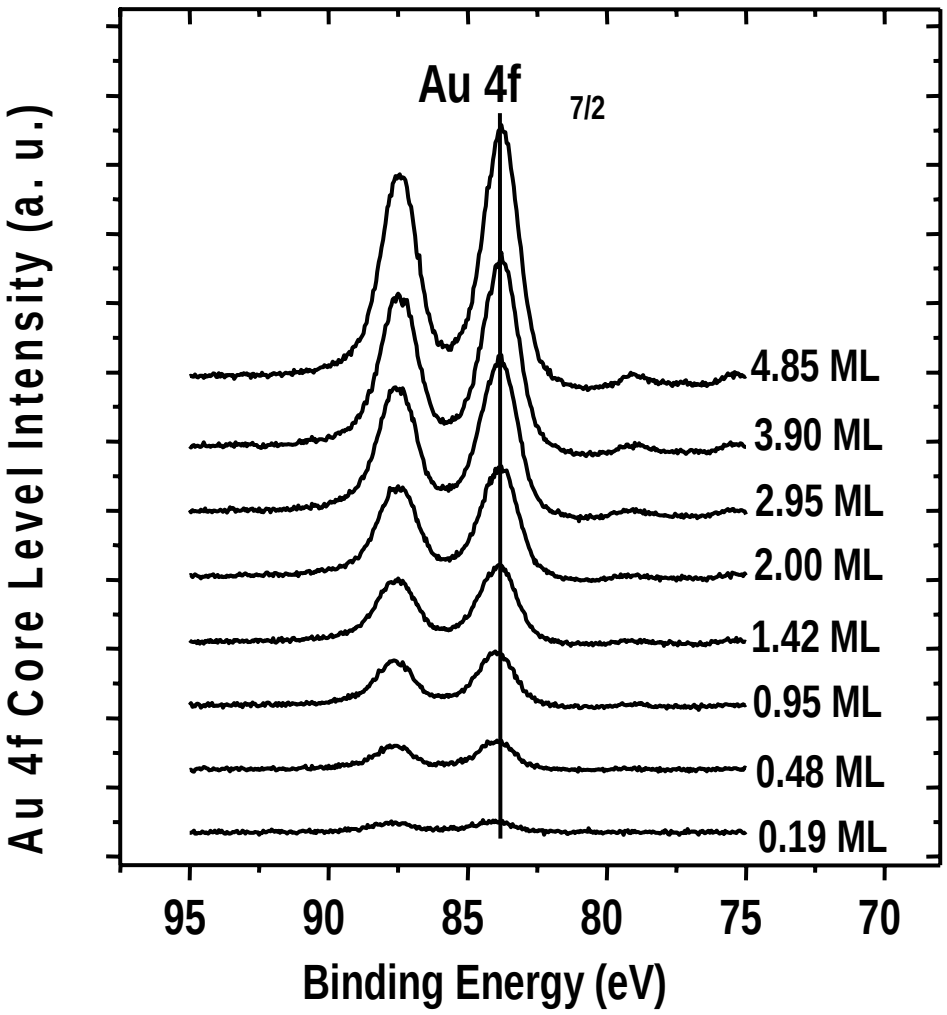

Figure 7. XPS Au 4f core level spectra as a function of Au coverage from 0.19 to 4.85 ML.

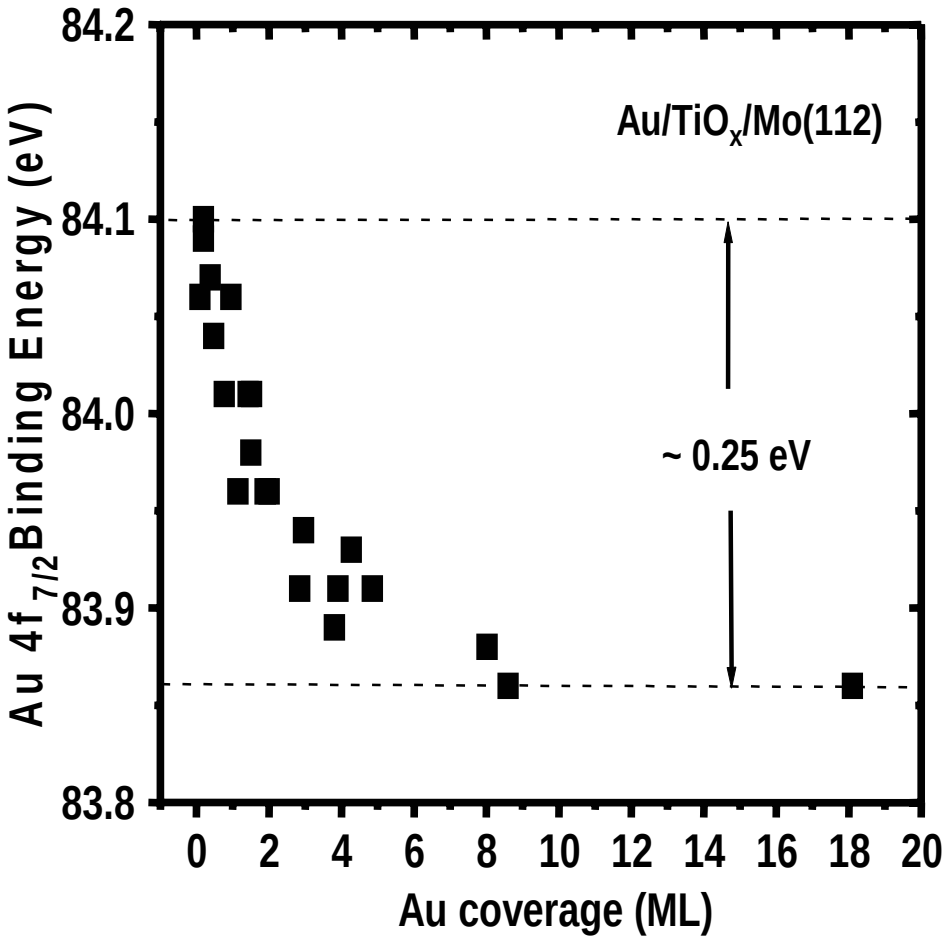

Figure 8. Au $4f_{7/2}$ core level binding energy as a function of Au coverage on TiO_x/Mo(112).

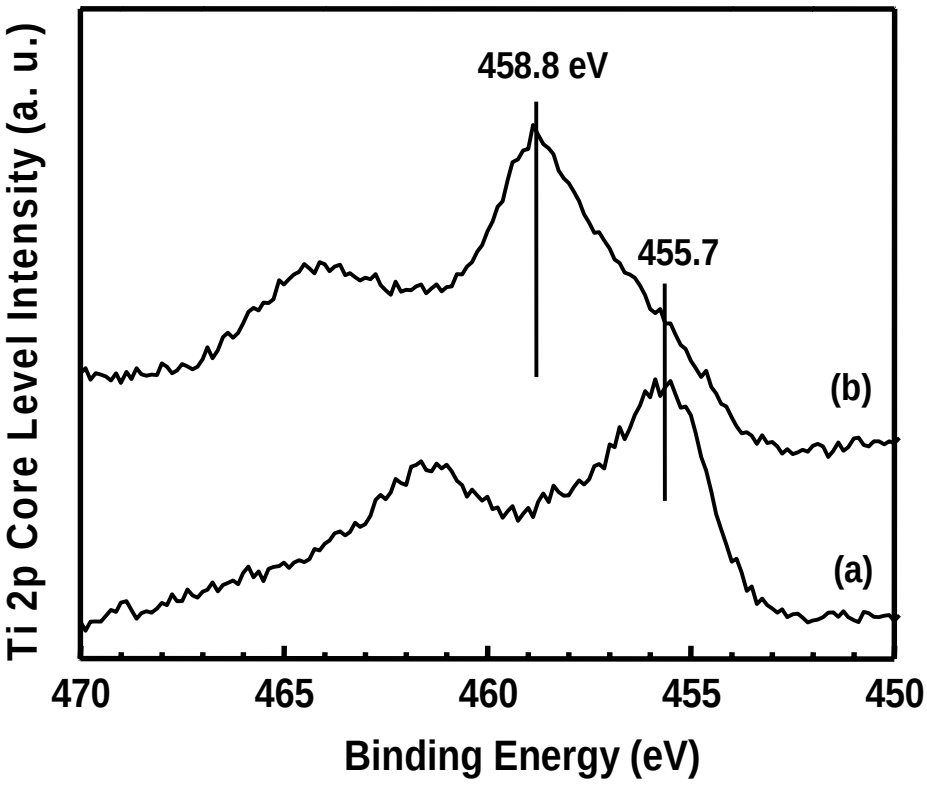

Figure 9. XPS Ti 2p spectra of: (a) the (8x2)-TiO_x ultra-thin film/Mo(112); and (b) after deposition of 1.0 ML Au.

In Figure 9, the XPS Ti 2p peaks were presented for (a) the bare (8x2)-TiO_x film, and (b) after deposition of 1.0 ML Au. A Ti 2p feature for the bare TiO_x film was apparent with a Ti $2p_{2/3}$ centroid at *ca.* 455.7 eV; this feature was assigned to Ti^{3+} states.[11,68,80] Upon deposition of 1.0 ML Au, the main feature shifted markedly to higher BE with a peak maximum at 458.8 eV; this feature was assigned to Ti^{4+}. The intensity of the Ti^{3+} shoulder at 455.7 eV was also significantly reduced in Figure 9(b). The peak shift and shape change were observed for relatively small Au coverages, i.e., 0.3 ML, while the effect was maximized at a Au coverage of >1.0 ML. A BE shift toward higher values and a change in the shape of the Ti oxidation states were evident upon deposition of sub- to multi-layer coverages of Au.

Positive Au CLBE shifts on various oxide supports ranging from 0.4 - 0.8 eV have been reported for Au on titania[71,73] and from 1.3 - 1.6 eV for Au on silica.[69,85] As pointed out by Mason,[85] the variations in the magnitude of these shifts were due to varying contributions of initial and final state effects exhibited by the supports. Final state effects led to higher CLBE shifts whereas initial state effects could lead to CLBE shifts in either direction. The significant reduction in the Au BE shift from 1.6 eV for Au/SiO_2[69] to 0.8 eV for Au/TiO_2[73] and to 0.25 eV for Au/TiO_x was instructive with respect to the relative contributions of initial state and final state effects of the three different substrates on supported Au.[74,79,80] For SiO_2, the substrate p band does not overlap with the Au 5d valence band, and hence there was a relatively large final state contribution to the CLBE, i.e. a large positive shift with decreasing Au cluster size.[69,79,85] Lopez and Nørskov suggested that the interaction between Au and a defect-free TiO_2

support was relatively weak,[77] whereas a stronger interaction occurred between Au and a reduced TiO_2 support.[75-78,80] For Au/TiO_2, a relatively large initial state effect[79,80] combined with a final state contribution yielded a 0.8 eV BE shift. A clear interpretation of the CLBE shifts for Au/TiO_x is more complex compared with Au/SiO_2 or Au/TiO_2 because of band bending, surface CLBE shifts, etc.; however, the high density of reduced Ti^{3+} sites relative to Ti^{4+} sites on the (8 x 2)-TiO_x surface likely give rise to the peak shift and shape change of Figure 9 and, as a consequence, electron-rich Au.[12,79,80] The contribution of initial and final state effects resulted in a relatively large Au CLBE shift reduction for Au on TiO_x compared to Au on SiO_2 or Au on TiO_2. This conclusion is consistent with recent theoretical[86] and experimental[84] results. It was also noteworthy in this context that the O 1s peak also shifted slightly (*ca.* 0.2 eV) to higher BE after Au deposition with no apparent change in the peak shape.

TPD of Au from TiO_x was used to measure the Au sublimation energy (E_{sub}), a direct indicator of the bond strength between Au and the support. TPD data of Au for various Au coverages were shown for Au/Mo(112) in Figure 10(a) and for Au/(8x2)-TiO_x/Mo(112) in Figure 10(b), respectively. Although the first and second layer Au desorption features were not completely separated in the TPD spectra for Au/Mo(112) in Figure 10(a), first order desorption kinetics were clearly apparent for sub- to monolayer coverages of Au. The Au multilayer features overlapped extensively with the second layer Au feature. Applying a Redhead analysis, E_{sub} of the first Au layer was estimated to be *ca.* 92 kcal/mol using a peak maximum temperature of ~ 1450 K. For Au

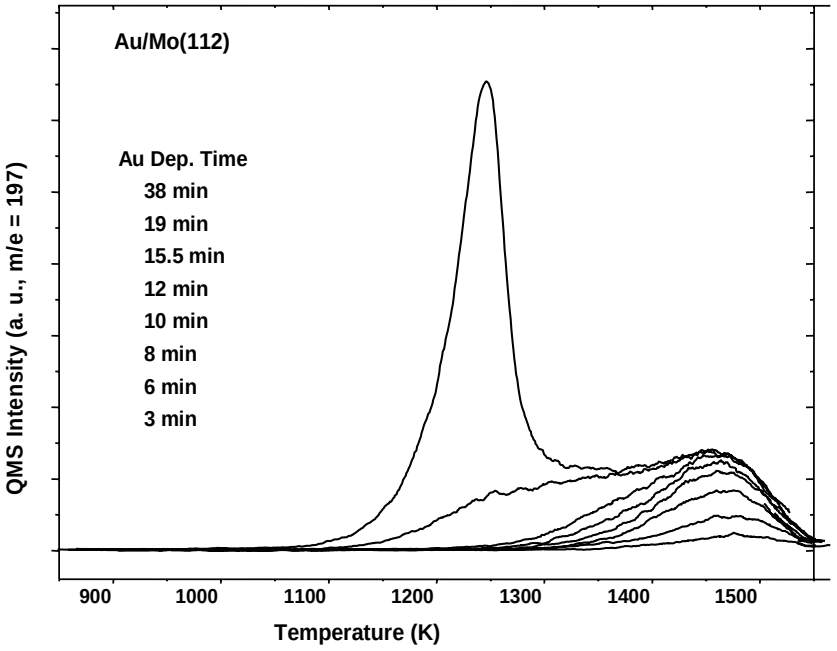

(a)

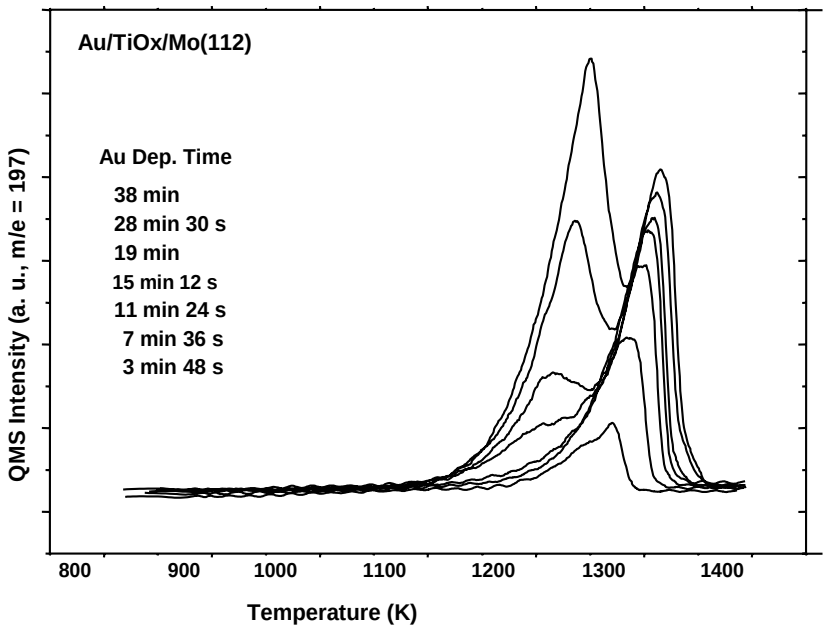

(b)

Figure 10. TPD spectra of Au from: (a) Mo(112); and (b) TiO_x/Mo(112).

multilayer desorption, a leading edge analysis yielded an E_{sub} of *ca.* 77 kcal/mol. This estimate for E_{sub} of a Au multilayer was lower than the previously reported values near 85 kcal/mol[69] and the Au bulk value of 90 kcal/mol, and may relate to Au clustering. In Figure 10(b), a first layer desorption feature was observed for Au coverages up to one monolayer. For Au coverages greater than one monolayer, overlapping desorption features appeared between 1100 and 1200 K. Unlike Au on TiO_2,[83] the Au desorption peak maxima shifted gradually with increasing Au coverage from sub- to monolayer coverages, with the desorption leading edges indicating fractional order desorption kinetics. A Redhead analysis yielded an E_{sub} for 1.0 ML Au/TiO_x of *ca.* 81.5 kcal/mol, 4.5 kcal/mol higher than the E_{sub} for multilayer Au, consistent with the wetting of first layer Au on TiO_x. Note that the E_{sub} for multilayer Au on TiO_x was the same as that of Au from Mo(112). The E_{sub} of 0.2 - 2 ML Au on TiO_2 (50 kcal/mol)[83] then was $\sim$ 30 kcal/mol less than the corresponding value for 1.0 ML Au on TiO_x and illustrated the significant enhancement of the bond strength between Au and TiO_x.

Bimetallic Model Catalysts

Au-Pd/Mo(110)*

TPD of Au-Pd/Mo(110)

The TPD spectra in Figure 11 depicts the desorption process of Au, Pd, and Au-Pd on Mo(110) surface. Desorption features of the first and second adlayers were clearly delineated: ~ 1450 and 1240 K for 1.5 ML Pd/Mo(110), and ~ 1350 and 1175 K for 1.5 ML Au/Mo(110). Figure 11(c) was a superimposition of both Au and Pd desorption signals for 1.0 ML Pd/1.0 ML Au/Mo(110)(Au deposition first).

The first desorption peak for Au (in solid line) in this bimetallic system appeared at about 1225 K, which was close to the inception of the desorption peak of the second Au layer observed in pure Au on Mo(110) (Figure 11(b)). A small peak shoulder for Au developed at 1250-1400 K, and the Au signal diminished after 1400 K. The main Pd feature (dashed line) stayed almost in the same temperature region as in Pd/Mo(110) in Figure 11(a) with a minor overlap with the Au main desorption feature. The results here indicated that the Pd in the Au-Pd alloy layers bonded much stronger to the Mo substrate. In effect, a majority of Au desorbed in the same temperature region as that of multilayer Au desorption. Also, the shoulders at the high temperature side for Au and low temperature side for Pd resulted from concomitant desorption of a Au-Pd alloy phase.

---

* Reproduced in part with permission from: Yi, C.-W.; Luo, K.; Wei, T; Goodman, D.W. *Journal of Physical Chemistry B* **2005**,109,18535, Copyright 2005 American Chemical Society; Chen, M. S.; Luo, K.; Wei, T.; Yan, Z.; Kumar, D.; Yi, C.-W.; Goodman, D. W. *Catalysis Today*, in press.

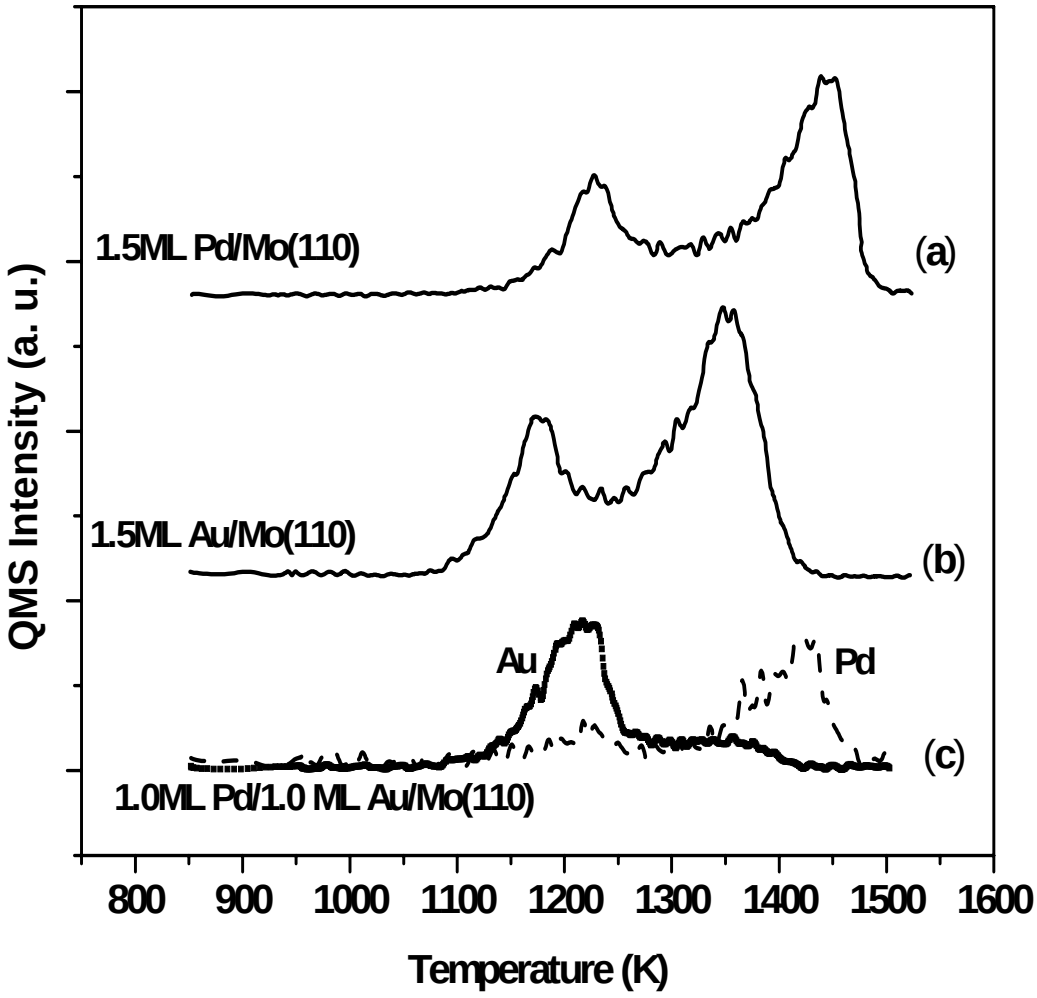

Figure 11. TPD of (a) 1.5 ML Pd/Mo(110); (b) 1.5 ML Au/Mo(110); and (c) 1.0 ML Pd/1.0 ML Au/Mo(110).

LEIS of 1.0 ML Au-1.0 ML Pd/Mo(110)

Sequential deposition of 1.0 ML Au followed by 1.0 ML Pd was performed onto a Mo(110) surface at 300 K; the system is hereafter designated as 1.0 ML Pd/1.0 ML Au/Mo(110). The prepared Au-Pd adlayer was flash-annealed at various temperatures from 400 – 1500 K. Figure 12 displays a series of LEIS spectra obtained for every 100 K-increment of annealing temperature. He^+ was used as probe ion for LEIS. All LEIS spectra were collected at 300 K. Scattering cross-sections follow the order: Au > Pd > Mo. Because of atomic weight differences, Mo and Pd peak intensities are smaller than that of Au.

The LEIS spectrum of 1.0 ML Pd/1.0 ML Au/Mo(110) at 300K revealed scattering peaks for Au and Pd at 1.03 and 0.97 keV, respectively. No Mo substrate feature (KE = 0.94 keV) was detected. As the annealing temperature was progressively ramped to 800 K, both Au and Pd intensities slightly decreased but the Au/Pd peak-intensity (height) ratio increased. At higher temperatures, the Pd peak intensity stayed almost the same as at 900 K, whereas the Au peak signal continued to dwindle until a Mo feature at 0.94 keV emerged at 1170 K. Desorption of both Au and Pd commenced at 1350 and 1415 K, as indicated by the drastic decline in corresponding peak intensities. At 1500 K, only the Mo scattering feature can be observed.

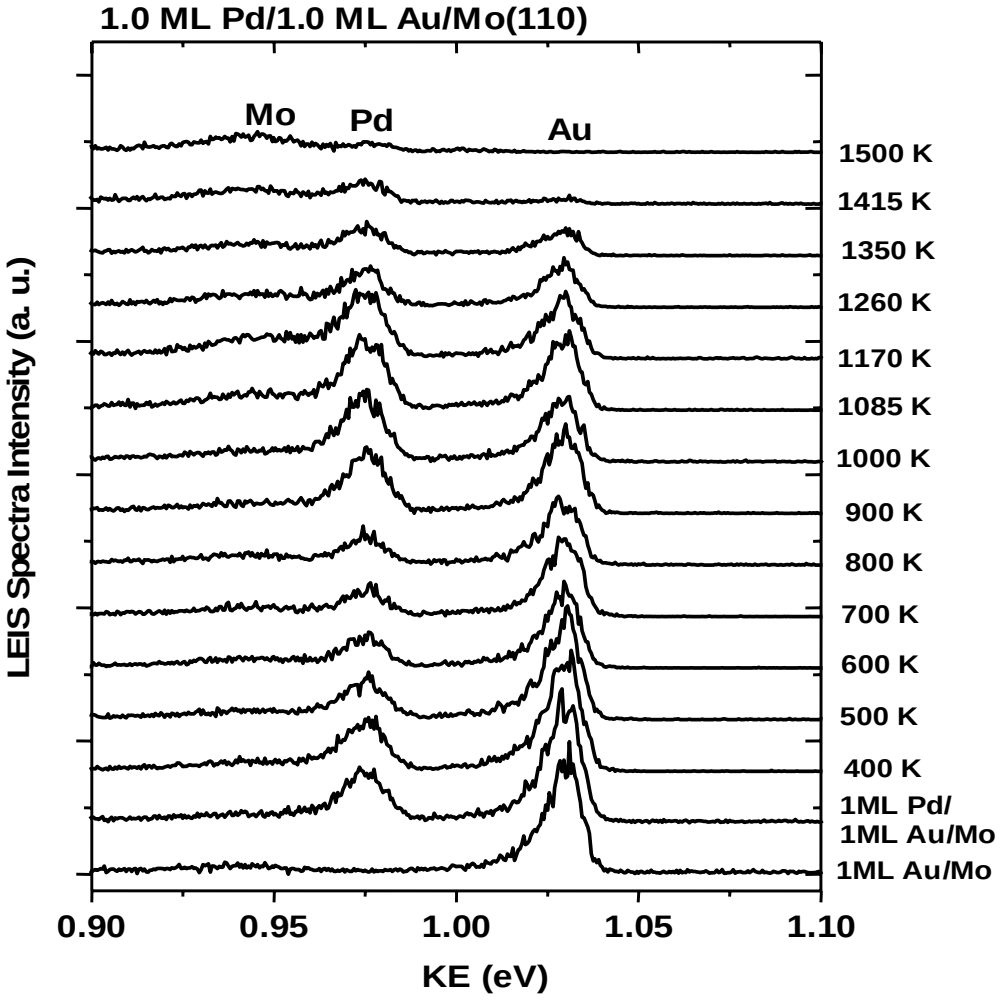

Figure 12. LEIS spectra of 1.0 ML Pd/1.0 ML Au/Mo(110) as a function of annealing temperature.

The deposition sequence was reversed to prepare the 1.0 ML Au/1.0 ML Pd/Mo(110) system. Corresponding LEIS spectra are shown in Figure 13. As expected, the Pd scattering peak intensity (0.97 keV) significantly decreased upon deposition of Au at 300 K. The characteristic Au feature appeared at 1.03 keV. At 900 K, the Pd peak intensity greatly increased with little changes in Au peak intensity. At higher annealing temperatures, the Pd peak intensity stayed almost the same, whereas the Au peak signal diminished until a clear Mo feature at 0.94 keV appeared at 1170 K. At 1415 K, both Au and Pd scattering peaks were almost completely extinguished, marking their desorption from the surface. At 1500 K, essentially only the Mo scattering feature remained.

For a bimetal planar surface, the surface concentrations of each specie, e.g. A, can be calculated using equation (3)

$$C_A = I_A/(I_A + \alpha_{A/B} * I_B) \quad (3)$$

where I_A and I_B represent LEIS peak intensities (height) for component species (Au and Pd here) from the collected spectra, and $\alpha_{A/B}$ represents the ratio of the peak intensity of species A and B in pristine surface conditions. Using the LEIS data in Figures 12 and 13, surface concentrations of Au and Pd can be plotted as a function of annealing temperature.

In Figure 14(a), the Au surface concentration was about 50-60% after carrying out the deposition at 300 K, no matter whether Pd or Au was deposited first. Meanwhile, it was evident in Figure 14(b) that Pd covered the rest (40-50%) of the surface top layer; the surface composition stayed at this ratio until 800 K. An increase in Pd concentration

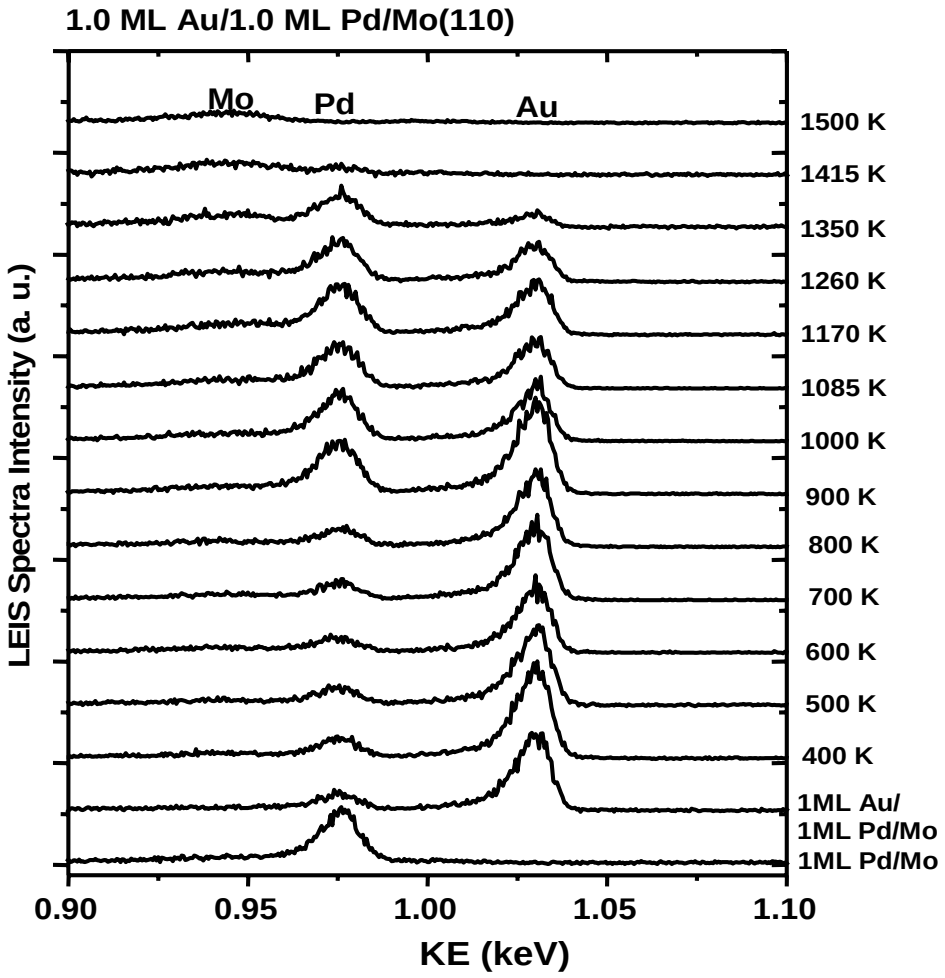

Figure 13. LEIS spectra of 1.0 ML Au/1.0 ML Pd/Mo(110) as a function of annealing temperature.

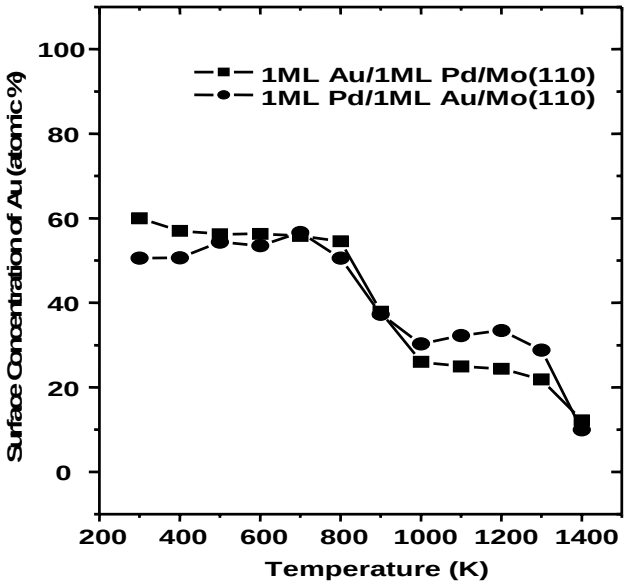

(a)

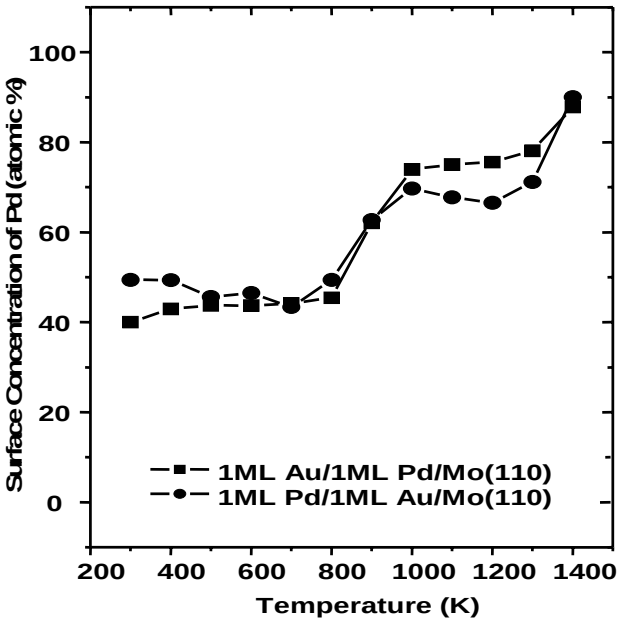

(b)

Figure 14. Surface concentrations of (a) Au and (b) Pd as a function of annealing temperature for 1.0 ML Au-1.0 ML Pd/Mo(110) surfaces.

was clearly observed at 900 K, possibly due to Au clustering before its desorption. The Pd-to-Au surface mole ratio reached 70: 30 at 1000 K, with the surface composition leveling off at the same value until 1350 K. At 1415 K, Au was completely desorbed, resulting to an increase in the Pd concentration. Throughout the whole annealing temperature range, two relatively stable surface compositions (expressed as Pd:Au mole ratio) were observed to be 40:60 at 300-800 K and 70:30 at 1000-1300 K.

Results from the 1.0 ML Au-1.0 ML Pd/Mo(110) indicated the Au and Pd atoms interdiffused quickly and extensively even at room temperature. The system became stable after certain annealing, and the surface composition was not affected by the deposition sequence of Au and Pd. A slightly Au enriched surface was observed at 300-800 K. At 1000-1300 K, the fact that more Pd surface was exposed to the vacuum is interpreted as Au desorption and/or clustering formation.

Previous photoemission studies of Pd/Au (111) and Au/Pd(111) both reported interdiffusion between Pd and Au.[43,44] About 30% Au surface coverage for the 1-10 ML Au/Pd(111) surface was concluded via matching photoemission feature of 0.3 ML Au after 5-20 minutes of annealing at 800 ^{o}C.[43] This result agreed with our present data for 1.0 ML Au-1.0 ML Pd/Mo(110) at 1100 K. However, for 1.0 ML Pd/Au(111), Au started to diffuse out through the Pd monolayer even at 240 K, and covered the surface up to 90% after 650 K annealing.[44] In our study of 1.0 ML Pd/1.0 ML Au/Mo(110) system, a 60% surface Au was seen at 300-800 K, and a reduction in Au surface coverage to 30% resulted after annealing to 1000-1200 K. Hence, a clear difference existed between our studies and the reference work.[44] However, it is noteworthy to point

out that Pd and Au molar ratio was 1-to-infinite in the reference work, whereas the ratio was 1 to 1 in our study. In addition, both Pd and Au monolayer atoms were strongly affected by the Mo substrates in our case. The difference between the chosen systems and substrate interactions was believed to be the reasons for the observed difference in surface composition.

XPS of 1.0 ML Au-1.0 ML Pd/Mo(110)

XPS spectra were collected after following the same deposition and annealing scheme as described in the LEIS experiments for 1.0 ML Au-1.0 ML Pd/Mo(110). Figure 15 shows the evolution of the Au 4f core level photoemission spectra as a function of annealing temperature. For the bimetallic system of 1.0 ML Au/1.0 ML Pd/Mo(110), the peak position of Au $4f_{7/2}$ was around 83.5 eV, which is 0.3 eV lower than that of bulk Au. Initially, the Au peak position stayed almost the same, but then slightly shifted positively until Au completely evaporated at 1415 K. At 1260 K, the Au peak intensity was observed to decrease significantly due to Au desorption. Similar temperature dependent XPS experiments were performed on 1.0 ML Pd/1.0 ML Au/Mo(110).

In Figure 16, Au $4f_{7/2}$ peak appeared around 83.7 eV at a surface coverage of 1.0 ML Au on Mo(110). The peak shifted to lower values (83.5 eV) upon depositing 1.0 ML Pd. Similar to the 1.0 ML Au/1.0 ML Pd/Mo(110) experiments, the peak position was observed to shift gradually to higher binding energy as the temperature was increased.

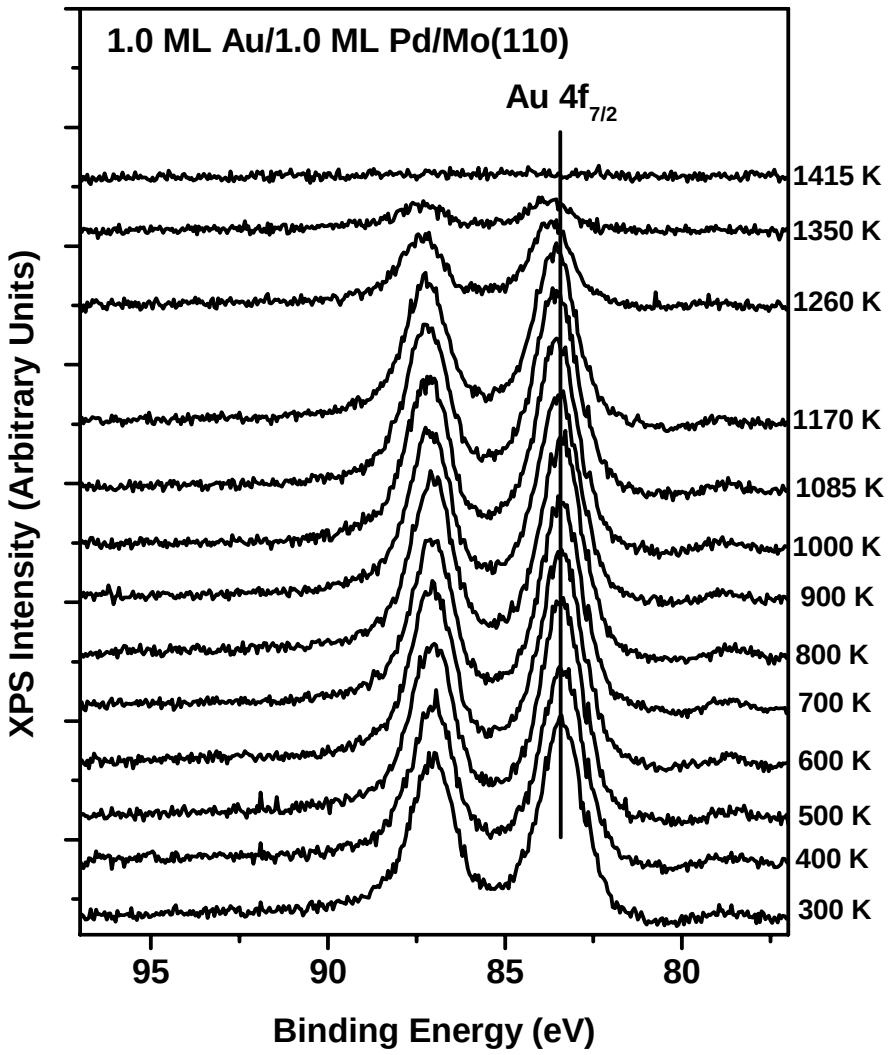

Figure 15. XPS Au 4f core level spectra of 1.0 ML Au/1.0 ML Pd/Mo(110) as a function of annealing temperature.

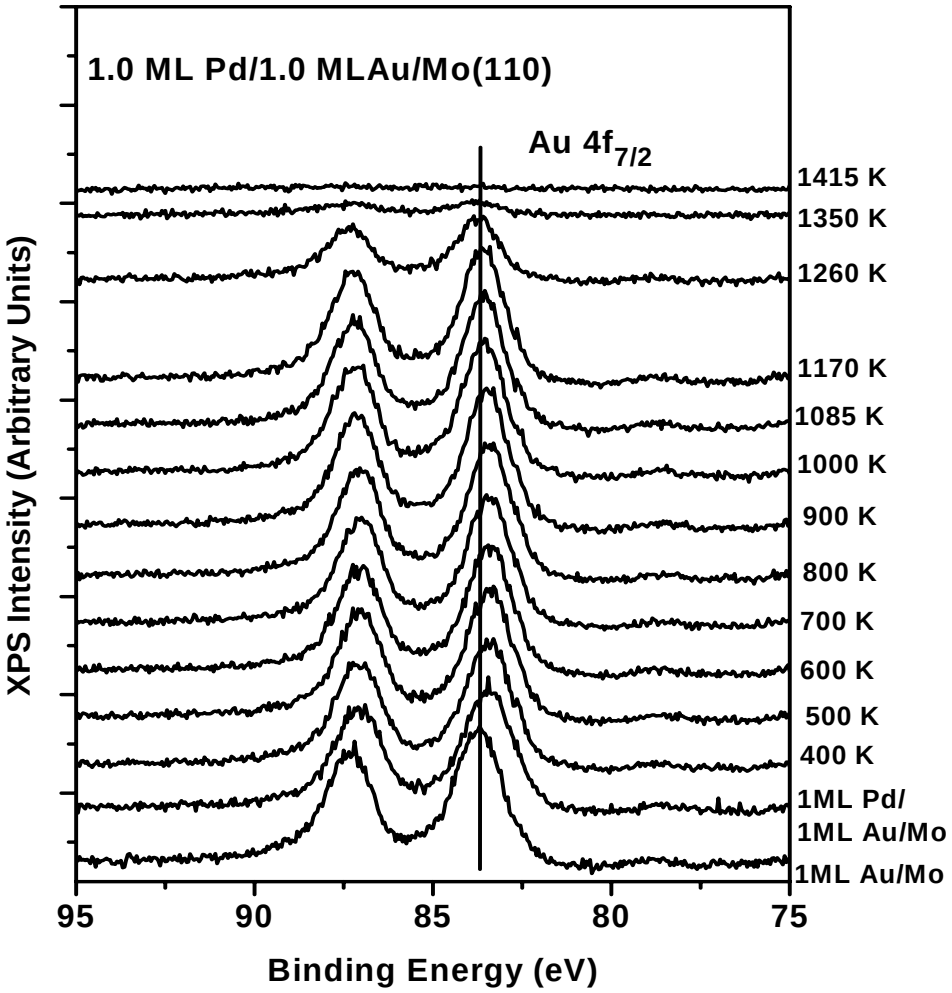

Figure 16. XPS of Au 4f core level spectra of 1.0 ML Pd/1.0 ML Au/Mo(110) as a function of annealing temperature.

The Pd 3d core level spectra were collected and laid out as a function of annealing temperature in Figures 17 and 18 for 1.0 ML Pd/1.0 ML Au/Mo(110) and 1.0 ML Au/1.0 ML Pd/Mo(110), respectively. Due to the overlap of Au 4d and Pd $3d_{5/2}$ features, the less intense Pd $3d_{3/2}$ feature was used to monitor the variation of CLBE and signal intensity. In Figure 17, no significant Pd CLBE shift was observed with initial variations in annealing temperatures. The Pd intensity also stayed almost unchanged as the temperature was raised up to 1085 K. An increase in the Pd intensity was observed at 1170 K when Au started to cluster. The intensity dropped at 1350 K due to the onset of Pd desorption. Similar trends in the Pd $3d_{3/2}$ CLBE shift and intensity were obtained for the 1.0 ML Au/1.0 ML Pd/Mo(110) system. The corresponding spectra are shown in Figure 18.

Au $4f_{7/2}$ and Pd $3d_{3/2}$ core level binding energies are plotted in Figure 19(a) and 19(b), respectively, as a function of annealing temperature for both 1.0 ML Au/1.0 ML Pd/Mo(110) and 1.0 ML Pd/1.0 ML Au/Mo(110). The higher binding energy position (83.7 eV) at 300 K in Figure 19(a) represented the Au $4f_{7/2}$ peak for 1.0 ML Au on a Mo(110) surface. A similar CLS due to d and sp orbital charge redistribution was reported by Rodriguez & Kuhn.[87] The Au $4f_{7/2}$ position stayed thereafter at *ca.* 83.4 eV until 800 K was reached. The Au 4f peak position positively shifted to 83.6 eV at 1000 K and stayed almost at the same position up to 1200 K. Such shifts were ascribed to Au clustering before the evaporation from the surface. In Figure 19(b), Pd $3d_{3/2}$ core

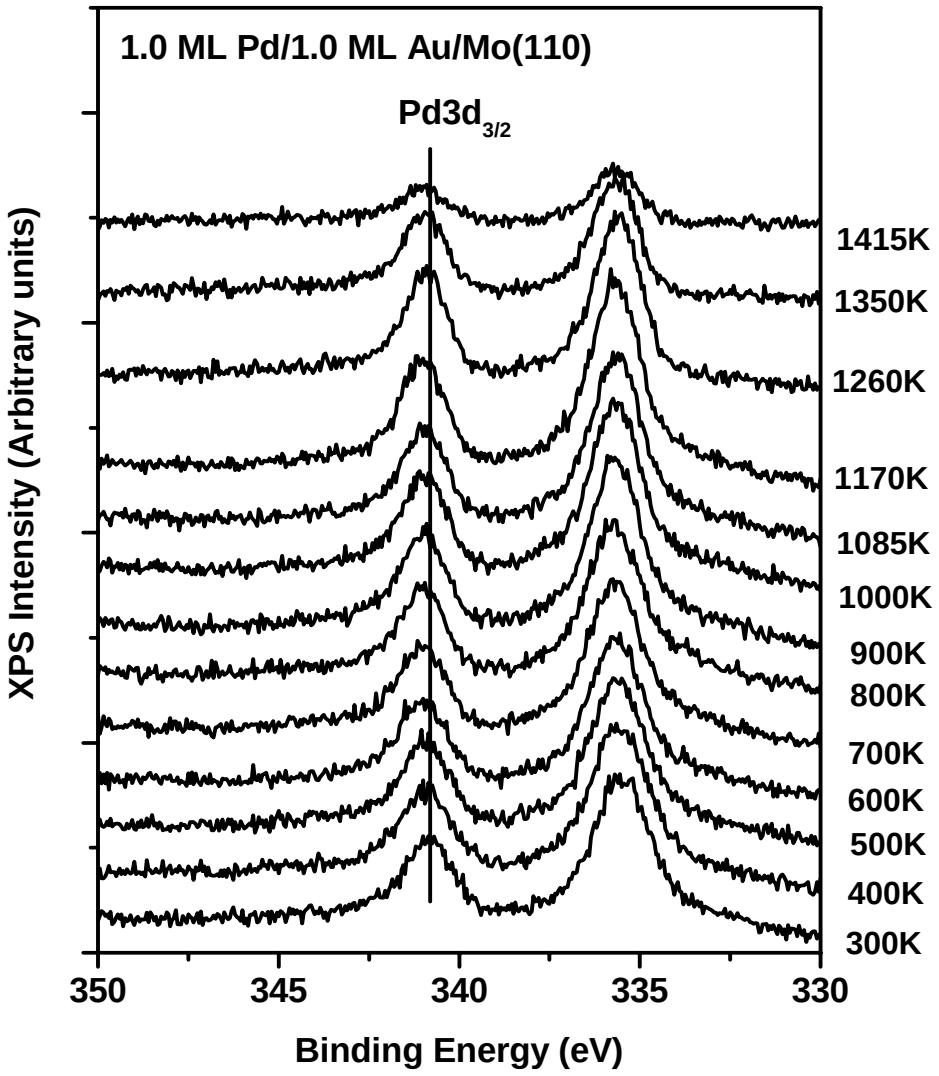

Figure 17. XPS Pd 3d core level spectra of 1.0 ML Pd/1.0 ML Au/Mo(110) as a function of annealing temperature.

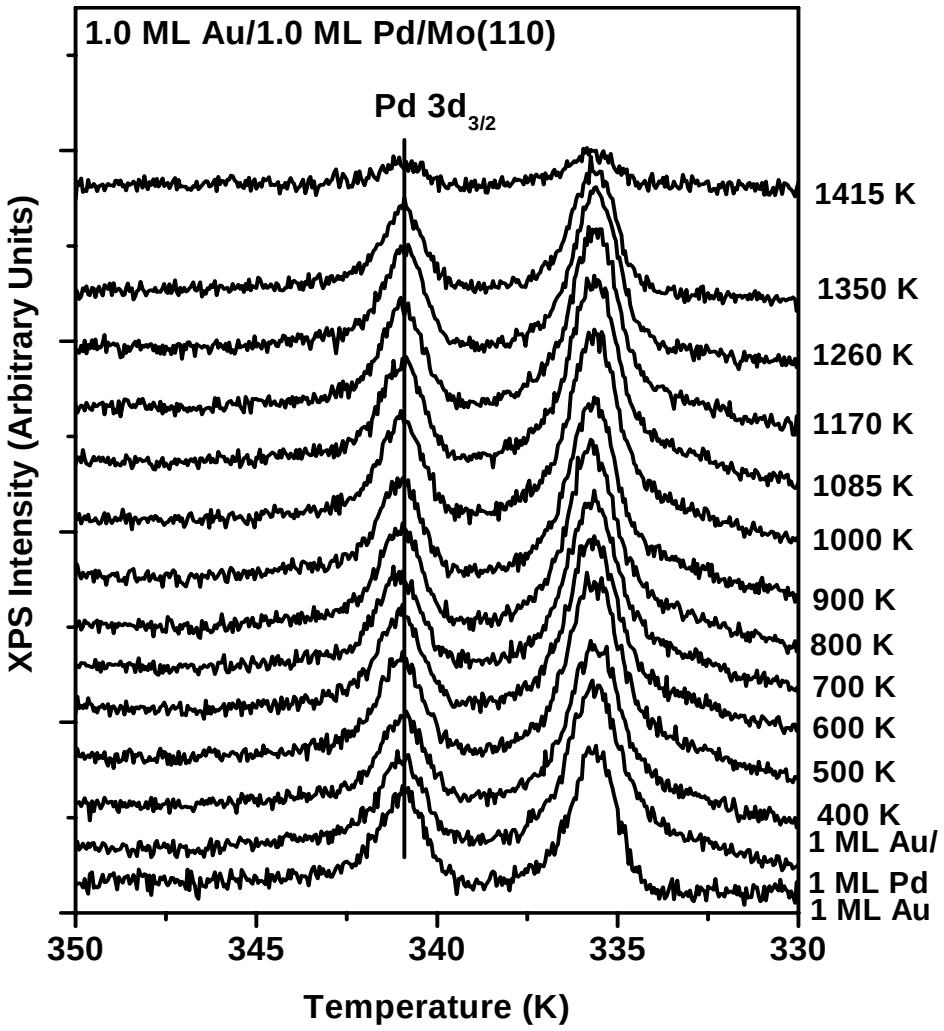

Figure 18. XPS Pd 3d core level spectra of 1.0 ML Au/1.0 ML Pd/Mo(110) as a function of annealing temperature.

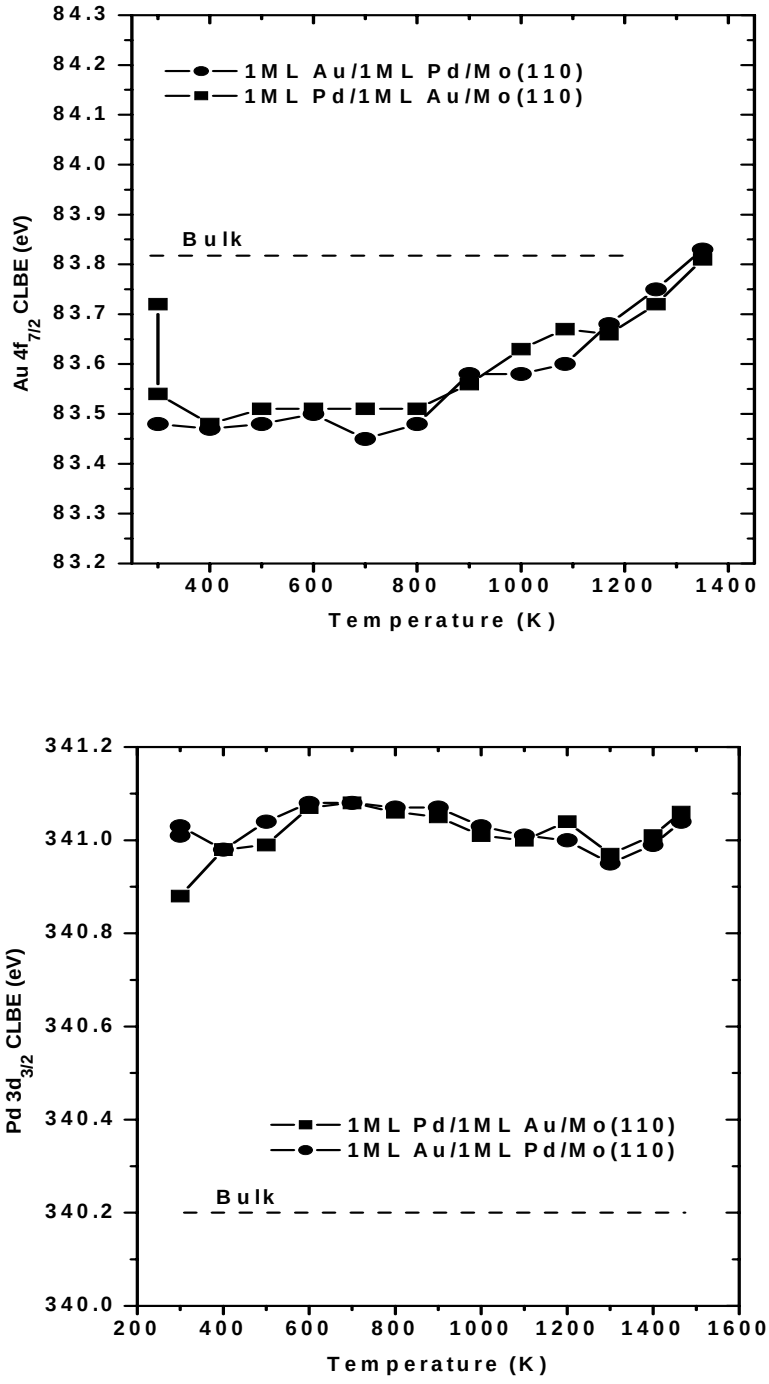

Figure 19. (a) CLBE of Au $4f_{7/2}$ for 1.0 ML Au/1.0 ML Pd/Mo(110) (-●- **)** and 1.0 ML Pd/1.0 ML Au/Mo(110) (-■-) as a function of annealing temperature; (b) CLBE of Pd $3d_{3/2}$ for 1.0 ML Pd/1.0 ML Au/Mo(110) (-■-) and 1.0 ML Au/1.0 ML Pd/Mo(110) (-●- **)** as a function of annealing temperature.

level position was 0.8 eV higher than the Pd bulk with 1.0 ML Pd deposition on 1.0 ML Au/Mo(110) or Mo substrate, and shifted very little upon annealing until it evaporated.

No XPS Pd 3d or Au 4f core level binding energy shifts were seen for 1.0 ML Pd on Au(111) surface from 150 to 550 K.[44] The Pd peak position at 340.1 eV when Au-Pd alloying occurred was close to that of Pd bulk. However, in our study, the $Pd_{3/2}$ peak position of *ca.* 341.0 eV, which was about + 0.7 eV higher than that of bulk position and close to the Pd peak position of 1.0 ML Pd/Mo(110), suggested a strong interaction between Pd-Mo here, as demonstrated in TPD and LEIS results earlier.

With Au(111) as the substrate,[44] no shifts in Au 4f binding energy was expected due to the high percentage of photo-emitted electrons from the Au bulk, i.e., the electronic properties were not disturbed as much. Whereas, in the case of one monolayer of Au atoms alloying with another monolayer of Pd atoms on Mo(110), such as in Figure 19(a), the Au core level binding energy was strongly affected by both neighboring Pd atoms and the bulk Mo. The core level Au position shifted from 83.7 to 83.4 eV (square lines) and showed a - 0.4 eV shift upon depositing 1.0 ML Pd on Au(1.0 ML)/Mo(110) at 300 K. The fact that the Au surface CLS is - 0.3 eV and that only 40-50% Au atoms are covered by Pd atoms to become the second layer atoms shown in Figure 14(a) data suggests that the Pd alloying contribution accounts for more than half of the observed - 0.4 eV shift. The higher Au binding energy shift (+ 0.2 eV) at 1000-1200 K can be ascribed to Au clustering.

LEIS of Au-Pd overlayers/Mo(110)

While ultra-thin films of Au and Pd constitute fascinating systems, thicker films that closely resemble the diameter of nano-size cluster in model or real catalysts deserve closer inspection. Here, 5.0 ML Au-5.0 ML Pd overlayers on Mo(110) substrate were investigated using methods similar to those employed in the 1.0 ML Au-1.0 ML Pd/Mo(110) experiments. The only difference is that the overlayer surfaces were annealed at pre-determined temperatures for 15 minutes before the characterization. All LEIS and XPS spectra were collected at room temperature.

Figure 20 shows the LEIS spectra of 5.0 ML Pd/5.0 ML Au/Mo(110) system annealed up to 1300 K. After depositing 5.0 ML Au at 300 K, the Au scattering peak feature appeared at a KE position of 1.03 keV. No Mo substrate feature (KE = 0.94 keV) was seen. Subsequent deposition of Pd at the same temperature led to a significant drop in the Au peak intensity and the appearance of the Pd feature (KE = 0.97 keV). At annealing temperatures spanning from 400-700 K, the Pd peak intensity decreased while the Au peak signals increased. Beyond 700 K, Au signals started to slowly decrease and Pd signals progressively increased with temperature until 1200 K was reached. Both Au and Pd intensities dropped greatly at 1200 K and 1300 K, respectively, due to the desorption of Au and Pd from the surface. At 1300 K, only the Mo scattering feature (KE = 0.94 keV) was observed.

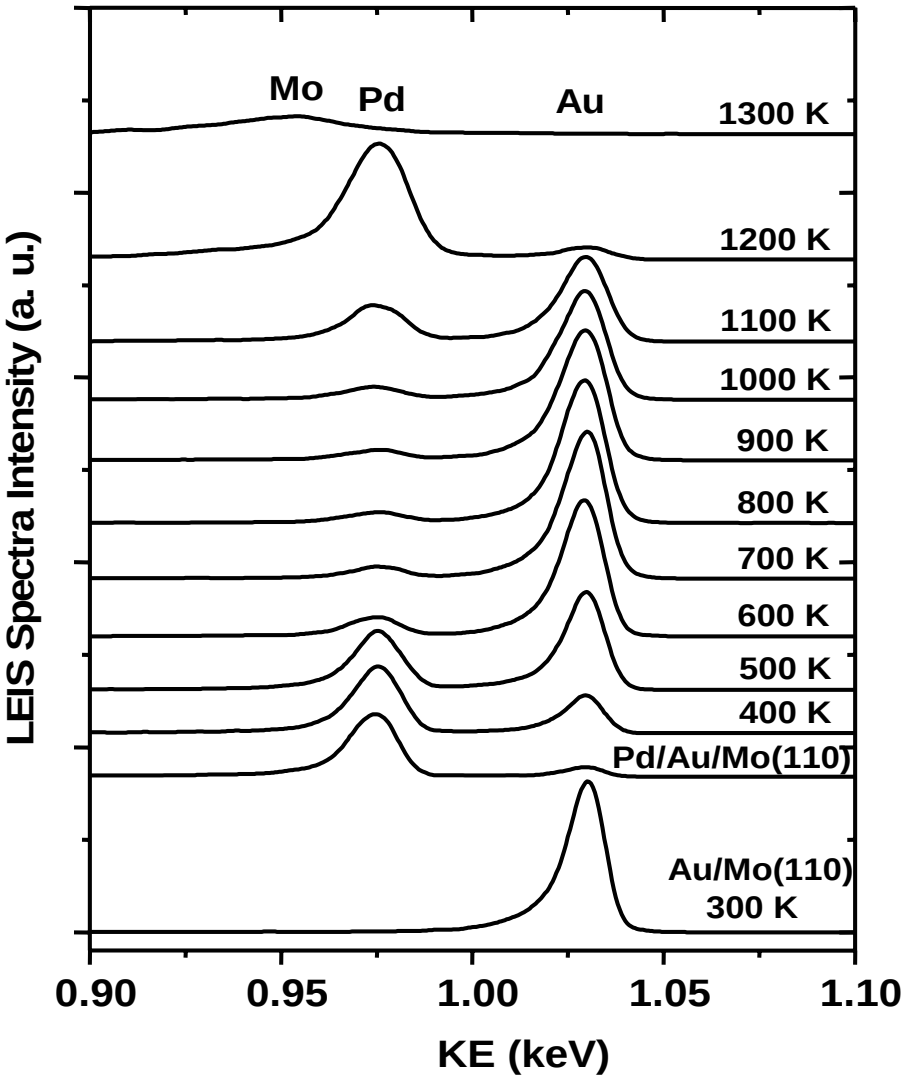

Figure 20. LEIS spectra of 5.0 ML Pd/5.0 ML Au/Mo(110) as a function of annealing temperature.

Similar LEIS experiments were conducted on 5.0 ML Au/5.0 ML Pd/Mo(110) (data not shown). Each surface was annealed to the indicated temperature for 15 minutes, and all LEIS spectra were collected at 300 K. Figure 21 shows the surface concentrations of (a) Au and (b) Pd plotted as a function of annealing temperature; the same methods are used as in Figure 14. Squares (-■-) represent data for the Au/Pd/Mo deposition sequence; circles (-●-) represent data for the Pd/Au/Mo deposition sequence.

In Figure 21(a), the variation of Au surface concentration for both systems in the temperature region of 300 to 600 K was due to thermally induced Au-Pd alloying. Within the region of 700 to 1000 K, a nearly constant Au surface concentration was detected. The sharp decrease in Au surface concentration from 1100 to 1200 K was due to the Au desorption.

Results of the Pd surface concentrations are shown in Figure 21(b). A distinct trend in the variation of Pd surface concentration could be delineated in three temperature regions: 300-600 K, 700-1000 K, and 1100-1200 K. LEIS studies of Au and Pd concentrations revealed that a stable surface alloy was formed in the temperature range of 700-1000 K regardless of the deposition sequence. Surface concentrations of Pd and Au were approximately 20 % and 80 %, respectively, under this situation. Hence, Au surface segregation was clearly indicated, in agreement with previous works on $AuPd_3$ single crystals [88,89] and Au-Pd alloy studies. [36,37,90]

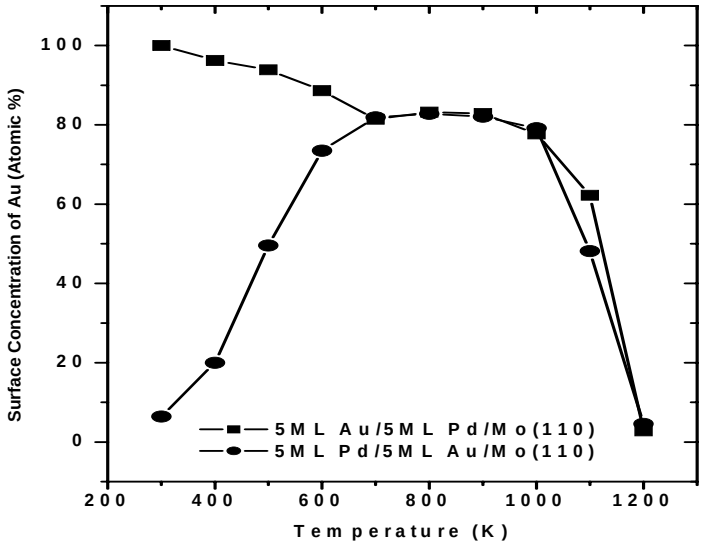

(a)

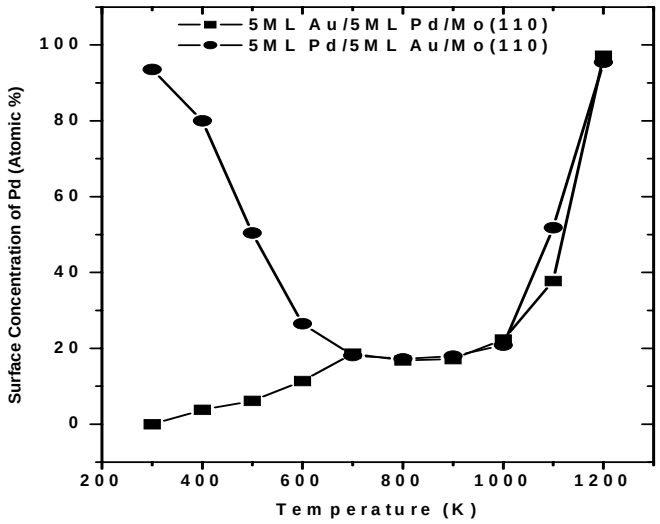

(b)

Figure 21. Surface concentration of (a) Au and (b) Pd as a function of annealing temperature for 5.0 ML Au-5.0 ML Pd/Mo(110).

To systematically study the surface composition for Au-Pd surface alloys with various Au: Pd atomic ratios, LEIS experiments were performed for 9.0 ML Pd-1.0 ML Au/Mo(110), 7.5 ML Pd-2.5 ML Au/Mo(110), 2.5 ML Pd-7.5 ML Au/Mo(110), and 1.0 ML Pd- 9.0 ML Au/Mo(110) with different deposition sequences.

Figure 22 displays surface concentrations of Au and Pd for 7.5 ML Au-2.5 ML Pd/Mo(110) system plotted as a function of annealing temperature. Similar to the findings in Figure 21, stable Au-Pd surface alloys were obtained within the temperature region of 700 K to 1000 K, with extensive Au surface segregation for different deposition sequences. For the 2.5 ML Au-7.5 ML Pd/Mo(110) system, surface concentrations of Au (Figure 23(a)) and Pd (Figure 23 (b)) converged at 800 K; however, a 10 % difference was observed for various Au-Pd deposition sequences between 900 to 1100 K, possibly due to different Pd or Au diffusion rates with high Pd concentration.

To study the surface composition as a function of annealing time, LEIS experiments were performed for 5.0 ML Au-5.0 ML Pd/Mo(110) system after annealing at 800 K. In Figure 24, the surface concentrations of Au are presented as closed circle (-●-) for 5.0 ML Pd/5.0 ML Au/Mo(110) and open circle (-○-) for 5.0 ML Au/5.0 ML Pd/Mo(110). The values of Pd are shown in closed square (-■-) for 5.0 ML Pd/5.0 ML Au/Mo(110) and open square (-□-) for 5.0 ML Au/5.0 ML Pd/Mo(110). The surface composition changed rapidly during the initial 15 minutes annealing and became stable thereafter. For example, the surface concentration of Au for 5.0 ML Pd/5.0 ML Au/Mo(110)(-●-)

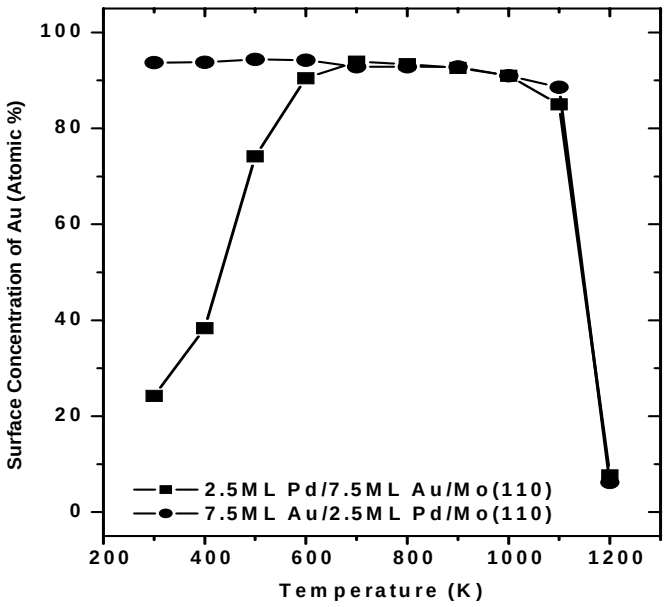

(a)

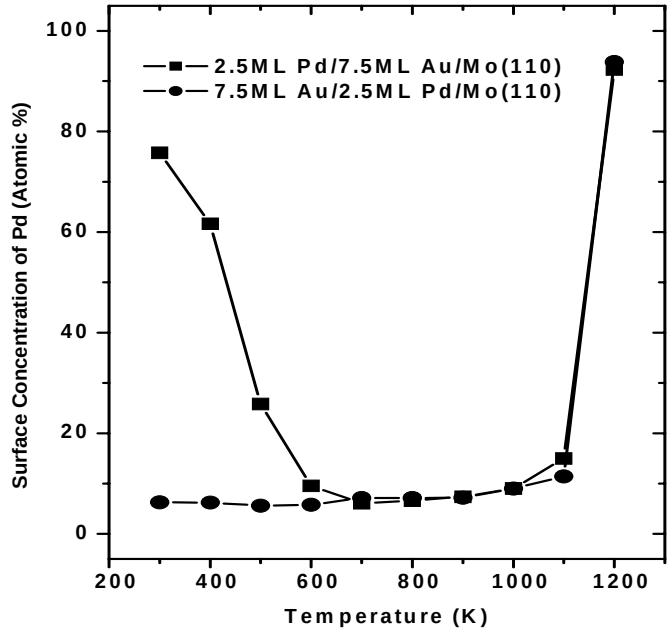

(b)

Figure 22. Surface concentration of (a) Au and (b) Pd as a function of annealing temperature for 7.5 ML Au-2.5 ML Pd/Mo(110).

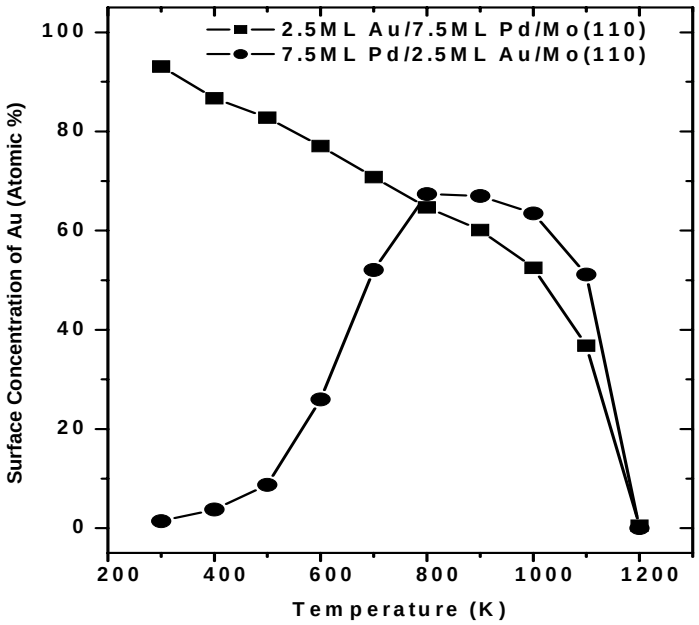

(a)

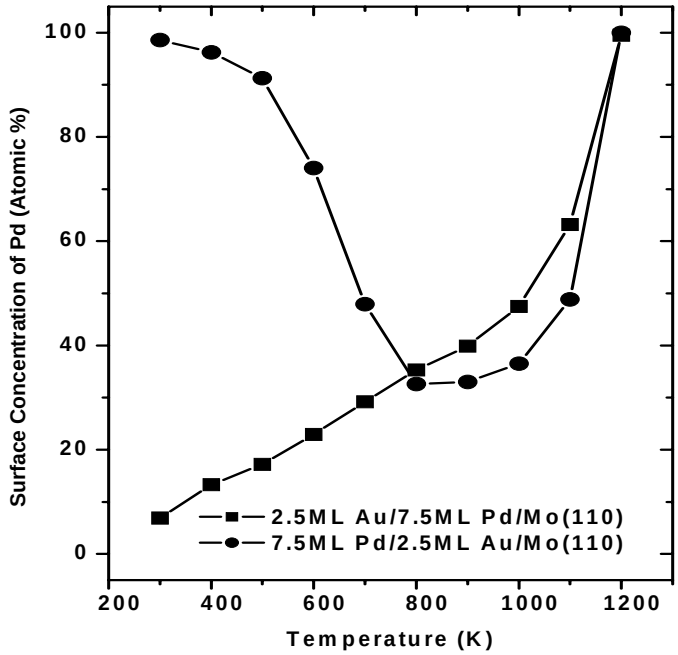

(b)

Figure 23. Surface concentration of (a) Au and (b) Pd as a function of annealing temperature for 2.5 ML Au-7.5 ML Pd/Mo(110).

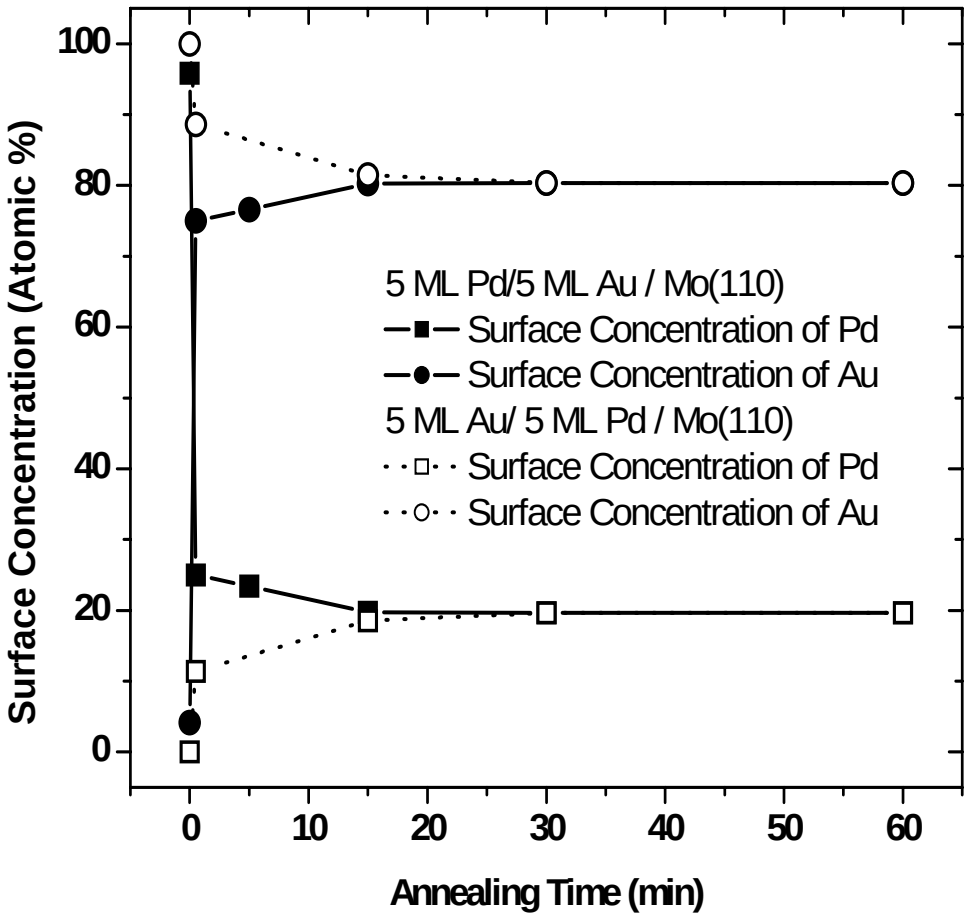

Figure 24. Surface concentration of Au and Pd of 5.0 ML Au-5.0 ML Pd/Mo(110) as a function of annealing time at 800 K.

was 4 % after depositing 5.0 ML Pd at 300 K. After 30 seconds of 800 K annealing, the surface concentration of Au dramatically increased to about 75 %. The Au surface concentration then increased to 77 % after 5 minutes of annealing and reached 80 % after 15 minutes. Surface concentration stayed essentially constant with annealing times longer than 15 minutes. The corresponding values of Pd are also shown in Figure 24. Reversing the deposition sequence of Au and Pd yielded similar surface concentration profiles at various annealing times. The results indicated that the Au-Pd alloying process occurred very fast at an annealing temperature of 800 K. Under the present experimental conditions, the Au-Pd surface alloys were compositionally stable, as earlier suggested by the results of Figure 21.

Temperature-dependent LEIS studies yielded a surface-versus-bulk Au-Pd alloy phase diagram upon 800 K annealing, shown in Figure 25. The solid line connecting the round points represent the ideal bulk Au/Pd concentration upon mixing, and the dash line connecting the square points represent the empirical surface Au/Pd composition. At a 10 % Au bulk concentration, the surface composition was 40 % Au. The Au surface concentration reached about 65 % at a 25 % bulk concentration, and approximately 80 % at a 1:1 Au : Pd bulk concentration ratio. These results clearly indicated that the surface composition varied with the bulk concentration; such surface Au enrichment emanated from the surface segregation of Au. These result agreed with those from the LEIS study of Au-Pd bulk alloy by Swartzfager et al. [40] and demonstrated a null correlation between the alloy bulk composition and reactivity toward real catalytic reactions.[24]

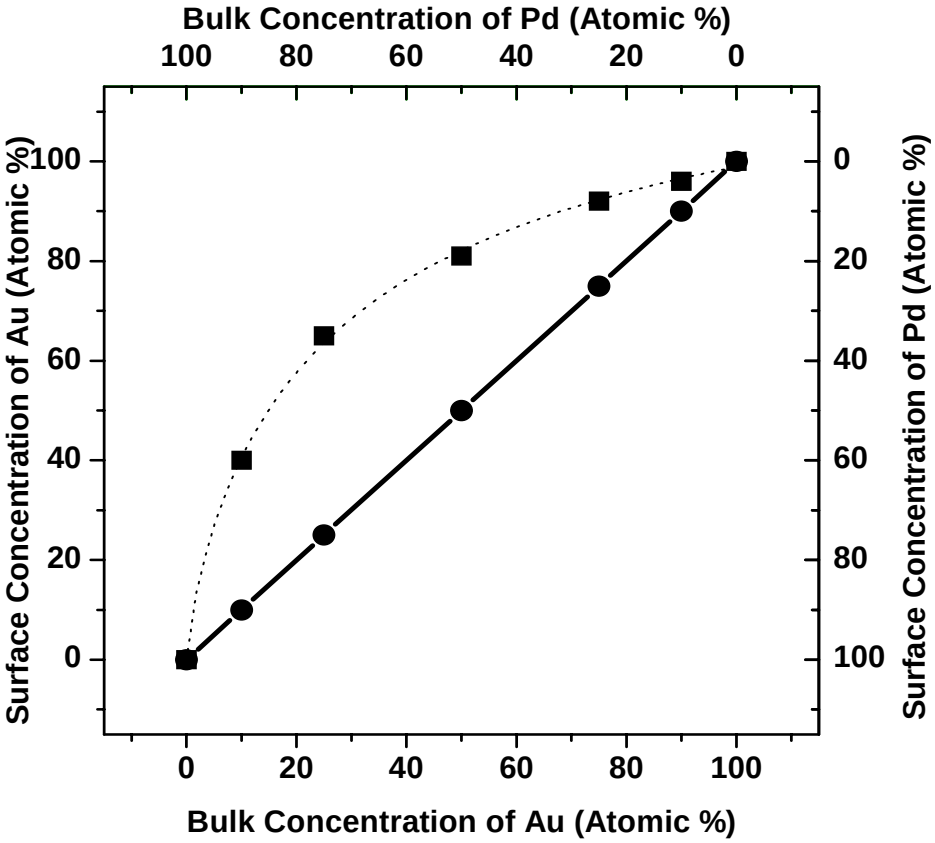

Figure 25. Surface vs. bulk composition phase diagram of Au-Pd alloy/Mo(110) upon annealing at 800 K.

XPS of Au-Pd overlayers/Mo(110)

XPS spectra were collected after each LEIS experiment performed for all Au-Pd/Mo(110) overlayers. In Figure 26, Au 4f core level photoemission spectra were plotted as a function of annealing temperature for 5.0 ML Pd/5.0 ML Au/Mo(110). The Au $4f_{7/2}$ feature was centered at 83.7 eV, a value that was only *ca.* 0.1 eV smaller than the bulk value. After depositing 5.0 ML Pd on 5.0 ML Au/Mo(110) at 300 K, the Au $4f_{7/2}$ feature was shifted slightly to a lower value. The Au peak position continued to shift to lower binding energy up to 600 K and then remained stable through 800 K. At 1100 K, a slight shift in peak position to a higher binding energy was observed.

The Pd 3d core level spectra were recorded in Figure 27 as a function of annealing temperature for 5.0 ML Pd/5.0 ML Au/Mo(110). Because the Au $4d_{5/2}$ feature overlapped with the Pd $3d_{5/2}$ peak, the Pd $3d_{3/2}$ peak was used to monitor CLBE shift. After Pd deposition, a Pd $3d_{3/2}$ peak position of 340.6 eV was recorded. Slight negative binding energy shifts were observed upon annealing up to 700 K; and the direction of peak shift was reversed at annealing temperatures above 700 K.

Core level shifts of Au $4f_{7/2}$ (Figure 28(a)) and Pd $3d_{3/2}$ (Figure 28(b)) for the 5.0 ML Au-5.0 ML Pd/Mo(110) were monitored as a function of annealing temperature for both Au-on-Pd and Pd-on-Au deposition sequences. Regardless of the Au-Pd deposition sequence, both Au $4f_{7/2}$ and Pd $3d_{3/2}$ peaks began at approximately the same positions as their bulk values. These peaks then shifted to lower binding energies with annealing up to 700 K. This shift is an indication of alloy formation and in agreement with the

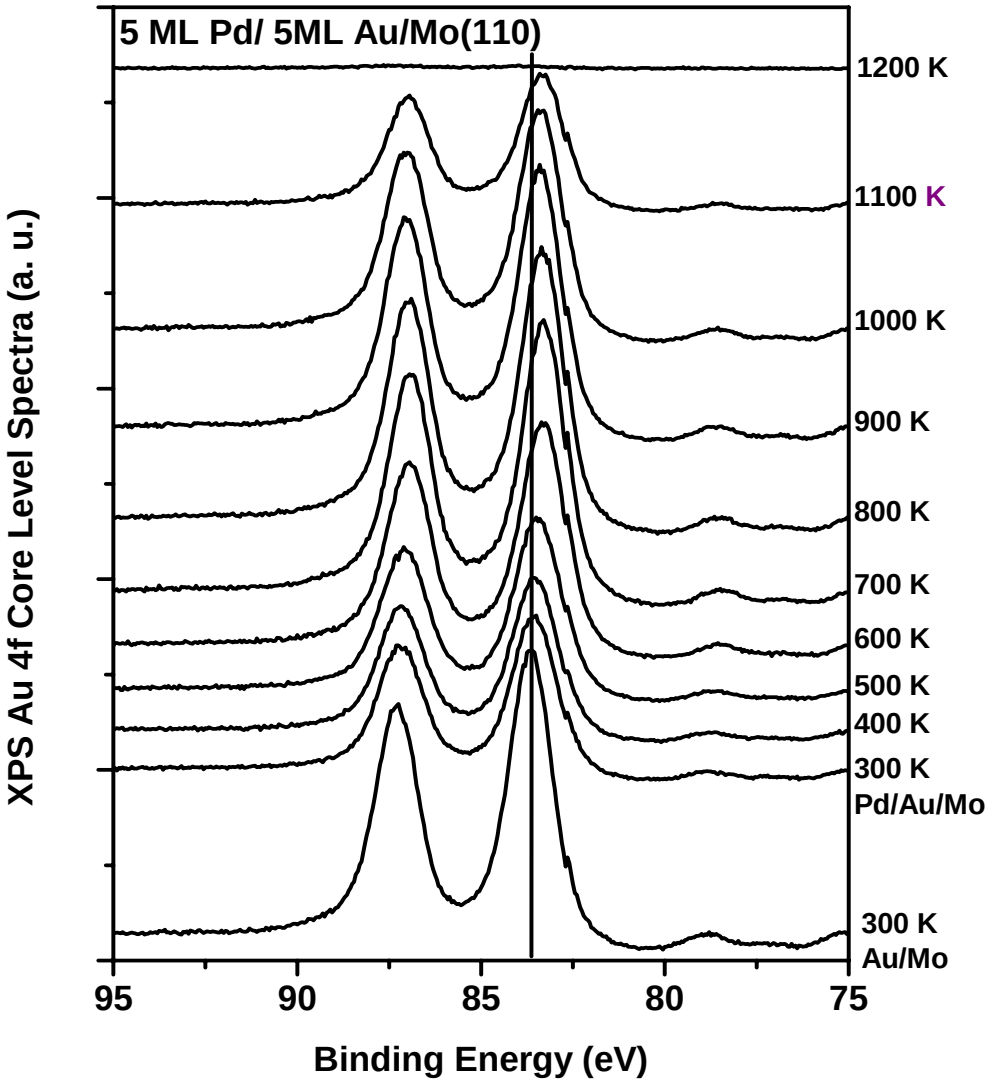

Figure 26. XPS Au 4f core level spectra of 5.0 ML Pd/5.0 ML Au/Mo(110) as a function of annealing temperature.

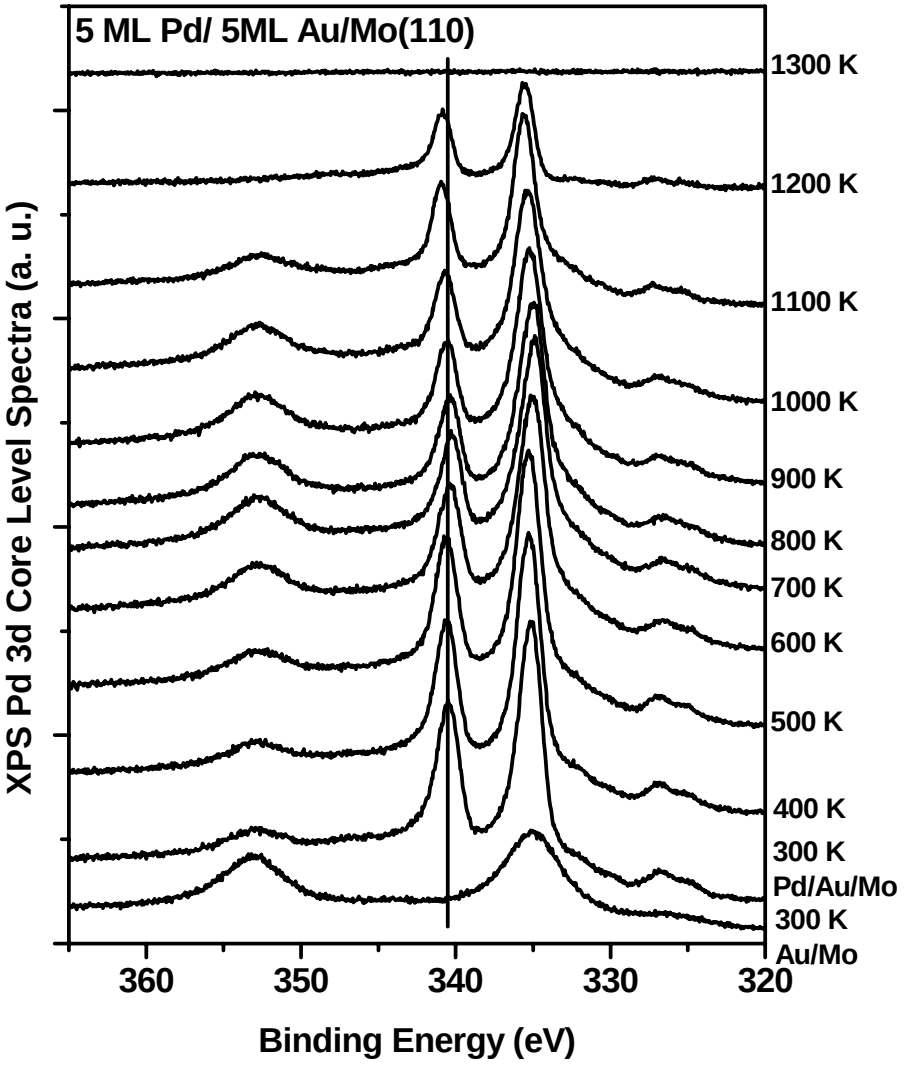

Figure 27. XPS Pd 3d core level spectra of 5.0 ML Pd/5.0 ML Au/Mo(110) as a function of annealing temperature.

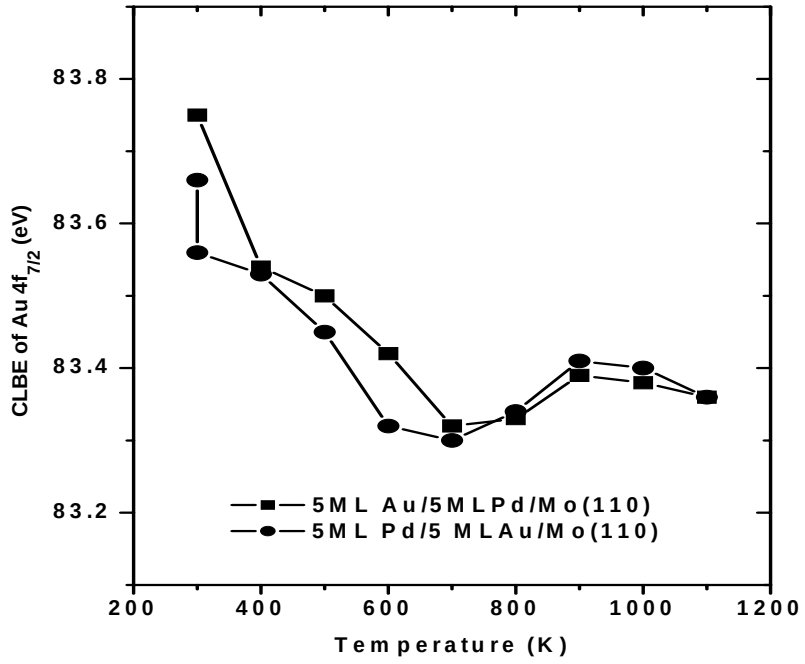

(a)

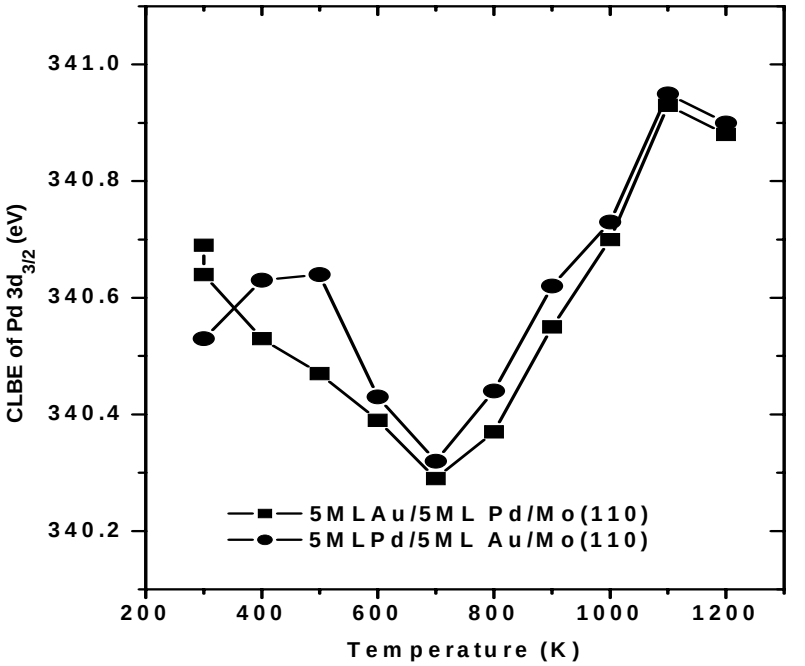

(b)

Figure 28. XPS CLBE of (a) Au $4f_{7/2}$ and (b) Pd $3d_{3/2}$ for 5.0 ML Au-5.0 ML Pd/Mo(110) as a function of annealing temperature.

reported CLS due to Pd-Au alloying.[42] At temperatures of 700-900 K, the Au 4f CLS ceased and a 0.2 eV reversal of Pd 3d CLS occurred. At temperatures over 1000 K, the Pd peak shifted to a position approximately the same as that of the 1.0 ML-1.0 ML Pd-Au/Mo(110) system; such shift was ascribed to Au and Pd clustering or desorption. The formation of stable Au-Pd alloys was indicated by the convergence of Au and Pd XPS CLBE positions at high temperatures (>700 K).

Mo 3d core level spectra were collected along in addition to Au and Pd spectra. In Figure 29, Mo 3d spectra for 5.0 ML Pd/5.0 ML Au/Mo(110) were recorded as a function of annealing temperature. Although the intensity of the Mo 3d feature fluctuated due to the deposition and subsequent annealing of Au and Pd, the Mo $3d_{5/2}$ appeared approximately at the same position as that of the bulk; thus, it can be inferred that, during the Au-Pd alloying process, substrate-overlayer interaction (substrate effect) was essentially negligible.

The normalized Mo $3d_{5/2}$ peak area intensity was shown in Figure 30 as a function of annealing temperature. A 55% attenuation of the Mo peak area intensity was observed upon depositing 5.0 ML Au onto the substrate; subsequent deposition of 5.0 ML Pd at 300 K diminished the Mo signal to 25% of the original value. No significant variation in Mo 3d peak area intensity was observed until the annealing temperature exceeded 800 K. At an annealing temperature of 900 K or higher, the Mo 3d intensity increased rapidly, implying possible morphological changes brought about by like clustering and/or Au/Pd desorption.

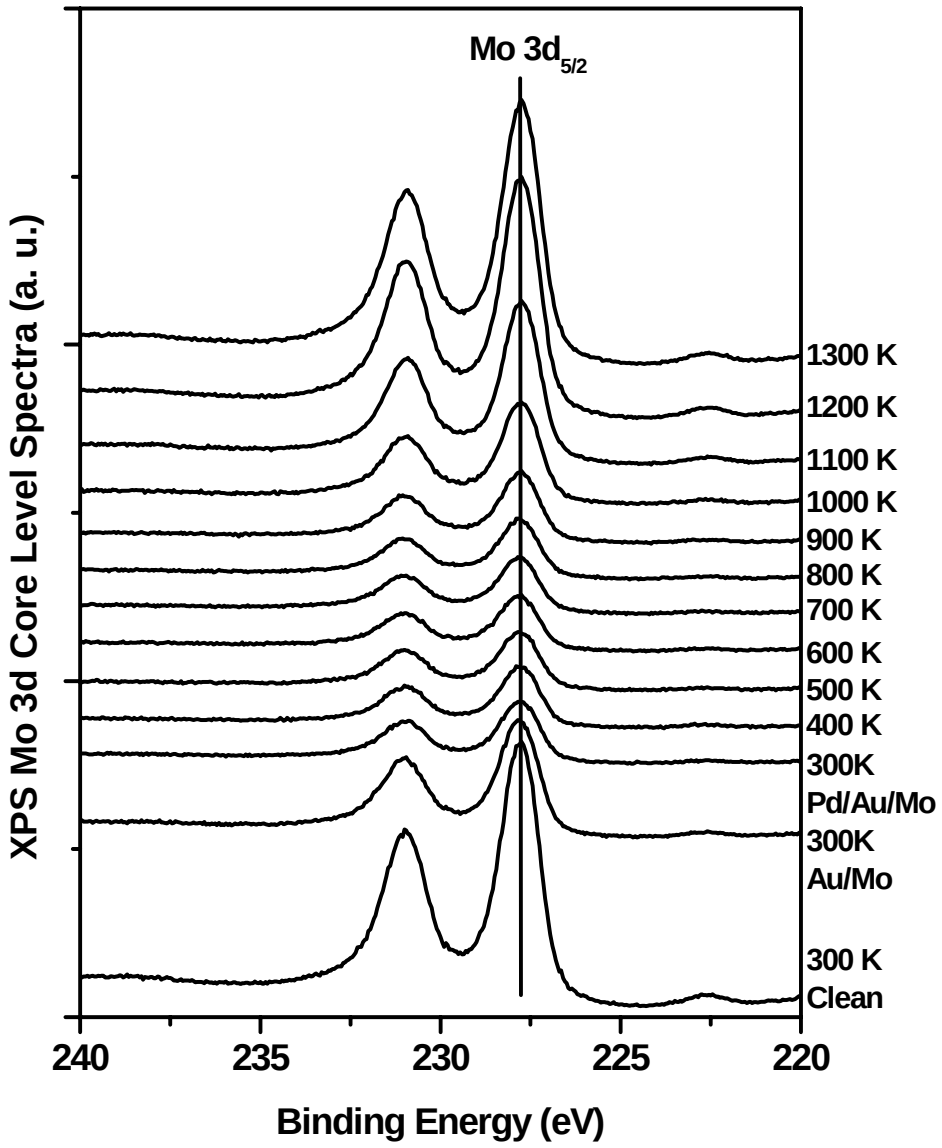

Figure 29. XPS Mo 3d core level spectra of 5.0 ML Pd/5.0 ML Au/Mo(110) as a function of annealing temperature.

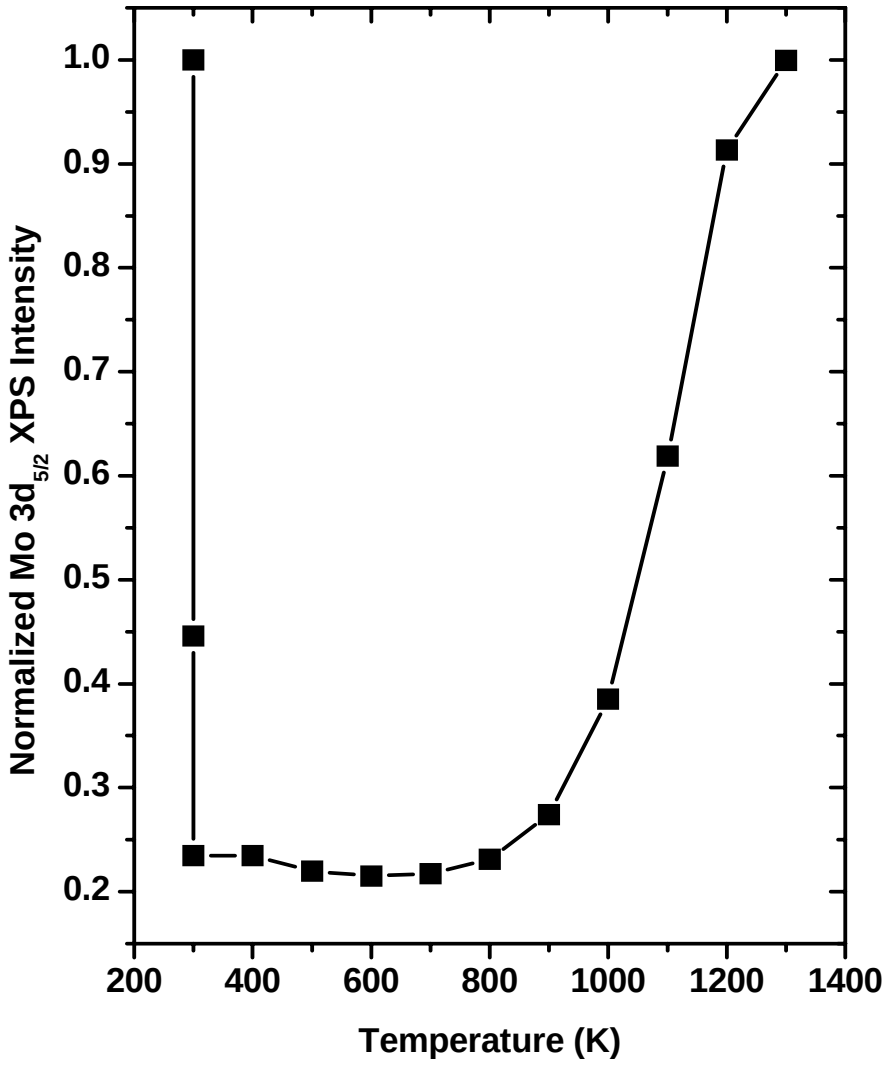

Figure 30. Normalized XPS Mo $3d_{5/2}$ core level peak area intensity as a function of annealing temperature.

To further analyze the alloy composition near the surface region, the ratio of Pd $3d_{3/2}$/Au $4f_{7/2}$ XPS core level peak areas was calculated and plotted versus the annealing temperature for the 5.0 ML Au-5.0 ML Pd/Mo(110) system (Figure 31).

At temperatures below 700 K, the large variation in Pd/Au ratios indicated a thermally induced Au-Pd interdiffusion during the annealing process. The plateau at 700-1000 K reflected the stability of the alloy formed near the surface region; the peak area ratio leveled off at *ca*. 3/7.

It is important to recall the proximity of the sensitivity factors for the XPS Pd 3d and Au 4f peak signals when comparing the compositional information derived from XPS and LEIS. Since XPS essentially collects more bulk information (up to a sampling depth of 10 ~100 Å) than the topmost-surface-sensitive LEIS, the ratio difference between XPS and LEIS data, therefore, represents the compositional difference between the surface layer and the near-surface region. Consolidated XPS and LEIS data suggested the existence of a Au-enriched transition region between the Au-segregated top layer and bulk alloy.

CO-TPD

TPD experiments were performed on 800-K pre-annealed 10 ML Pd/Mo(110) and 10 ML Au/Mo(110) surfaces at various CO dosages. The substrate temperature was 90 K; during the CO dose, a linear heating rate of 5 K per second was used.

In Figure 32, a CO desorption peak was recorded with a center at *ca.* 460 K, subsequent to the lowest CO dosage of 0.1 Langmuir (L). According to previous CO-

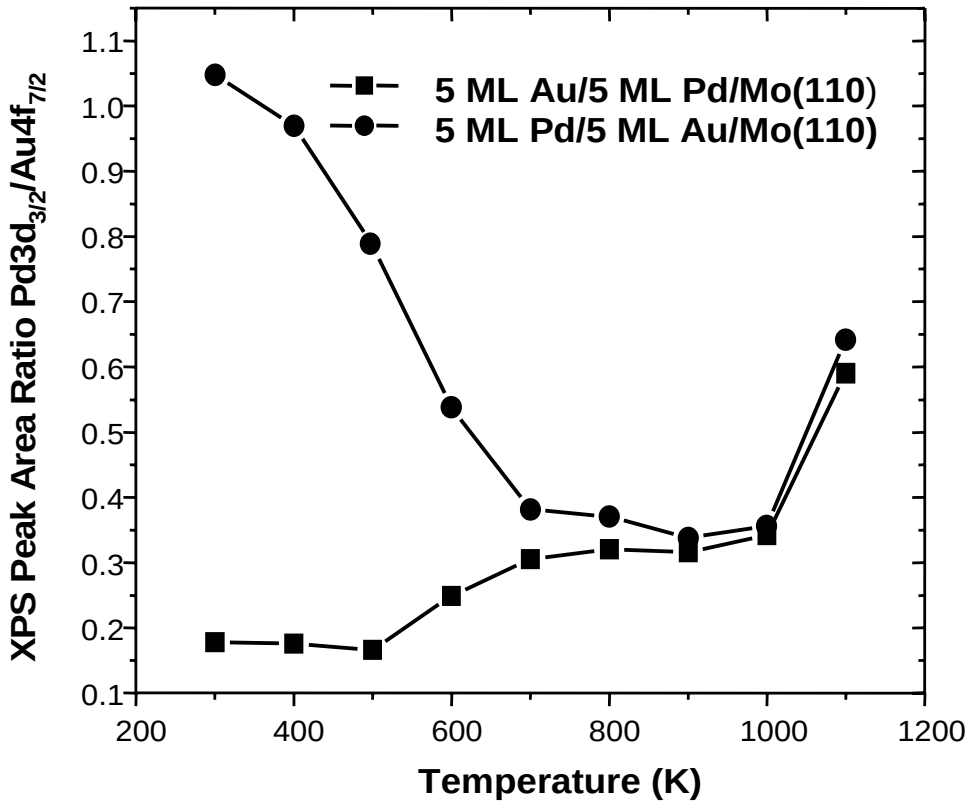

Figure 31. XPS core level Pd 3d $_{3/2}$/Au 4f $_{7/2}$ peak area ratio as a function of annealing temperature for 5.0 ML Au/5.0 ML Pd/Mo(110)(-■-) and 5.0 ML Pd/ 5.0 ML Au/Mo(110) (-●-).

IRAS and TPD studies on Pd(111) and multilayers of Pd on Mo(110),[91,92] the feature is attributed to CO on multi-fold (bridging and three-fold hollow) Pd sites. At higher CO dosages, the peak intensity increased until saturation was reached at *ca.* 0.25 L CO. A new feature centered at *ca.* 300 K was recorded at much higher CO dosages; such feature was assigned to CO adsorption on atop Pd sites.

TPD spectra resulting from dosages of 0.1 to 10 L CO on 10 ML Au/Mo(110) are presented in Figure 33. No strong CO desorption feature was observed above 200 K for all CO dosages. Weak, nondescript features were observed at temperatures ranging from 100 to 200 K; these were attributed to weak CO adsorption on Au.

Similar CO-TPD experiments were conducted on bimetallic Au-Pd surfaces on Mo substrate. Displayed in Figure 34 are the resulting spectra for the 5.0 ML Pd/5.0 ML Au/Mo(110) surface treated with various CO dosages. At a very low CO dosage of 0.01 L, a CO desorption feature was recorded with a centroid at *ca*. 310 K. With increasing CO dosages, the intensity of this feature also increased, became saturated, and developed a shoulder below 150 K. From the absence of CO desorption features in the 400-500 K, it can be surmised that Pd bridging or three-fold hollow sites did not exist on the surface. It can be recalled that LEIS analysis of this Au-Pd bimetallic surface [*vide supra*] demonstrated the existence of a highly Au-enriched adlayer of 20 % Pd and 80 % Au. Our explanations for CO TPD are that most of Pd atoms are surrounded by Au atoms and form a special surface ensemble- isolated Pd sites on the Au-Pd alloy surface. This results in CO only adsorbing on a-top Pd sites as indicated in TPD studies here. Further

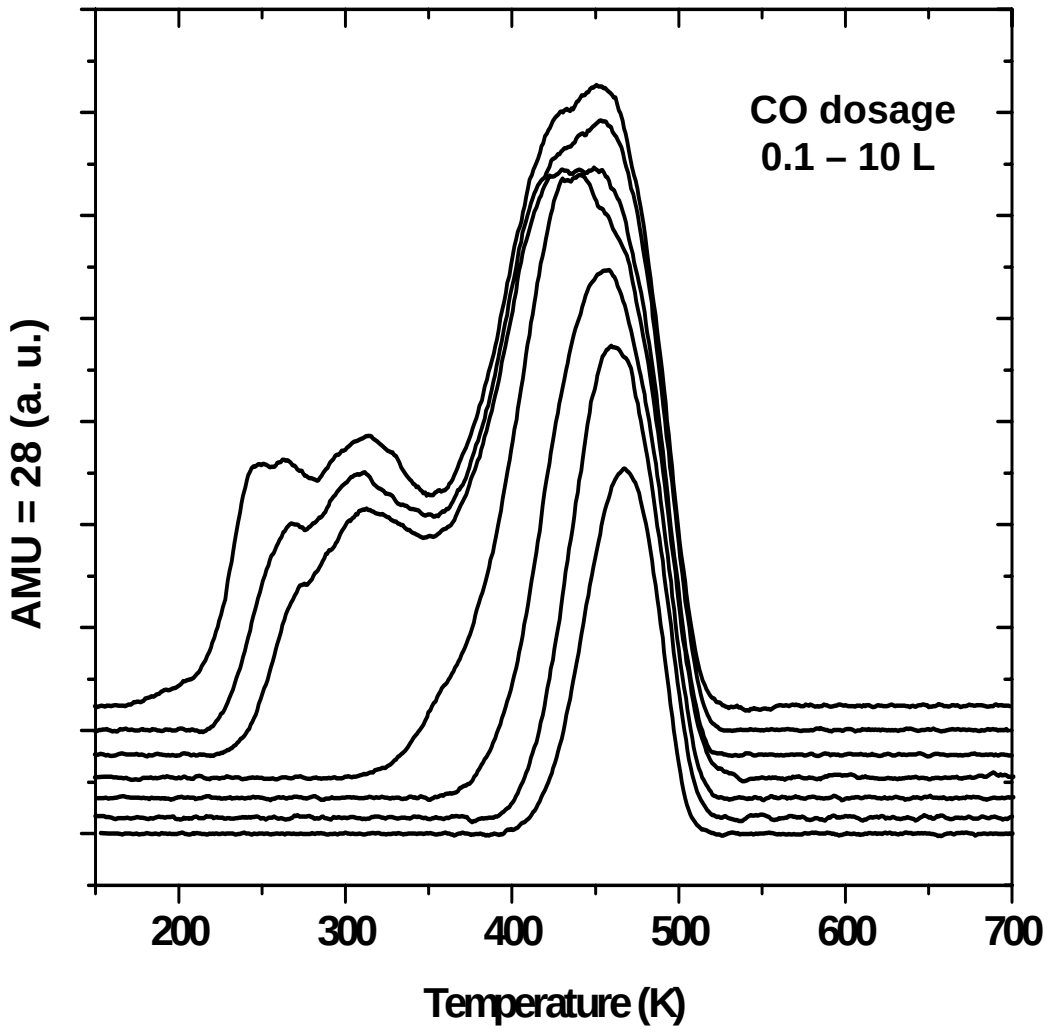

Figure 32. TPD of CO on 10 ML Pd/Mo(110) 800 K pre-annealed surface with CO dosage from 0.10 to 10 L.

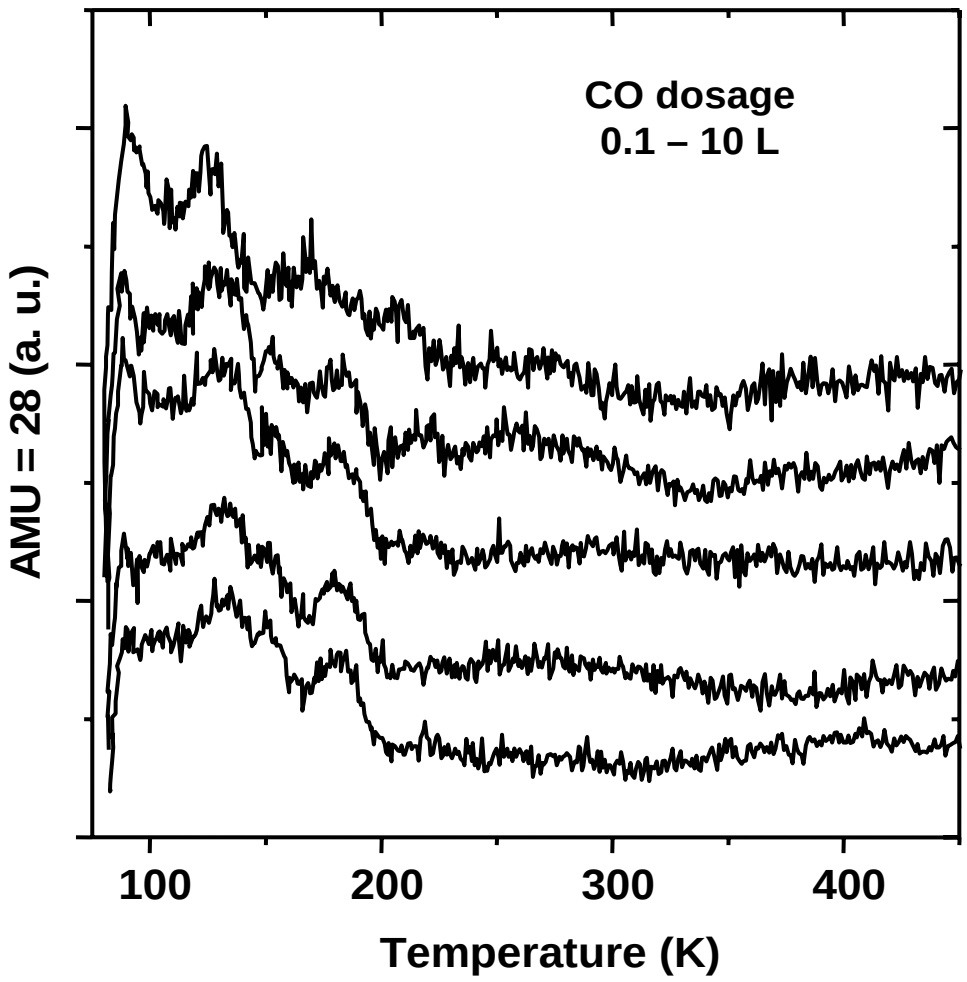

Figure 33. TPD of CO on 10 ML Au/Mo(110) 800 K pre-annealed surface with CO dosage from 0.10 to 10 L.

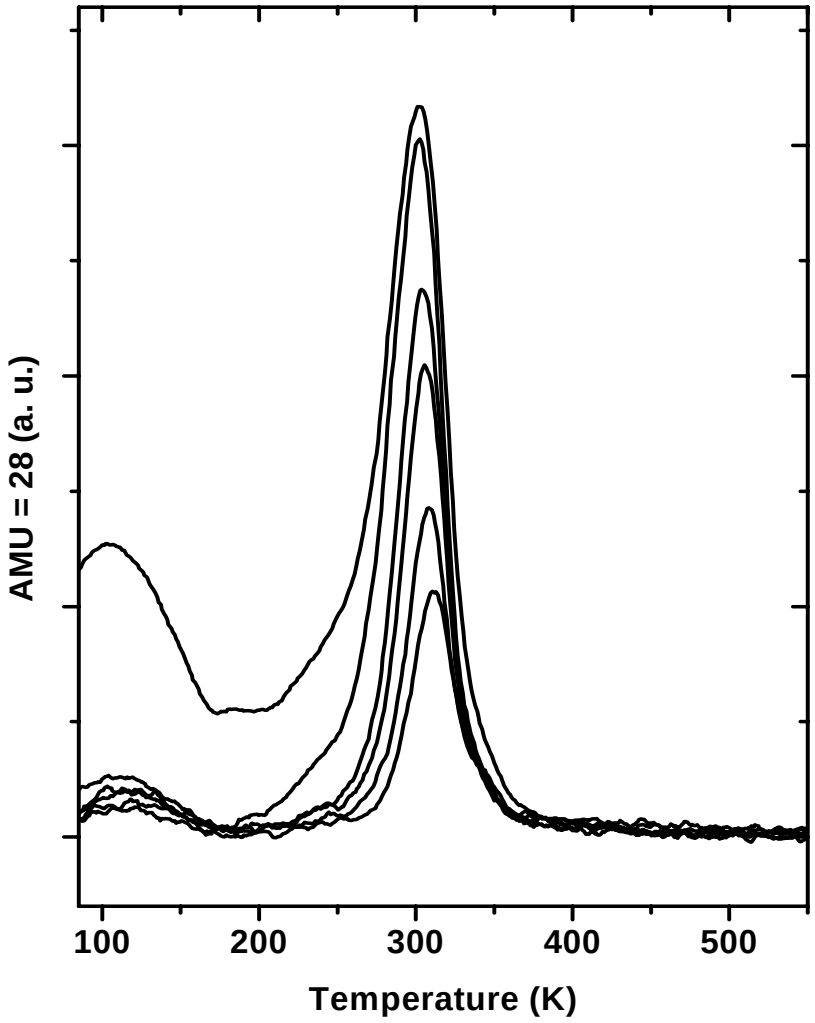

Figure 34. TPD of CO on 5.0 ML Pd/5.0 ML Au/Mo(110) 800 K pre-annealed surface with CO dosage from 0.01 L to 0.5 L.

discussions regarding to the identification of this unique surface ensemble will be included in the following section of CO IRAS studies.

Additional CO-TPD experiments were conducted on the Au-Pd bimetallic surfaces with various Au-Pd atomic ratios. A saturated CO dosage of 1.0 L was applied in all cases.

Figure 35 shows that no CO desorption was detected at temperatures below 200 K in the spectra for CO TPD on 10 ML Au/Mo(110), as observed previously. Given that the surface layer composition for 7.5 ML Au/2.5 ML Pd/Mo(110) surface was 90% Au and 10 % Pd (from LEIS results in Figure 22), the small peak recorded at approximately 300 K was assigned to CO on a-top Pd sites. The broad feature occurring at temperatures below 200 K was assigned to CO on Au. A dominant peak recorded at a temperature of 300 K represented CO desorption from 5.0 ML Au/ 5.0 ML Pd/Mo(110), and the surface layer is believed to be composed prevalently of isolated Pd sites. The results are also in agreement with CO TPD for the reversed Au-Pd deposition recorded in Figure 34. With increasing Pd deposition ratios in the alloy overlayers, CO TPD demonstrated multi-fold CO adsorption features as a prominent shoulder at 360 K beside the a-top adsorbed CO for 2.5 ML Au/7.5 ML Pd/Mo(110) surface and a broad strong feature between 350- 490 K for 1.0 ML Au/9.0 ML Pd/Mo(110) surface. CO desorption from both a-top and multi-fold Pd sites was detected for 10 ML Pd/Mo(110) as discussed earlier.

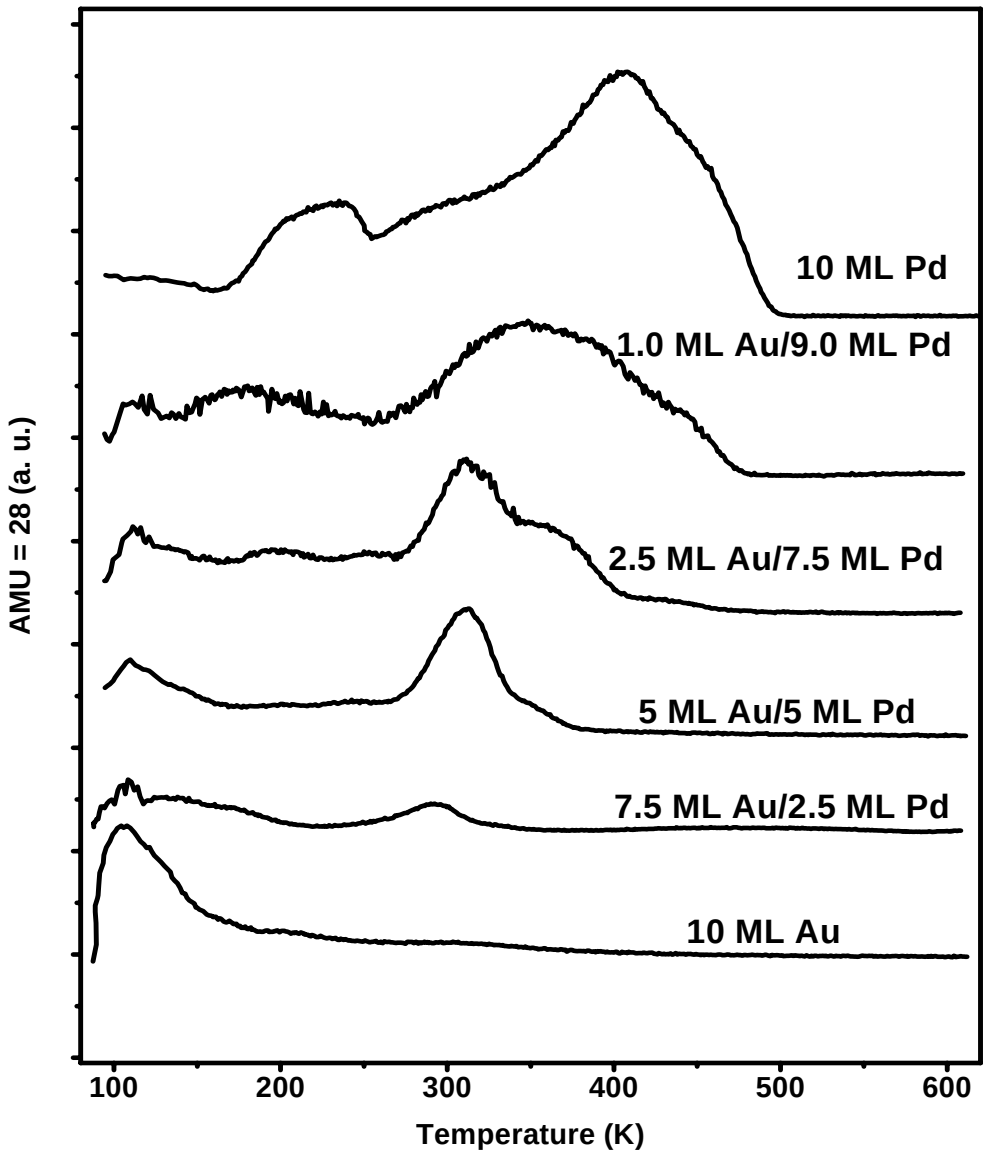

Figure 35. TPD of CO on 800 K pre-annealed Au-Pd surfaces with various Au : Pd atomic ratios with saturated dosage- 1.0 L CO.

As a result of the variation in mass spectrometer and chamber conditions, the CO TPD spectra slightly differed for CO on 10 ML Au/Mo(110) and 10 ML Pd/Mo(110), as can be gleaned by comparing Figure 35 with Figures 32, 33. However, the essential desorption peak intensities and desorption temperature ranges are in good agreement.

It is evident from the results in Figure 35 that, by alloying with Pd, Au exhibits the propensity to modify the desorptive behavior of CO from Pd. The formation of the isolated Pd sites can be controlled by systematically varying the Au-Pd surface ratio. The potential of this surface-composition–controlled reactivity is expected to exert a significant impact on the designs of multimetallic heterogeneous catalysts.

Ethylene and Acetic Acid TPD

To further study the correlation of surface structure-reactivity of Au-Pd planar alloy surfaces, deuterated ethylene (C_2D_4) TPD was used as a probe for studying bimetallic Au-Pd catalysts on Mo(110) surfaces with different Au-Pd atomic ratios. C_2D_4 adsorption was done at 90 K with a saturated C_2D_4 dosage of 2.0 L.

According to previous studies,[93-97] ethylene can adsorb to the Pd surface on a single Pd atom via a π-bonding or on a pair of adjacent Pd atoms via a di-σ bonding in the low temperature and high temperature region of 100-300 K. The dearth of TPD and related vibrational spectroscopic studies of ethylene adsorption on Au stems from the conventional notion that Au is an inert metal for heterogeneous catalysis.

The TPD spectra of C_2D_4 on Au, Au-Pd, and Pd/Mo(110) surfaces are shown in Figure 36. The mass unit of 30 was selected as a measure to avoid overlap with O_2 in the vacuum.

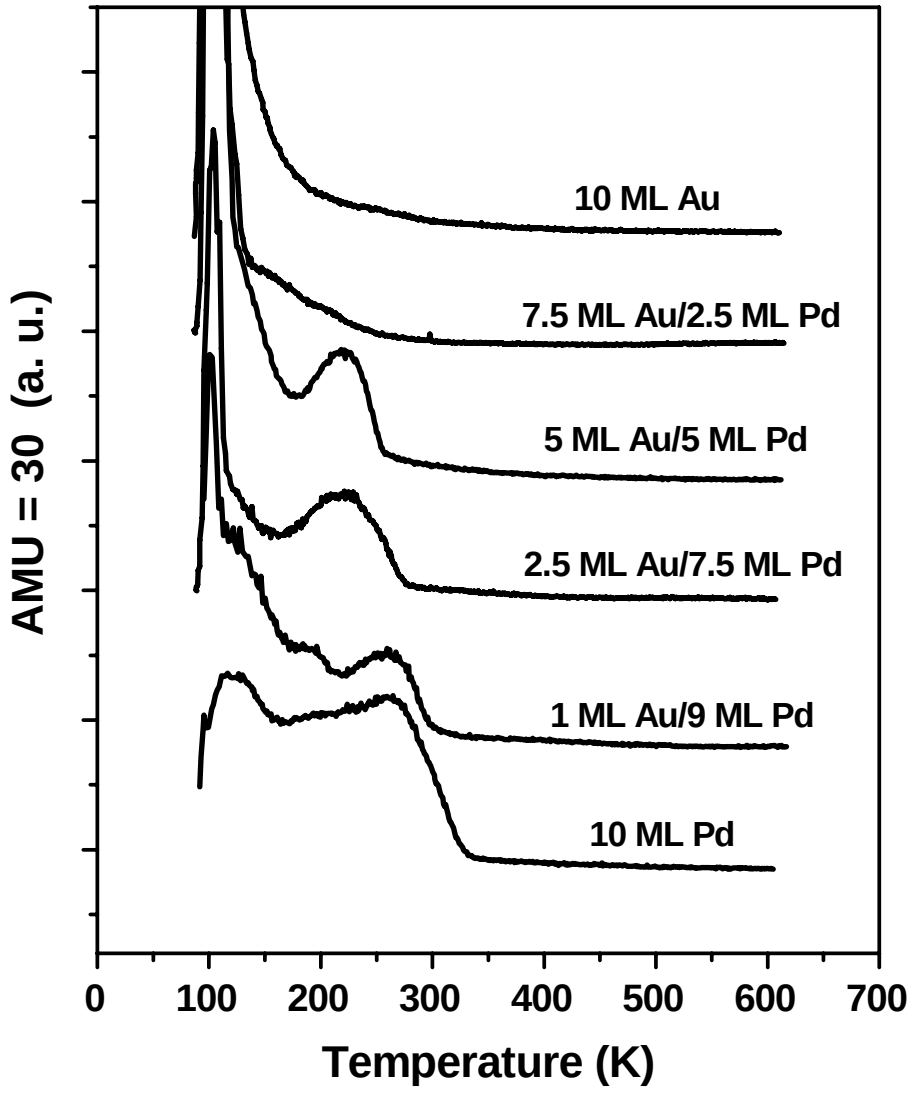

Figure 36. C_2D_4 TPD on 800 K pre-annealed Au-Pd/Mo(110) surfaces with saturated dosage-2.0 L C_2D_4.

C_2D_4 TPD on 10 ML Au/Mo(110) is displayed as the topmost spectral line. Strong desorption signals were observed at temperatures below 200 K, and only a small shoulder was observed for those above 200 K. The data indicated a weak Au-C_2D_4 interaction.

Because only the features recorded at temperatures above 150 K are of concern in this study, peaks recorded at temperatures below 150 K are not displayed. The features recorded between 150 – 200 K were increased in intensity for C_2D_4 on 7.5 ML Au/2.5 ML Pd/Mo(110). The previous LEIS, IRAS, TPD studies indicated that π bonded C_2D_4 on a small number of isolated Pd sites may account for this finding. The same reasoning was invoked to explain the distinct feature centered at 230 K observed from C_2D_4 TPD on 5 ML Au/ 5 ML Pd/Mo(110). For surfaces with relatively higher Pd concentrations, like 2.5 ML Au/7.5 ML Pd/Mo(110), the feature was broadened, and the center shifted positively by 10-15 K. Due to the existence of multi-fold Pd sites on surfaces with higher Pd concentrations, the existence of di-σ bonded C_2D_4 could account for the peak broadening and temperature desorption shifts.

C_2D_4 TPD spectra for 1.0 ML Au/9.0 ML Pd/Mo(110) gave two features whose centers were located at 200 and 280 K. The peak at the higher temperature was clearly larger than the one at the lower temperature, indicating more di-σ bonded C_2D_4 than π bonded C_2D_4. The peak centered at 280 K increased in intensity in the TPD spectra of C_2D_4 on 10 ML Pd/Mo(110), as a result of increased amounts of di-σ bonded C_2D_4 on pure Pd surfaces.[95]

Ethylene dehydrogenation on Pd planar surfaces or oxide-supported clusters has been reported in the literature;[93-95] hydrogen is one of the major products. These studies demonstrated that di-σ bonded C_2D_4 dehydrogenates into different reaction intermediates, e.g., ethylidyne ($\equiv CCH_3$) and vinyl ($=CH\text{-}CH_2$) on Pd(111) and Pd(100) facets, respectively, before these intermediates further evolve into final products.

D_2 production from C_2D_4 TPD dehydrogenation process of Pd, Au-Pd, and Au/Mo(110) surfaces is presented in Figure 37. The background D_2 feature from C_2D_4 cracking has been subtracted from the spectra lines. An intense peak feature, centered at 325 K, with a strong shoulder at temperatures of 350-500 K was detected. This peak and high temperature shoulder were assigned to the β and γ states (the combination of γ_1 and γ_2 states), respectively.[93-95,97] Data from C_2D_4 dehydrogenation on 1.0 ML Au/9.0 ML Pd/Mo(110) suggested that β and γ states were well separated, possibly, as a result of the ensemble effects brought about by Au mixed into the Pd matrix. Data from C_2D_4 TPD on 2.5 ML Au/7.5 ML Pd/Mo(110) demonstrated a much smaller β state with the γ features seen as a small bump in the high temperature region. On the 5.0 ML Au/5.0 ML Pd/Mo(110) surface, D_2 production from C_2D_4 dehydrogenation was negligible as illustrated in the mid spectra line of Figure 37. When more Au was present on the surface, as in 7.5 ML Au/2.5 ML Pd/Mo(110) and 10 ML Au/Mo(110), no D_2 production was detected from C_2D_4 TPD.

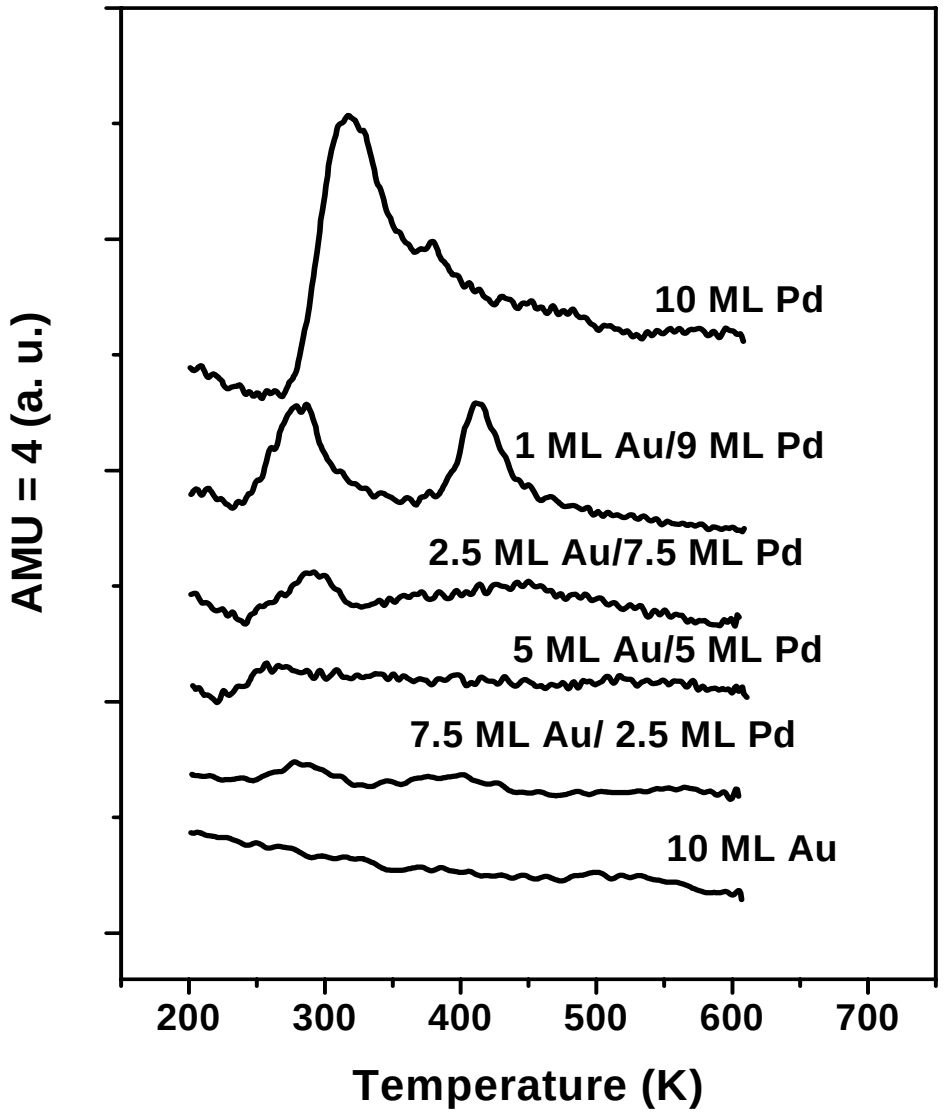

Figure 37. D_2 signals from C_2D_4 dehydrogenation in C_2D_4 TPD experiments on 800 K pre-annealed Au-Pd/Mo(110) surfaces with saturated dosage- 2.0 L C_2D_4.

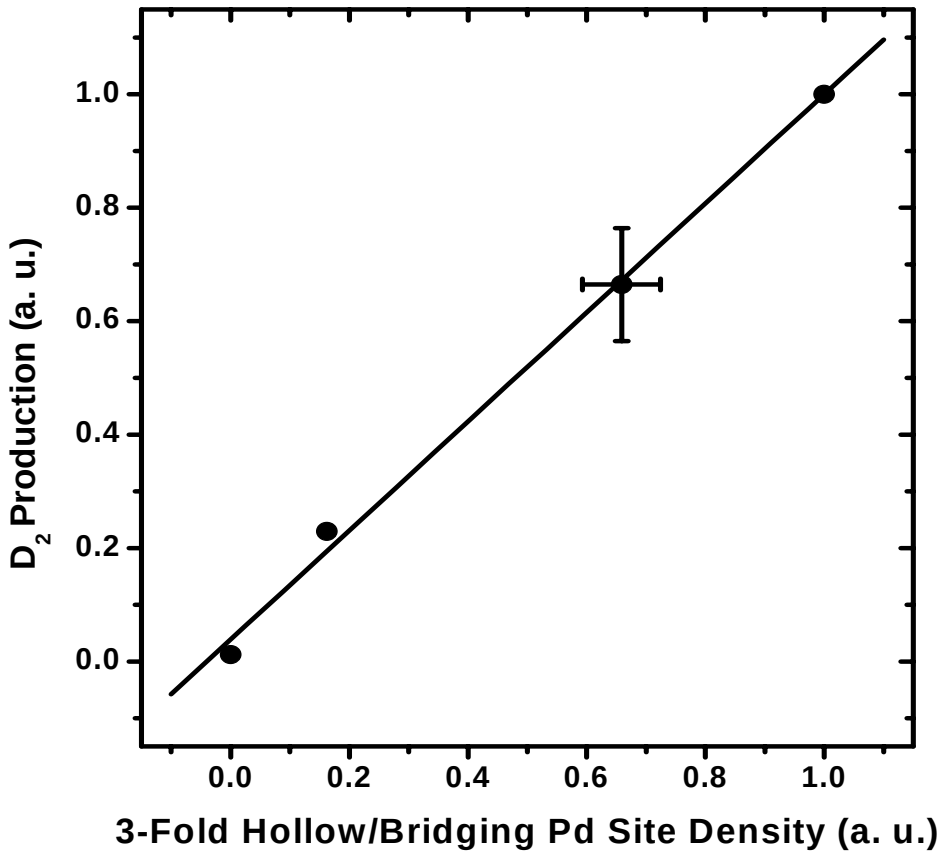

Figure 38. Normalized D_2 production yield as a function of multi-fold Pd site density on Au-Pd/Mo(110) surfaces.

Evidently, D_2 yield was maximized on a 10 ML Pd/Mo(110) surface where the density of multi-fold Pd sites was highest. On a 5.0 ML Au/5.0 ML Pd/Mo(110) surface where isolated Pd sites were prevalent, no di-σ bonded C_2D_4 existed and D_2 production was completely suppressed. It can be inferred that these multi-fold Pd sites are crucial for the conversion of reaction intermediates, such as ethylidyne (≡C-CD_3) or vinylidene (=CD-CD_2), into final products.

To better understand the correlation between the surface reactivity and adsorption sites, the D_2 production yield was normalized to that obtained for 10 ML Pd/Mo(110). The results are plotted in Figure 38 as a function of the density of the multi-fold Pd sites (three-fold hollow and bridging sites) on Au-Pd surface alloys with various Au:Pd atomic ratios and presented. The density of multi-fold Pd sites was obtained by subtracting the CO adsorption signals on a-top Pd and Au sites in the spectrum of 5.0 ML Au/5.0 ML Pd/Mo(110) from other spectra with smaller Au:Pd atomic ratios (as recorded in Figure 35) and normalized to that observed for 10 ML Pd/Mo(110). That a linear relationship (Figure 38) existed between the D_2 yield and multi-fold Pd site density indicated a strong correlation between surface structure and chemical reactivity for Au-Pd alloy planar surfaces.

CH_3COOH adsorption on Au-Pd catalysts is a key issue in studying the vinyl acetate synthesis reaction. In Figure 39, CH_3COOH TPD spectra on 800 K pre-annealed 10 ML Pd/Mo(110) and 5.0 ML Au/5.0 ML Pd/Mo(110) were denoted with solid and dashed lines, respectively. Note that CH_3COOH adsorption was performed at 170 K and 1.0 L

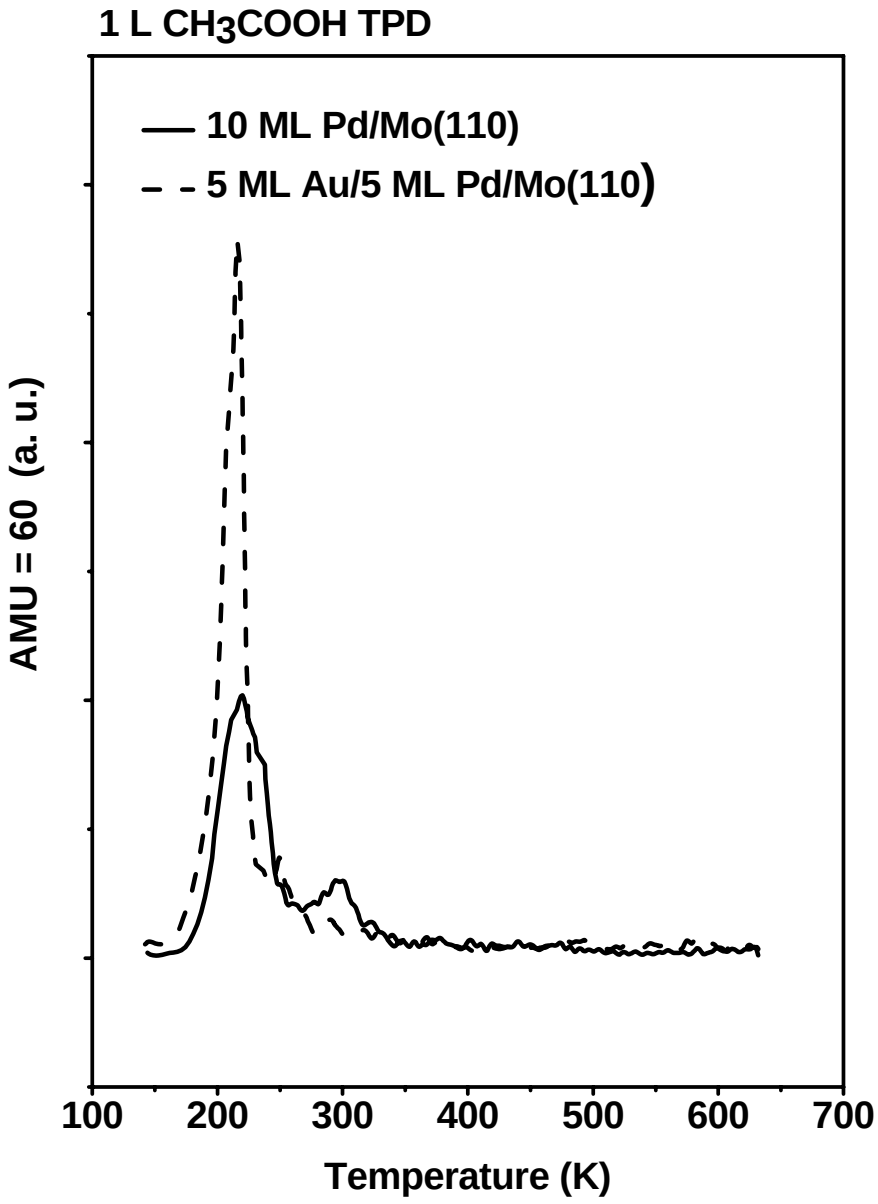

Figure 39. TPD of CH_3COOH on 800 K pre-annealed 10 ML Pd/Mo(110) in solid line and 5.0 ML Au/5.0 ML Pd/Mo(110) in dashed line with saturated CH_3COOH dosage-1.0 L.

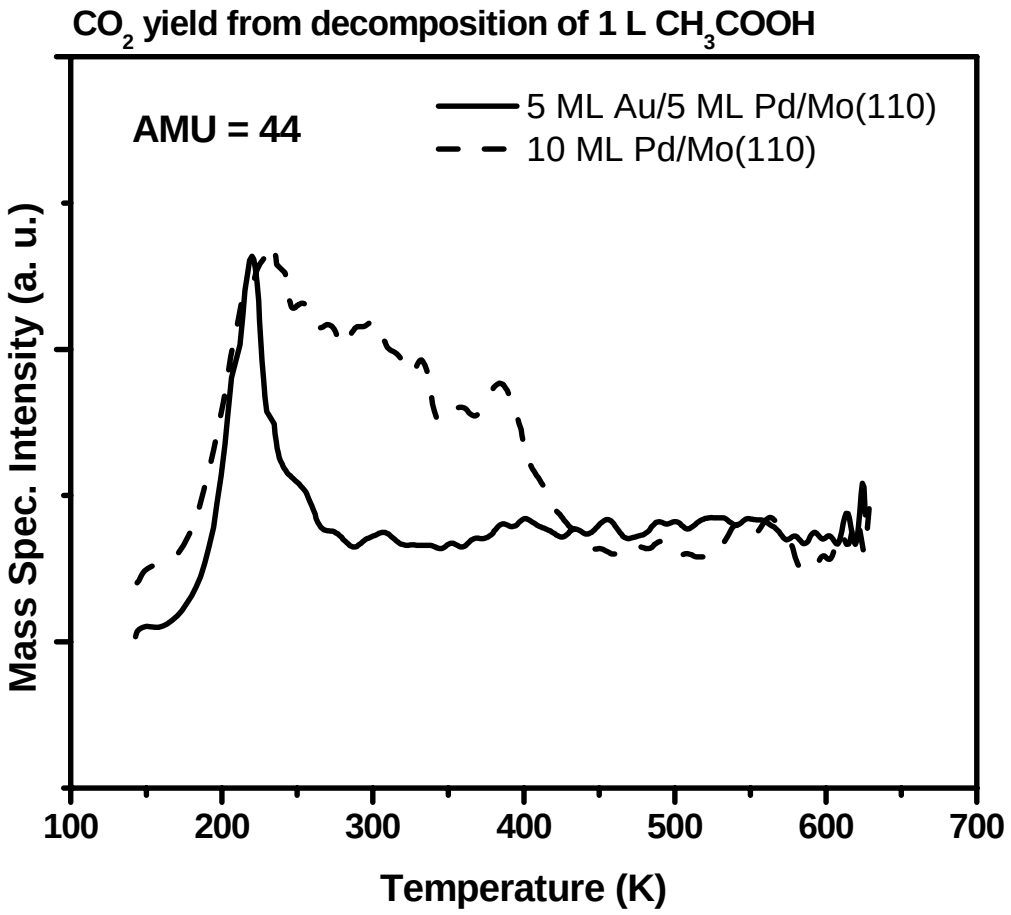

Figure 40. CO_2 signal from CH_3COOH decomposition in CH_3COOH TPD on 800 K pre-annealed 5.0 ML Au/5.0 ML Pd/Mo(110) in solid line and 10 ML Pd/Mo(110) in dashed line with saturated CH_3COOH dosage-1.0 L.

CH_3COOH corresponds to the saturated coverage. Apparently, two desorption features from the CH_3COOH TPD on 10 ML/Pd(110) were centered at ~ 230 and 300 K. The agreement of the relative peak intensity and position with the previous study of CH_3COOH TPD on Pd(111) surface[98] indicated that the surface under investigation had bonding sites that resembled those on the Pd(111) surface. According to Lambert et al., the features at 230 K and 300 K corresponded to CH_3COOH adsorption on atop Pd sites via monodentate species and on bridging Pd sites via bidentate species, respectively. On 5.0 ML Au/5.0 ML Pd/Mo(110) whose surface was predominantly strewn with isolated Pd sites (cf. Figure 39), the bidentate feature associated with Pd bridging sites disappeared; this is a result of the non-availability of multi-fold Pd sites, as indicated by LEIS, CO- and ethylene-TPD, and dehydrogenation experiments. The peak intensity increase and downward temperature desorption shift were ascribed to CH_3COOH desorption from both Au and isolated Pd sites. Although CH_3COOH could adsorb onto isolated Pd sites in a mono-dentate mode, recent HREELS studies hinted at the existence of a special isolated Pd site associated bi-dentate species on this Au-Pd surface.[99]

Previous studies listed CO_2 [98,100,101] as one of the main products in Pd catalyzed CH_3COOH decomposition. Lambert et al. claimed that CO_2 can be produced from the decomposition of mono-dentate and bi-dentate species and CO + O recombination in the temperature range of 200-400 K on Pd (111) surface.[98] In agreement with such finding, CO_2 was detected as a wide peak feature (Figure 40) at temperatures ranging from 200 to 400 K during adsorption experiments of CH_3COOH onto 10 ML Pd/Mo(110). However, a complete diminution of the CO_2 feature at temperatures above 250 K (shown as solid

line) was observed from CH_3COOH TPD on 5.0 ML Au/5.0 ML Pd/Mo(110), the cause of which is thought to be due to the absence of strongly bonded bidentate species on Pd bridging sites.

CO-IRAS

CO-IRAS studies were utilized as a technique to probe the Au-Pd alloy adsorption sites and surface structure. In Figure 41, IRAS spectra of CO adsorption on a 600 K pre-annealed 5.0 ML Pd/5.0 ML Au/Mo(110) surface were presented as a function of CO dosage at 80 K. At 0.02 L CO dosage, two low intensity features were observed with CO stretching frequency centered at 2070 cm^{-1} and 1950 cm^{-1}, respectively; these two features are assigned to CO bonding on a-top and bridging Pd sites, respectively.[47,63,97,102-104] No clear evidence was detected for CO bound onto Pd three-fold hollow site at 1900 to 1800 cm^{-1}. With increasing CO dosages, features for CO on atop and bridging Pd sites increased in intensity and shifted slightly toward higher frequency. Additionally, a peak at 2105 cm^{-1} was recorded with 0.05 L CO as a shoulder of CO on atop Pd sites feature, and was assigned to Au-bound CO.[81] With a CO dosage of 0.2 L or greater, stable peaks appeared with centroids of 2105 cm^{-1}, 2085 cm^{-1}, 1940 cm^{-1}, representing CO bound onto Au, a-top Pd sites, and bridging Pd sites, respectively From LEIS and IRAS results, it can, therefore, be argued that this 600-K pre-annealed Pd-Au surface, which consisted of 30 % Pd, possessed both isolated and bridging Pd ensembles on the surface.

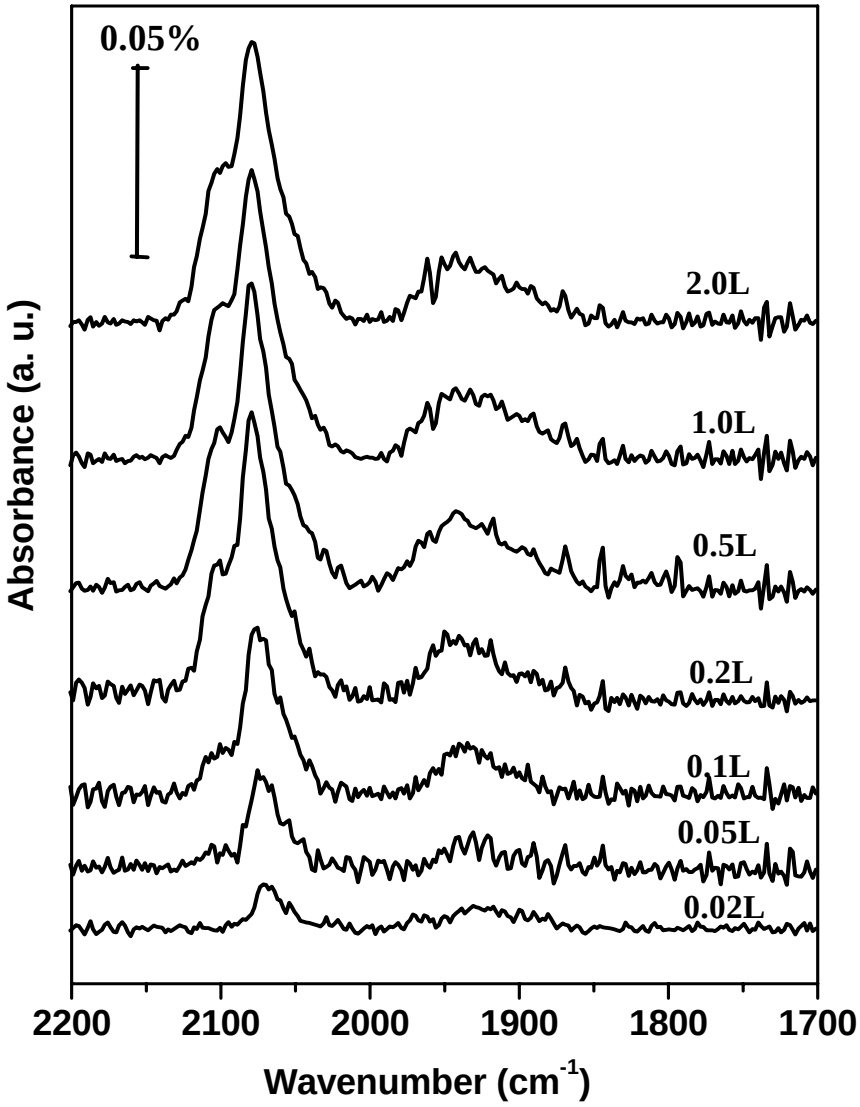

Figure 41. IRAS of CO adsorption at 80 K on 600 K pre-annealed 5.0 ML Pd/5.0 ML Au/Mo(110) as a function of CO dosage.

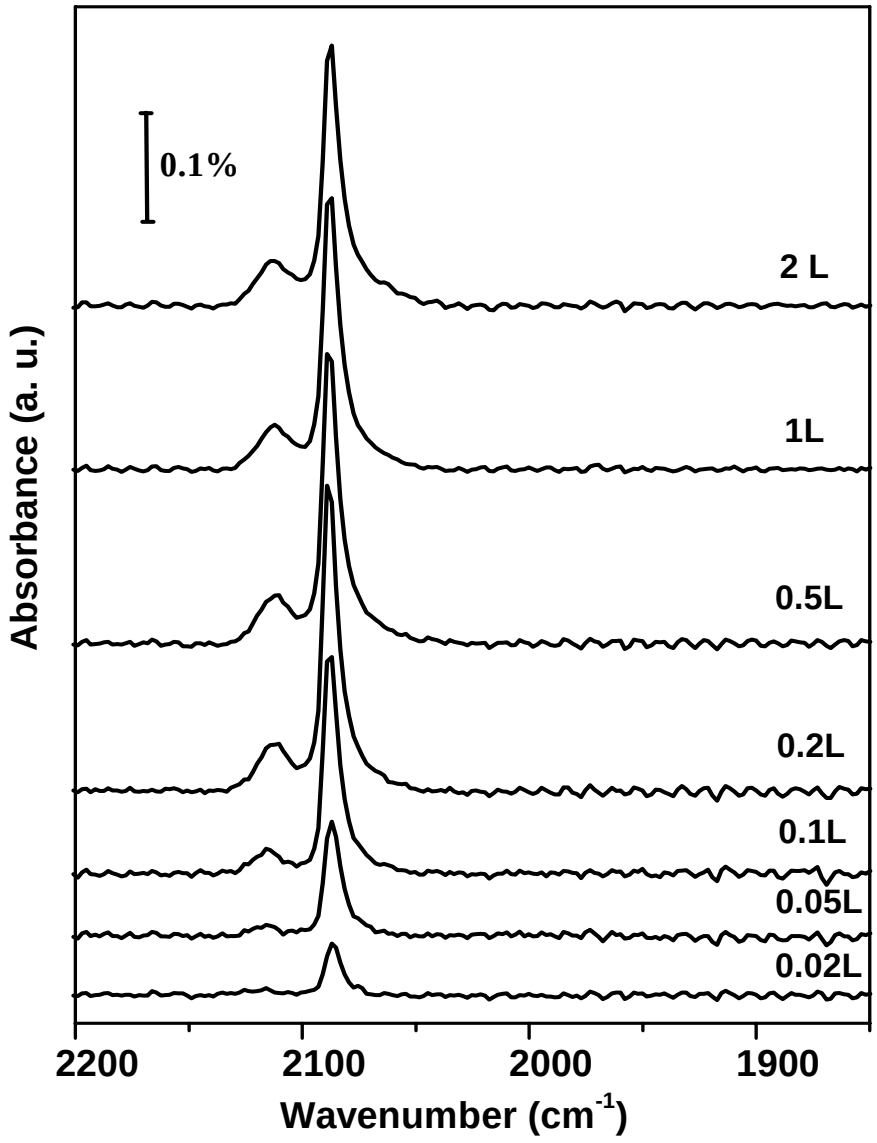

Figure 42. IRAS of CO adsorption at 80 K on 800 K pre-annealed 5.0 ML Pd/5.0 ML Au/Mo(110) as a function of CO dosage.

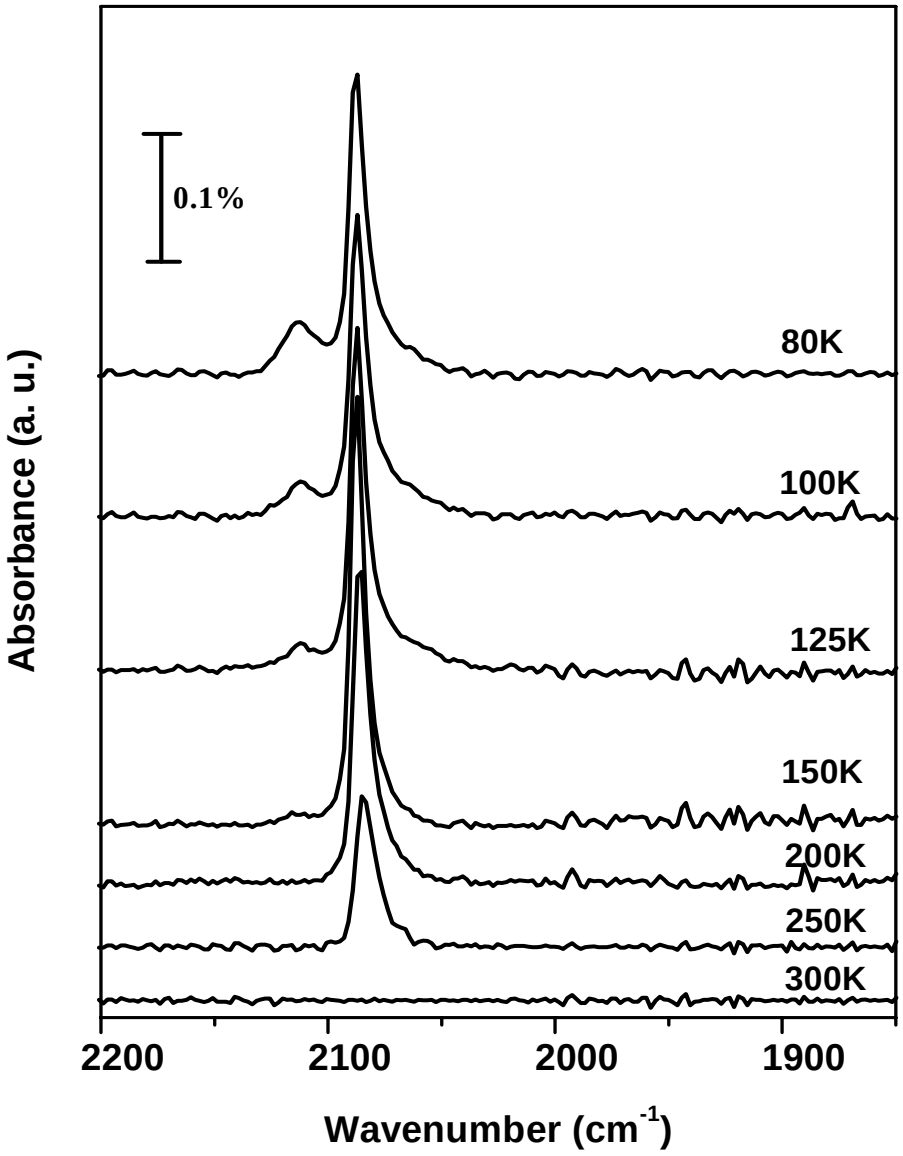

Figure 43. IRAS of CO adsorption at Pco = 1 x 10 $^{-8}$ torr on 800 K pre- annealed 5.0 ML Pd/5.0 ML Au/Mo(110) as a function of substrate temperature.

The IRAS spectra of CO adsorption onto the Pd-Au bimetallic surface, pre-annealed at 800 K, were monitored at different CO dosages. In Figure 42, no adsorption features were observed in the stretching frequency region characteristic for CO bonding on Pd bridging or three-fold hollow sites. With a 0.02 L CO dosage, only a single feature was recorded with a centroid at ~ 2087 cm^{-1}. A small shoulder centered at 2113 cm^{-1} was observed at higher CO dosage of 0.05 L; this feature corresponded to CO bonding on Au. With a CO dosage of 0.5 L or higher, both peak intensities became saturated. No significant shift in peak position was observed for the CO stretching feature at 2087 cm^{-1} with varying CO dosages.

Effects of varying the substrate temperature on the IRAS spectra of CO at saturating dosages were investigated. Figure 43 revealed two features, at 80 K, centered at 2113 cm^{-1} and 2088 cm^{-1}; these peaks were attributed to CO occupying Au and atop Pd sites, respectively. With increasing the substrate temperature, desorption of CO from Au was favored as evidenced by the concomitant decrease of the high frequency feature at 2113 cm^{-1}. At 200 K, the only peak observed corresponded to CO adsorption on Pd a-top sites. The intensity of this feature decreased at 250 K and was completely quenched at 300 K. According to previous LEIS results, thermal annealing of 5.0 ML Pd/5.0 ML Au/Mo(110) at 800 K produced an 80 % Au and 20 % Pd alloy surface. Combined data from temperature-dependent IRAS experiments and CO coverage measurements clearly demonstrated that the Pd adatoms were decorated by a large number of Au atoms to form isolated Pd sites that act as special surface ensembles on a 800-K annealed 5.0 ML Pd/5.0 ML Au/Mo(110) surface.

Au-Pd/SiO_2*

Growth of Au-Pd Alloy Clusters

The growth and characterization of nano-sized clusters of Au and Pd on SiO_2 surfaces have been discussed in the literature.[69,105-108] In general, Pd clusters were more highly dispersed for a given coverage and were more sinter-resistant compared to Au.[106-108] In the present study, amorphous SiO_2 films (2 - 5 nm) were used to support Au-Pd clusters. To synthesize the clusters, 1.0 ML Pd was first deposited on SiO_2 and then annealed to 800 K for 10 minutes. Subsequently, Au was deposited at 300 K, and annealed to 800 K for 10 minutes. LEIS was used to characterize the surface composition and morphology for each deposition condition with all spectra being collected with a substrate temperature of 300 K. The LEIS spectrum in Figure 44(a) was that following the deposition of 1.0 ML Pd on the SiO_2 film and a subsequent 800 K anneal. Three LEIS features with kinetic energy (KE) at 0.45, 0.70, and 0.97 keV were assigned to O, Si, and Pd, respectively. A Mo feature at 0.94 keV was not present, consistent with the Mo substrate being fully covered by the SiO_2 thin film. Upon deposition of 1.0 ML Au at 300 K, the intensity of the Pd feature dramatically decreased by ~ 65%. Concomitantly, a large Au scattering feature appeared at 1.03 keV. The significant decrease of the Pd feature upon deposition of Au indicated that a significant

---

* Reproduced in part with permission from: Luo, K.; Yi, C.-W.; Wei, T; Axnanda, S.; Goodman, D.W. *Journal of Physical Chemistry B* **2005**, 109, 23517, Copyright 2005 American Chemical Society; Chen, M. S.; Luo, K.; Wei, T.; Yan, Z.; Kumar, D.; Yi, C.-W.; Goodman, D. W. *Catalysis Today*, in press.

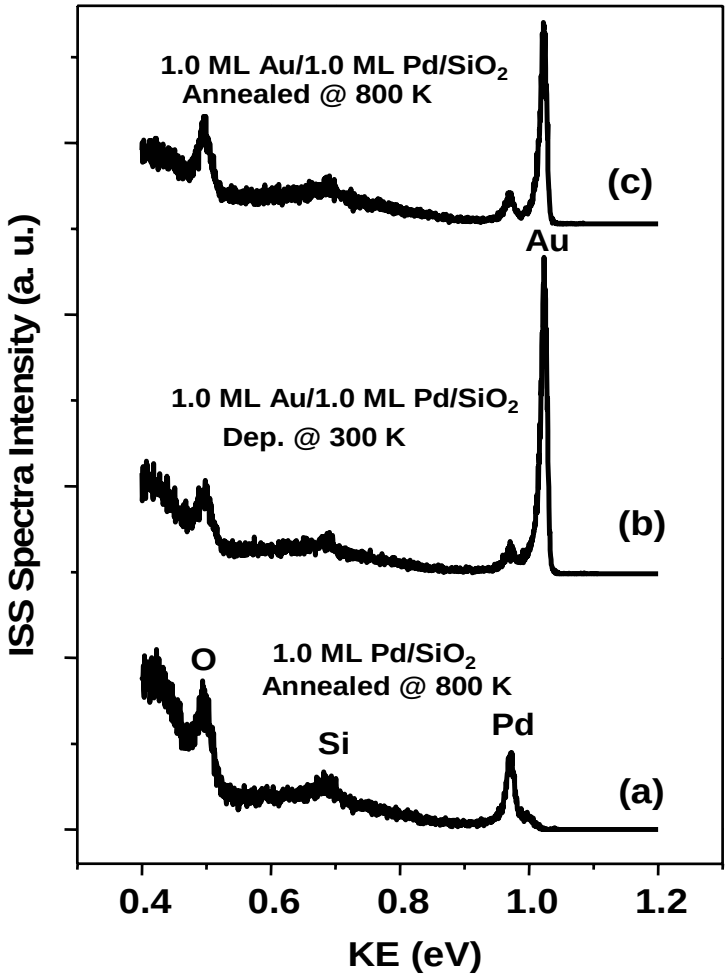

Figure 44. LEIS spectra of (a) 1.0 ML Pd/SiO_2 after a 800 K anneal; (b) after deposition of 1.0 ML Au deposition 300 K on 800 K pre-annealed 1.0 ML Pd/SiO_2; and (c) 1.0 ML Au/1.0 ML Pd/SiO_2 annealed to 800 K. All spectra were collected at 300 K.

amount of the deposited Au decorated the Pd clusters. Upon annealing 1.0 ML Au/1.0 ML Pd/SiO_2 to 800 K, the Pd feature intensity remained essentially constant; however, the Au intensity decreased by ~ 30 %, likely due to Au-Pd alloying and/or certain amount of Au, not directly deposited on Pd, sintered with Pd seeding clusters and self-sintered to form larger Au clusters. Similar LEIS measurements were carried out by reversing the deposition sequence, i.e. 1.0 ML Pd/1.0 ML Au/SiO_2 (data not shown here). The Au scattering intensity was unchanged following Pd deposition, likely because only a small fraction of the added Pd nucleated on the Au clusters with the remainder forming Pd-only clusters.[107,108] Based on data above, the deposition of Pd first was clearly preferable for the synthesis of more uniform Au-Pd alloy clusters.

LEIS Au-Pd scattering data for Au-Pd silica supported clusters, i.e., 1.0 ML Au/1.0 ML Pd/SiO_2, and a planar Au-Pd surface, i. e., 5.0 ML Au/5.0 ML Pd/Mo(110), were shown in Figure 45 as solid and dashed lines, respectively. Note that each of these was annealed to 800 K prior to acquisition of the LEIS spectrum at 300 K. The preparation details of the planar 5.0 ML Au/5.0 ML Pd/Mo(110) surface were described elsewhere.[63] Those data showed that the planar surface composition consisted of ~ 20% Pd and ~ 80 % Au. For 1.0 ML Au/1.0 ML Pd/SiO_2, the LEIS data showed Pd had a similar relative intensity compared to the extended Au-Pd surface spectrum. The Au LEIS spectral intensity for the Au-Pd clusters, however, was significantly less in Figure 45 compared to the Au LEIS signal for the extended Au-Pd surface, implying that the Au-Pd cluster surfaces were more Pd-rich compared to the corresponding Au-Pd extended surface.

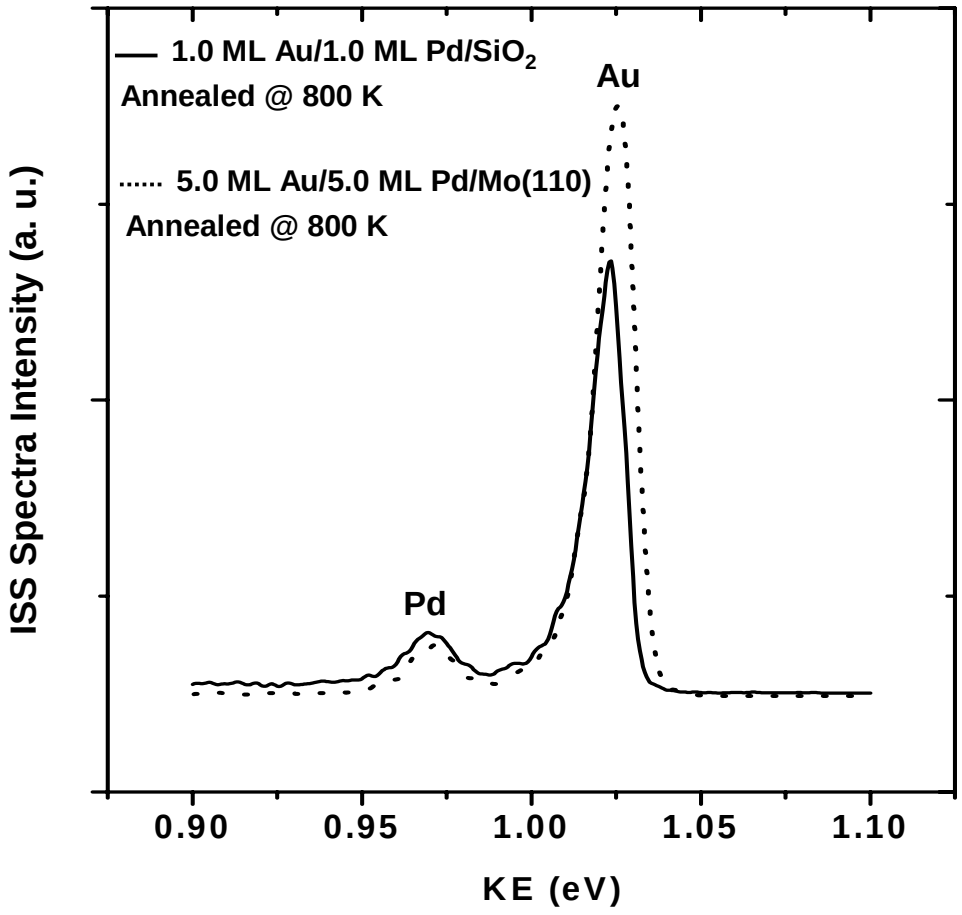

Figure 45. LEIS data for 1.0 ML Au/1.0 ML Pd/SiO_2 after 800 K annealing (solid line) and 5.0 ML Au/5.0 ML Pd/Mo(110) after 800 K annealing (dashed line). All spectra were collected at 300 K.

Normalization of the Pd LEIS intensity suggested that the cluster surface concentration consisted of ~ 33% Pd and ~ 67% Au. We also note that XPS of supported Pd clusters on the silica films here after annealing to temperatures as high as 800 K indicated no silicide formation as previously reported for Pd growth on monolayer SiO_2.[106,107]

In previous studies of Au-Pd surface alloys on Mo(110) surface, CO TPD was used to distinguish isolated Pd sites from Pd bridging/three fold hollow sites. This same methodology was used in the present studies for the silica supported Au-Pd clusters. TPD from a saturated coverage of CO (1.0 L) was carried out for the bare SiO_2 and SiO_2-supported Au-Pd clusters, each annealed to 800 K. In Figure 46, CO TPD spectra for the bare SiO_2 surface, 1.0 ML Pd/SiO_2, and 1.0 ML Au/SiO_2 were shown in Figure 46(a), (b), and (c), respectively. In Figure 46(a) for CO on bare SiO_2, a single broad low temperature feature centered at 135 K was observed from CO adsorbed on the SiO_2 support. In spectrum 46(b) for CO/1.0 ML Pd/SiO_2, additional features centered at 465, 320, and 250 K were observed. Based on previous studies of CO TPD on Pd low index single crystal surfaces and oxide supported clusters,[47,63,92,102-104,109,110] the 465 K feature was assigned to CO adsorbed on Pd three-fold hollow sites. The features at 250 and 320 K were likely due to CO adsorbed on a-top Pd sites at various Pd facets, e.g. Pd(100), Pd(111), corners/edges, etc. The desorption features between 320 and 465 K were assigned to CO on Pd bridging sites, in agreement with the studies of Carlsson, et al., of CO adsorption on Pd/Al_2O_3 surfaces.[109] Figure 46(c) showed CO TPD from 1.0 ML Au/SiO_2, with no strong desorption features apparent above 200 K, indicating weak CO bonding as reported previously.[108,111] In Figure 46(d) and (e), CO TPD from 1.0 ML

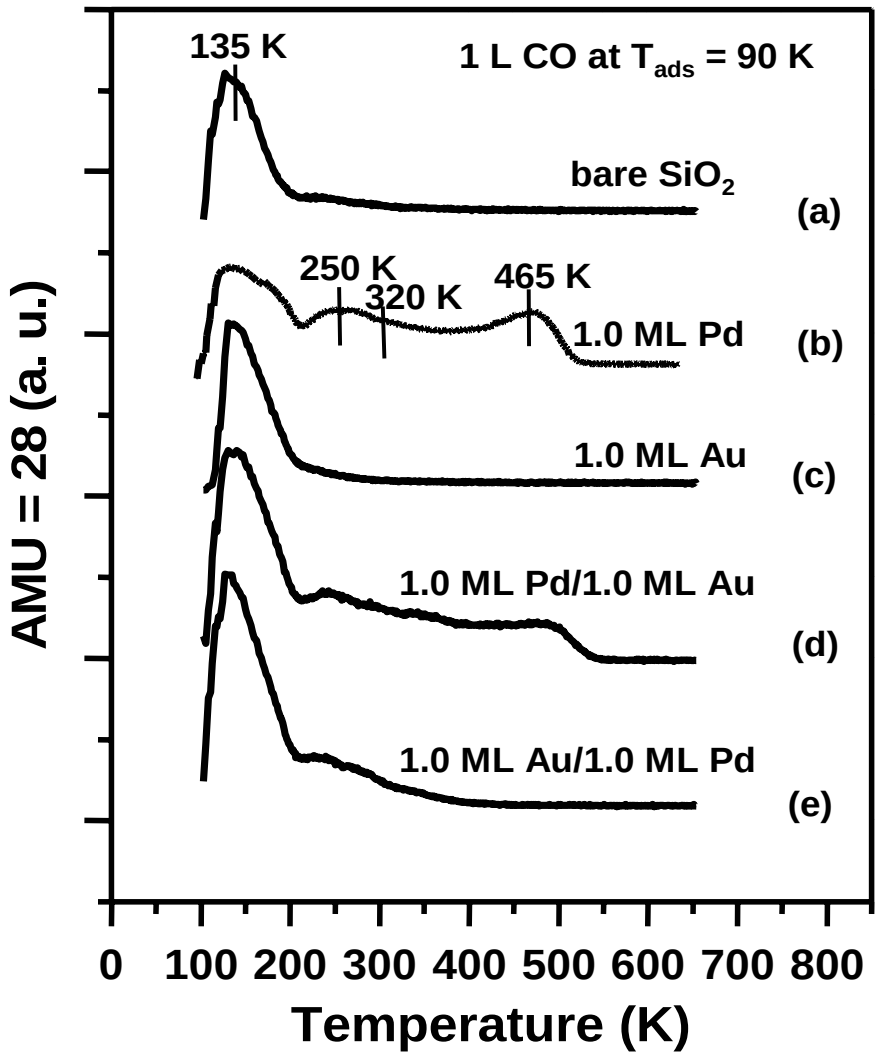

Figure 46. TPD spectra of CO: with 1.0 L CO exposure at 90 K on (a) bare SiO_2); (b) 1.0 ML Pd/SiO_2; (c) 1.0 ML Au/SiO_2 ; (d) 1.0 ML Pd/1.0 ML Au/SiO_2; and (e) 1.0 ML Au/1.0 ML Pd/SiO_2.

Pd/1.0 ML Au/SiO_2 and 1.0 ML Au/1.0 ML Pd/SiO_2 were shown, respectively. In Figure 46(d), a slight decrease of CO desorption was apparent for all the features above 200 K, compared to Figure 46(b) of CO /1.0 ML Pd/SiO_2. In comparison to spectrum 46(a), (b), and (c), an increase in intensity for the low temperature feature at 135 K was observed due to the additional weakly bonded CO on Au. In this deposition sequence, the surface exhibited the primary CO desorption features associated with pure Pd clusters, i.e. 1.0 ML Pd/SiO_2, and was consistent with the primary nucleation of Pd-only, rather than Au-Pd clusters. However, in spectrum 46(e), both the high temperature feature at 465 K and the features between 320 and 465 K completely disappeared for 1.0 ML Au/1.0 ML Pd/SiO_2. The intensity of the a-top Pd sites at 250 and 320 K remained with ~ 30 % attenuation. These results were significantly different from those of Figure 46(b), implying considerable alloying with Au deposition onto pre-deposited Pd clusters and a subsequent anneal.

Surface Pd Sites

LEIS, CO-TPD, and CO-IRAS were combined to characterize the compositional and structural properties of the Au-Pd alloy clusters. First, LEIS experiments of various Au coverages (0.1 -1.0 ML) on 1.0 ML Pd/SiO_2 were carried out. Note that the surface was annealed to 800 K for 10 minutes after each Au deposition and all LEIS spectra were collected at 300 K. Using the same method used to acquire the data of Figures 44 and 45, the surface concentration of Pd on Au-Pd alloy clusters was measured with various Au coverages and plotted as a function of the Au/Pd atomic ratio in the filled square data of

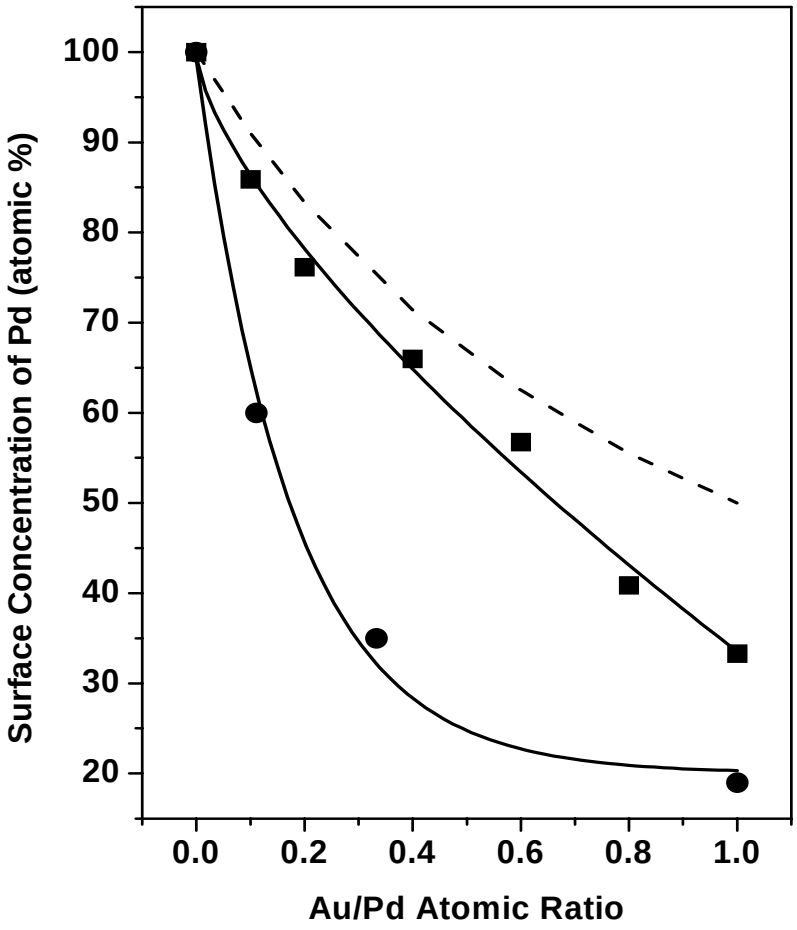

Figure 47. Surface concentration of Pd as a function of Au/Pd atomic ratio for various Au coverage (0.1-1.0 ML) on 1.0 ML Pd/SiO_2 after 800 K annealing (■); for Au-Pd/Mo(110) after 800 K annealing (●).

Figure 47. The dashed line was the calculated Pd concentration assuming that the surface composition reflects the bulk composition. The concentration of Pd at the cluster surface decreased more rapidly than did the dashed line data, indicating that the cluster surfaces were Au-rich compared to the bulk. For comparison, the surface concentration of Pd for Au-Pd/Mo(110) planar surfaces as a function of the Au/Pd atomic ratio had been extracted in earlier section and plotted in Figure 47 as the filled circle data. For Au-Pd planar surfaces, segregation of Au to the surface as a function of the Au/Pd ratio was much more significant. For example, for a Au/Pd atomic ratio of ~ 0.11, only ~ 60 % Pd was observed at the surface, whereas for a Au/Pd ratio of 1: 1, the surface was only ~ 20 % Pd. In any case, for Au-Pd clusters and extended surfaces, the outermost surface layer was enriched significantly in Au, with the surface concentration of Pd on Au-Pd clusters being greater than that for planar surfaces with an identical Au/Pd bulk composition.

To further characterize the surface composition, CO TPD experiments were carried out to probe the surface structure and absorption sites on 0.1 - 1.0 ML Au/1.0 ML Pd/SiO_2. Note that each surface was annealed to 800 K for 10 minutes, then cooled to 90 K prior to CO adsorption and TPD. In Figure 48, CO TPD spectra were shown as a function of Au coverage. As discussed earlier, spectrum 48(a) exhibited multiple CO adsorption features on Pd: a-top, bridging, three fold hollow sites, and support related sites for 1.0 ML Pd/SiO_2. With a very small amount of Au deposition, e.g. 0.1 ML, an obvious signal reduction was detected for the three-fold hollow sites at 465 K in 48(b), and a slight intensity increase for the a-top site features at 250 and 320 K.

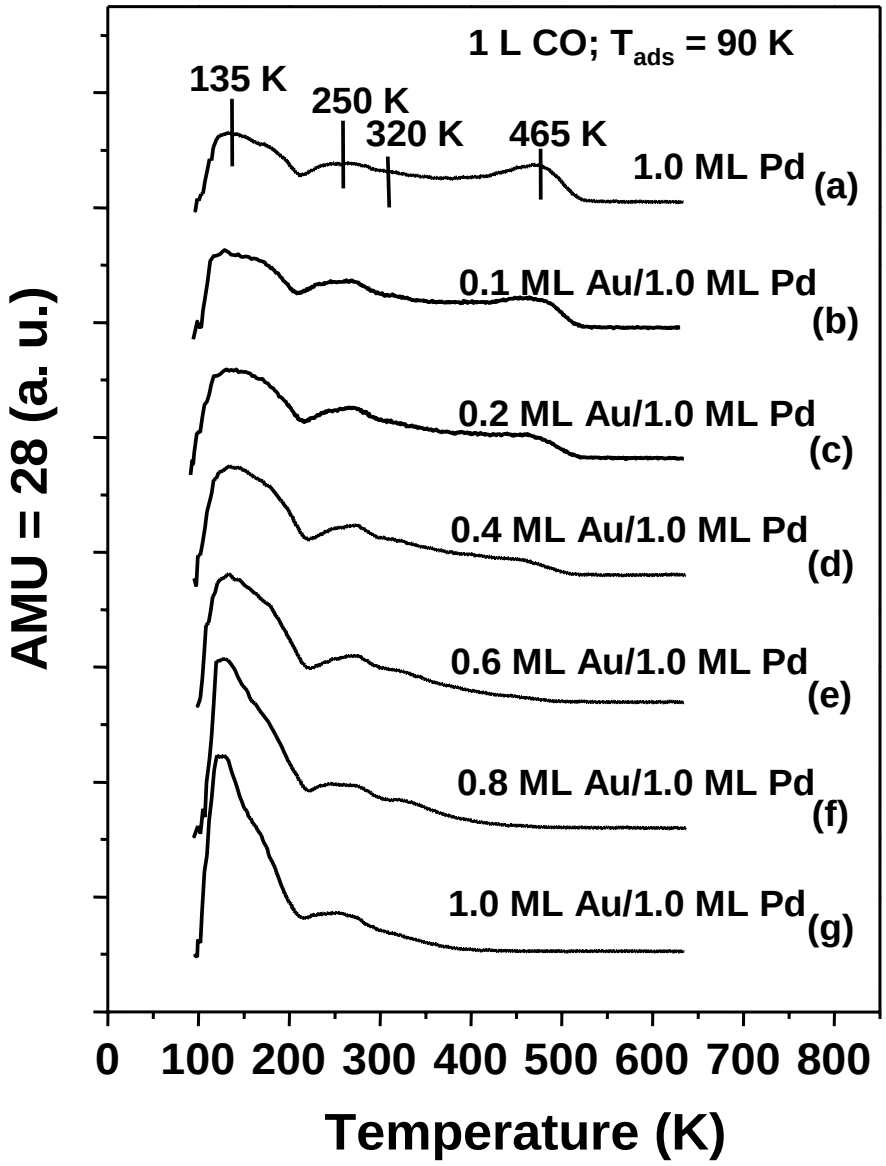

Figure 48. CO TPD with 1.0 L CO exposure at 90 K of different Au coverage (0.1-1.0 ML) on 1.0 ML Pd/SiO_2.

Simultaneously, an increase in the low temperature desorption feature at 135 K was observed due to the addition of Au. Considering the relatively large density of Pd clusters,[106,107] the higher sticking coefficients of Au on Pd versus Au on silica, and the low Au coverage at 0.1 ML, we assumed that all Au atoms nucleated on Pd clusters to form alloy clusters after annealing. Alloying led to the following: (a) the formation of 85% Pd versus 15% Au on the alloy cluster surfaces (from the LEIS data in Figure 47 with a Au/Pd ratio of 0.1); (b) diminution of the Pd three-fold hollow site density; and (c) an increase in the density of the Pd a-top sites. As the Au coverage increased from spectrum 48(b) to (d), the density of the Pd three-fold hollow features progressively decreased. These features completely vanished at a Au coverage of 0.6 ML in spectrum 48(e). In this transition, the signal intensity of the feature between 320 and 465 K, assigned to be Pd bridging sites, also gradually decreased at 0.6 ML Au coverage. However, the Pd a-top features at 250 and 320 K remained unchanged up to 0.6 ML Au. With increasing Au coverage to 1.0 ML, the bridging sites completely disappeared and the intensity of the a-top feature decreased ~ 30%. As a result, the loss of Pd bridging/three fold hollow sites and the prevalence of a-top sites were apparent on the Au-Pd alloy cluster surfaces.

IRAS studies addressing the surface morphology of the Au-Pd clusters were first carried out by adsorbing CO on 1.0 ML Au/SiO_2/Mo(110). The spectra as a function of temperature were shown in Figure 49. Only a single, sharp feature at 2109 cm^{-1} was evident at 80 K, and was assigned to CO on Au a-top sites.[47,111] The intensity of this

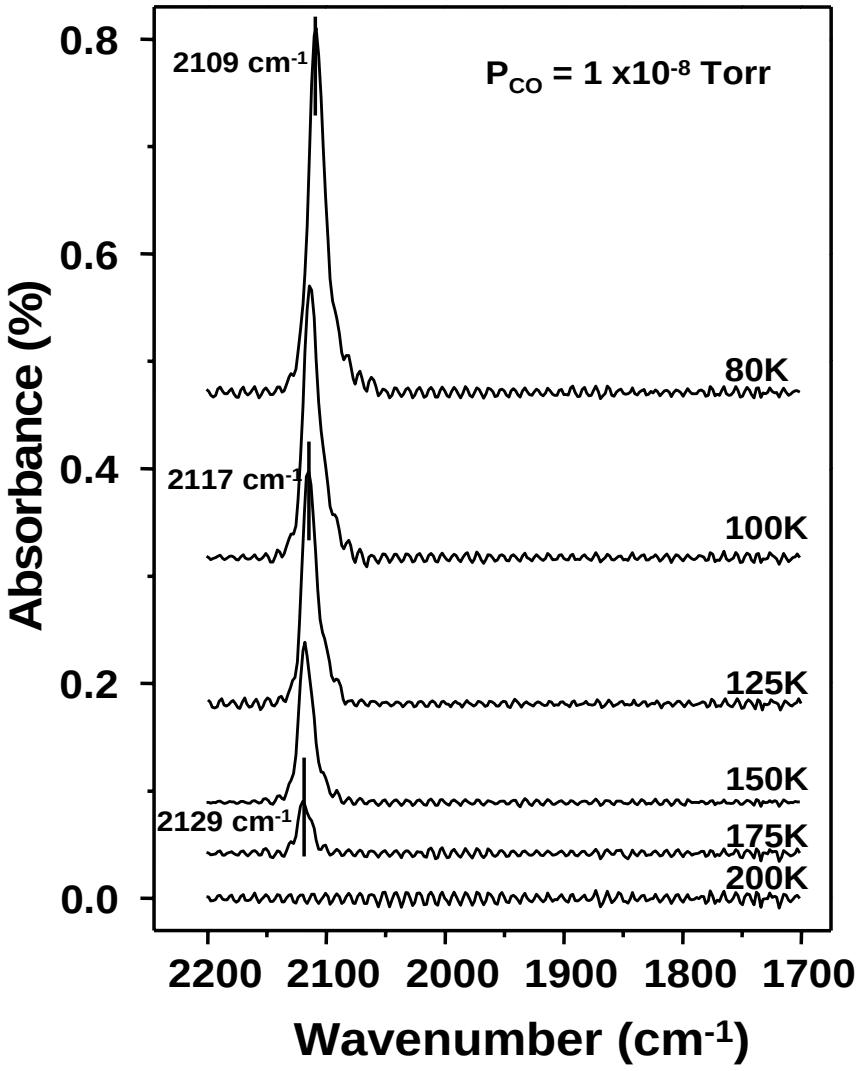

Figure 49. IRAS spectra of CO adsorption on 1.0 ML $Au/SiO_2/Mo(110)$ as a function of temperature.

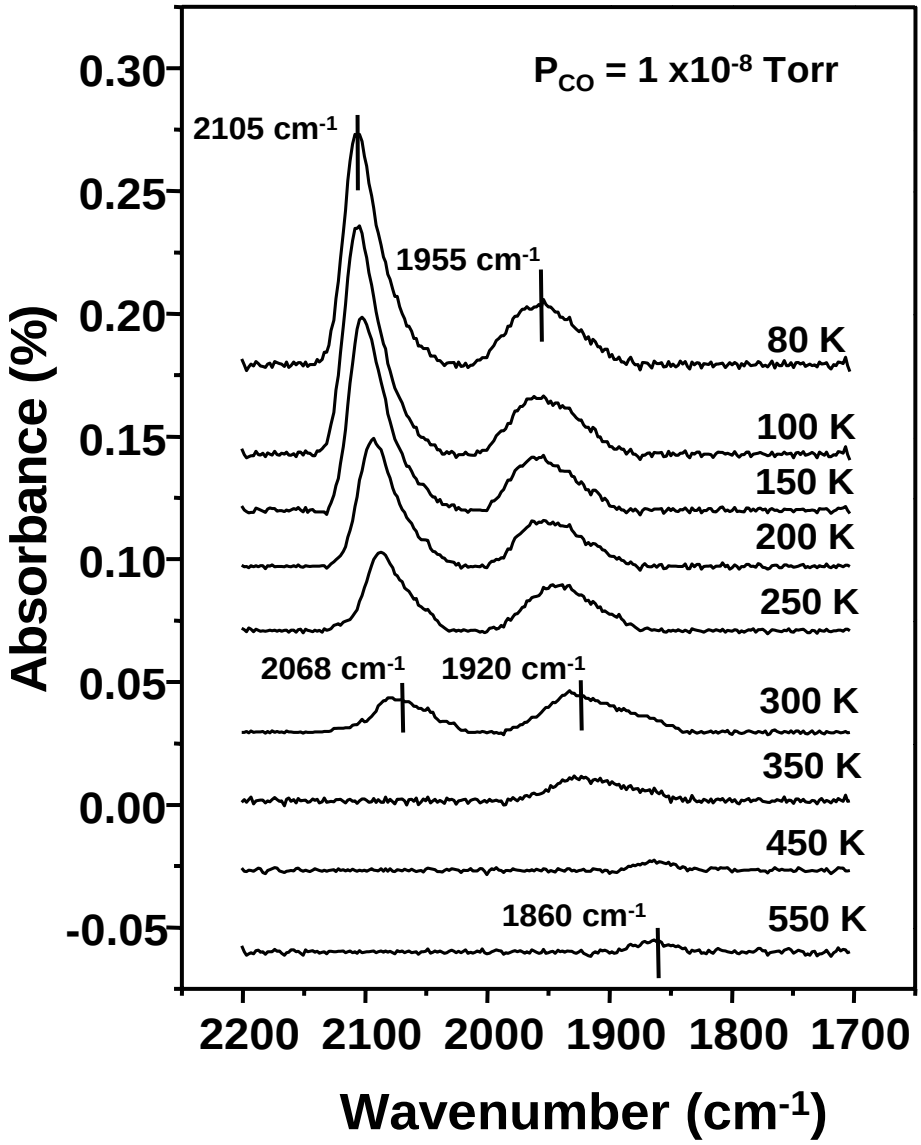

Figure 50. IRAS spectra of CO adsorption on 1.0 ML Pd/SiO_2/Mo(110) as a function of temperature.

feature decreased with an increase temperature, and its position blue-shifted to 2129 cm^{-1} at 175 K; at 200 K the intensity of this feature vanished. This behavior paralleled closely the TPD results of Figure 46(c), where no CO desorption was detected above 200 K. The blue- shift for the Au clusters was decidedly different from the red-shift for CO adsorption on Pd clusters.[47] The blue-shift was characteristic of CO on Au clusters and accordingly can be used to identify Au-only clusters. In Figure 50, IRAS spectra of CO adsorption on 1.0 ML Pd/SiO_2 were shown as a function of temperature. A relatively narrow feature at ~ 2105 cm^{-1} and a broad feature extending from 2000 to 1875 cm^{-1} were apparent at 80 K. Extensive studies have been carried out with IRAS of CO adsorption on Pd(111), Pd(100), and oxide supported nano-size Pd particles.[47,102-104,110,112] From studies on Pd(111) and Pd(100), three CO adsorption sites, a-top, bridging, and three fold hollow sites were observed with CO stretching frequency ranging from 2090 – 2120 cm^{-1}, 1895-2000 cm^{-1}, and 1830-1920 cm^{-1}, respectively. For alumina- or silica-supported Pd clusters,[47,92,103,104,112,113] the CO adsorption sites and their corresponding frequencies were in agreement with previous work on Pd(100) and Pd(111). Accordingly, the high frequency feature at ~ 2105 cm^{-1} was assigned to CO on Pd a-top sites and the broad band at 2000 cm^{-1} -1875 cm^{-1}, to CO on bridging and three fold hollow sites.[47,92,103,104,112,113] With increasing temperature, the a-top feature red-shifted to 2068 cm^{-1} at 300 K; the signal intensity gradually decreased and completely vanished at 350 K. Concomitantly, the intensity of CO on bridging/three fold hollow sites also decreased. The peak position red-shifted to ~ 1860 cm^{-1} before the signals

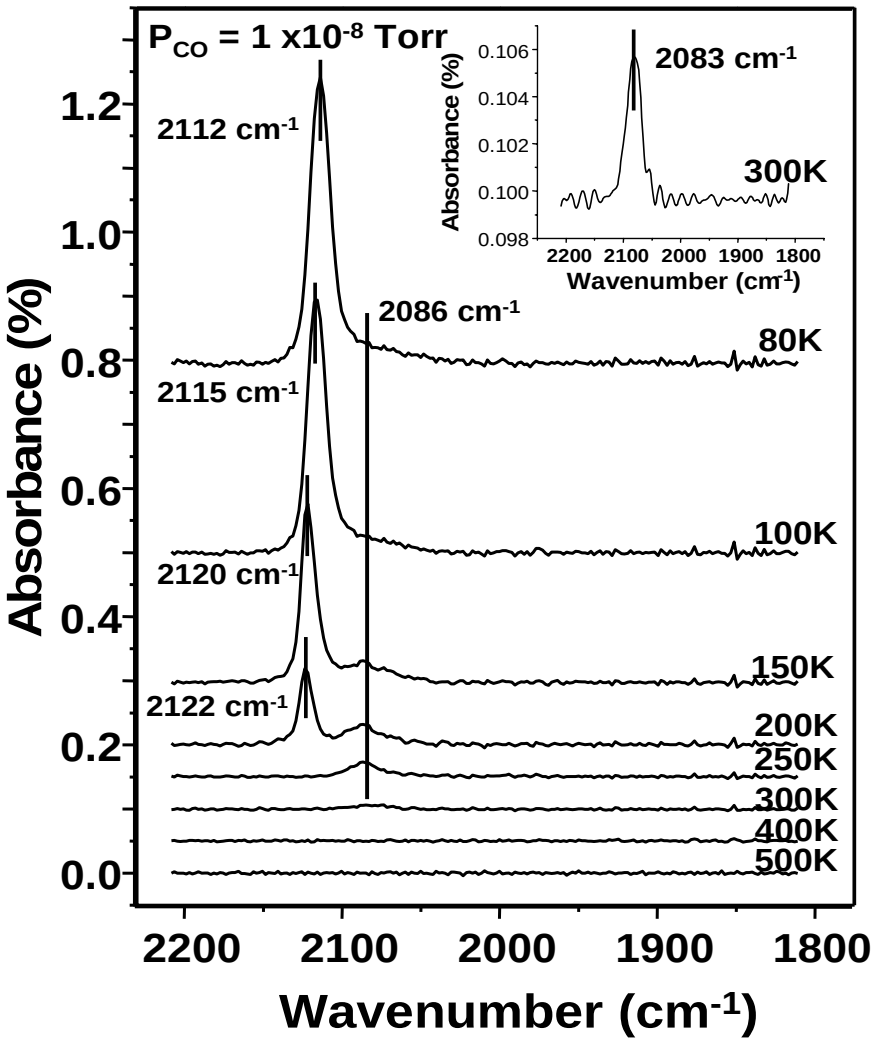

Figure 51. IRAS spectra of CO adsorption on 1.0 ML Au/1.0 ML Pd/SiO_2/Mo(110) as a function of temperature.

completely disappeared above 550 K. Our data closely agreed with the previously reported IRAS data for small Pd particles grown on SiO_2 and Al_2O_3.[47,92,103,104,112,113] The CO adsorption sites and the corresponding desorption temperatures agreed with the CO TPD results discussed above.

In Figure 51, the IRAS spectra of CO adsorbed on 1.0 ML Au/1.0 ML $Pd/SiO_2/Mo(110)$ were presented as a function of temperature. At 80 K, a sharp feature at 2112 cm^{-1} with a small shoulder at lower frequency side was apparent with no features corresponding to CO adsorbed on Pd in bridging or three fold hollow sites. As the temperature was increased, the primary feature blue-shifted to 2122 cm^{-1} at 200 K and completely vanished at 250 K. According to the distinctive blue-shift exhibited by CO stretching frequency on Au clusters upon annealing in Figure 49 and the complete loss of signal intensity at 250 K, we concluded that the feature at 2112 cm^{-1} was from CO adsorbed on Au a-top sites. The shoulder observed on the low frequency side of the 2112 cm^{-1} peak at 80 K was clearly evident at 150 K with a stretching frequency at 2086 cm^{-1} and distinctly resolved from the Au a-top sites at 200 K. Furthermore, it was the only CO feature present at 250 K. In the inset of Figure 51, this feature can still be seen at 2083 cm^{-1} at 300 K. This unique feature, with a frequency of ~ 20 cm^{-1} lower than CO adsorbed on regular Pd a-top sites on Pd single crystal substrates and oxides supported clusters,[47,63,102-104,110] was characteristic of a Au-Pd alloy cluster surface, and has been observed for Au-Pd planar alloy surfaces and for alumina supported Au-Pd clusters.[47,63] No significant frequency shift was observed over the entire temperature range investigated. With consideration of enhanced surface segregation of Au and the

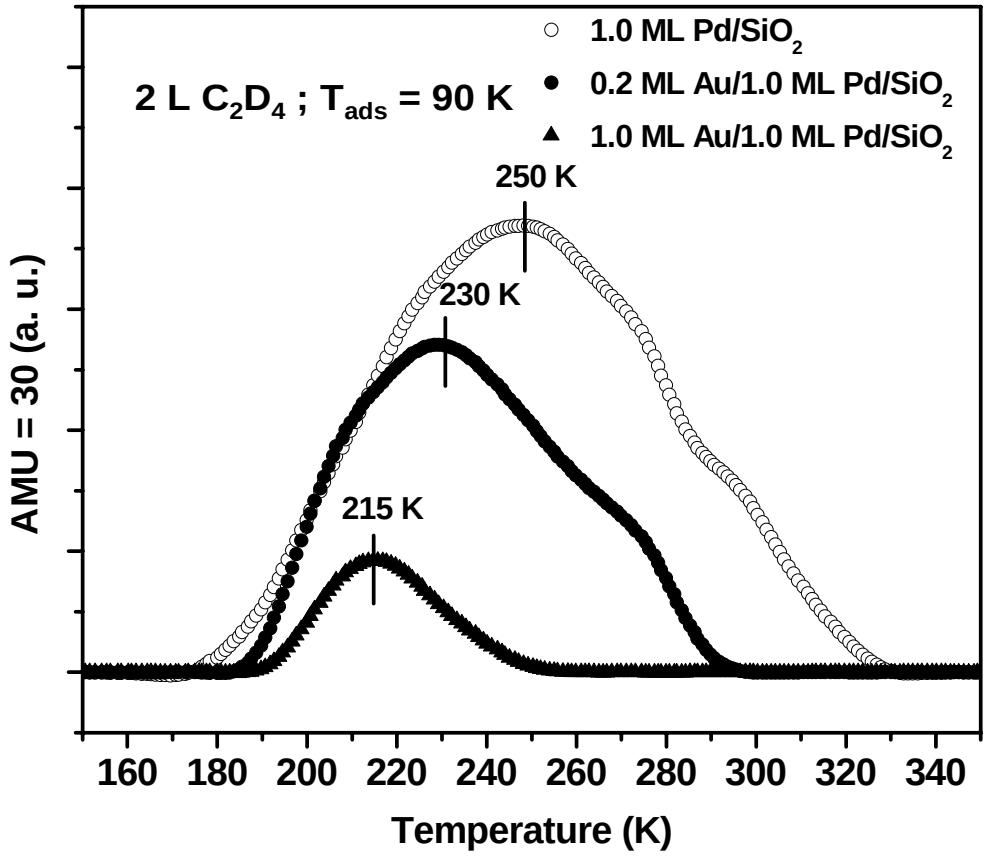

Figure 52. TPD of C_2D_4 with 2.0 L C_2D_4 exposure at 90 K on 1.0 ML Pd/SiO_2 (○); 0.2 ML Au/1.0 ML Pd/SiO_2 (●); and 1.0 ML Au/1.0 ML Pd/SiO_2 (▲).

characteristic a-top Pd sites observed by CO TPD, the Pd atoms were believed to be surrounded by Au atoms, forming isolated Pd sites on the alloy clusters of 1.0 ML Au/1.0 ML Pd/SiO_2. The red-shift can be due either to stronger bonding of CO to the isolated Pd or to reduced lateral destabilization of CO on the surrounding Au atoms. Additionally, there was still a Au feature in the IRAS spectra at 2122cm^{-1} in Figure 51 with the substrate temperature of 200 K, but no feature observed for pure Au clusters at this temperature in Figure 49. The difference could be due to the perturbation of the electronic properties in the Au-Pd alloying process, i.e., a ligand effect on CO adsorption on Au.

Correlation of Surface Structure and Reactivity

To probe the surface structure of the Au-Pd alloy clusters as well as their catalytic reactivity, a TPD study of deuterated ethylene (C_2D_4) adsorption and dehydrogenation on the silica supported Pd and Au-Pd alloy clusters was carried out. In Figure 52, the TPD spectra acquired following 2.0 L C_2D_4 adsorption on 1.0 ML Pd/SiO_2/Mo(112) was shown as the open circle line. The C_2D_4 spectra were shown after subtraction of the background contribution below 170 K. A broad feature was observed with a desorption temperature peak maximum at 250 K, assigned to contributions from π-bonded and di-σ bonded C_2D_4.[46-48] The broadness of the desorption features was likely due to the inhomogeneity of adsorption sites on the clusters.[93-97] The data shown in the solid circles were acquired after the addition of 0.2 ML Au to the 1.0 ML Pd/SiO_2 clusters followed by a 800 K anneal. Compared to C_2D_4/1.0 ML Pd, the C_2D_4 TPD showed a reduction in the signal intensity and a shift in the peak desorption maximum from 250 to 230 K.

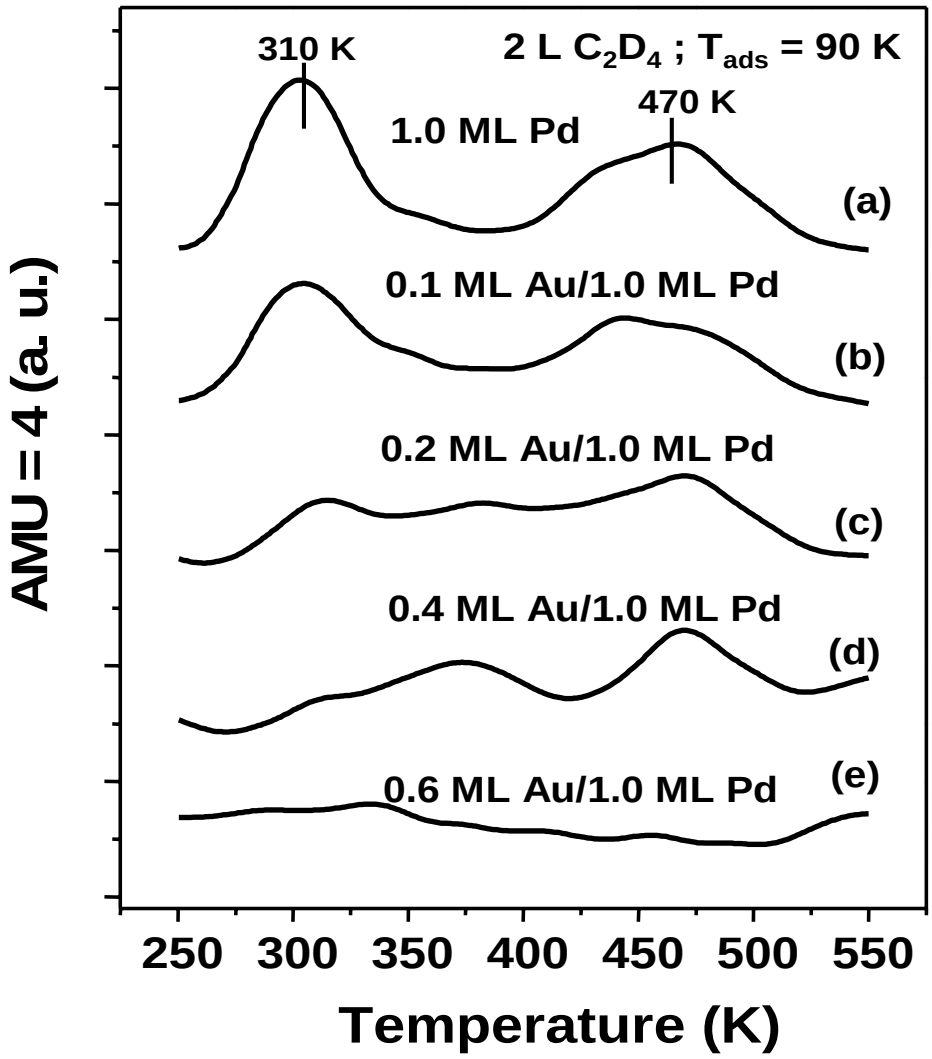

Figure 53. D_2 signals collected from C_2D_4 TPD with 2.0 L C_2D_4 exposure at 90 K on: (a) 1.0 ML Pd/SiO_2; (b) 0.1 ML; (c) 0.2 ML; (d) 0.4 ML; and (e) 0.6 ML Au /1.0 ML Pd/SiO_2 surfaces.

These changes were attributed to dilution of the Pd surface concentration upon Au deposition. With 1.0 ML Au deposition to 1.0 ML Pd/SiO_2 and annealing, a significant further loss of C_2D_4 desorption intensity was obvious, together with a desorption peak maximum shift to 215 K. These data indicated that the addition of Au to Pd clusters led to attenuation of the stronger di-σ bonded C_2D_4 requiring adjacent Pd atoms. C_2D_4, in contrast, bonded primarily to isolated Pd sites via π-bonding. These results were in agreement with the CO-IRAS and CO-TPD data discussed above.

D_2 formation from ethylene dehydrogenation was also monitored with TPD. Pd catalyzed ethylene dehydrogenation has been studied extensively on Pd(111), Pd(100) and alumina supported Pd cluster surfaces.[93-95] From these studies, a strong interaction between ethylene adsorbates and two adjacent Pd atoms via di-σ bonding was purported to be responsible for ethlyene dehydrogenation. Ethylidyne (≡C-CH_3) and vinylidene (=CH-CH_2) species were proposed to be the reaction intermediates on Pd(111) and Pd(100) facets, respectively, with the reaction site requiring three-fold hollow and bridging Pd sites. In Figure 53, D_2 produced in the TPD following C_2D_4 adsorption on silica supported Pd and Au-Pd clusters were shown after subtracting the background signals for C_2D_4/SiO_2. In spectrum 53(a) for C_2D_4 dehydrogenation on 1.0 ML Pd/SiO_2/Mo(112), two D_2 features appeared with the desorption peak maxima at 310 and 470 K. These features were assigned to the β and γ states (the combination of γ_1 and γ_2 states), respectively.[93-95,97] With the addition of 0.1 ML, 0.2 ML and 0.4 ML Au to 1.0

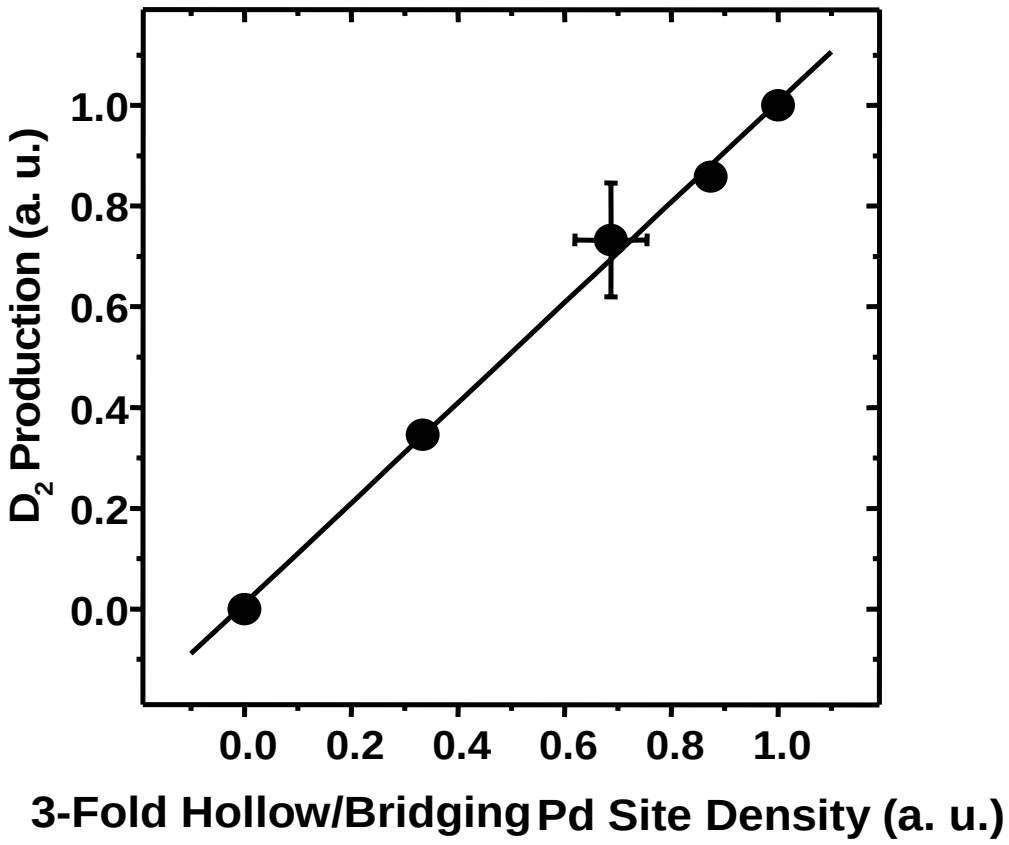

Figure 54. D_2 production yield as a function of 3-hollow/bridging Pd site density for C_2D_4 dehydrogenation of Au-Pd/SiO_2 alloy cluster surfaces.

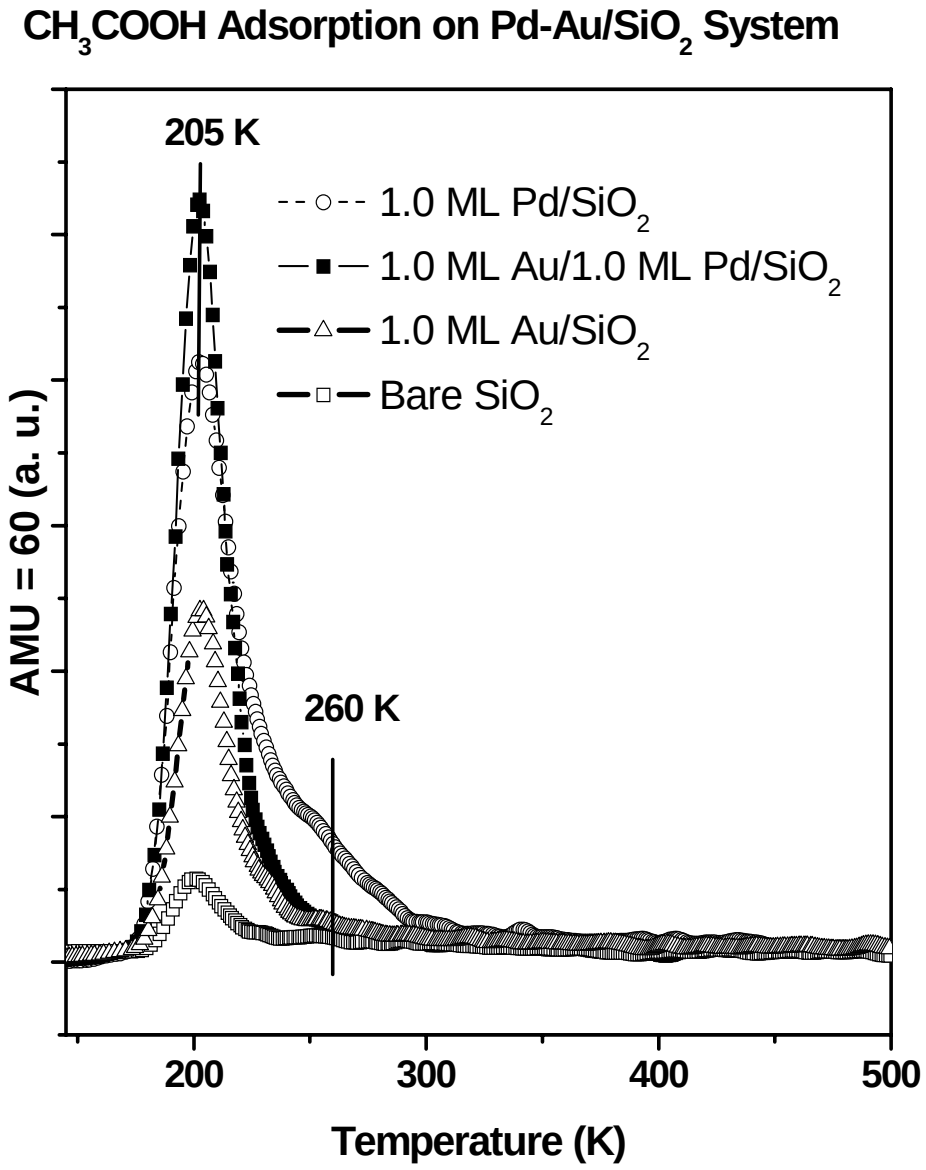

Figure 55. TPD of CH_3COOH with 1.0 L CH_3COOH exposure at 90 K on 1.0 ML Pd/SiO_2 (○); 1.0 ML Au/1.0 ML Pd/SiO_2 (■); 1.0 ML Au/SiO_2 (Δ); and bare SiO_2 (□).

ML Pd/SiO_2 and a subsequent annealing at 800 K, the production of D_2 from C_2D_4 TPD gradually decreased from spectrum 53(b) to (d). Upon addition of 0.6 ML Au in 53(e), the D_2 production yield was negligible. As demonstrated by the CO IRAS/TPD and C_2D_4 TPD data, the loss of active sites, i.e., adjacent Pd atoms for di-σ bonded C_2D_4, was clearly responsible for attenuation of the C_2D_4 dehydrogenation reaction on the Au-Pd alloy cluster surface. The lack of suitable surface adsorption sites, i.e., three-fold hollow/bridging sites for the reaction intermediates, i.e., ethylidyne ($\equiv C\text{-}CD_3$) or vinylidene ($=CD\text{-}CD_2$), could also account for the loss of D_2 production. In Figure 54, the D_2 production yield, normalized to that obtained for1.0 ML Pd/SiO_2, was plotted as a function of the density of the multi-fold Pd sites, i.e. bridging and three-fold hollow sites, after deposition of Au from 0 to 0.6 ML. The density of multi-fold Pd sites was obtained by subtracting the CO adsorption signals of a-top Pd and Au sites in spectrum 48(e) from spectrum 48(a)-(d), normalized to that observed for 1.0 ML Pd/SiO_2. The plot in Figure 54 exhibited an excellent linear relationship for the D_2 formation as a function of the density of multi-fold Pd sites.

CH_3COOH TPD spectra from 800 K pre-annealed Pd, Au-Pd, Au clusters and bare SiO_2 were performed and shown in Figure 55. As the open circle line delineated for CH_3COOH desorption on 1.0 ML Pd/ SiO_2, two main features were observed as a major desorption peak centering at 205 K and a shoulder existing with a centroid at 260 K. As

discussed earlier in CH_3COOH adsorption in 10 ML Pd/Mo(110) and Pd(111),[98] the high temperature desorption feature at 260 K was assigned to CH_3COOH adsorption on two Pd bridging atoms as bi-dentate species. The low temperature feature at 205 K resulted from CH_3COOH adsorption as mono-dentate species. With the addition of 1.0 ML Au to 1.0 ML Pd/ SiO_2, the Pd bridging sites related bi-dentate feature at 260 K disappeared as indicated in the filled square line due to the lack of bridging Pd adsorption sites, consistent with the results on the 5.0 ML Pd/5.0 ML Au/Mo(110) planar surface. The intensity increase for the low temperature peak at 205 K could be due to additional CH_3COOH desorption from surface Au sites, which was demonstrated from CH_3COOH TPD on 1.0 ML Au/ SiO_2 (Δ). Also, the CH_3COOH TPD on bare SiO_2 (□) showed no evidence of strong CH_3COOH adsorption on bare SiO_2. Again, the CH_3COOH TPD on Au-Pd alloy clusters demonstrated a strong correlation of the surface Pd sites and reactant adsorption properties on the surface, as evidenced on Au-Pd planar surfaces.

Cu-Pd/Mo(110)

Surface Composition

Sequential deposition of 5.0 ML Cu followed by 5.0 ML Pd (hereafter designated as 5.0 ML Pd/5.0 ML Cu) was performed on a Mo(110) surface at 300 K. The resulting adlayer was then annealed for 20 minutes at the desired temperature (not exceeding 1400 K). LEIS experiments were performed after each annealing and all the spectra were collected at 300 K.

The LEIS spectra (Figure 56) were recorded as a function of annealing temperature. At 300 K, a Cu peak appeared with a kinetic energy of 0.905 keV for scattered He^+ ions. Note that no Mo signals were detectable at 0.94 keV, indicating that the Mo substrate was fully covered. After 5.0 ML Pd deposition, the intensity of the Cu peak decreased by about 80%. The remaining Cu intensity on the surface suggested an Cu-Pd alloy formation at 300 K. Another strong peak detected at 0.97 keV was assigned to the Pd scattering signals. When annealing temperature was ramped to 600 K, the intensity of Cu peaks increased with temperature, while that of Pd decreased concomitantly. At much higher annealing temperatures (700 to 1000 K), a reversal of peak intensity trends was observed, indicating significant changes in the surface composition. At 1100 K, the intensity of the Cu signal remained very low, with the signal disappearing at 1200 K. In contrast, the Pd signal intensity reached a maximum at 1200 K, with the signal disappearing at 1400 K.

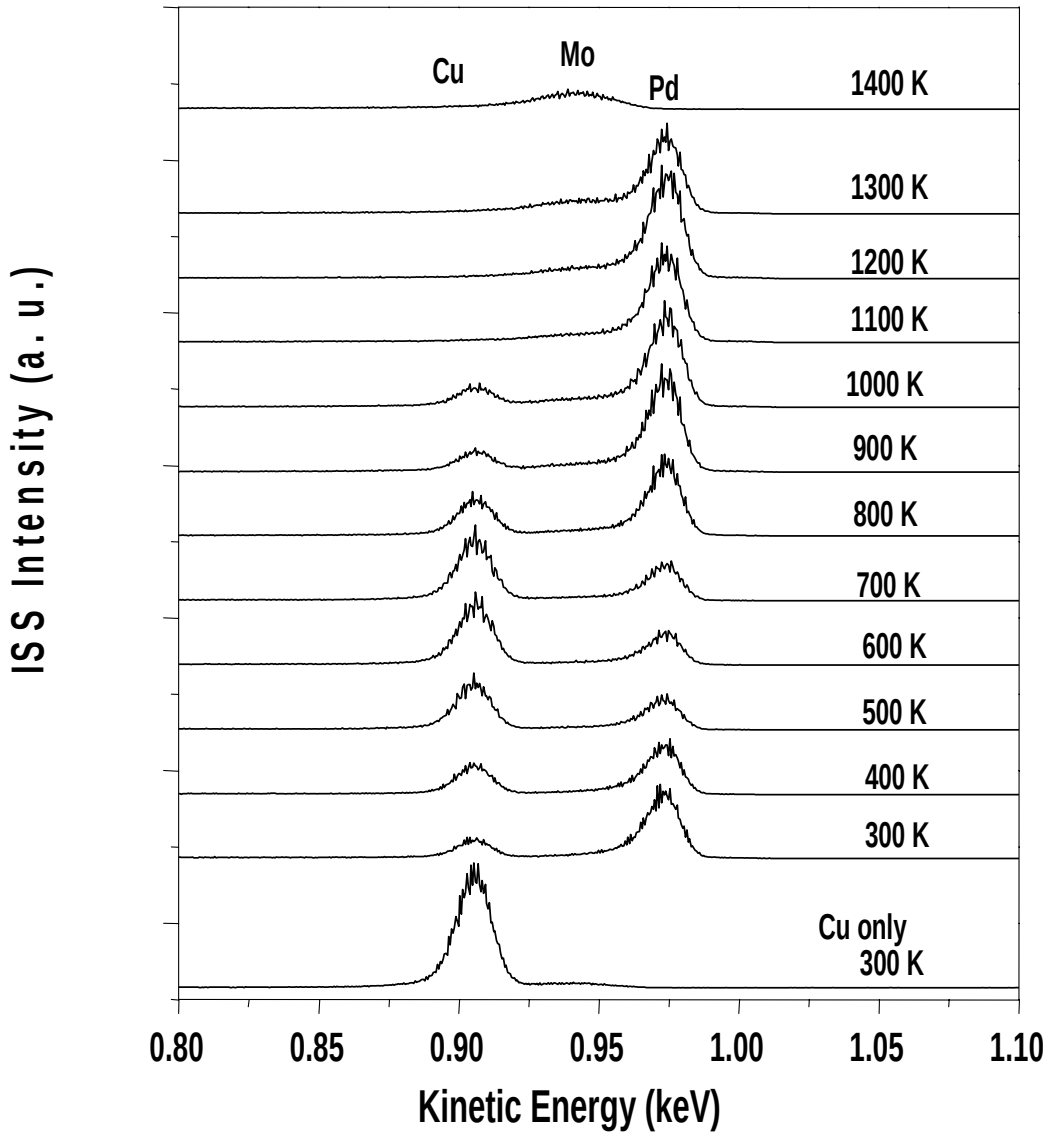

Figure 56. LEIS spectra of 5.0 ML Pd/5.0 ML Cu/Mo(110) as a function of annealing temperature.

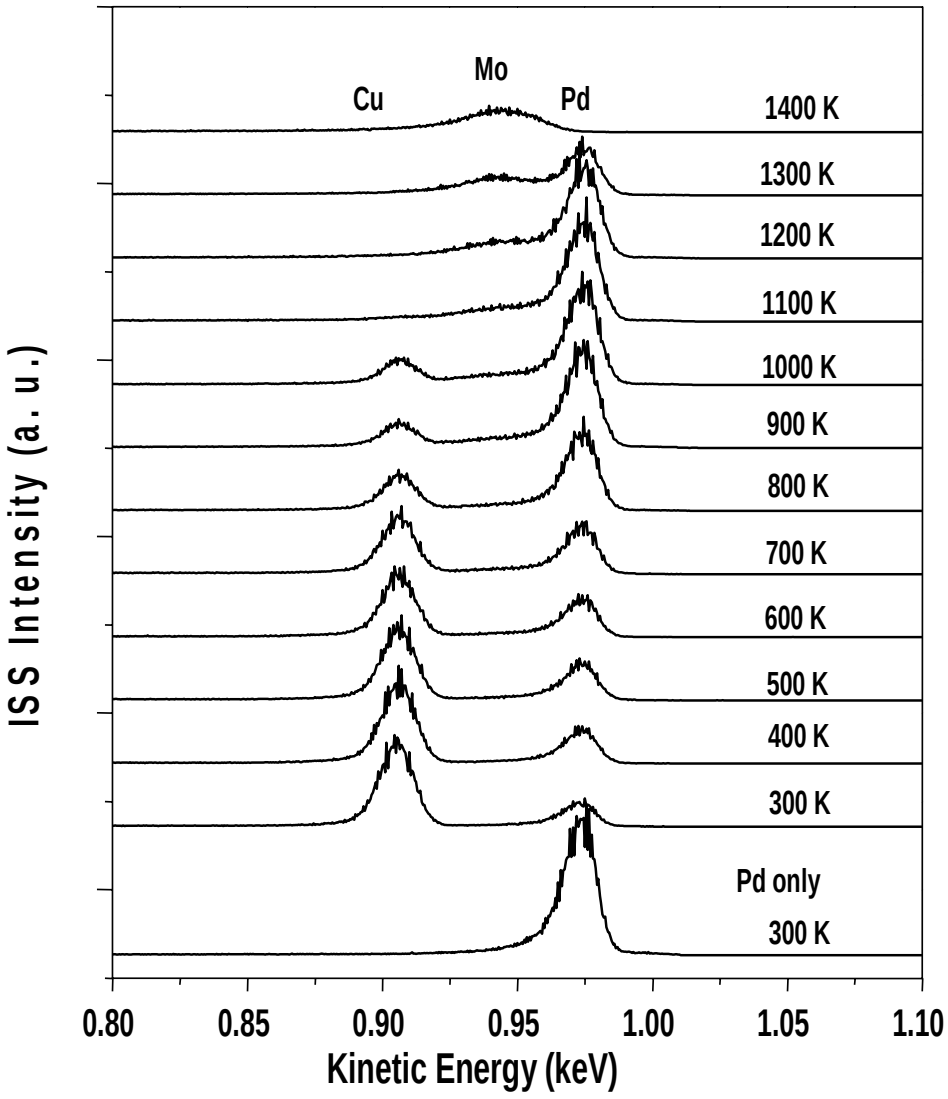

Figure 57. LEIS spectra of 5.0 ML Cu/5.0 ML Pd/Mo(110) as a function of annealing temperature.

LEIS signals from the Mo substrate were recorded, beginning at 1100 K, and were found to dominate the surface signal profile at 1400 K. The variation in Pd, Cu, and Mo signal intensities, observed between 1100 - 1400 K, was mainly due to the desorption of Cu, commencing at 1100 K, and that of Pd at temperatures greater than 1200 K.

The deposition sequence was reversed to form 5.0 ML Cu/5.0 Pd/Mo(110). LEIS results plotted as a function of annealing temperature were displayed in Figure 57. Upon Pd deposition at 300 K, the Pd LEIS signal appeared at 0.97 keV, but was greatly reduced upon the deposition of 5.0 ML Cu. A progressive decrease in Cu signal intensity and increase in Pd scattering intensity were observed upon annealing the adlayers to 1000 K. In agreement with the data from 5.0 ML Pd/5.0 ML Cu/Mo(110), Cu and Pd scattering signals disappeared at 1100 and 1400 K, respectively. Upon annealing at 1400 K, extensive desorption of Cu and Pd transpired, thus Mo scattering signal became dominant.

The surface concentrations of Pd and Cu were calculated using equation (3) in the Au-Pd/Mo(110) study, for both the 5.0 ML Cu/5.0 ML Pd/Mo(110) and 5.0 ML Pd/5.0 ML Cu/Mo(110) systems; results were plotted as a function of temperature in Figure 58. The two lines defined by the filled circle and square symbols represented the surface concentrations of Cu for 5.0 ML Pd/5.0 ML Cu/Mo(110) and 5.0 ML Cu/5.0 ML Pd/Mo(110), respectively. On the other hand, the surface concentrations of Pd for 5.0 ML Pd/5.0 ML Cu/Mo(110) and 5.0 ML Cu/5.0 ML Pd/Mo(110) were represented by

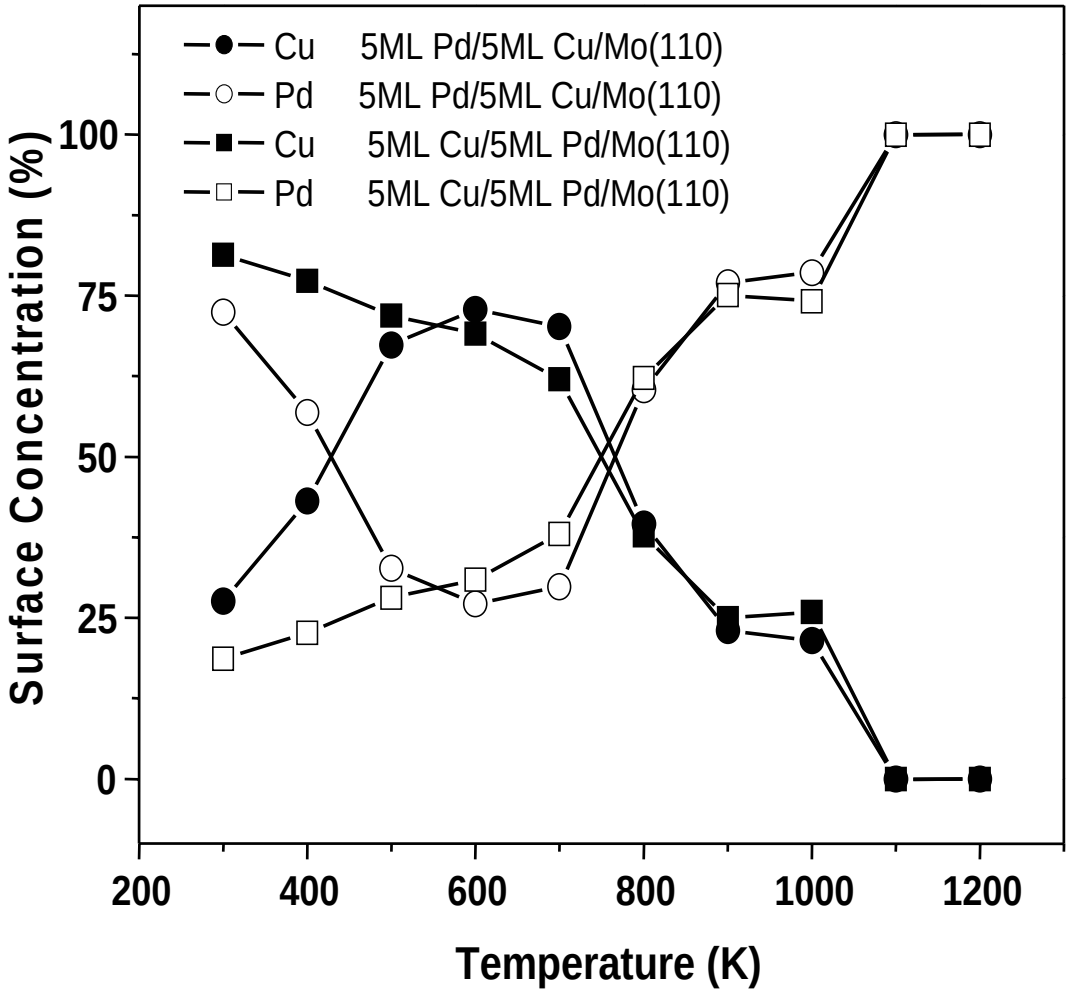

Figure 58. Surface Cu and Pd concentration of 5.0 ML Cu-5.0 Pd/Mo(110) as a function of annealing temperature.

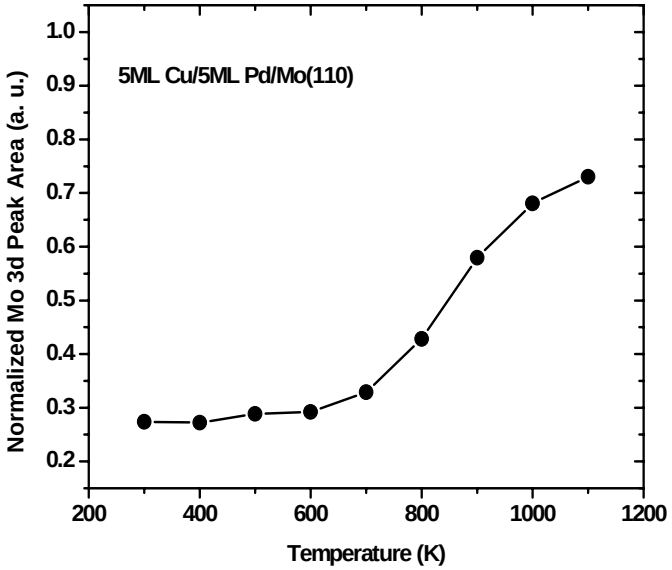

(a)

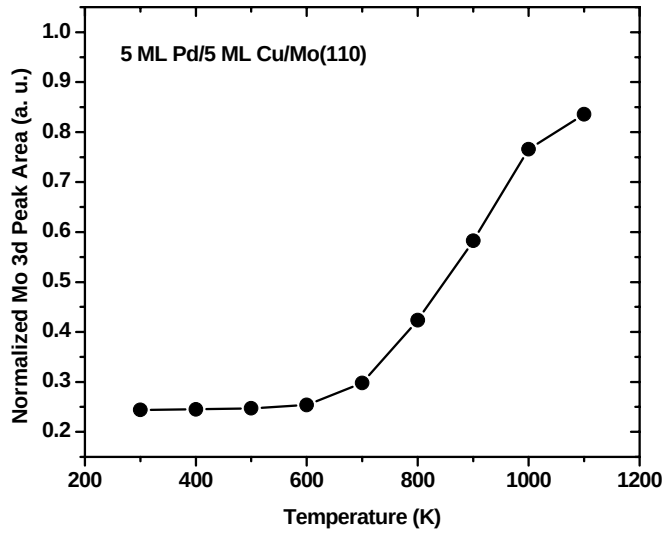

(b)

Figure 59. XPS normalized Mo 3d peak area as a function of annealing temperature for (a) 5.0 ML Cu/5.0 ML Pd/Mo(110); (b) 5.0 ML Pd/5.0 ML Cu/Mo(110).

the lines defined by the open circle and square, respectively. As shown in Figure 58, Cu and Pd surface concentrations varied from 300 to 500 K and with different deposition sequences, implying the occurrence of Cu-Pd alloying in this temperature range. At higher annealing temperatures in the range of 500 to 700 K, the Cu and Pd surface concentrations plateaued at about 70 % Cu and 30 % Pd on the surface layer. The surface composition was independent of the deposition sequence, indicating that a stable surface alloy formed in this temperature range. At temperatures above 700 K, the data showed the surface concentrations of Pd continued to increase, reaching a maximum of almost 100% after Cu desorbed with annealing at 1100 K.

To better understand the correlation between surface morphology and annealing temperature, XPS spectra were collected after the LEIS experiments at each annealing temperature. Figure 59 showed XPS Mo 3d core level normalized peak areas plotted as a function of annealing temperature for both Cu-Pd deposition sequences. In Figure 59(a), Mo 3d peak intensity remained steady as 0.27 ~ 0.29 from 300 to 600 K for 5.0 ML Cu/5.0 ML Pd/Mo(110), implying that no significant surface morphology variation occurred in this temperature range. After a 700 K anneal, the Mo intensity increased from 0.29 to 0.32 and further increased from 0.43 to 0.68 in the range of 800 to 1000 K. The increase in Mo peak intensity clearly indicated a radical change in the surface morphology, e.g. Cu or Pd clustering, although details of such changes were not extensively pursued in this current investigation on planar alloy surfaces. When the Cu-Pd deposition sequence was reversed, very similar results were obtained with respect to the Mo substrate intensity upon annealing (Figure 59(b)).

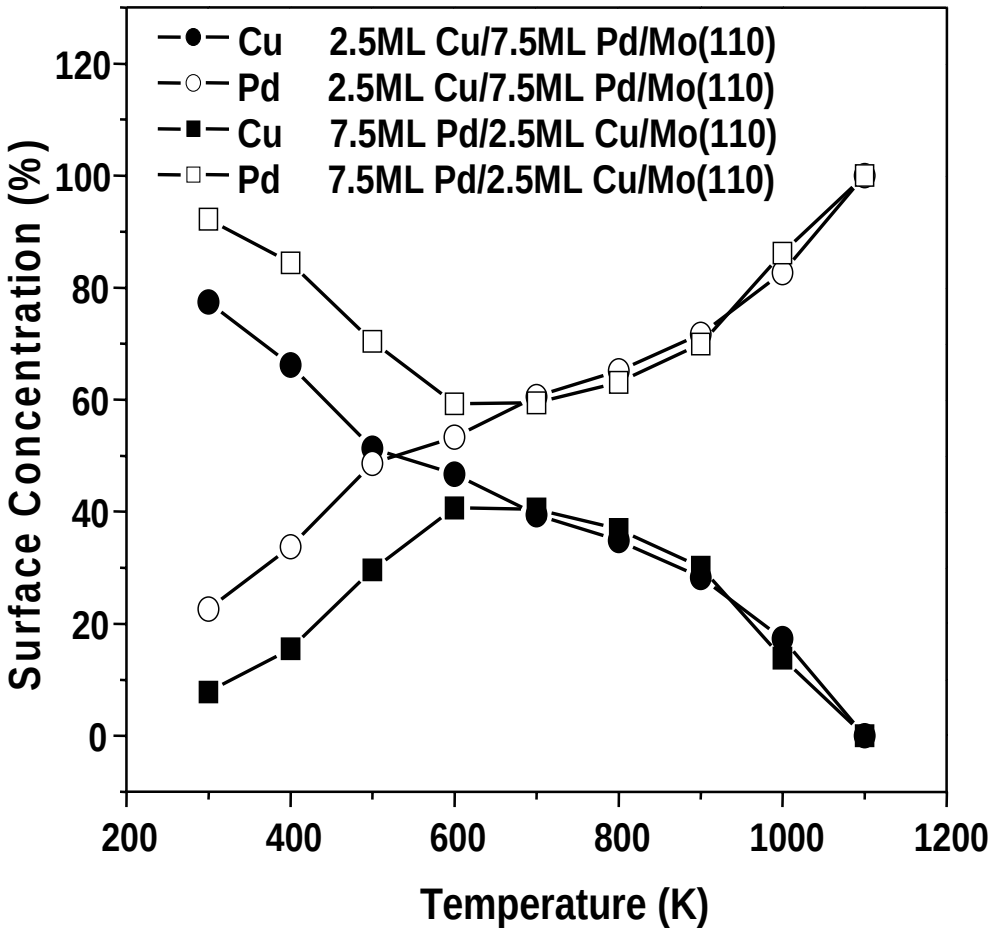

Figure 60. Surface concentration of Cu and Pd as a function of annealing temperature for 2.5 ML Cu-7.5 Pd/Mo(110).

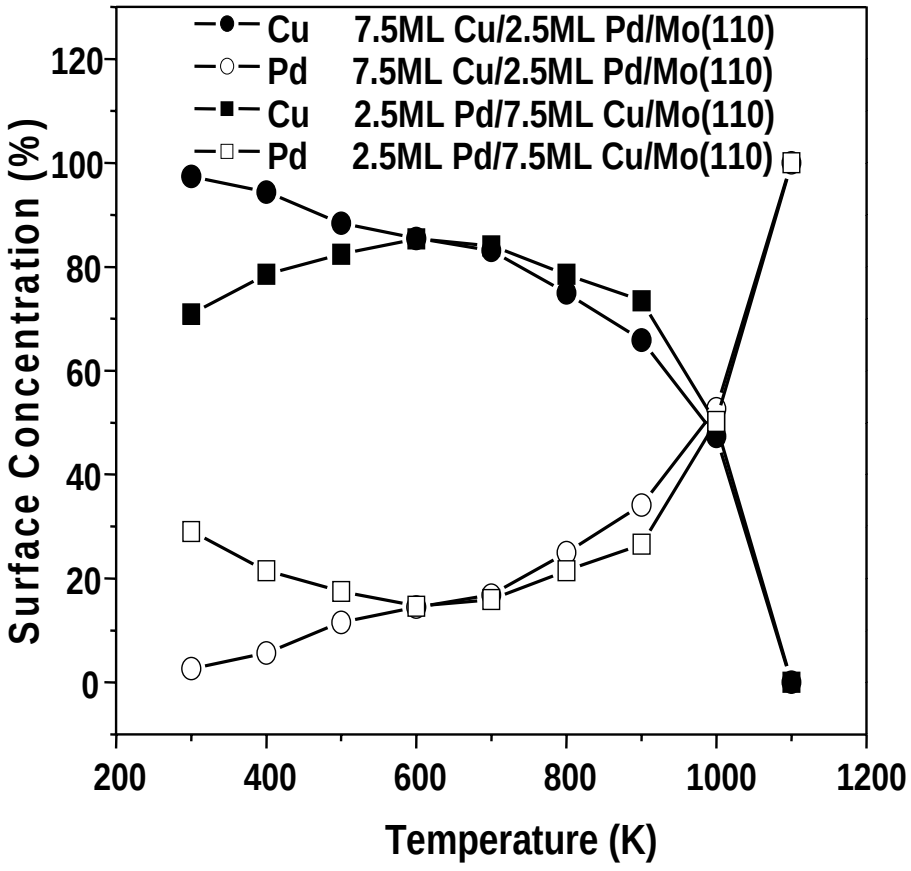

Figure 61. Surface concentration of Cu and Pd as a function of annealing temperature for 7.5 ML Cu-2.5 Pd/Mo(110).

LEIS experiments were performed on 2.5 ML Cu-7.5 ML Pd/Mo(110) and 7.5 ML Cu-2.5 ML Pd/Mo(110) systems using the same approach as for the 5.0 ML Pd-5.0 ML Cu/Mo(110) system, with different deposition sequences and annealing temperatures. The resulting surface concentrations of Cu and Pd were calculated and plotted as a function of annealing temperature in Figures 60 and 61, respectively. It can be gleaned from Figure 60 that the surface concentrations of Cu and Pd converged at *ca.* 600 K regardless of the Cu-Pd deposition sequence; about 42 % Cu and 58 % Pd were obtained on the surface at this temperature. At higher annealing temperatures, the Pd surface concentration continued to increase with a corresponding decrease in Cu surface concentration.

The results shown in Figure 61 agreed with those from Figures 58 and 60, i.e. the Cu and Pd surface concentrations converged to a value of *ca.* 85 % Cu and 15 % Pd at 600 K for 7.5 ML Cu-2.5 ML Pd/Mo(110). More dramatic changes in surface composition were detected at higher annealing temperatures. A contributory factor to these compositional changes was the observed morphology variation observed at annealing temperatures higher than 700 K (cf. Figure 59). At 1000 K or higher, Cu desorption was assigned as the main cause for the surface compositional changes.

To further analyze the results, a surface-vs-bulk composition phase diagram (Figure 62) was constructed for the Cu/Au – Pd overlayers/Mo(110). The data points were obtained from the stable Cu-Pd surface alloys annealed at 600 K and the stable Au-Pd

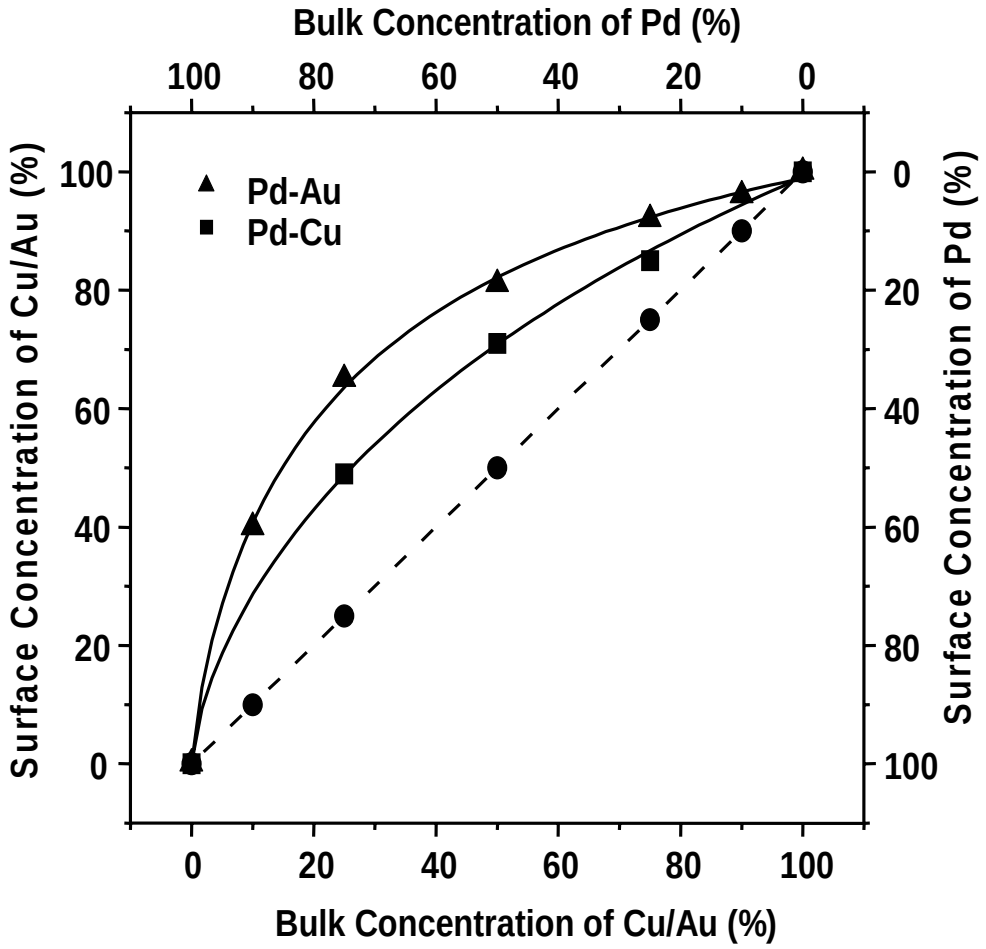

Figure 62. Surface vs. bulk composition phase diagram of Cu/Au-Pd overlayers/Mo(110).

surface alloys annealed at 800 K (Figure 25). The line defined by the filled square /triangle symbols represented the surface composition of Cu/Au which can be read on the left axis; the surface concentrations of Pd were displayed on the right axis. The dashed line represented the bulk Cu/Au and Pd concentrations upon Cu/Au-Pd deposition. A bulk Cu concentration of 25 %, 50 % or 75% corresponded to a surface Cu concentration of 49 %, 71 % and 85 %, respectively; the remainder of the surface was covered by Pd.

Cu surface segregation was evident after a 600-K annealing. In contrast, Au-Pd/Mo(110) surfaces with 800-K annealing,[63] (filled triangle symbols in Figure 62) exhibited less extensive Cu surface segregation than Au.

The surface free energies of Pd and Au are 2.04 J/m^2 and 1.63 J/m^2, respectively.[114,115] The surface tends to minimize the surface free energy and results in Au surface segregation. The relatively higher aptitude of Au to surface-segregate, compared to Cu, in bimetallic Pd-based alloys, stems from the fact that the surface free energy of Cu (1.75 J/m^2)[115] is slightly higher than that of Au.

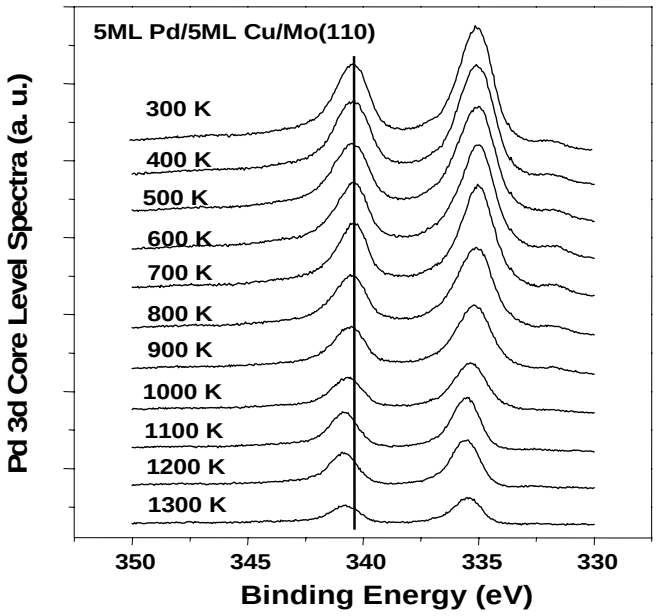

(a)

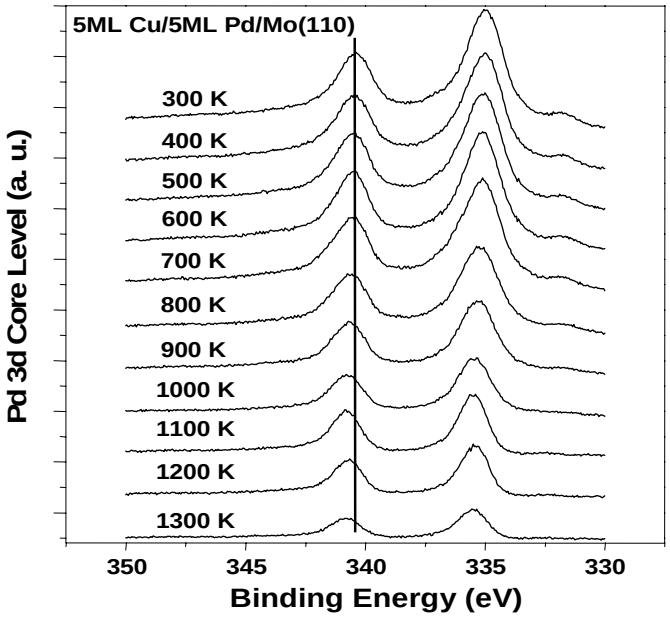

(b)

Figure 63. Pd 3d core level spectra of (a) 5.0 ML Pd/5.0 ML Cu/Mo(110); and (b) 5.0 ML Cu/5.0 ML Pd/Mo(110) vs. annealing temperature.

Electronic Properties

XPS was used to explore the electronic properties of Cu-Pd/Mo(110). Pd 3d core level spectra were recorded as a function of annealing temperature for 5.0 ML Pd/5.0 ML Cu/Mo(110) and 5.0 ML Cu/5.0 ML Pd/Mo(110) in Figure 63(a) and (b), respectively. The surfaces were annealed at each temperature for 20 minutes and all spectra were collected at 300 K. Similarly, in both Figure 63 (a) and (b), the centroid of the Pd 3d core level peak did not shift much with an increase in the initial temperature up to 600 K; a positive CLBE shift was observed with temperatures higher than 600 K.

To better illustrate the CLBE shifts, the centroids of Pd $3d_{3/2}$ position were plotted as a function of annealing temperature in Figure 64 (a) and (b), respectively, for 5.0 ML Pd/5.0 ML Cu/Mo(110) and 5.0 ML Cu/5.0 ML Pd/Mo(110). In Figure 64(a), the Pd $3d_{3/2}$ position was very close to the bulk value with 5.0 ML Pd deposition on the pre-deposited 5.0 ML Cu surface at 300 K. Upon annealing at 400 K, the peak position shifted slightly in the positive direction, and then remained stable up to 700 K. More peak position shifting in the positive direction was observed at temperatures ranging from 700 to 1000 K. The stable + 0.2 eV Pd 3d CLBE shift from the bulk value observed at temperatures between 400 and 700 K indicated a perturbation of Pd core level electronic properties upon Cu-Pd alloying. For annealing temperatures of 800 K or higher, the larger binding energy shift could be a reflection of large variations in surface morphology as previously discussed. Likewise, a similar trend of Pd CLBE shift was

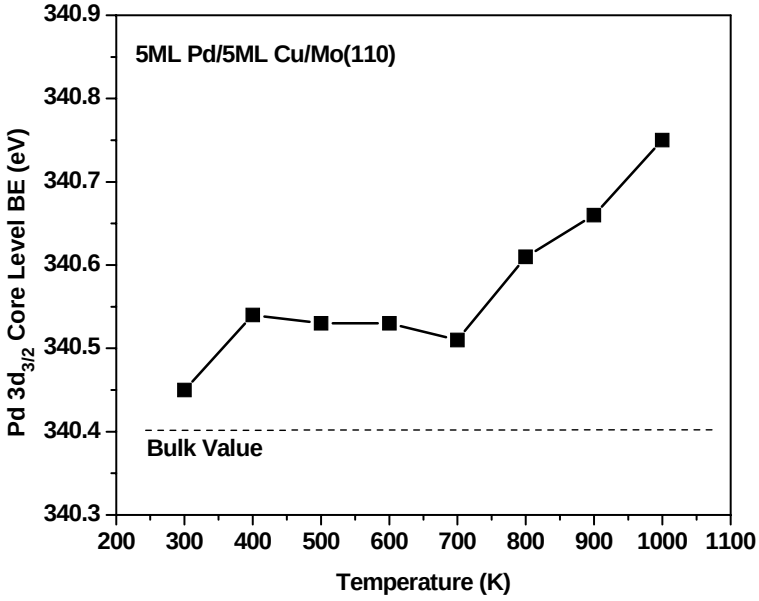

(a)

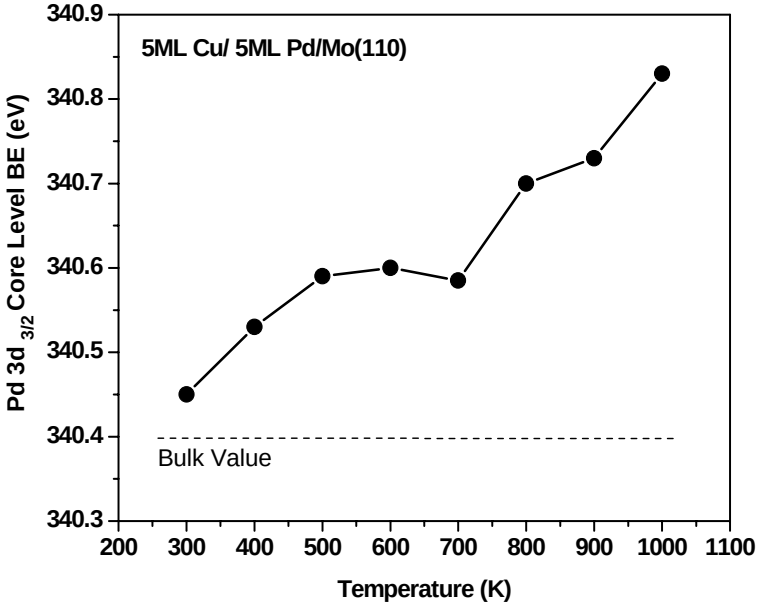

(b)

Figure 64. XPS Pd 3d $_{3/2}$ CLBE of (a) 5.0 ML Pd/5.0 ML Cu/Mo(110) and (b) 5.0 ML Cu/5.0 ML Pd/Mo(110) as a function of annealing temperature.

exhibited in Figure 64 (b) for 5.0 ML Cu/5.0 ML Pd/Mo(110). With 600 K annealing, the Pd 3d core level peak was about 0.2 eV higher than the bulk value. Larger shifts were detected with higher annealing temperatures.

To monitor the Cu-Pd alloying process, the Pd $3d_{3/2}$ peak area was plotted in Figure 65 as a function of annealing temperature for 5.0 ML Pd/5.0 ML Cu/Mo(110) and 5.0 ML Cu/5.0 ML Pd/Mo(110). For 5.0 ML Pd/5.0 ML Cu/Mo(110) in Figure 65(a), no Pd peak intensity change was seen at temperatures ranging from 300 to 400 K. At higher annealing temperatures, the Pd intensity continued to decrease due to Cu-Pd alloying; it decreased *ca.* 25% after annealing at 600 K. The results agreed closely with the aforementioned LEIS findings, i.e., Cu-Pd alloying started even at 300 K and surface segregation of Cu was maximized at 600 K. The relatively smaller decrease in intensity from 300 - 600 K in XPS data could result from signals from the near surface region probed by XPS (10-100 Å) versus information for only the surface layer from LEIS. With annealing at temperatures of 700 K and above, the XPS Pd intensity decreased, conflicting with the LEIS data in Figure 58. Although the lack of direct information on surface morphology variation made it difficult to hypothesize, the difference between the Pd intensity in the top surface layer in LEIS and that of the larger quantity in the near surface region in XPS may be related to surface morphology changes as proposed in Figure 59.

In Figure 65(b), the Pd intensity remained stable at annealing temperature ranging to 600 K. A continuous decrease in intensity was seen with annealing temperatures of 700

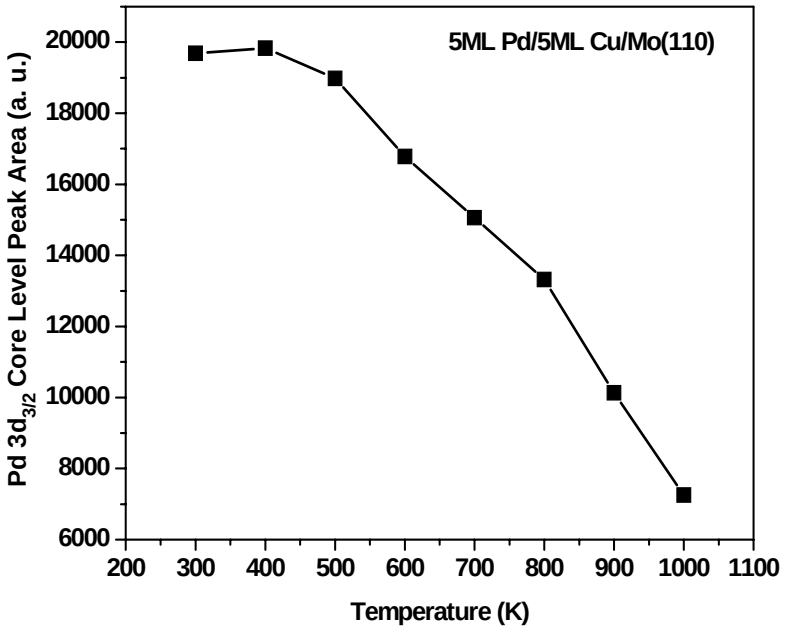

(a)

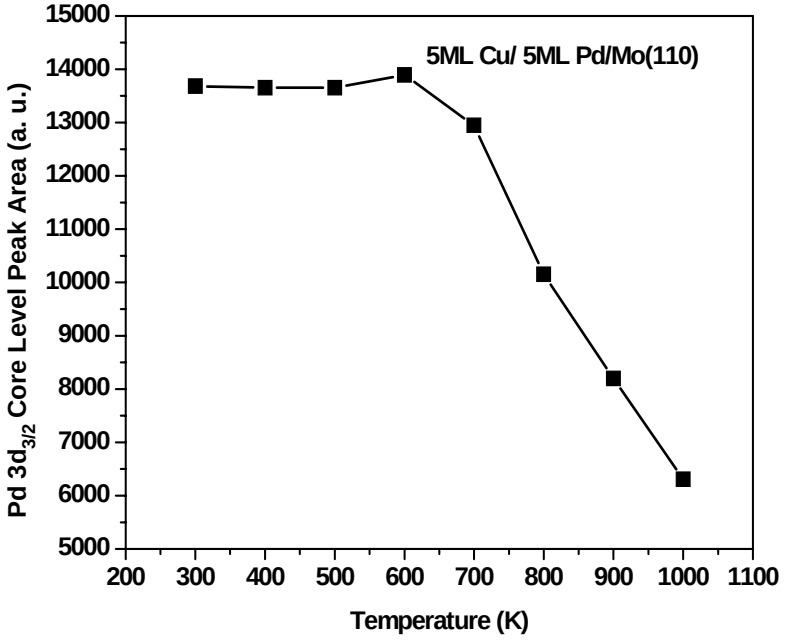

(b)

Figure 65. XPS Pd 3d $_{3/2}$ core level peak area of (a) 5.0 ML Pd/5.0 ML Cu/Mo(110) and (b) 5.0 ML Cu/5.0 ML Pd/Mo(110) as a function of annealing temperature.

K or higher, of which the explanation is similar to that given for Figure 65(a). Determining the effect of XPS Pd intensity upon the alloying process was not an effective method to monitor the alloying process, possibly because of the intrinsic property of X-ray penetration into the near surface region and the relatively small sensitivity of the Pd 3d core level (compared to Cu 2p core level).

XPS Cu 2p core level spectra were recorded in Figure 66 for 5.0 ML Pd/5.0 ML Cu/Mo(110) and 5.0 ML Cu/5.0 ML Pd/Mo(110) as a function of annealing temperature. The relatively less intense Cu $2p_{1/2}$ feature was used to study the Cu core level binding energy shift and intensity variation due to the overlap of Cu $2p_{2/3}$ and Pd Auger features. In Figure 66(a), after 5.0 ML Pd deposition on 5.0 ML Cu/Mo(110) at 300 K, a negative binding energy shift and intensity reduction were observed for Cu $2p_{1/2}$. No significant shift was seen with annealing temperatures of 1000 K or less, before Cu desorbed from the surface. In Figure 66(b), a continuous negative BE shift of Cu $2p_{1/2}$ was observed for annealing temperatures up to 600 K, whereas the peak position remained stable for temperatures ranging up to 1000 K before Cu evaporated to a vacuum.

To further investigate the binding energy shift, the CLBE position of Cu $2p_{1/2}$ was plotted as a function of annealing temperature in Figure 67. In Figure 67(a) for 5.0 ML Pd/5.0 ML Cu/Mo(110), a *ca.* 0.6 eV negative bind energy shift was observed relative to the Cu bulk value after 5.0 ML Pd deposition on top of Cu at 300 K. This finding was a strong indication of Cu-Pd alloying at this temperature. The peak position did not show increased shifts upon annealing at 1000 K. The - 0.6 eV Cu 2p core level binding energy shift that resulted from the Cu-Pd surface alloying implied a large perturbation of the

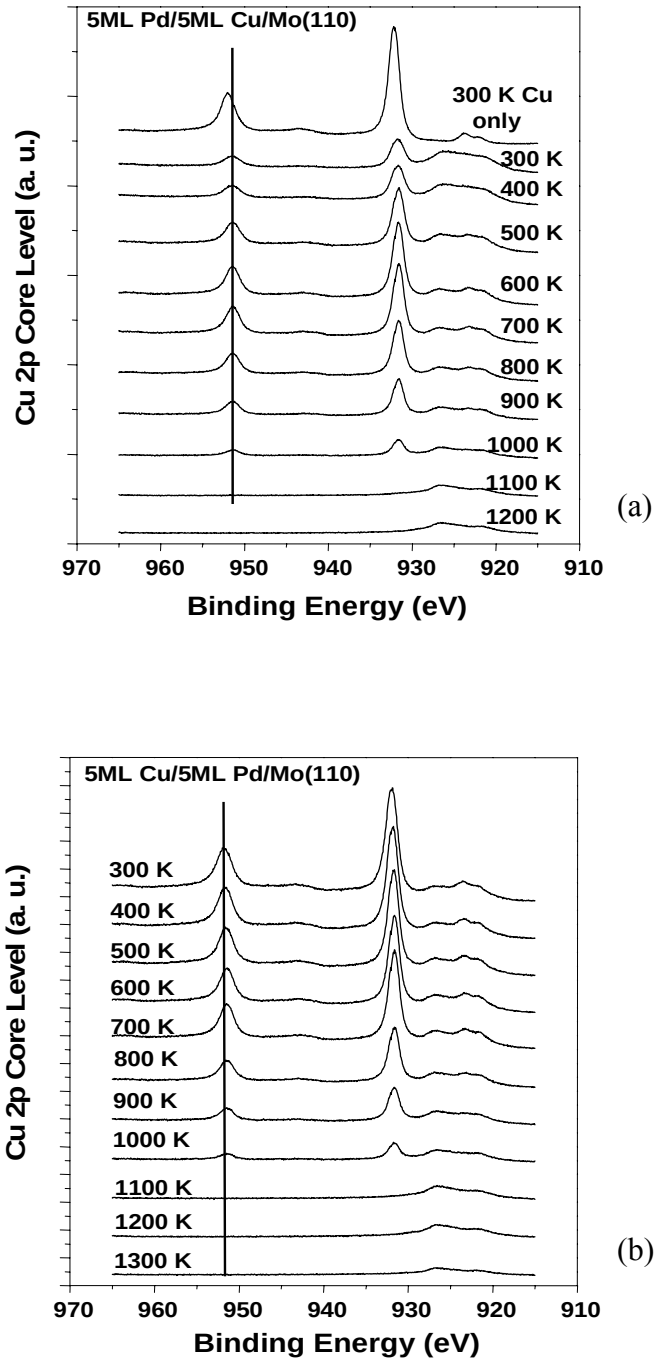

Figure 66. XPS of Cu 2p core level spectra of (a) 5.0 ML Pd/5.0 ML Cu/Mo(110) and (b) 5.0 ML Cu/5.0 ML Pd/Mo(110) as a function of annealing temperature.

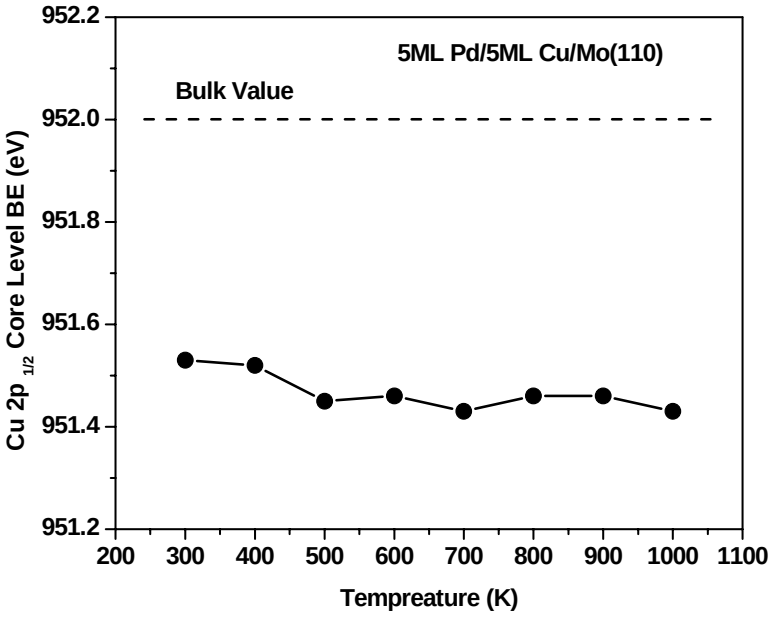

(a)

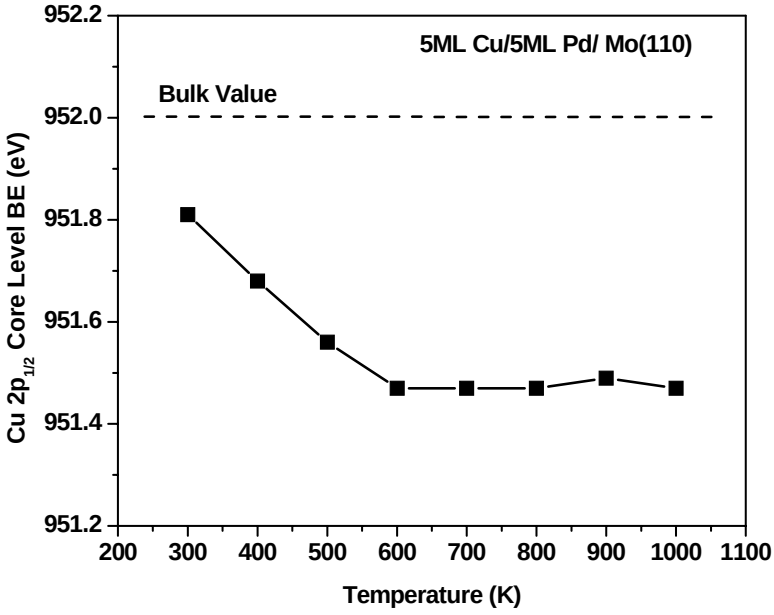

(b)

Figure 67. Cu 2p CLBE position of (a) 5.0 ML Pd/5.0 ML Cu/Mo(110); and (b) 5.0 ML Cu/5.0 ML Pd/Mo(110) as a function of annealing temperature.

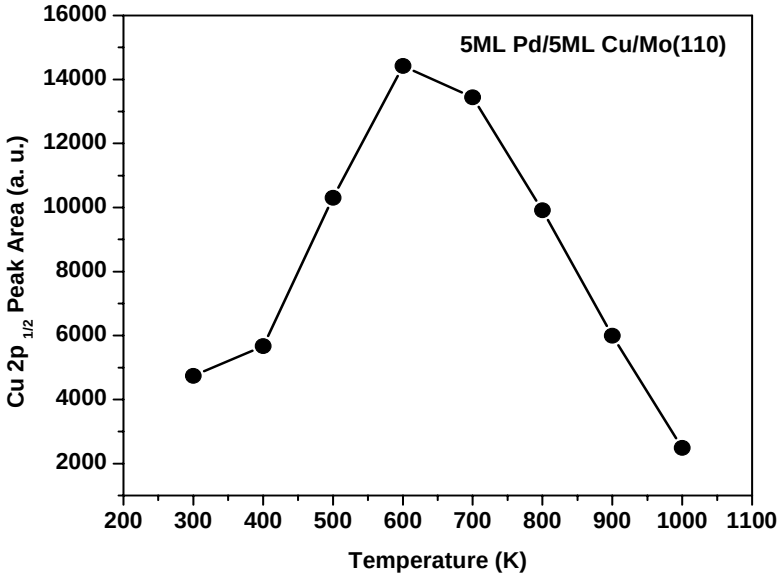

(a)

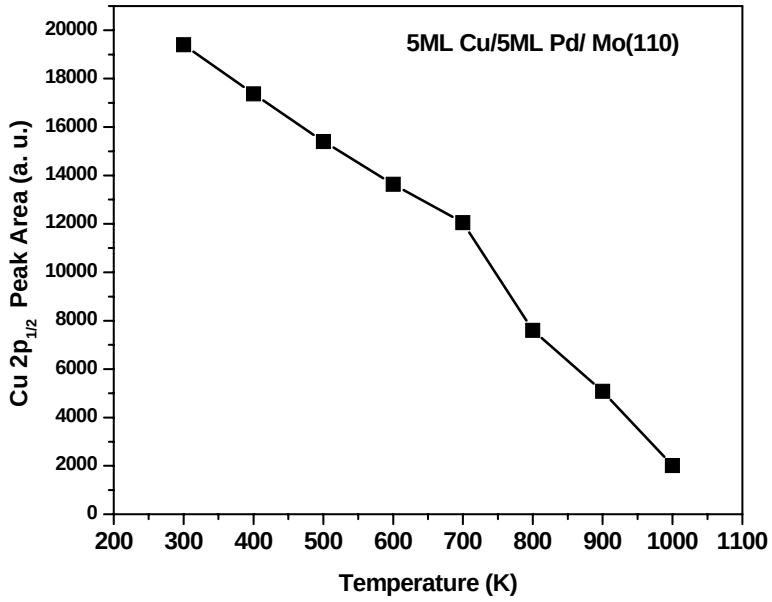

(b)

Figure 68. Cu core level peak area of (a) 5.0 ML Pd/5.0 ML Cu/Mo(110); and (b) 5.0 ML Cu/5.0 ML Pd/Mo(110) as a function of annealing temperature.

electronic structure of Cu. In Figure 67(b), with 5.0 ML Cu deposition on 5.0 ML Pd/Mo(110) at 300 K, a - 0.2 eV shift of the Cu $2p_{1/2}$ core level peak was detected relative to that of the bulk. With annealing at higher temperatures, the peak position decreased to *ca.* 951.4 V at 600 K, and remained steady at temperatures ranging to 1000 K. These results were in agreement with the data from the reversed deposition system of Figure 67(a). The difference in binding energy position observed between 300 to 500 K stemmed from the tendency of Cu to remain on the surface resulting in a slower Cu-Pd alloying process (Figure 67(b)).

Cu $2p_{1/2}$ peak area was plotted as a function of annealing temperature for 5.0 ML Pd/5.0 ML Cu/Mo(110) in Figure 68(a). Clearly, the Cu peak intensity increased with increasing the annealing temperature and reached a maximum at 600 K. The peak intensity decreased as the temperature was increased from 600 K to 1000 K. These data agreed well with LEIS data illustrating Cu surface segregation in Figure 58, i.e., the Cu surface concentration was maximized around 600 K. For 5.0 ML Cu/5.0 ML Pd/Mo(110) in Figure 68(b), the Cu $2p_{1/2}$ peak area decreased with increasing annealing temperatures. A smaller decrease in intensity was observed from 300 to 700 K during the Cu-Pd alloying process. The greater decrease in intensity that occurred in the range of 800 to 1000 K could be due to surface morphology variation.

The reported XPS studies of 5.0 ML Cu-5.0 ML Pd/ Mo(110) basically agreed with the LEIS results. A stable Cu-Pd surface alloy was obtained with a 600 K anneal. At this temperature, Pd 3d and Cu 2p exhibited + 0.15 - 0.2 eV and - 0.6 eV CLBE shifts

relative to their bulk values, respectively. Cu and Pd XPS core level peak areas also indicated that the Cu-Pd alloying occurred.

The preceding analyses presented herein is an illustrative case where complementary information regarding the topmost and subsurface layers was acquired by the tandem use of LEIS (surface-sensitive) and XPS (near surface region-probing).

It is noteworthy to mention that Mo 3d core level features have been monitored while Pd and Cu data were collected. Mo 3d spectra were recorded as a function of annealing temperature for 5.0 ML Cu/5.0 ML Pd/Mo(110) in Figure 69. Although the intensity of Mo peak area varied with different annealing temperatures as discussed in Figure 59, the Mo 3d CLBE peak position remained stable throughout the entire temperature range. This result indicated that no strong Pd-Mo or Cu-Mo interaction existed during the deposition and annealing processes, thereby eliminating the concern of any substrate effect in this work.

A similar approach was utilized to study the 7.5 ML Cu-2.5 ML Pd/Mo(110) and 2.5 ML Cu-7.5 ML Pd/Mo(110) systems using XPS. In Table 1(a), the Cu $2p_{1/2}$ and Pd $3d_{2/3}$ CLBE shifts were summarized for the stable Cu-Pd surface alloys prepared with 600 K annealing. As a comparison, the Au $4f_{7/2}$ and Pd $3d_{2/3}$ CLBE shifts for Au-Pd/Mo(110) stable alloy systems were included in Table 1(b). Data in Table 1(b) were obtained from the stable Au-Pd surface alloys prepared with 800 K annealing as shown in the earlier Au-Pd /Mo(110) section. In general, more positive binding energy shifts of Pd 3d core

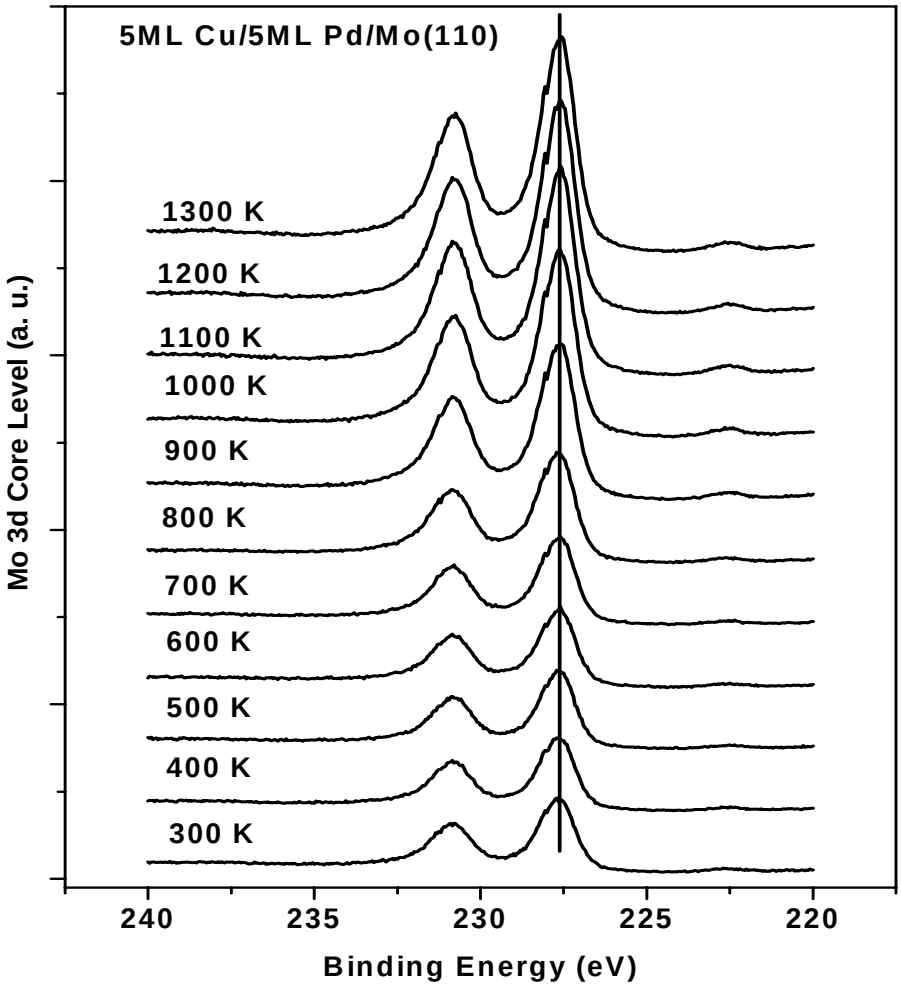

Figure 69. XPS Mo 3d core level spectra of 5.0 ML Cu/5.0 ML Pd/Mo(110) vs. annealing temperature.

Table 1. XPS core level binding energy shift of stable Cu-Pd and Au-Pd surface alloy on Mo(110).

CLBE Shift of Cu-Pd/Mo(110)

Cu (ML)	Pd (ML)	Cu $2p_{1/2}$ CLBE (eV)	Pd $3d_{2/3}$ CLBE (eV)
7.5	2.5	-0.3 ~ -0.4	+0.1 ~ +0.15
5	5	-0.55 ~ -0.6	+0.15 ~ +0.2
2.5	7.5	-0.8 ~ -0.9	+0.4

(a)

CLBE Shift of Au-Pd/Mo(110)

Au (ML)	Pd (ML)	Au $4f_{7/2}$ CLBE (eV)	Pd $3d_{2/3}$ CLBE (eV)
7.5	2.5	-0.2	-0.2 ~ -0.25
5	5	-0.4	-0.2
2.5	7.5	-0.5	+0.05

(b)

level were observed for Cu-Pd alloys than those for Au-Pd alloys. For example, in the 7.5 ML Cu (or Au)-2.5 ML Pd case, a negative Pd 3d shift (- 0.2 ~ - 0.25 eV) occurred for Au-Pd alloys, but a small positive shift (+ 0.1 ~ + 0.15 eV) was detected in the case of Cu-Pd. For the 2.5 ML Cu (or Au)-7.5 ML Pd systems, the Pd 3d peak shifted positively (0.4 eV) for Cu-Pd whereas only a tiny positive shift (+ 0.05 eV) or no shift was observed for Au-Pd. As seen in Table 1, with different Cu (or Au) : Pd atomic ratios, Pd 3d CLBE positions in Cu-Pd were always *ca.* 0.35 eV more positive than those in Au-Pd, indicating a difference of electronic structures between the two alloying systems. The data for Cu and Au CLBE indicated that both Cu $2p_{1/2}$ and Au $4f_{7/2}$ shift negatively upon alloying with Pd, and Cu 2p exhibited a more negative shift than Au 4f with different Cu (or Au) : Pd ratios. The difference in binding energy shift was 0.1 - 0.2 eV for 7.5 ML Cu (or Au)-2.5 ML Pd and 5.0 ML Cu (or Au)-5.0 ML Pd cases; the difference increased to *ca.* 0.3 - 0.4 eV for the surface alloys with lesser Cu (or Au) such as the case for 2.5 ML Cu (or Au)-7.5 ML Pd.

The data above suggested that core level d-band electron density Pd was diminished, with charge being transferred to Cu, as a result of Cu-Pd alloying. In the case of Au-Pd, Pd 3d shifted negatively together with Au 4f as shown in Table 1(b). With observations from XANE/XPS and computation modeling, Lee et al. [42]claimed that Pd gains d-band charge and loses sp band electron density in Au-Pd alloys. The net effect was that Pd

still loses electron density to Au. Regardless of the details of electron charge-transfer mechanism, the results obtained in the current investigation signified that Pd 3d definitely has less electron density in Cu-Pd than in Au-Pd.

CO-TPD

CO TPD experiments were carried out to probe the surface absorption sites to elucidate ensemble and ligand effects on Cu-Pd alloy surfaces. Various CO dosages (0.01 to 1.0 L) were applied to a 600 K pre-annealed 5.0 ML Cu/5.0 ML Pd/Mo(110) surface with the substrate temperature of 85 K. The saturation CO dosage for the surface was 1.0 L CO.

In Figure 70, TPD spectra were recorded as a function of CO dosages ranging from 0.01 to 1.0 L. A small peak centered around 400 K was observed, beginning with 0.01 L CO dosage; such feature was ascribed to multi-fold (bridging and/or three-fold hollow) Pd sites on Cu-Pd alloy surface.[47,63,64] In the LEIS work discussed earlier, the surface composition of 600 K pre-annealed 5.0 ML Cu/5.0 ML Pd/Mo(110) was 30 % Pd and 70 %, which suggested that a certain amount of multi-fold Pd sites could exist on the surface. With increasing CO dosage, the CO desorption features increased in intensity and shifted gradually toward lower temperatures. With 0.1 L CO dosage, a more

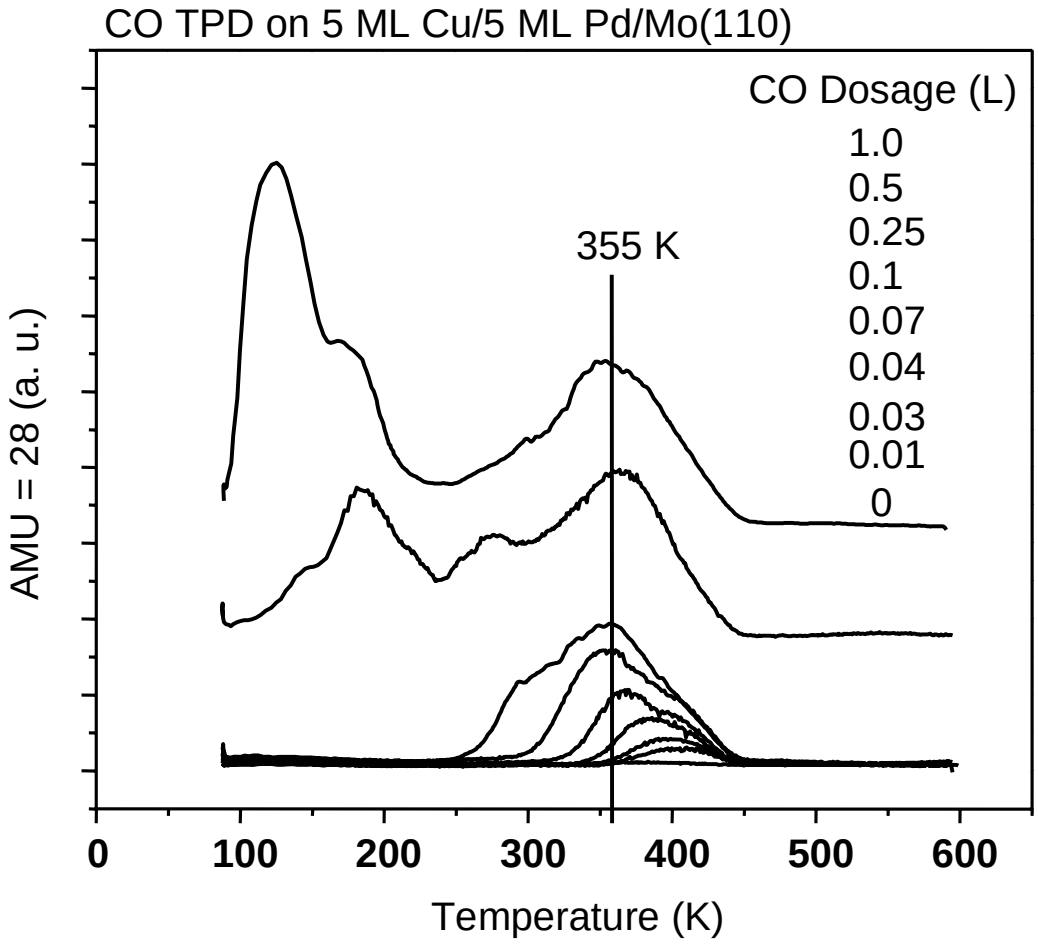

Figure 70. CO TPD of 5.0 ML Cu/5.0 ML Pd/Mo(110) 600 K pre-annealed surface. CO dosage is 0.01 to 1.0 L, and the adsorption temperature is 85 K.

pronounced feature, centered at 355 K, can be observed; this peak was believed to result mainly from CO adsorption on Pd a-top sites, considering the previous evidence from IRAS.[47] With higher CO dosages, more features appeared in the lower temperature range of 100-300 K. The large features that were observed at temperatures below 200 K, with 1.0 L CO dosage, were believed to originate from CO on Au a-top sites. Regardless, the main feature of CO on a-top Pd sites reported by us was near 355 K, a value that was about 50 K higher than the CO desorption feature on a-top Pd sites in Au-Pd alloy surfaces.[63] This temperature difference was attributed to the difference of ligand effects in Cu-Pd and Au-Pd alloying. It can be argued that a stronger bonding between CO-Pd developed on Cu-Pd surfaces. IRAS data also showed a lower CO stretching frequency (2068 cm^{-1})[47] for CO adsorption on a-top Pd sites of Cu-Pd alloy cluster surfaces than that (2088 cm^{-1}) of Au-Pd alloy surfaces,[63,64] indicating a stronger CO bonding to Pd a-top sites on Cu-Pd surfaces than on Au-Pd surfaces.

Sn/Pd(100)

Surface Composition and Structure

LEIS and LEED were combined to study the surface composition and structural properties of Sn on Pd (100) surface. In Figure 71, Ne^+ scattered LEIS spectra of 1.0 ML Sn/Pd(100) were displayed as a function of annealing temperature. The surface was annealed at each indicated temperature for 1 minute, and all spectra were collected at 300 K.

As expected, a single scattering peak feature from clean Pd(100) substrate was observed with KE of *ca.* 0.47 keV. After depositing 1.0 ML Sn, the Pd scattering peak was attenuated and a new scattering feature, ascribed to Sn, emerged at 0.49 keV. The Pd scattering intensity did not drop to zero at the 1.0 ML Sn coverage, although the Pd peak was much smaller and overlapped with the Sn feature. This may be due to the Sn-Pd interdiffusion at 300 K and the contribution of LEIS signals from the second Pd layer atoms on the open fcc (100) surface.[116] As the annealing temperature was increased, the Pd peak intensity increased while the Sn peak intensity decreased. This change in Pd and Sn intensity was considered as a signpost for the interdiffusion of Sn-Pd, i.e., an alloying effect.

The details of LEED pattern variation vs. the surface annealing temperature were summarized in Table 2. The (1x1) LEED spots of clean Pd(100) substrate became diffuse upon depositing 1.0 ML Sn at 300 K. Weak *c*(2x2) spots started to appear in the

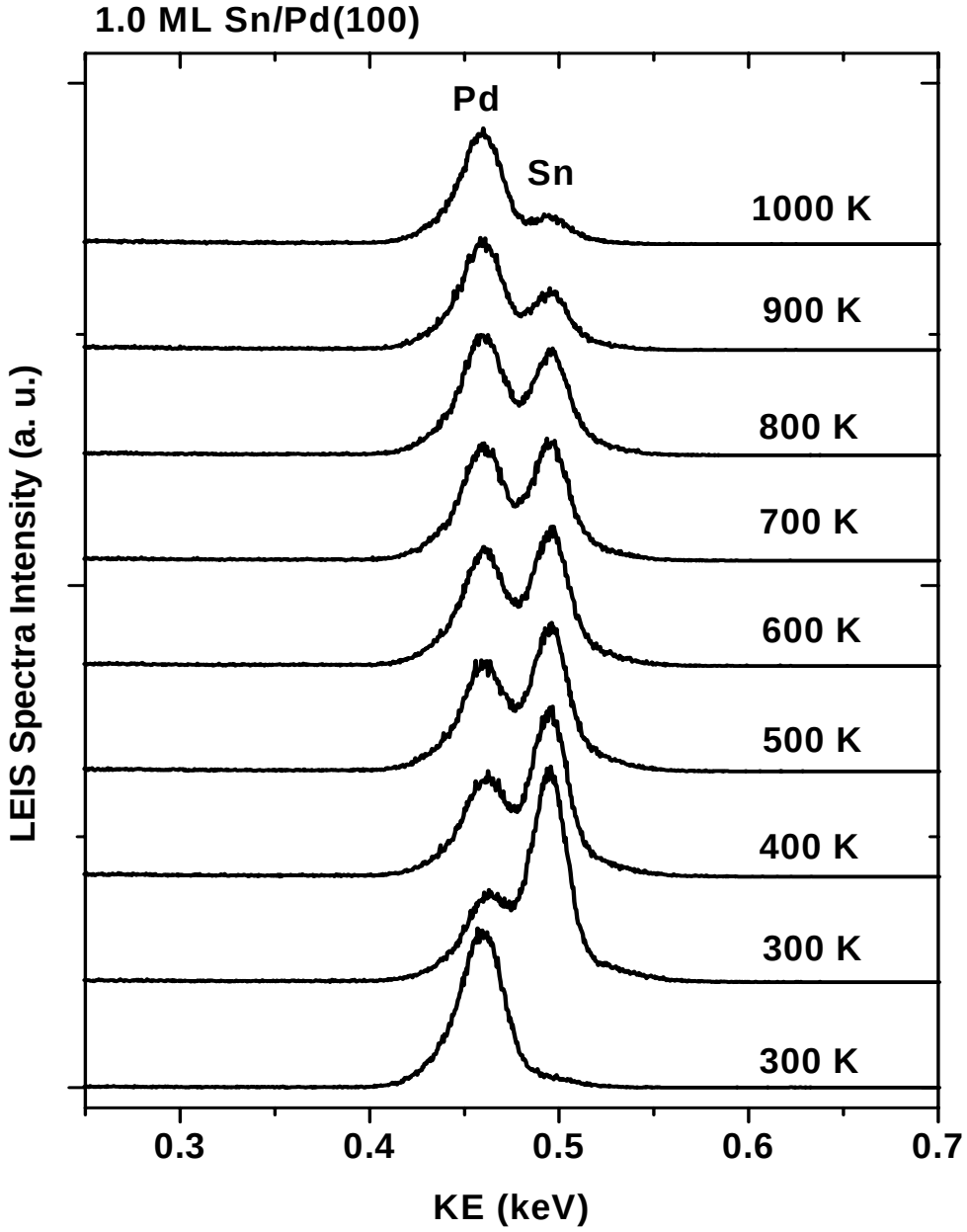

Figure 71. Ne^{+} scattering LEIS spectra of 1.5 ML Sn/Pd(100) as a function of annealing temperature.

Table 2. LEED pattern of 1.0 ML Sn/Pd(100) surface vs. annealing temperature.

Surface Condition	LEED Pattern
Pd(100) at 300 K	clear 1x1
1.0 ML Sn at 300 K	diffusive 1x1
400 K x 60 s	weak 1x1/diffusive c(2x2)
500 K x 60 s	diffusive c(2x2)
600 K x 60 s	clear c(2x2)
700 K x 60 s	diffusive 1x1
800 K x 60 s	clear 1x1
900 K x 60 s	clear 1x1

center of the (1x1) spots with 400 K annealing. The *c*(2x2) LEED spots became more intense as the temperature was increased above 400 K, until a clear *c*(2x2) was evident at the temperature of 600 K. Above temperatures of 700 K, a (1x1) LEED pattern re-appeared.

The LEED patterns of (1x1)-Pd(100) and *c*(2x2)- Sn/Pd(100) and the corresponding real-space ball structures were presented in Figure 72. In the top part of Figure 72, the filled circles on the left represented the primary 1x1 spots from a clean Pd(100) substrate. After depositing 1.0 ML Sn and subsequent annealing at 600 K, some spots (open circles) developed at the center of the 1x1 spots, ultimately giving rise to a *c*(2x2) LEED pattern. The difference between the radii of Sn and Pd atoms and their variation from the surface plane may contribute to the *c*(2x2) LEED pattern. At the bottom of Figure 72, the shadowed balls on the left represented surface Pd atoms aligned in 1x1crystallographic orientation. On the right, a *c*(2x2) alloy surface structure was depicted. It is important to note that evenly separated Pd atoms optimized the density of non-contiguous Pd dimer surface ensembles.[65] Such a surface structure served as an excellent model catalyst for further studies of vinyl acetate synthesis and related reactions.

To analyze the surface composition, the surface concentrations of Sn and Pd were calculated using equation (3) in combination with the LEIS data in Figure 71. The influence of annealing temperature on surface concentration was graphically presented in Figure 73. A decrease in Sn surface concentration (●) and an increase of Pd surface concentration (■) were observed with an increase in temperature. At 600 K, the surface

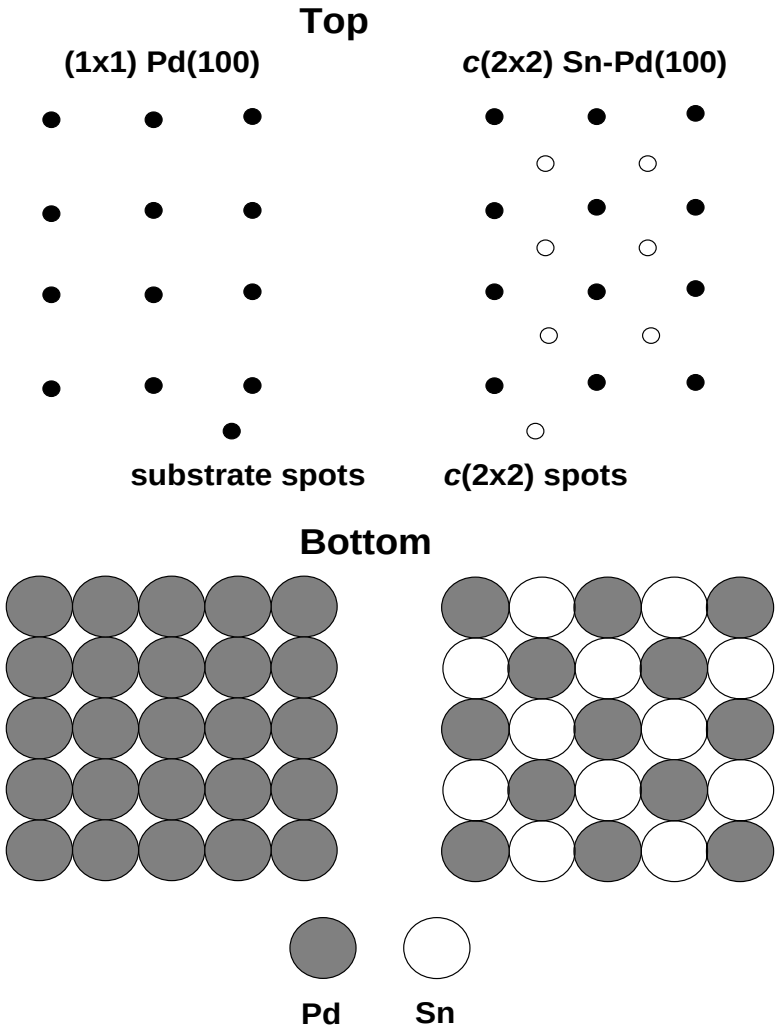

Figure 72. Top: LEED pattern of (1x1) Pd(100) surface (left) and *c*(2x2) Sn/Pd(100) surface (right). Bottom: ball structure of (1x1) Pd(100) surface (left) and *c*(2x2) Sn/Pd(100) surface (right).

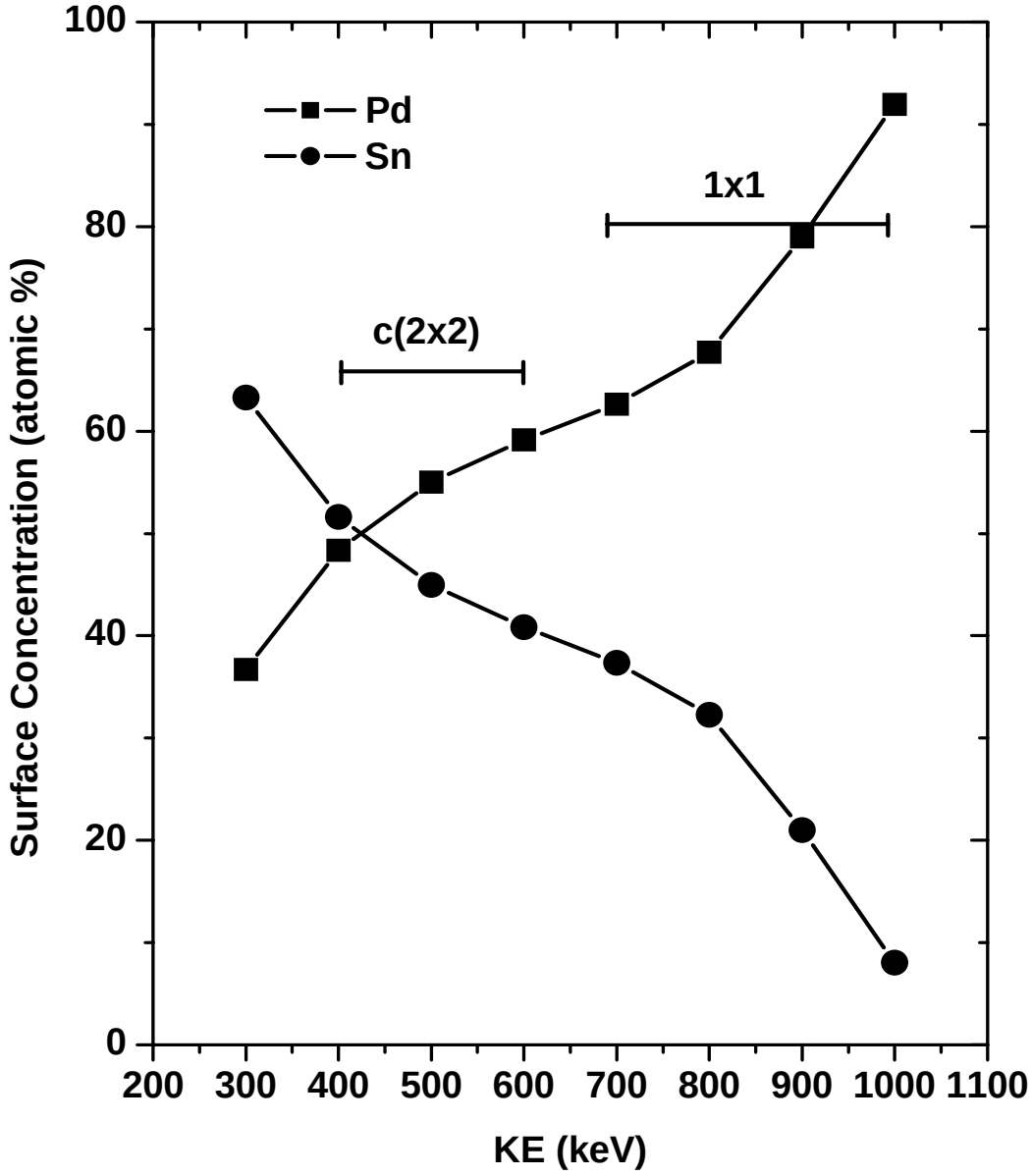

Figure 73. Surface concentration of Sn and Pd of 1.0 ML Sn/Pd(100) as a function of annealing temperature.

concentrations of Sn and Pd were *ca.* 57 % and 43 %, respectively. This result agreed well with the expected Sn-Pd atomic ratio for a *c*(2x2) 1:1 Sn-Pd adlayer (Figure 72). As the temperature rose above 700 K, the diffusion of Sn into the Pd subsurface became more pronounced as evidenced by the decrease in surface Sn concentration; ultimately, the surface reverted to the (1x1) structure, leaving only Pd in the topmost surface.

LEIS and LEED studies of higher Sn coverages (4.0 ML) on Pd(100) were pursued. Ne^+ LEIS spectra of 4.0 ML Sn/Pd(100) were shown as a function of annealing temperature in Figure 74. At 300 K, the Pd scattering intensity was detected as a tiny shoulder on the low kinetic energy side of the Sn peak. As the temperature increased, the intensity of the Pd peak progressively increased while the Sn scattering intensity decreased. No discernible LEED pattern was observed following deposition of 4.0 ML Sn at 300 K and annealing at temperatures up to 500 K. However, a diffuse *c*(2x2) pattern was detected after annealing at 600 K. The *c*(2x2) spots became clearer with annealing temperatures of 700 K and 800 K; this indicated the formation of a *c*(2x2) Sn-Pd(100) surface alloy. The 1x1 LEED pattern was formed once again with annealing at 900 K or greater temperatures.

The surface concentrations of Sn and Pd for 4.0 ML Sn/Pd(100) were calculated and plotted in Figure 75. A continuous increase in Pd surface concentration was observed at temperatures ranging from 300 to 900 K, with a simultaneous decrease in the Sn surface concentration with an identical temperature range. At 800 K, when the *c*(2x2) LEED

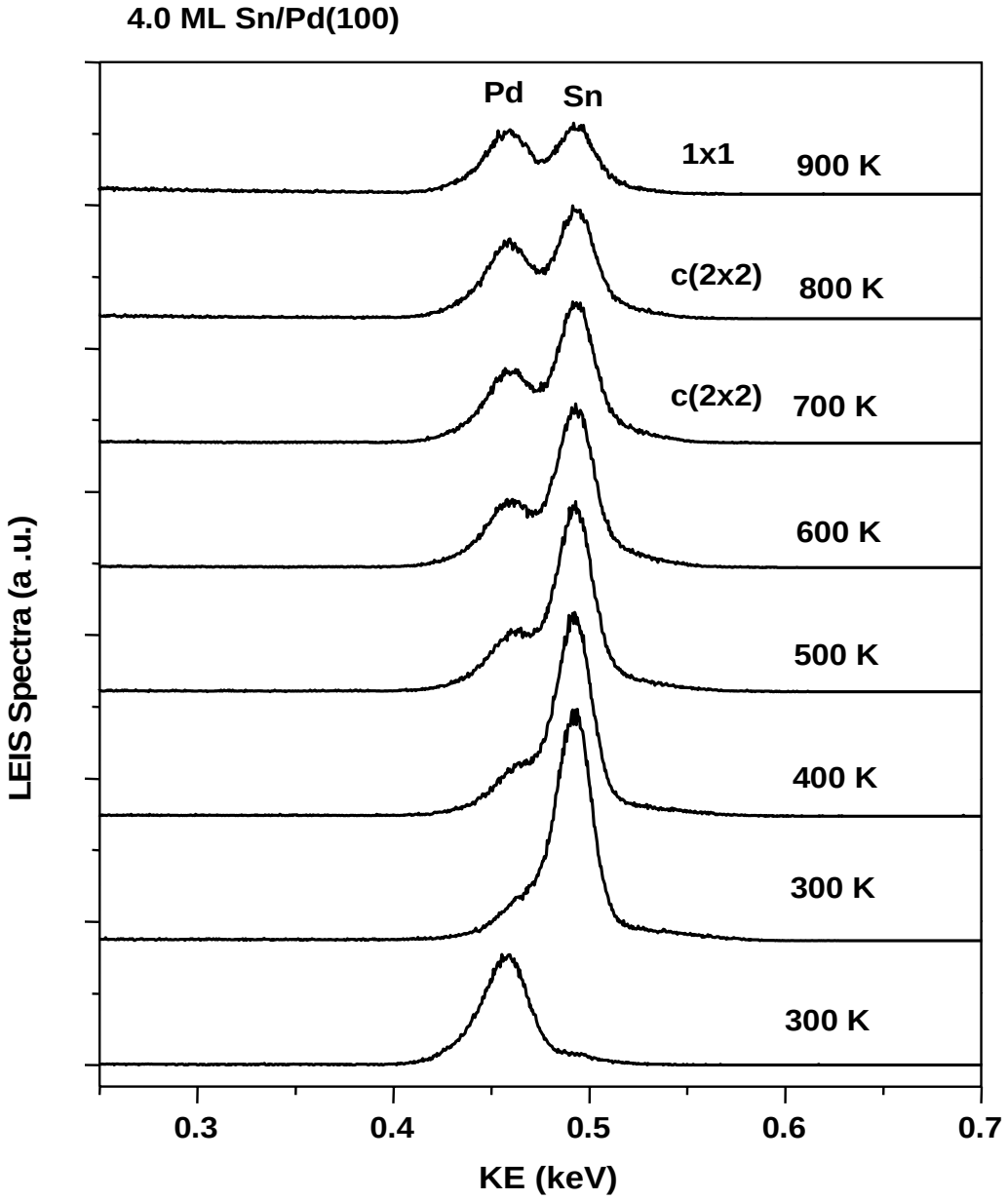

Figure 74. Ne^+ scattering LEIS spectra of 4.0 ML Sn/Pd(100) as a function of annealing temperature.

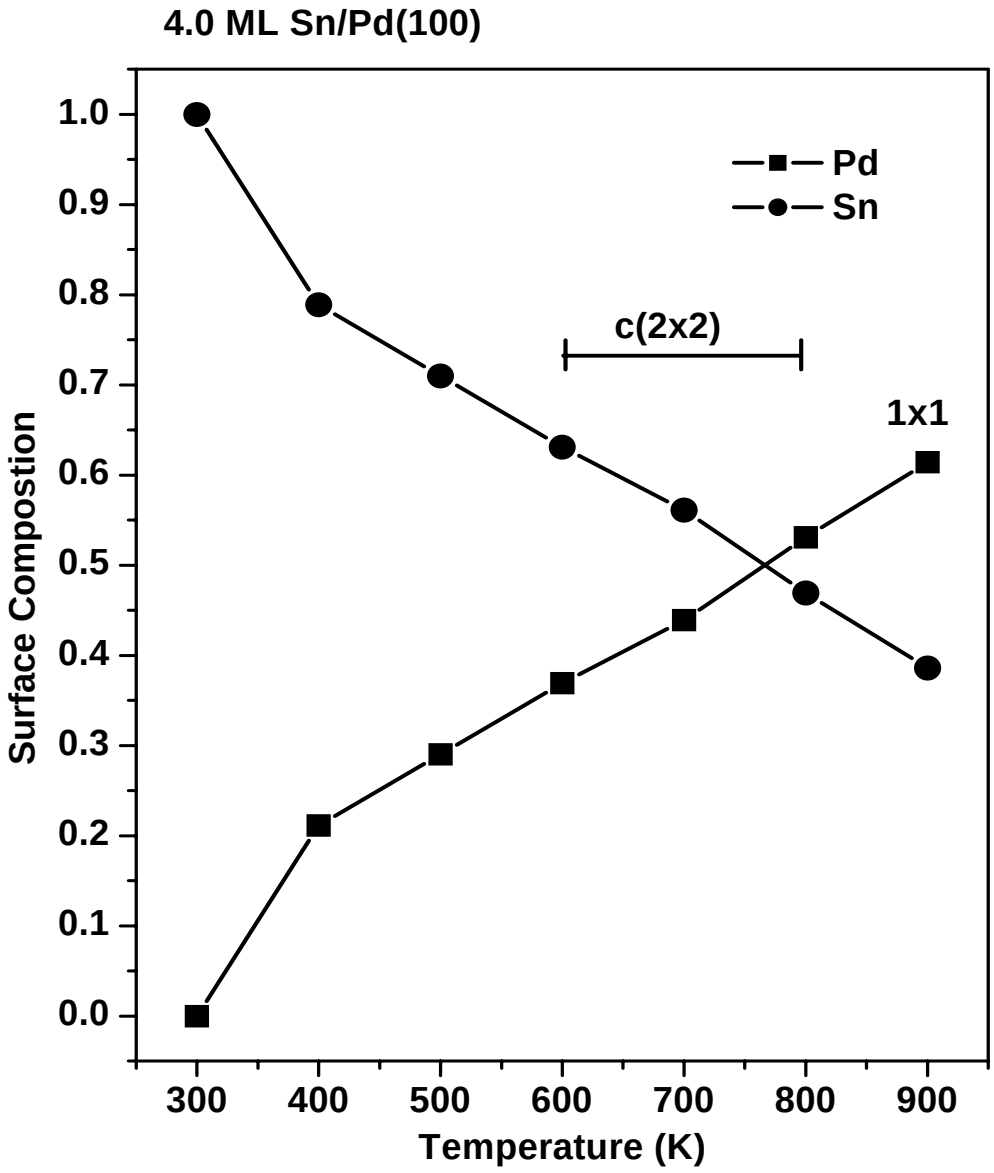

Figure 75. Surface concentration of Sn and Pd of 4.0 ML Sn/Pd(100) as a function of annealing temperature.

pattern was distinct, the surface concentrations of Sn and Pd were 47 % and 53%, respectively. These results suggested that a 1 : 1 Sn : Pd atomic ratio on the *c*(2x2) surface was formed, similar to the one illustrated in Figure 72.

Finally, the deposition of 1.0 ML and 4.0 ML Sn on a Pd(100) substrate with various annealing temperatures was studied with LEIS and LEED. The *c*(2x2) surface structure was obtained with a 1: 1 Sn: Pd atomic ratio by annealing an adlayer at certain temperatures.

Electronic Properties

XPS was used to probe the electronic structures of Sn-Pd. In Figure 76, the XPS Sn 3d core level spectra were displayed as a function of Sn coverage on Pd(100) at 300 K. Sn $3d_{5/2}$ and $3d_{3/2}$ core level peaks were observed with a Sn coverage of 0.2 ML. . The relatively high cross-section of the Sn $3d_{5/2}$ feature allowed a convenient tag for monitoring the Sn peak position and intensity variation. With increasing Sn coverages, the intensity of the Sn core level peak continued to increase; the centroid of the Sn $3d_{5/2}$ feature gradually shifted toward higher BE.

Pd 3d core level spectra were also collected, as shown in Figure 77, as a function of Sn coverage at 300 K. While the intensity of the Pd 3d feature decreased as the Sn coverage increased, the Pd $3d_{5/2}$ peak position shifted toward higher BE with the Sn coverage.

Sn $3d_{5/2}$ and Pd $3d_{5/2}$ core level binding energy positions were plotted as a function of Sn dosage, in Figures 78 and 79, respectively. In Figure 78, the Sn $3d_{5/2}$ CLBE appeared

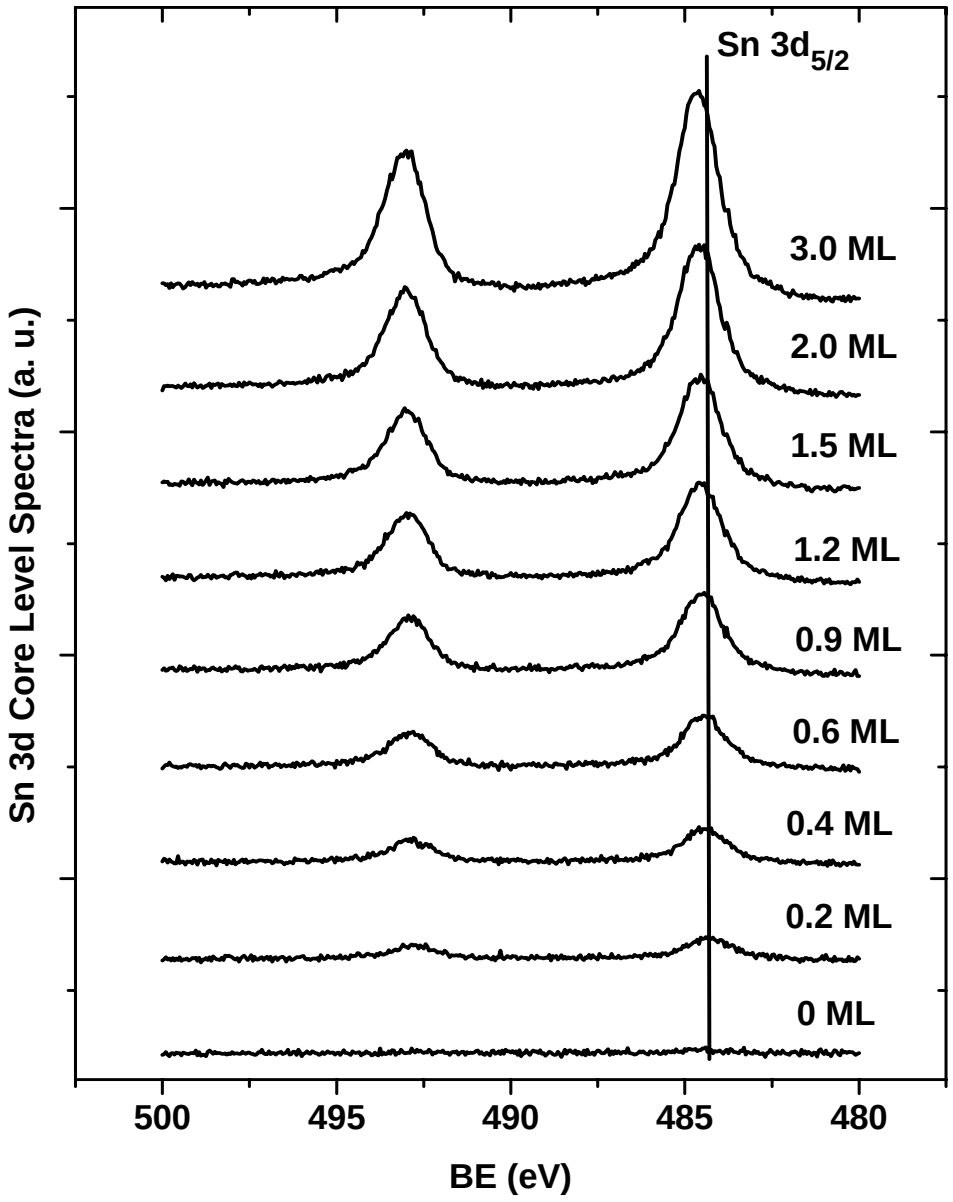

Figure 76. XPS Sn 3d core level spectra as a function of Sn coverage.

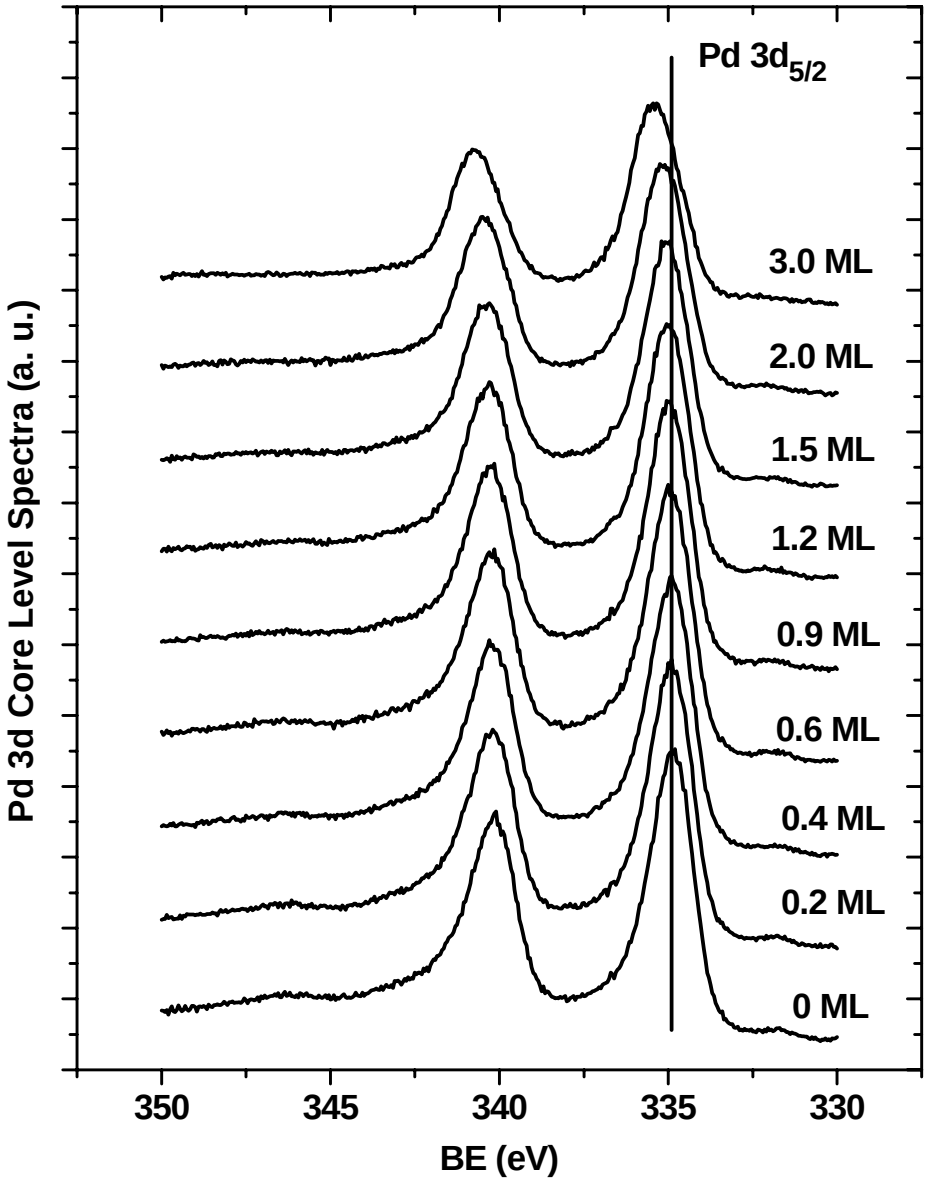

Figure 77. XPS Pd 3d core level spectra as a function of Sn coverage.

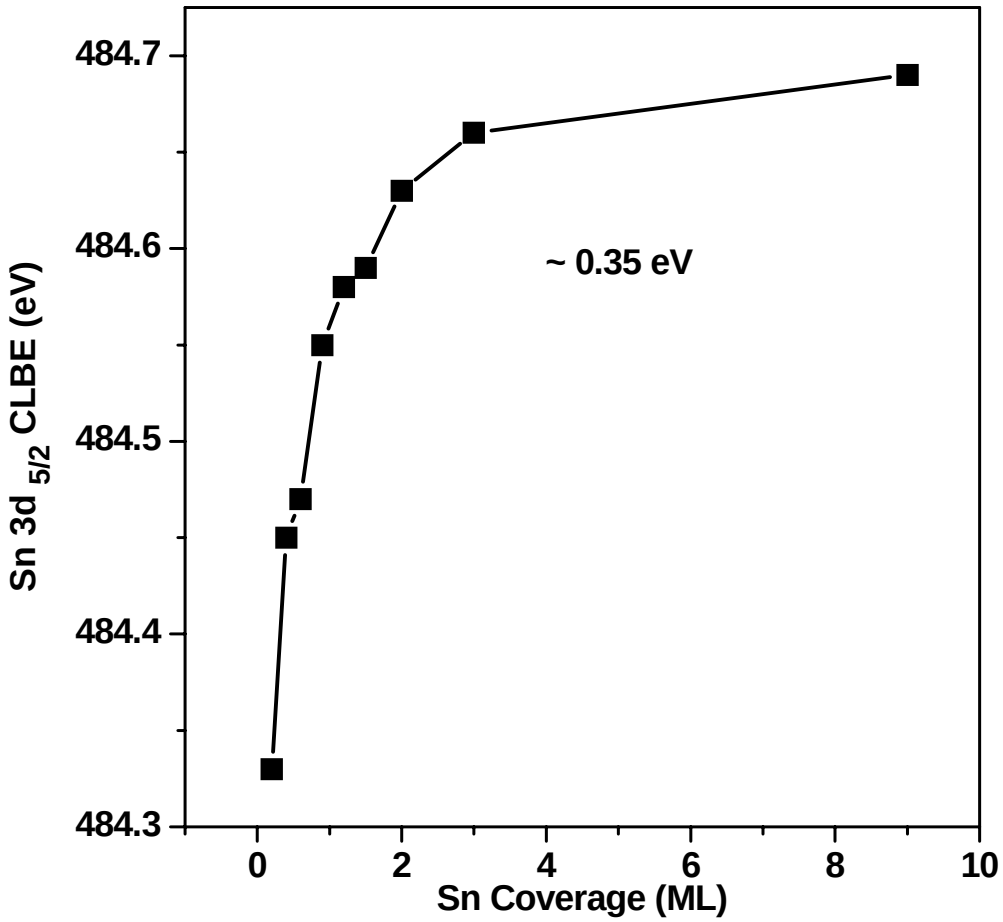

Figure 78. Sn $3d_{5/2}$ CLBE as a function of Sn coverage.

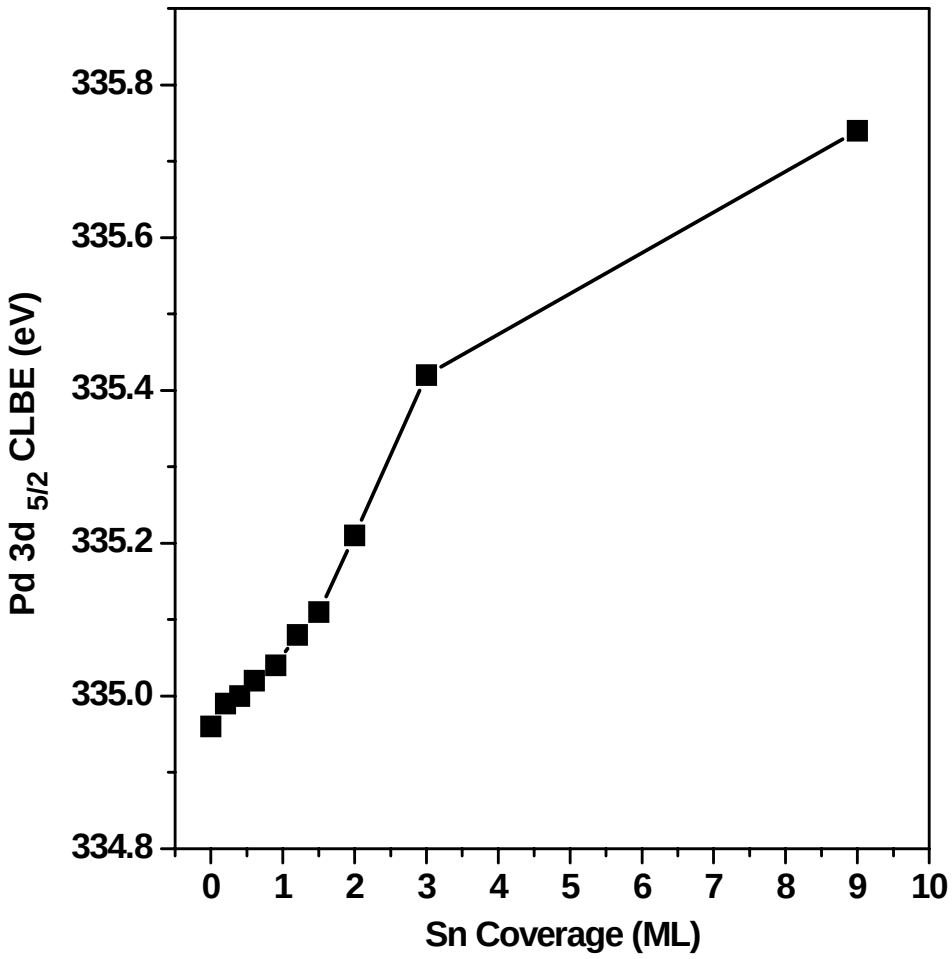

Figure 79. XPS Pd $3d_{5/2}$ CLBE as a function of Sn coverage.

at *ca.* 484.3 eV with 0.2 ML Sn on Pd(100). An exponential shift toward higher BE was observed when the Sn coverage increased to 3.0 ML. This feature reached the bulk Sn value of 484.7 eV at a Sn coverage of 10 ML. At a Sn coverage of 0.2 ML, a - 0.35 eV CLBE shift was observed relative to the bulk Sn value.

In Figure 79, the Pd $3d_{5/2}$ feature appeared at the bulk value of 335.0 eV and gradually shifted toward higher BE as the Sn coverage was increased. A + 0.7 eV shift was detected for $Pd3d_{5/2}$ CLBE relative to the Pd bulk value at 10 ML Sn coverage.

Similar XPS studies were performed by Tsud et al. and Lee et al. on Sn/Pd(110)[31] and Sn/Pd(111)[32] surfaces, respectively. Their synchrotron radiation studies for Sn/Pd(110) showed a negative 0.2 eV shift for Sn 4d core level at low Sn coverage relative to the bulk Sn value. A shift of about 1.1 eV positive CLBE shift for Pd $3d_{5/2}$ core level peak was shown with high Sn coverages. A strong chemical reaction between Sn and Pd was concluded in their studies.[31] However, in the report of Sn on Pd(111),[32] the Sn $3d_{5/2}$ core level feature appeared at the Sn bulk value and shifted toward lower binding energy, as the Sn coverage increased. The maximum shift was found to be – 0.8 eV relative to the Sn bulk value. No distinct CLBE shift was observed for Pd core level features. Our results are in agreement with the work on the Sn/Pd(110) system.[31] The negative shift (- 0.35 eV) observed in Sn $3d_{5/2}$ at low coverage implied a large perturbation of the electronic structure of Sn atoms. At high Sn coverages, the large positive CLBE shift in Pd $3d_{5/2}$ also indicated a strong Sn-Pd interaction at the interface between the Sn overlayer and the Pd surface layers. This was the result of a high

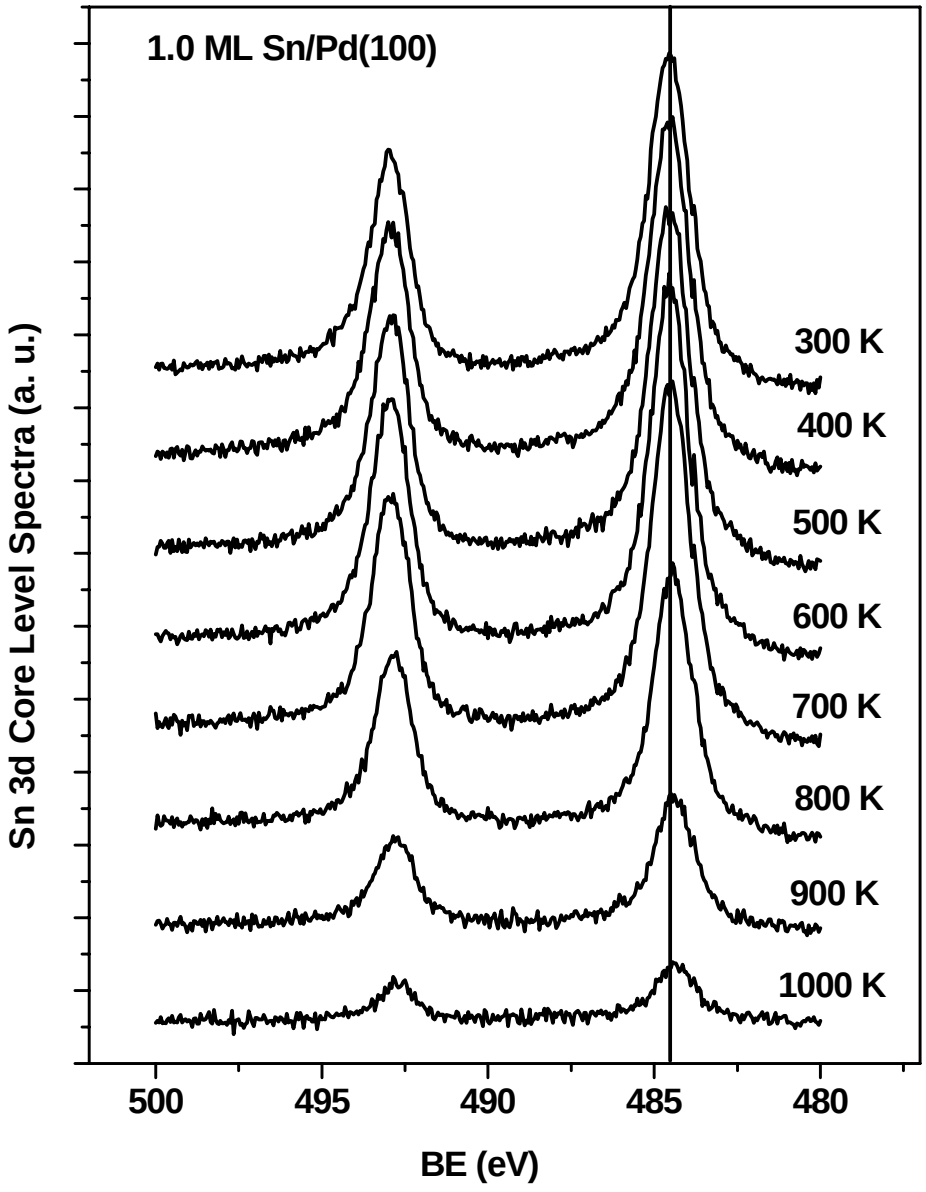

Figure 80. XPS Sn 3d core level spectra of 1.0 ML Sn/Pd(100) as a function of annealing temperature.

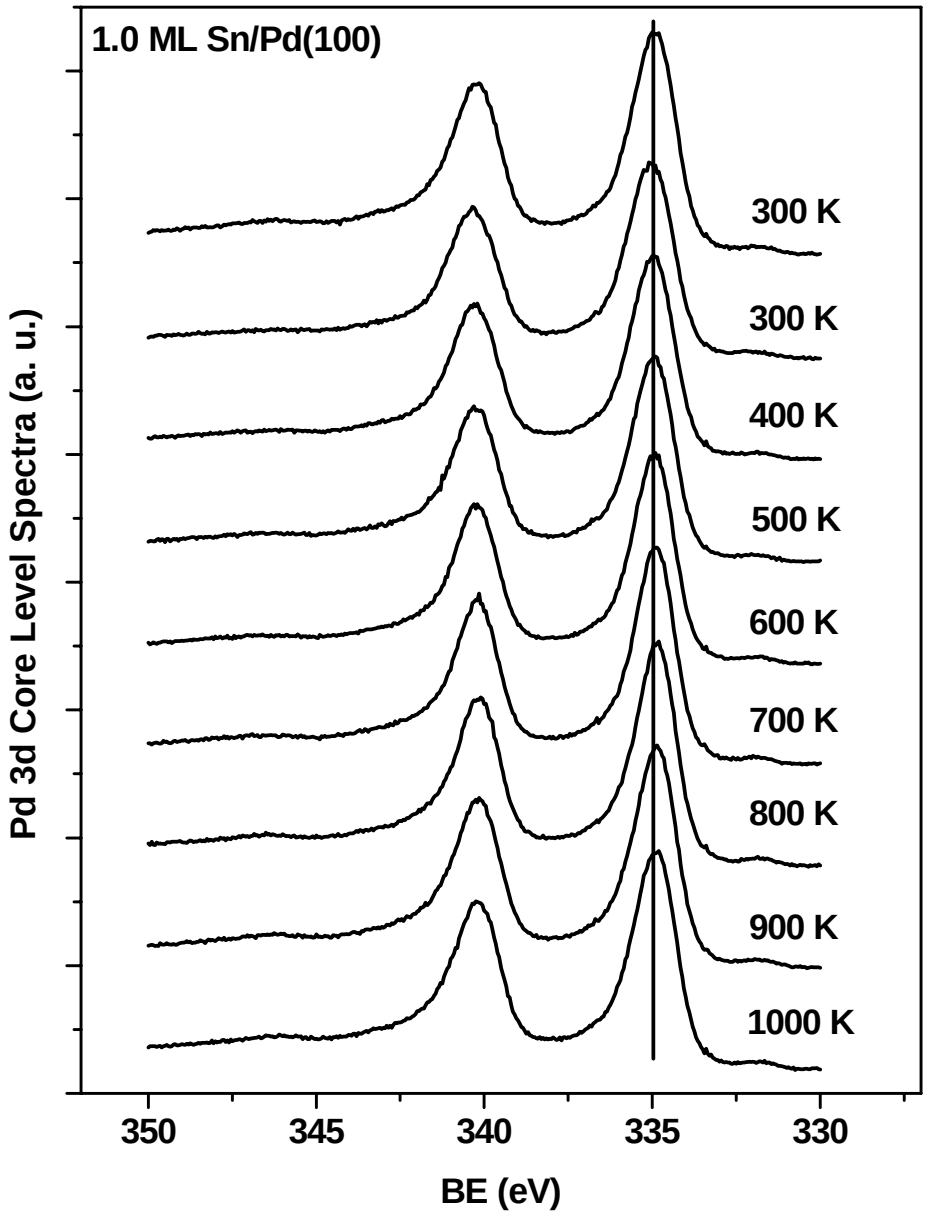

Figure 81. XPS Pd 3d core level spectra of 1.0 ML Sn/Pd(100) as a function of annealing temperature.

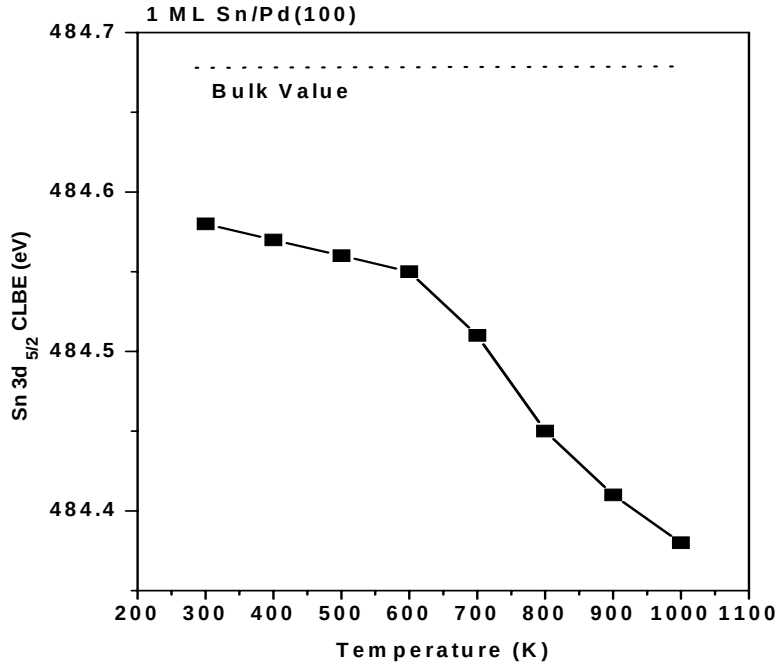

(a)

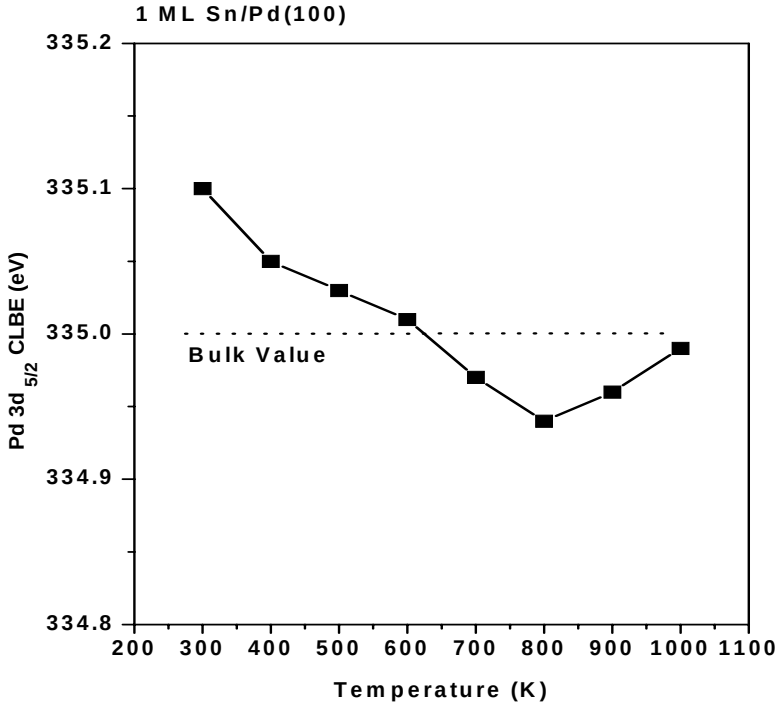

(b)

Figure 82. XPS (a) Sn $3d_{5/2}$ and (b) Pd $3d_{5/2}$ CLBE of 1.0 ML Sn/Pd(100) as a function of annealing temperature.

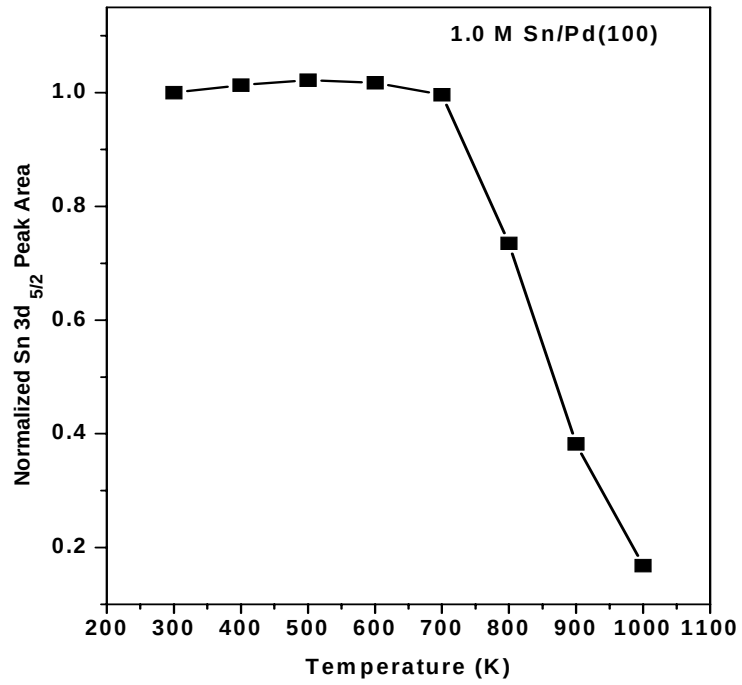

(a)

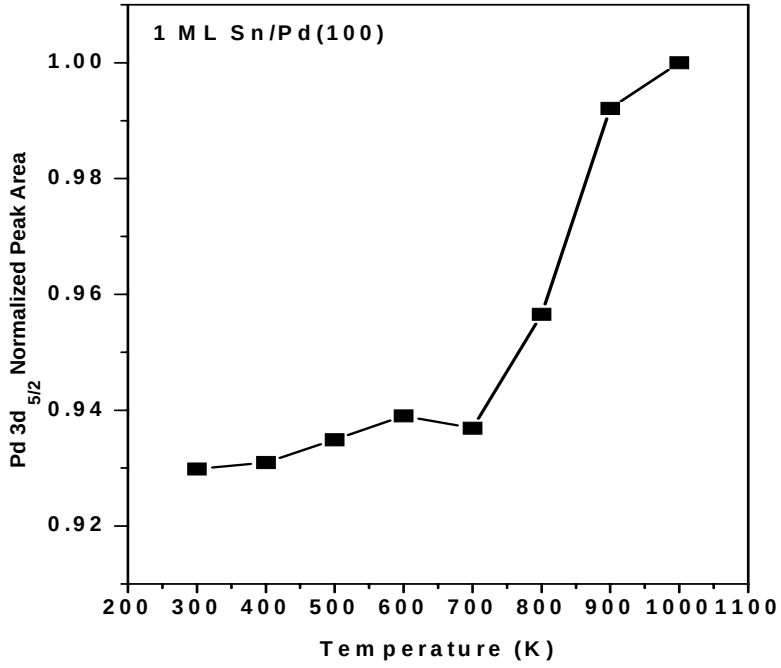

(b)

Figure 83. XPS (a) Sn $3d_{5/2}$ and (b) Pd $3d_{5/2}$ normalized peak area of 1.0 ML Sn/Pd(100) as a function of annealing temperature.

percentage of Pd $3d_{5/2}$ signal intensity originating from the Pd interfacial layer with a high coverage of Sn on top. The difference between the results of Sn/Pd(110), Sn/Pd(100), and Sn/Pd(111) was not well understood here and required further investigations.

The XPS studies were further performed on thermal-related processes on Sn/Pd(100) with various Sn coverages. In Figure 80, Sn 3d core level spectra were shown as a function of annealing temperature for 1.0 ML Sn/Pd(100). No strong peak intensity or CLBE variation occurred as the annealing temperature was scaled to 700 K. A large decrease in intensity and a lower binding energy shift were detected after annealing at 700 K.

The Pd 3d core level peaks were shown in Figure 81 and the CLBE values did not change significantly following Sn deposition and annealing at different temperatures. The CLBE's of Sn $3d_{5/2}$ and Pd $3d_{5/2}$ were plotted as a function of annealing temperature in Figure 82 (a) and (b), respectively. The CLBE position of Sn $3d_{5/2}$ began at *ca.* 0.1 eV less than the bulk value and showed no significant shift at annealing temperatures up to 600 K, where the *c*(2x2) structure was observed. After annealing at 700 K, the peak position shifted toward lower BE, reaching *ca.* 484.4 eV at 1000 K. For Pd $3d_{5/2}$, the CLBE position appeared at 335.1 eV after 1.0 ML Sn deposition, a value slightly higher than the bulk value (335.0 eV). A very small binding energy shift toward the bulk value, after annealing, was observed in Figure 82(b).

To study the intensity variation of the Sn features, the Sn $3d_{5/2}$ (Figure 83 (a)) and Pd $3d_{5/2}$ (Figure 83 (b)) peak intensities were normalized and plotted as a function of

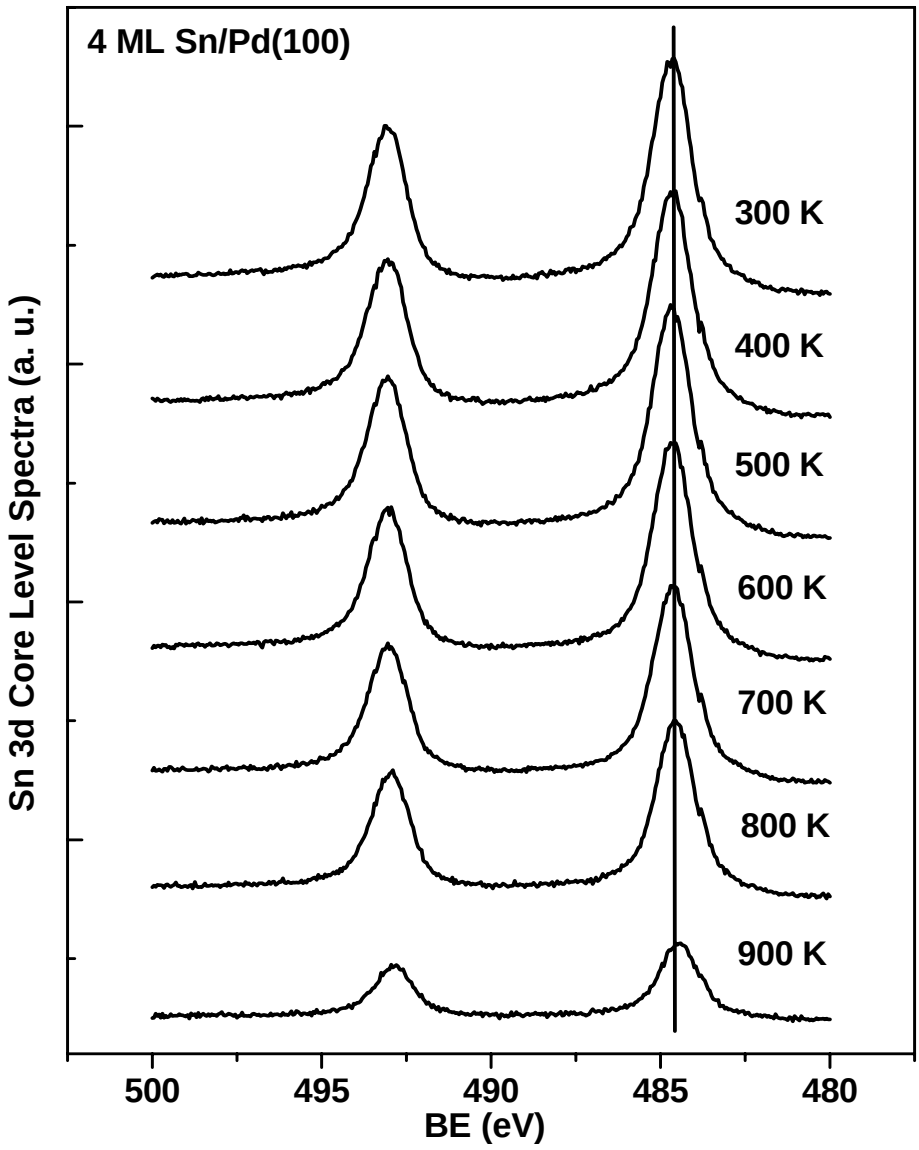

Figure 84. XPS Sn 3d core level spectra of 4.0 ML Sn/Pd(100) as a function of annealing temperature.

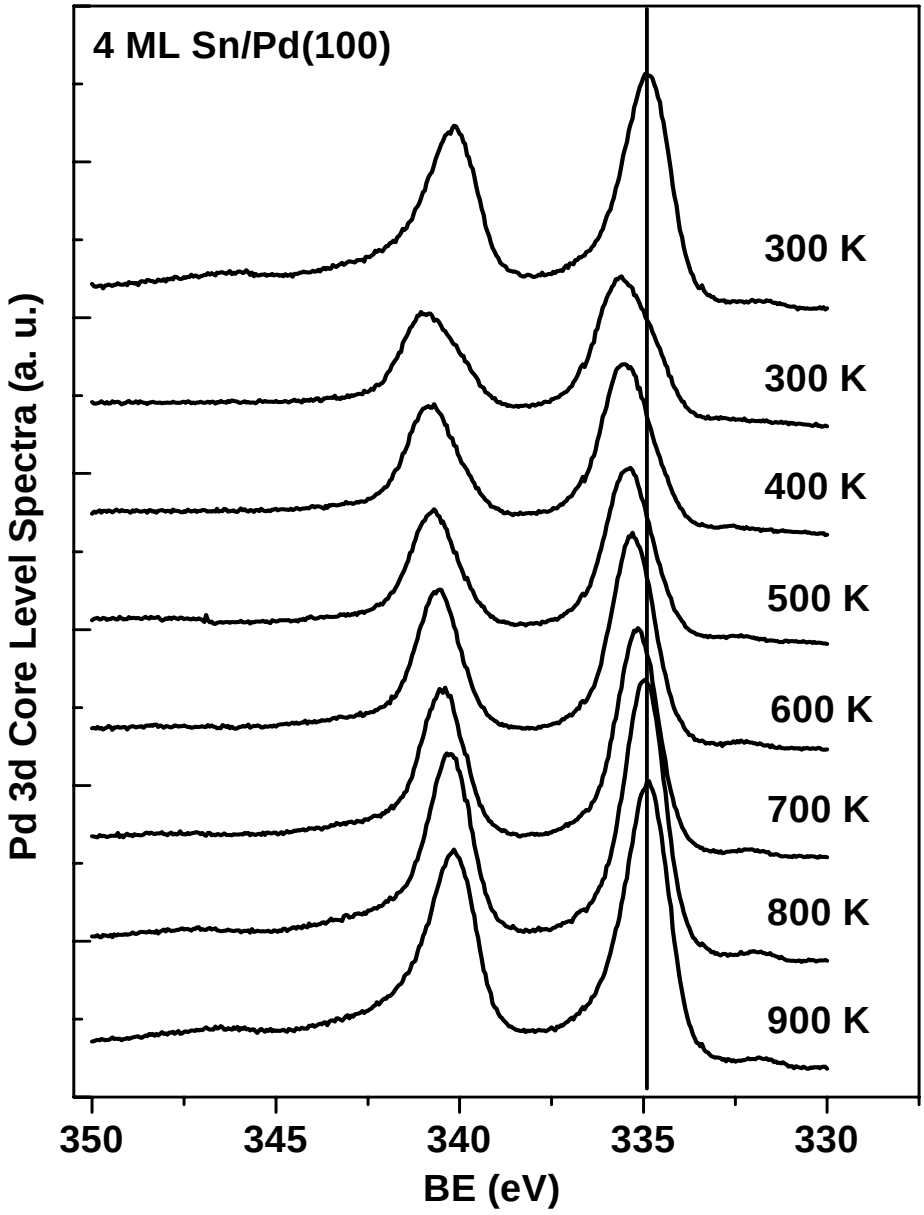

Figure 85. XPS Pd 3d core level spectra of 4.0 ML Sn/Pd(100) as a function of annealing temperature.

temperature. The Sn 3d intensity showed little variation with the annealing temperatures ranging up to 700 K indicating that most Sn components were located in the near surface region. With annealing temperatures of 800 K or above, the Sn 3d intensity decreased rapidly as a result of the diffusion of Sn into the bulk region of the substrate. The flat regions of Sn 3d CLBE and peak intensity at temperatures ranging from 300 to 600 K suggested that the Sn remained on the surface region instead of diffusing into the bulk. This finding may be of benefit in the synthesis of surface alloys.

The Pd 3d intensity, in Figure 83(b), remained essentially constant at annealing temperatures up to 700 K, and then increased rapidly at temperatures higher than 800 K. Based on the different temperature regimes required for Sn surface retention and diffusion, the same conclusions could be drawn from the studies of Pd core level features.

For 4.0 ML Sn/Pd(100), Sn 3d core level spectra were shown as a function of annealing temperature in Figure 84. A decrease in peak intensity, along with a slightly lower BE shift, was detected as the temperature was increased. In Figure 85, a distinctly higher CLBE shift in Pd $3d_{5/2}$ was observed with a large intensity reduction after the deposition of 4.0 ML Sn. A reversal in trends for both BE position and peak intensity was observed as the annealing temperature increased.

In Figure 86(a) and (b), peak positions of Sn $3d_{5/2}$ and Pd $3d_{5/2}$, respectively, are plotted as a function of annealing temperature. The Sn $3d_{5/2}$ BE remained stable as the temperature was increased to 500 K, but later on shifted to lower values at temperatures higher than 600 K. A 0.25 eV negative BE shift relative to the bulk value was detected

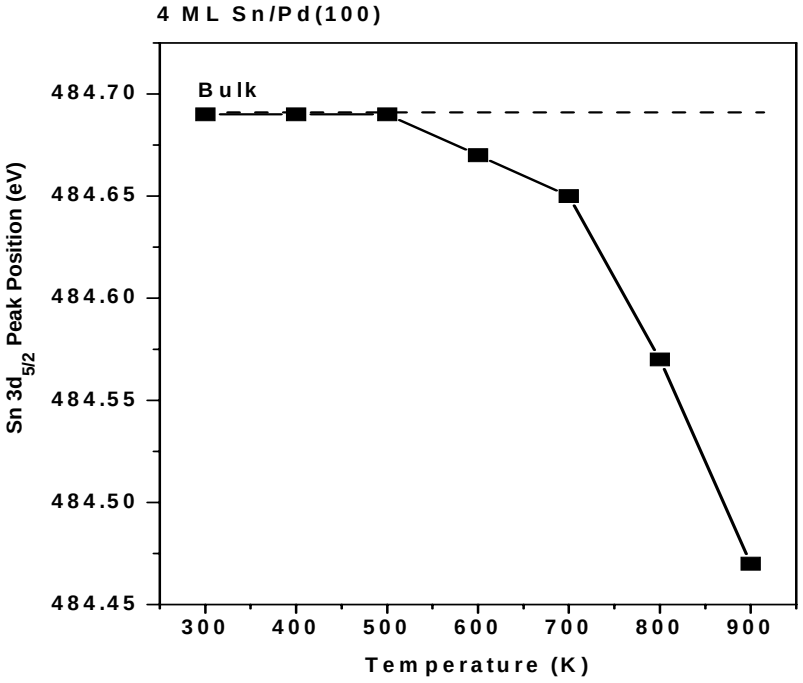

(a)

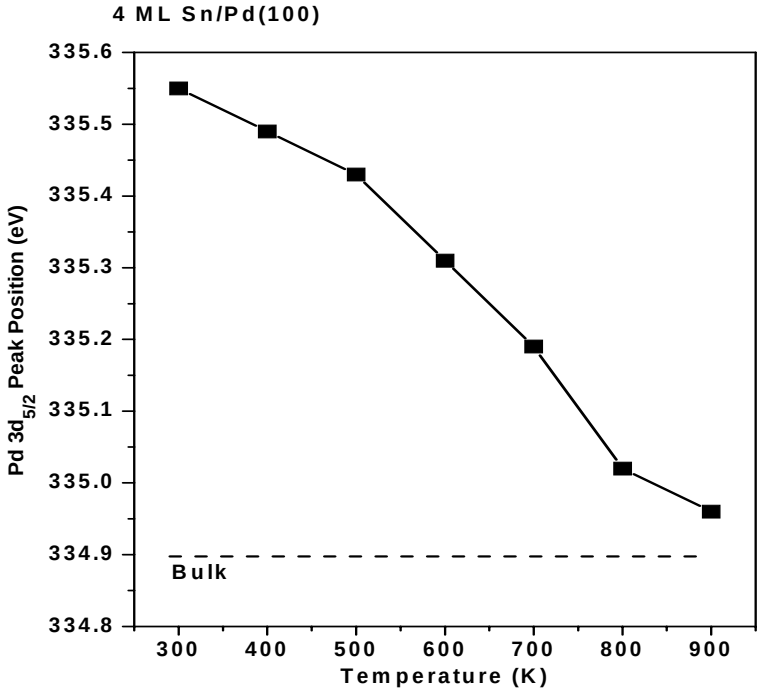

(b)

Figure 86. XPS (a) Sn $3d_{5/2}$ and (b) Pd $3d_{5/2}$ CLBE of 4.0 ML Sn/Pd(100) as a function of annealing temperature.

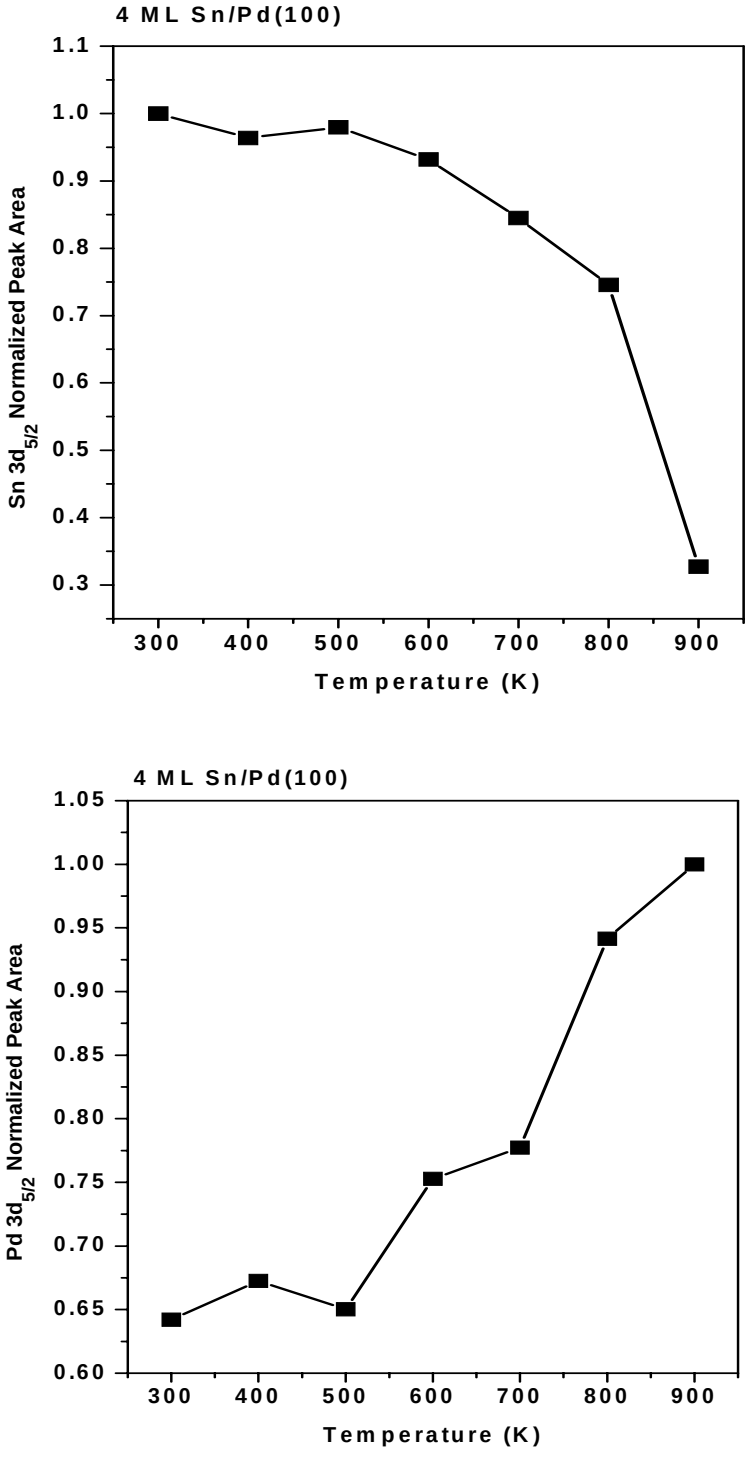

Figure 87. XPS (a) Sn $3d_{5/2}$ and (b) Pd $3d_{5/2}$ normalized peak area of 4.0 ML Sn/Pd(100) as a function of annealing temperature.

after annealing at 900 K. With a large positive (*ca.* 0.7 eV) at the beginning, the Pd $3d_{5/2}$ BE shifted toward lower BE as the temperature increased, reaching approximately the bulk value after a 900 K anneal.

The normalized peak area plots for Sn $3d_{5/2}$ and Pd $3d_{5/2}$ were displayed in Figure 87 (a) and (b), respectively. For Sn $3d_{5/2}$, a gradual decrease in intensity occurred between 300 to 500 K with no significant BE shift, implying that the majority of the Sn existed as overlayers on top of the Pd substrate. Between 600 to 800 K, peak intensity decreased to about 20% of its initial value; a *c*(2x2) pattern was observed using LEED. These changes suggested that Sn atoms diffused into the Pd substrate, leaving a surface layer composed of *ca.* 50 % Sn. Upon an annealing at 900 K, the Sn peak intensity decreased to 30% of the value at 300 K. LEED results also indicated that the surface reverted to a 1x1 structure. The dramatic decrease in XPS Sn 3d intensity suggested that Sn on the near surface region diffused extensively into the bulk. A similar conclusion could be drawn from the variation of Pd core level peak intensity, as seen in Figure 87(b).

In short, both coverage- and temperature-dependent studies of Sn and Pd core level features indicated a strong Sn-Pd interaction in the Sn/Pd(100) system. The surface retained a high percentage of Sn coverage with a well-defined *c*(2x2) alloying structure at certain temperature regions.

CO TPD

CO TPD was used to further study the gas adsorption of the Sn/Pd(100) system. The adsorption/desorption properties of CO on a *c*(2x2) Sn-Pd(100) surface were examined

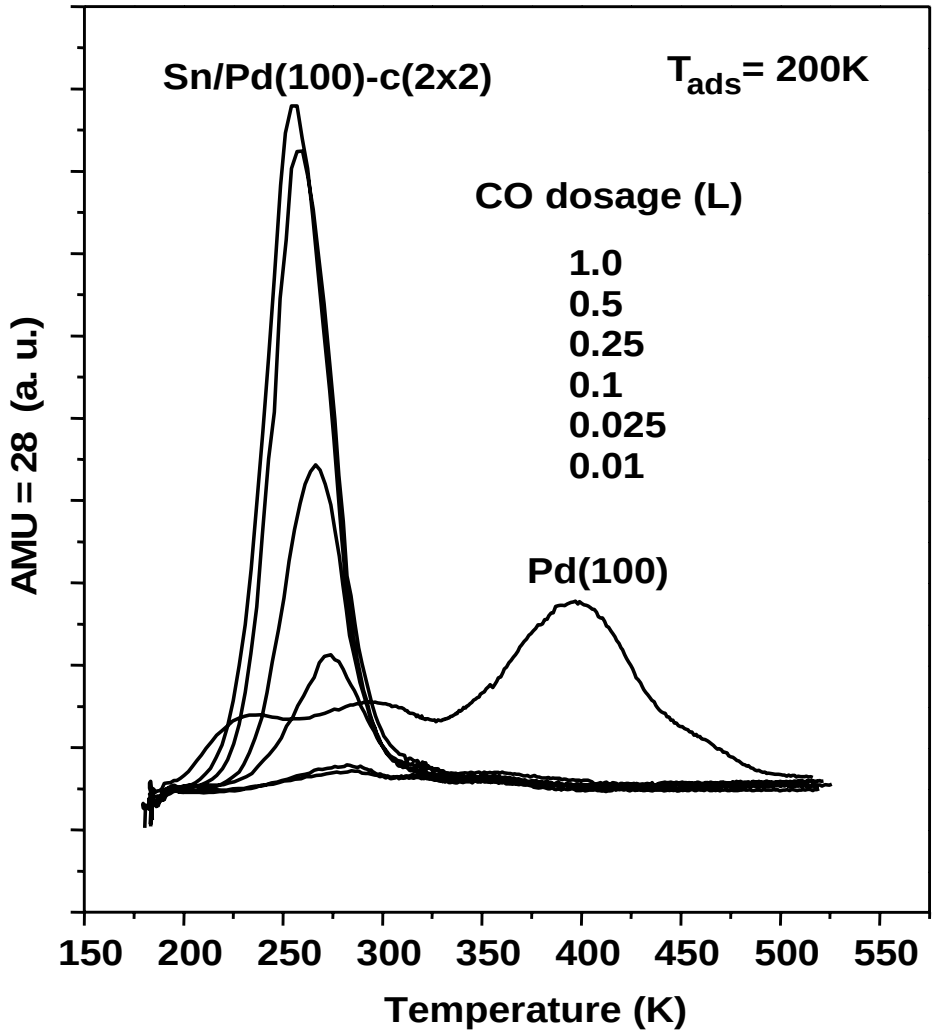

Figure 88. TPD spectra of CO on c(2x2)-1.5 ML Sn/Pd(100) and Pd(100) surfaces.

and compared with of CO on a clean Pd(100). In Figure 88, the CO TPD spectra on a *c*(2x2) Sn-Pd(100) alloy surface, obtained with a coverage of 1.5 ML Sn and a subsequent 600 K annealing, were shown as a function of CO dosage. In addition, CO TPD on a clean Pd(100) surface with saturated CO dosage was also presented. CO adsorption was performed with the substrate temperature of 200 K. On a Pd(100) surface, the largest peak feature was centered at *ca.* 400 K. As was pointed out in earlier discussions of CO-IRAS and TPD studies on different facets of Pd surfaces,[47,63,102,110] this feature was assigned to the adsorption of CO on Pd bridging sites. The features observed in the temperature region from 200 to 300 K were attributed to CO adsorption on atop Pd sites.

With 0.01 L CO dosage on the *c*(2x2) Sn-Pd alloy surface, a small CO desorption feature was observed with a centroid at ~ 275 K. The intensity of the feature increased as the CO dosage increased. The peak position also gradually shifted toward lower temperature with increasing CO dosage. With a saturated CO dosage of 1.0 L, a fairly symmetric CO desorption peak was observed centered at *ca.* 260 K. The peak was assigned to CO adsorbed on a-top Pd sites, i.e., the isolated Pd sites. The center of the desorption feature was about 40 K lower than that of CO on isolated Pd sites in Au-Pd alloy surfaces,[63] indicating a possible difference in Pd electronic structures between two alloy systems, i.e., a ligand effect. When compared to the CO desorption intensity on Pd(100) surface, the large peak intensity from the *c*(2x2) Sn-Pd alloy surface demonstrated that the Sn atoms were greatly dispersed on the Pd(100) surface and had effectively isolated surface Pd atoms. Considering the 1:1 Sn : Pd atomic ratio from

LEIS results and the ball structure derived from the *c*(2x2) LEED pattern in Figure 72, it is likely that a large density of non-contiguous Pd dimers existed on this surface.

Similar CO TPD experiments were performed on the *c*(2x2) Sn-Pd alloy surface obtained with 4.0 ML Sn/Pd(100) and a subsequent 800 K annealing. No significant differences in peak intensity or position were observed when compared to the CO desorption features on the *c*(2x2) alloy surface obtained from 1.5 ML Sn/Pd(100).

CONCLUSIONS

Extensive surface characterization of Au/TiO_x, Au-Pd/Mo(110), Au-Pd/SiO_2, Cu-Pd/Mo(110), and Sn/Pd(100) model catalysts was carried out using a combination of X-ray photoemission spectroscopy (XPS), low energy ion scattering spectroscopy (LEIS), low energy electron diffraction (LEED), infrared reflection absorption spectroscopy (IRAS), and temperature programmed desorption (TPD).

The studies of Au on TiO_x demonstrate a strong interaction between Au and a reduced titania surface. Two-dimensional growth of Au is apparent during initial Au deposition. Furthermore the relatively strong interaction between the reduced titania support with Au compared with Au and TiO_2 leads to electron-rich Au, a likely contributor to the unique chemical/catalytic properties of supported Au clusters.

Au-Pd bimetallic model catalysts were synthesized under ultra-high vacuum conditions as planar surfaces on Mo(110) and well-dispersed alloy clusters on SiO_2 ultra-thin films. Stable Pd-Au alloy surfaces, where the surface was significantly enriched in Au relative to the bulk, were obtained upon sequential deposition of Pd and Au followed by an anneal. Characteristic isolated Pd sites were identified on the Au-Pd planar surfaces and silica supported Au-Pd clusters. Thermal desorption of ethylene and acetic acid on these surfaces show a clear structure-activity correlation with respect to these Au-Pd model surfaces.

The surface composition with various annealing temperatures and bulk Cu/Pd atomic ratios was quantitatively studied, and significant Cu surface enrichment results upon annealing to 600 K. At temperatures higher than 600K, surface morphological changes

are proposed. In contrast to the Au-Pd systems with the same atomic ratio, surface segregation of Cu was not as extensive as that for Au. The electronic properties were monitored during the alloying process and the differences are discussed for both systems.

A *c*(2x2) adlattice of equimolar Sn and Pd was generated upon thermally annealing Sn films on Pd(100). This adlayer geometry maximizes the density of noncontiguous Pd dimers on the surface and provides an excellent model for further surface reaction studies.

In this work, we successfully synthesized and probed a few surface model catalysts using the UHV and surface science techniques. Among them, the approach of growing bimetal atomic overlayers on a third refractory metal substrate (or an oxide support) and subsequent thermal treatments offers a new methodology to conveniently synthesize bimetallic model catalysts with different surface vs. bulk compositions. From the observation of isolated Pd active sites on Au-Pd surfaces to the optimization of this surface ensemble density on Sn-Pd surfaces, our studies show a clear pathway for developing and designing new model catalysts for atomic-level investigations. These studies offer unlimited possibilities for investigating a spectrum of mixed-metal systems and how their surface structure relates to catalytic function.

REFERENCES

(1) Davis, B. H. Development of the Science of Catalysis. In *Handbook of Heterogeneous Catalysis*; Ertl, G., Knozinger, H., Weitkamp, J., Eds.; VCH: Weinheim, Federal Republic of Germany, 1997; Vol. 1; p 12.

(2) Somorjai, G. A. *Introduction to Surface Chemistry and Catalysis*; John Wiley and Sons: Ithaca, NY, 1994.

(3) Gaines, G. L.; Wise, G. *Heterogeneous Catalysis. Selected American Histories*; Davis, B. H., Hettinger, W. P., Eds., American Chemical Society, Washington, D. C., 1983; Vol. 222; p 13.

(4) Haruta, M.; Tsubota, S.; Kobayashi, T.; Kageyama, H.; Genet, M. J.; Delmon, B. *J. Catal.* **1993**, *144*, 175.

(5) Arrii, S.; Morfin, F.; Renouprez, A. J.; Rousset, J. L. *J. Am. Chem. Soc.* **2004**, *126*, 1199.

(6) Haruta, M. *Catal. Today* **1997**, *36*, 153.

(7) Haruta, M. *CATTECH* **2002**, *6*, 102.

(8) Pietron, J. J.; Stround, R. M.; Rolison, D. R. *Nano. Lett.* **2002**, *2*, 545.

(9) Schubert, M. M.; Hackenberg, S.; van Veen, A. C.; Muhler, M.; Plzak, V.; Behm, R. J. *J. Catal.* **2001**, *197*, 113.

(10) Guzman, J.; Gates, B. C. *J. Am. Chem. Soc. Commu.* **2004**, *126*, 2672.

(11) Chen, M. S.; Goodman, D. W. *Science* **2004**, *306*, 252.

(12) Goodman, D. W. *Catal. Lett.* **2005**, *99*, 1.

(13) Campbell, C. T. Bimetallic Model Catalysts. In *Handbook of Heterogeneous Catalysis*; Ertl, G., Knozinger, H., Weitkamp, J., Eds.; VCH: Weinheim, Federal Republic of Germany, 1997; Vol. 2; p 814.

(14) Campbell, C. T. *Annu. Rev. Phys. Chem.* **1990**, *41*, 775.

(15) Chen, X.; Goodman, D. W. *Surf. Sci.* **1996**, *360*, 249.

(16) Sellidj, A.; Koel, B. E. *Surf. Sci.* **1993**, *284*, 139.

(17) Yang, Y.-W.; Lin, J. C.; Engel, T. *Surf. Sci.* **1993**, *289*, 267.

(18) Zhao, H.; Koel, B. E. *Surf. Sci.* **2004**, *572*, 261.

(19) Zhao, H.; Koel, B. E. *J. Catal* **2005**, *234*, 24.

(20) Provine, W. D. M., P. L.; Lerou, J. J. *Stud. Surf. Catal.* **1996**, *101*, 191.

(21) Choudhary, T. V.; Sivadinarayana, C.; Datye, A. K.; Kumar, D.; Goodman, D. W. *Catal. Lett.* **2003**, *86*, 1.

(22) Bissot, C. T. *US Patent* **1977**, 4.

(23) Crathorne, C. T.; MacGowan, D.; Morris, S. R.; Rawlinson, A. P. *J. Catal.* **1994**, *149*, 54.

(24) Bonarowska, M.; Malinowski, A.; Juszceyk, W.; Karpinski, Z. *Appl. Catal. B: Environment* **2001**, *30*, 187.

(25) Malinowski, A. *Polish J. Chem.* **2002**, *76*, 1461.

(26) Choi, K. I.; Vannice, M. A. *J. Catal.* **1991**, *131*, 36.

(27) Anderson, J. A.; Fernández-Garcis, M.; Haler, G. L. *J. Catal.* **1996**, *164*, 477.

(28) Illas, F.; López, N.; Ricart, J. M.; Clotet, A. *J. Phys. Chem. B* **1998**, *102*, 1913.

(29) Logan, A. D.; Paffett, M. T. *J. Catal.* **1992**, *133*, 179.

(30) Hamm, G.; Schmidt, T.; Breitbach, J.; Franke, D.; Becker, C.; Wandelt, K. *Surf. Sci.* **2004**, *562*, 170.

(31) Tsud, N.; Skala, T.; Sutara, F.; Veltruska, K.; Dudr, V.; Fabik, S.; Sedlacek, L.; Chab, V.; Prince, K. C.; Matolin, V. *Surf. Sci.* **2005**, *595*, 138.

(32) Lee, A. F.; Baddeley, C. J.; Tikhov, M. S.; Lambert, R. M. *Surf. Sci.* **1997**, *373*, 195.

(33) Okamoto, H.; Massalski, T. B. In *Binary Alloy Phase Diagrams*; 2nd ed.; Massalski, T. B., Ed.; ASM International, 1990; Vol. 1; p 409.

(34) Okamoto, H.; Massalski, T. B. *Bulletin of Alloy Phase Diagram* **1985**, *6*, 229.

(35) Wood, B. J.; Wise, H. *Surf. Sci.* **1975**, *52*, 151.

(36) Jablonski, A.; Overbury, S. H.; Somorjai, G. A. *Surf. Sci.* **1977**, *65*, 578.

(37) Varga, P.; Hetzendorf, G. *Surf. Sci.* **1985**, *162*, 544.

(38) Yamanaka, J.; Nakamura, Y.; Nittono, O. *Mat. Sci. Eng.* **1994**, *A179/A180*, 401.

(39) Hilaure, L.; Legare, P.; Holl, Y.; Maire, G. *Surf. Sci.* **1981**, *103*, 125.

(40) Swartzfager, D. G.; Ziemecki, S. B.; Kelley, M. J. *J. Vac. Sci. Technol.* **1981**, *19*, 185.

(41) Anton, R.; Eggers, H.; Veletas, J. *Thin Solid Films* **1993**, *226*, 39.

(42) Lee, Y.-S.; Jeon, Y.; Chung, Y.-D.; Lim, K.-Y.; Whang, C.-N.; Oh, S.-J. *J. Korean Phys. Soc.* **2000**, *37*, 451.

(43) Weissman-Wenocur, D. L.; Stefan, P. M.; Pate, B. B.; Shek, M. L.; Lindau, I.; Spicer, W. E. *Phys. Rev. B* **1983**, *27*, 3308.

(44) Koel, B. E.; Sellidj, A. *Phys. Rev. B* **1992**, *46*, 7846.

(45) Maroun, F.; Ozanam, F.; Magnussen, O. M.; Behm, R. J. *Science* **2001**, *293*, 1811.

(46) Rainer, D. R.; Corneille, J. S.; Goodman, D. W. *J. Vac. Sci. Technol. A* **1995**, *13*, 1595.

(47) Rainer, D. R.; Xu, C.; Holmblad, P. M.; Goodman, D. W. *J. Vac. Sci. Technol. A* **1997**, *15*, 1653.

(48) Davis, R. J.; Boudart, M. *J. Phys. Chem.* **1994**, *98*, 5471.

(49) Refsnyder, S. N.; Lamb, H. H. *J. Phys. Chem. B* **1999**, *103*, 321.

(50) Kaszkur, Z. *Phys. Chem. Chem. Phys.* **2004**, *6*, 193.

(51) de Siervo, A.; Soares, E. A.; Landers, R.; Fazan, A.; Morais, J.; Kleiman, G. G. *Surf. Sci.* **2002**, *504*, 515.

(52) Reilly, J. P.; Barnes, C. J.; Price, N. J.; Bennett, R. A.; Poulston, S.; Stone, P.; Bowker, M. *J. Phys. Chem. B* **1999**, *103*, 6251.

(53) Garces, J. E.; Bozzolo, G. H.; Abel, P.; Mosca, H. O. *Appl. Surf. Sci.* **2000**, *167*, 18.

(54) Garces, J. E.; Bozzolo, G. H.; Mosca, H. O. *Surf. Sci.* **2000**, *459*, 365.

(55) Pope, T. D.; Vos, M.; Tang, H. T.; Griffiths, K.; Mitchell, I. V.; Norton, P. R.; Liu, W.; Li, Y. S.; Mitchell, K. A. R.; Tian, Z.-J.; Black, J. E. *Surf. Sci.* **1995**, *337*, 79.

(56) Liu, G.; St. Clair, T. P.; Goodman, D. W. *J. Phys. Chem. B* **1999**, *103*, 8578.

(57) Asonen, H.; Barnes, C.; Salokatve, A.; Vuoristo, A. *Appl. Surf. Sci.* **1985**, *22/23*, 556.

(58) Mårtenssson, N.; Nyholm, R.; Calén, H.; Hedman, J. *Phys. Rev. B* **1981**, *24*, 1725.

(59) Menon, M.; Khanra, B. C. *Indian Journal of Chemistry* **1998**, *37A*, 795.

(60) Anderson, T. H.; Bech, L.; Li, Z.; Hoffmann, S. V.; Onsgaard, J. *Surf. Sci.* **2004**, *559*, 111.

(61) Loboda-Cackovic, J. *Vacuum* **1996**, *47*, 1405.

(62) Logan, A. D.; Paffett, M. T. In *Proceedings of the 12th North American Conference on Catalysis,* Lexington, KY **1991,** A20.

(63) Yi, C.-W.; Luo, K.; Wei, T.; Goodman, D. W. *J. Phys. Chem. B* **2005**, *109*, 18535.

(64) Luo, K.; Wei, T.; C.-W., Y.; Axanada, S.; Goodman, D. W. *J. Phys. Chem. B* **2005**, *109*, 23517.

(65) Chen, M. S.; Kumar, D.; Yi, C.-W.; Goodman, D. W. *Science* **2005**, *310*, 291.

(66) Luo, K. Spectroscopic Studies of Metal Growth on Oxides. Master's Thesis, Texas A&M University, 2000.

(67) Woodruff, D. P.; Delchar, T. A. *Modern Techniques of Surface Science*, 2nd ed., Cambridge University Press: Cambridge, 1994.

(68) Chen, M. S.; Wallace, W. T.; Kumar, D.; Zen, Y.; Gath, K. K.; Cai, Y.; Kuroda, Y.; Goodman, D. W. *Surf. Sci.* **2005**, *581*, L115.

(69) Luo, K.; Kim, D. Y.; Goodman, D. W. *J. Mol. Catal. A: Chemical* **2001**, *167*, 191.

(70) Musket, R. G.; McLean, W.; Colmenares, C. A.; Makowieki, D. W. *Surf. Sci.* **1982**, *10*, 143.

(71) Zhang, L.; Persaud, R.; Madey, T. E. *Phys. Rev. B* **1997**, *56*, 10549.

(72) Valden, M.; Lai, X.; Goodman, D. W. *Science* **1998**, *281*, 1647.

(73) Chusuei, C.; Lai, X.; Luo, K.; Guo, Q.; Goodman, D. W. *Topics in Catal.* **2001**, *14*, 71.

(74) Yang, Z.; Wu, R. *Phys. Rev. B* **2000**, *61*, 14066.

(75) Yang, Z.; Wu, R. *Phys. Rev. B* **2003**, *67*, 081403.

(76) Okazaki, K.; Morilawa, Y.; Tanaka, K.; Kohyama, M. *Phys. Rev. B* **2004**, *69*, 235404.

(77) Lopez, N.; Nørskov, J. K. **2002**, *515*, 175.

(78) Lopez, N.; Nørskov, J. K.; Janssens, T. V. W.; Carlsson, A.; Puig-Molina, A.; Clausen, B. S.; Grunwaldt, J.-D. *J. Catal.* **2004**, *225*, 86.

(79) Goodman, D. W. Catalysis by Supported Gold Nanoclusters. In *Dekker Encyclopedia Of Nanoscience And Nanotechnology;* Schwarz , J. A., Contescu, C. I., Putyera, K., Eds.; Marcel Dekker: New York, 2004.

(80) Rodriguez, J. A.; Liu, G.; Jirsak, T.; Chang, Z.; Dvorak, J.; Maiti, A. *J. Am. Chem. Soc.* **2002**, *124*, 5242.

(81) Meier, D. C.; Goodman, D. W. *J. Am. Chem. Soc.* **2004**, *126*, 1892.

(82) Sykes, E. C. H.; Williams, F. J.; Tikhov, M. S.; Lambert, R. M. *J. Phys. Chem. B* **2002**, *106*, 5390.

(83) Xu, C.; Oh, W. S.; Liu, G.; Kim, D. Y.; Goodman, D. W. *J. Vac. Sci. Technol. A* **1997**, *15*, 1261.

(84) Magkoev, T. T.; Rosenthal, D.; Schröder, S. L. M.; Christmann, K. *Technical Physics Letters* **2000**, *26*, 894.

(85) Mason, M. G. *Phys. Rev. B* **1983**, *27*, 748.

(86) Vijay, A.; Mills, G.; Metiu, H. *J. Chem. Phys.* **2003**, *118*, 6536.

(87) Rodriguez, J. A.; Kuhn, M. *Surf. Sci.* **1995**, *330*, L657.

(88) Kuntze, J.; Speller, S.; Heiland, W. *Phys. Rev. B* **2000**, *60*, 1535.

(89) Piaszenski, G.; Aschoff, M.; Speller, S.; Heiland, W. *Nucl. Instr. Meth. Phys. Reas. B* **1998**, *135*, 331.

(90) Litovchenko, V. G.; Gorbanyuk, T. I.; Efremov, A. A.; Evtukh, A. A.; Schipanski, D. *Sensors and Actuators: A: Physical A* **1999**, *74*, 233.

(91) Xu, C.; Goodman, D. W. *Surf. Sci.* **1996**, *360*, 249.

(92) Guo, X. C.; Yates, J. T. *J. Chem. Phys.* **1989**, *90*, 6761.

(93) Guo, X.; Madix, R. J. *J. Am. Chem. Soc.* **1995**, *117*, 5523.

(94) Shaikhutdinov, S.; Heemeier, M.; Baumer, M.; Lear, T.; Lennon, D.; Oldman, R. J.; Jackson, S. D.; Freund, H.-J. *J. Catal.* **2001**, *200*, 330.

(95) Stuve, E. M.; Madix, R. J. *Surf. Sci.* **1985**, *152/153*, 1985.

(96) Frank, M.; Baumer, M. *Phys. Chem. Chem. Phys.* **2000**, *2*, 3723.

(97) Gates, J. A.; Kesmodel, L. L. *Surf. Sci.* **1983**, *124*, 68.

(98) Haley, R. D.; Tikhov, M. S.; Lambert, R. M. *Catal. Lett.* **2001**, *76*, 125.

(99) Chen, M. S.; Luo, K.; Wei, T.; Yan, Z.; Kumar, D.; Yi, C.-W.; Goodman, D. W. *Catalysis Today*, *in press*.

(100) Bowker, M.; Morgan, C.; Couves, J. *Surf. Sci.* **2004**, *555*, 145.

(101) Davis, J. L.; Barteau, M. A. *Langmuir* **1989**, *5*, 1299.

(102) Unterhalt, H.; Rupprecher, H.; Freund, H.-J. *J. Phys. Chem. B* **2002**, *106*, 356.

(103) Wolter, K.; Seiferth, O.; Kuhlenbeck, H.; Baumer, M.; Freund, H.-J. *Surf. Sci.* **1998**, *399*, 190.

(104) Xu, X.; Goodman, D. W. *J. Phys. Chem.* **1993**, *97*, 7711.

(105) Xu, X.; Szanyi, J.; Xu, Q.; Goodman, D. W. *Catal. Today* **1994**, *21*, 57.

(106) Min, B. K.; Santra, A. K.; Goodman, D. W. *J. Vac. Sci. Technol. A* **2003**, *21*, 2319.

(107) Min, B. K.; Santra, A. K.; Goodman, D. W. *Catal. Today* **2003**, *85*, 113.

(108) Min, B. K.; Wallace, W. T.; Santra, A. K.; Goodman, D. W. *J. Phys. Chem. B* **2004**, *108*, 16339.

(109) Carlsson, A. F.; Naschitzki, M.; Baumer, M.; Freund, H.-J. *J. Phys. Chem. B* **2003**, *107*, 778.

(110) Szanyi, J.; Kuhn, W. K.; Goodman, D. W. *J. Vac. Sci. Technol. A* **1993**, *11*, 1971.

(111) Lemire, C.; Meyer, R.; Shaikhutdinov, S. K.; Freund, H.-J. *Surf. Sci.* **2004**, *552*, 27.

(112) Gelin, P.; Siedle, A. R.; Yates, J. T. *J. Phys. Chem.* **1984**, *88*, 2978.

(113) Rainer, D. R.; Wu, M.-C.; Mahon, D. I.; Goodman, D. W. *J. Vac. Sci. Technol. A* **1996**, *14*, 1184.

(114) Mezey, L. Z.; Giber, J. *J. Jpn. J. Appl. Phys.* **1982**, *21*, 1569.

(115) Overbury, S. H.; Bertrand, P. A.; A., S. G. *Chemical Review* **1975**, *75*, 547.

(116) Ross, P. N.; Haner, A. N. *Surf. Sci.* **1991**, *249*, 15.

VITA

Kai Luo
Department of Chemistry
Texas A&M University
College Station, TX 77843-3255

EDUCATION

2004-2006 Texas A&M University, College Station, Texas
Ph. D. Chemistry

1997-2000 Texas A&M University, College Station, Texas
M. S. Chemistry

1989-1993 Jilin University, Changchun, China
B. S. Chemistry

SELECTED PUBLICATIONS

Luo, K.; Yi, C.-W.; Wei, T.; Axnanda, S.; Goodman, D.W. "Preparation and characterization of silica supported Au-Pd model catalysts." *Journal of Physical Chemistry B* **2005**, 109, 23517.

Yi, C.-W.; **Luo, K.**; Wei, T; Goodman, D.W. "Surface composition and structure of Pd-Au surfaces." *Journal of Physical Chemistry B* **2005**,109,18535.

Luo, K.; Lai, X.; Yi, C.-W.; Davis, K. A.; Goodman, D. W. "Silver growth on an ordered alumina surface." *Journal of Physical Chemistry B* **2005**,109, 4064.

Chen, M. S.; **Luo, K**.; Wei, T.; Yan, Z.; Kumar, D.; Yi, C.-W.; Goodman, D. W. "The nature of the active site for vinyl acetate synthesis over Pd-Au." *Catalysis Today*, in press.

Luo, K.; Kim D. Y.; Goodman, D.W. "The nucleation and growth of gold on silica." *Journal of Molecular Catalysis A: Chemical* **2001**, 167,191.

Luo, K.; St. Clair, T. P.; Lai, X.; Goodman, D.W. "Silver growth on TiO_2(110) (1x1) and (1x2)" *Journal of Physical Chemistry B* **2000**,104,3050.